Radio Spectral Index Distribution in Galaxy Cluster Radio Halos

A thesis
Submitted in partial fulfillment of the requirements
of the degree of
Doctor of Philosophy

by

A. Shweta

INDIAN INSTITUTE OF SCIENCE EDUCATION AND RESEARCH, PUNE

December, 2018

DEDICATION
Mother, Father and Anvita

CERTIFICATE

Certified that the work incorporated in this thesis entitled 'Radio Spectral Index Distribution in Galaxy Cluster Radio Halos' submitted by A. Shweta was carried out by the candidate, under my supervision. The work presented here or any part of it has not been included in any other thesis submitted previously for the award of any degree or diploma from any other University or institution.

Date: 26.12.2018

Dr. Ramana Athreya
Supervisor

DECLARATION

I declare that, this written submission represents my ideas in my own words and where others' ideas have been included, I have adequately cited and referenced the original sources. I also declare that I have adhered to all principles of academic honesty and integrity and have not misrepresented or fabricated or falsified any idea/data/fact/source in my submission. I understand that violation of the above will be cause for disciplinary action by the Institute and can also evoke penal action from the sources which have thus not been properly cited or from whom proper permission has not been taken when needed.

Date: 26.12.2018

A. Shweta
Roll No: 20113144

ACKNOWLEDGEMENTS

I would like to thank my supervisor Dr. Ramana Athreya for his continuous help and support throughout my PhD. During the course of my PhD years, there have been various hurdles at a personal front. I am especially grateful to him for understanding my constraints and giving me the freedom to work at my own pace. I am also thankful to my RAC members Dr. Ishwara Chandra and Dr. Prasad Subramanian for their suggestions, which has helped me in my research work.

I would like to thank IISER Pune for the facilities, financial support and a good working environment. IISER Pune has evolved a lot in all these years; walking through the campus has inspired various thoughts in me. I would like to thank the GMRT commitee for the telescope time; staff for help in carrying out the observations.

I thank my lab-mate Krishna who has developed some of the software tools that has been used in this thesis work. I am extremely grateful to my friends Amruta, Kajari, Mahendra, Shishir for being there for me in some of the most difficult phases of my life.

My PhD would have definitely not been possible without the strong support of my family. I thank my husband Vasu, and my sister for encouraging me to carry on in times when I lost all hope. Immense help has been provided by my parents, especially my father, my aunts (Kiran Mousi and Usha Mousi) and in-laws, who have gone out of their ways to look after me and my baby. If it had not been for them, I would not have been able to successfully pursue my PhD. Lastly, I am thankful to my 'chubby two-year-old', who kept me entertained and stress-free in the later stages of my PhD.

Synopsis

The aim of the thesis is to investigate locations, and the process therein, in which the energization of galaxy cluster radio halos happen. This was carried out using spatial distribution of radio spectral index in radio halos using low frequency ($\leq$ 610 MHz) observations with the GMRT (Giant Metrewave Radio Telescope, Pune, India).

Radio halos are diffuse, Mpc-sized radio structures that fill the intra-cluster medium (ICM) of clusters of galaxies. They are not associated with any individual cluster galaxy and are exclusively found in merging clusters (identified by signs of disturbance in optical and X-ray). The Mpc-scale of emission implies that relativistic particles (Lorentz γ=10^4-10^5), and magnetic fields fill the cluster volume. From Faraday rotation measures micro-Gauss magnetic field is inferred to be present in clusters. Unlike radio galaxies, where synchrotron emitting electrons in lobes originate from compact cores, in radio halos the source of energetic electrons is still unknown. Their low diffusion speed (of the order of 100 km/s) requires that the travel time for electrons to traverse the Mpc scale halo is an order of magnitude higher than the time duration over which they lose most of their energies ($10^7 - 10^8$ years). This implies that a halo cannot have a single location of energization but the electrons have to be locally energized throughout the halo. It is believed that shocks and turbulence generated during cluster mergers impart energy to the electrons (*Primary model* for the origin of halos). However, particle acceleration mechanisms are not fully understood in cluster environments, due to the observed low shock Mach number, and turbulence which is a less efficient process (and has yet to be detected). Simulations suggest that up to 30% of the thermal energy of ICM can be stored in the form of turbulent waves; the halo phenomenon can be explained if just a few per cent of the turbulent energy is dissipated while energizing the non-thermal components. This model fits with the observations that all halos discovered till now have been associated with dynamically disturbed clusters, where we expect shocks and turbulence in the ICM. Also, this model assumes that there is a pre-existing population of mildly relativistic electrons in the ICM. Spatially resolved radio spectral index images can provide clues to the energization locations in halos. As per our current understanding, the signatures seen in spectral index images, should therefore correlate with the cluster merger geometry.

In last 5 decades more than 60 halos have been discovered. Their faint emission and lack of definite structure pose a problem in imaging them with good detail. As such, spectral index images are available for only a dozen halos mostly between 325 and 1400 MHz, and with arcminute resolution. They have very steep spectra ($\alpha = -1$ to -2), which means they are better targets at low radio frequencies ($<$ 400 MHz). However, RFI is a major problem at low frequencies and only 10 halos have been observed below 200 MHz. A clear link between halo features and cluster merger geometry has been observed on only a small fraction of objects, even of those with a spectral index image.

The GMRT offers good UV-coverage to image these objects with sufficient sensitivity and resolution. We targeted five halos — A2163, A665, A2744, A520 and A773 – at 150, 325 and 610 MHz. At 150 MHz radio frequency interference (RFI) is a major issue, which makes imaging of diffuse and extended halo emission difficult. The results

presented here are some of the most sensitive images of halos at 150 MHz. For three halos, we have observed a link between spectral index images and the cluster merger geometry. This fits with the current notion that cluster mergers power halos.

Data was processed using the standard Astronomical Image Processing Software (AIPS) and Common Astronomy Software Applications (CASA), as well as in-house tools (RfiX and GRIDFLAG) developed to mitigate RFI. Rfix was applied on the raw GMRT data to mitigate persistent and broadband RFI, while salvaging the true visibilities under the RFI. Intermittent RFI in post-imaging residual visibilities were flagged using GRIDFLAG. We anchored our flux density scale to that defined by sources common to both NVSS and TGSS catalogues. We constructed spectral indices images by matching resolution between frequencies through regridding in the image plane as well as imaging using matched UV in the visibility plane. The resulting spectral index images were compared to optical and X-ray images to understand the relationships between the three.

An important result of the current work is the first detection of a sharply-defined bright structure in the halo in A2163. This structure, which we call the '*ridge*', is detected at a high significance in the 153 and 332 MHz images, is the only halo structure detected in the archival 617 MHz image, and is also prominent in the spectral index image. The *ridge* has the flattest spectrum in the entire halo, and lies between two merging sub-clusters. The flat-spectrum nature of the *ridge*, suggesting that it may be one of the principal sites of energisation of electrons, and its location in the region of a recent merger activity, makes a strong case that cluster mergers power radio halos.

We have also observed a similar flat-spectrum feature in the halo in the cluster A665. Although, here the intensity images do not show a very strong jump in surface brightness. For A2744, we have again detected flat-spectrum structures co-spatial with merging galaxy groups. Observations of these halos do not favour the secondary model of halo origin, thus indirectly favouring the alternative of turbulent-acceleration.

The complex merging geometries, lack of dominant features in spectral index images, presence of confounding, superposed point sources within the halo, and low halo brightness and size have made the interpretation of spectral index images of A520 and A773 difficult. Although, we did observe a peak in radio emission at the location of shock in A520, which is consistent with shock acceleration of electrons.

Based on the presence of a number of radio galaxies in and around the halo A2163, we propose a model to account for the presence of synchrotron electrons and magnetic fields in the ICM. Our model is based on the premise that radio galaxies show multiple episodes of jet activities. We propose that a halo is a collection of many dead lobes of AGNs, currently invisible due to our sensitivity limit, and re-energised by shocks and turbulence during a cluster merger. We calculated the time-scale for disappearance of the dead radio lobes and the energy required to make them visible again. Our estimates suggest that cluster turbulence/shocks have to increase the energies of the lobes by only a factor of few to account for halo emission. The number of radio galaxies required to 'constitute' a halo, is well within range of the product of number of radio sources presently visible and the number of jet activities possible since z=3 (when significant radio activity began in the Universe). In this model, halos should occur at lower redshifts,

when radio galaxies have had enough time to spew sufficient synchrotron electrons and magnetic fields into the intracluster medium.

We also have a radio relic in our sample (A2744). Relics are similar to halos in terms of their brightness and integrated spectral properties, but are usually found in cluster peripheries and are tangential in extent. It is believed that relics are tracers of outward going merger shocks. A shock front of Mach number 1.7 is detected at the location of the relic. Our spectral index image of the relic shows two components – a radially inward steepening towards the cluster centre, and a gradient in the lateral section of the relic. The spectral index starts out with a compact region of -0.7 in the southern tip of the relic, which shows a progessive steepening ($\alpha \sim -1.7$) towards the north. Roughly in the region where it meets the shock, the spectrum becomes flat again. Both the inward steepening and the north-south gradient are more strongly visible in the images made with the 617 MHz data. This is expected as losses are more severe at higher frequencies. Based on our spectral index images, and weak shock Mach number we suggest that a dead cluster AGN is providing the fossil electrons for relic emission. However, the presence of a radio AGN core and an optical galaxy needs to be verified by future studies.

With the upcoming LOFAR surveys and upgraded GMRT, we can detect many more of these objects and study them in greater detail. Low frequency spectral index imaging will greatly help to understand the energization process within the halos.

Contents

List of Figures

List of Tables

Chapter 1

Introduction

1.1 Clusters of galaxies

Clusters of galaxies are the largest gravitationally bound objects that are formed by accumulating matter due to initial density fluctuations in the Universe. The typical mass of clusters is $\sim 10^{14} - 10^{15} M_{\odot}$ contained within Mpc^3 volume. They consist of up to thousands of galaxies ($\sim$10% of total cluster mass), hot gas (15$-$20%) and dark matter ($\sim$70%). The space between the galaxies is known as intra-cluster medium (ICM). It is a deep potential well containing hot ($10^7 - 10^8$ K), and diffuse gas. Matter typically falls into the ICM with velocities greater than 1000 km s^{-1} generating shock waves which are the principal heating mechanism of the ICM, accounting for its high temperature. But, other form of heating like feedback from active galactic nuclei (AGN) is also present (McNamara et al., 2000, 2005; Nulsen et al., 2005).

By virtue of its high temperature, the ICM is a bright emitter in X-ray, with luminosities of the order of $10^{43} - 10^{45}$ erg s^{-1}. The X-ray emission is primarily due to thermal bremsstrahlung and line radiation. The gas in the ICM is highly rarefied with electron density $n_e \sim 10^{-3} - 10^{-4}$ cm^{-3}.

Cluster mergers are the most energetic events in the Universe, releasing gravitational binding energy of the order of $10^{63} - 10^{64}$ergs. Cluster mergers are identified by substructures in optical surface densities and/or velocity distribution. In X-ray, the ICM gas of a fairly relaxed cluster has a regular, symmetric distribution with a bright peak at the centre. Non-relaxed clusters show disturbed X-ray morphology, for instance multiple peaks or distorted surface brightness contours, etc. The non-relaxed nature is also visible in temperature, pressure and entropy maps of the ICM (Million and Allen, 2009).

The ICM emits even in the radio regime. This form of emission is not common to all the clusters. Observationally, it is found that the radio emission of the ICM is associated exclusively with the merging clusters. Known as 'Radio Halos', these are the largest radio emitting structures in terms of volume (Ferrari et al., 2008; Feretti et al., 2012; Venturi et al., 2011). The radio emission comes from the centre of the clusters and elicits the existence of large-scale magnetic field, as well as a population of relativistic electrons in the ICM. Another form of emission from the ICM similar to radio halos

are known as 'Radio Relics'. These are mostly located in the cluster outskirts and are usually elongated and tangential in extent. The present thesis work primarily deals with Radio Halos.

1.2 Radio Halos

Radio halos are Mpc-scale, diffuse and low surface brightness radio structures that fill the intra-cluster medium of clusters of galaxies. The radio emission implies synchrotron radiation with Lorentz factor (γ) of relativistic electrons of the order $10^4 - 10^5$ (energy of the order of GeV) and magnetic field of the order of micro-Gauss in the ICM. Halos occupy the cluster centres and are usually regular in morphology, although some show irregular structure. Figure 1.1 shows the halo in the Coma cluster of galaxies, which was the first instance where large-scale non-thermal emission, not associated with any individual cluster galaxy, was identified (Willson, 1970; Hanisch, 1980; Kim et al., 1990; Giovannini et al., 1993; Deiss et al., 1997; Thierbach et al., 2003). Another famous cluster hosting a radio halo is the Bullet Cluster (Liang et al., 2000), which is also known to display a disturbed morphology in the X-ray (Markevitch et al., 2002; Govoni et al., 2004; Million and Allen, 2009).

Since the detection of Coma C halo in 1970 (Willson, 1970), many more such sources were rapidly discovered. Over sixty halos have been discovered till date (Giovannini et al., 2009; Feretti et al., 2012). The VLA survey at 1.4 GHz has been instrumental in detecting a large number of halos (Giovannini et al., 1999). A few more halos were discovered by the WSRT survey at 327 MHz (Kempner and Sarazin, 2001). Some observational characteristics common to most halos, are their large size, faint appearance, location at the cluster centre, association with merging clusters and steep integrated spectra (spectral index α typically in the range -1 to -1.5; Flux density S $\propto \nu^{\alpha}$). More recent and sensitive surveys with the GMRT at 610/235 MHz have resulted in the discovery of a new range of halos with ultra-steep spectrum (α -1.5 to -2) (Venturi et al., 2007, 2008; Kale et al., 2013; Kale et al., 2015). The examples of such halos are A697 and A521 (Macario et al., 2013). The steeper spectra imply higher emission (and perhaps even larger size) at low frequencies ($\leq$ 400 MHz).

Despite nearly fifty years that radio halos have been known, the key question pertaining to the processes which create and sustain them has remained unanswered. In fact, there is no 'definitive' evidence as yet of any associated energy source which powers the halos. The primary difficulty in explaining their origin is their Mpc-size, which cannot be a result of electrons diffusing out from a single location (as in the case of radio galaxies that are powered by AGN). The radiative lifetime of electrons is of the order of 10^8 years (Sarazin, 1999), while their diffusion velocity is of the order of $\sim$ 100 km s^{-1} (Brunetti and Jones, 2014). This implies that they would lose their energy faster compared to the time it would take them to diffuse out to the entire cluster volume ($\sim$ 10 Gyr). Cluster mergers are thought to impart energy to the electrons throughout the cluster volume. The existence of halos exclusively in clusters showing disturbed morphology supports the belief that mergers power halos. In this case, halo phenomena would persist for a

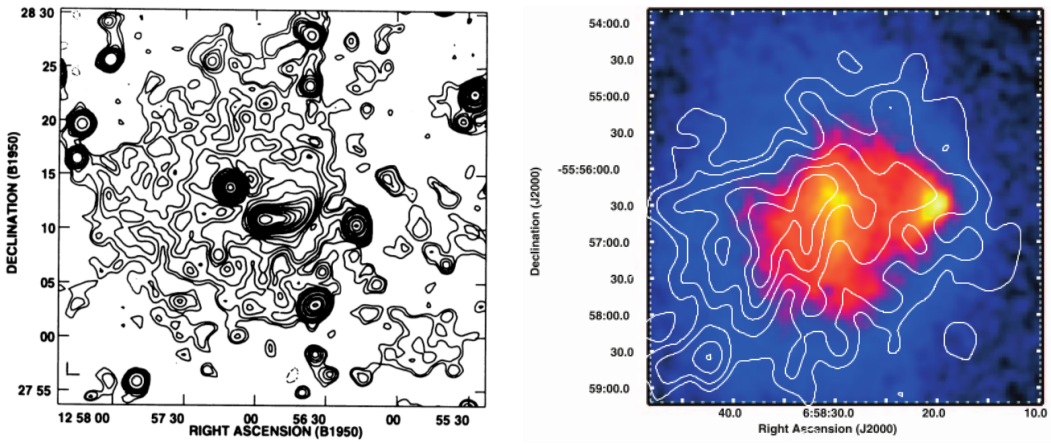

Figure 1.1: Examples of radio halo in two merging clusters of galaxies. *Left*: Contours show the radio halo in Coma C at 608.5 MHz observations from WSRT with 70″ resolution (Giovannini et al., 1993). Many radio galaxies also inhabit the cluster. The extensive diffuse contours represent the halo. *Right*: Contours denote halo in the Bullet Cluster at 1.3 GHz (Liang et al., 2000), overlaid on the X-ray image (Govoni et al., 2004). The radio image has a resolution of $24'' \times 22''$.

time duration less than the signatures of cluster merger; which would also account for its rare occurrence.

Below a brief outline of our knowledge about the statistical properties of halos and their correlation with other global properties of the host cluster is described.

1.2.1 Correlation of Radio Halos with X-ray Properties of host Clusters

There is a strong observational evidence that halos occur in clusters showing substructures in X-ray. However, not all merging clusters host halos. Buote (2001) first quantified the connection between dynamical state of the cluster and its ability to host halo, from a sample consisting of 14 halos. It was found that the most powerful halos appear in clusters currently showing larger departures from the virialized state. Cassano et al. (2010) further characterized the dynamical state of the cluster using X-ray data from *Chandra* archive for a sample of 32 galaxy clusters observed by the GMRT and the VLA. A clear separation in clusters with and without halos in terms of their dynamical state was found.

There is another remarkable connection of halos with the X-ray properties of the host cluster. More powerful halos are found in more massive and X-ray luminous clusters. The detection rate of halos in X-ray flux-limited sample consisting of 205 clusters observed in NVSS survey at 1.4 GHz, was found to be less than 5% for clusters with $L_X \leq 5 \times 10^{44}$ erg s^{-1}; which increased to ∼25% for $L_X \geq 5 \times 10^{44}$ erg s^{-1} (Giovannini et al., 1999; Giovannini and Feretti, 2002). The occurence of halos in the GMRT sample observed at 610/235 MHz consisting of 64 clusters in the redshift range 0.2−0.4 and X-ray luminosity

$\geq 5 \times 10^{44}$ erg s^{-1} is $\sim$22% (Venturi et al., 2007, 2008; Kale et al., 2013; Kale et al., 2015).

Brunetti et al. (2007) derived upper limits to the radio power for 20 clusters with non-detection of halos in the GMRT halo sample comprising 34 clusters at 610 MHz. The upper limit was found to be nearly two orders of magnitude less compared to the clusters with halos. Thus a clear bimodal behaviour was observed by clusters with and without halos. Figure 1.2 shows the correlation between radio power of halos at 1.4 GHz and X-ray luminosity of merging clusters (van Weeren et al., 2019).

Govoni et al. (2001) carried out point-to-point spatial comparison of the radio and X-ray surface brightness features for four halos and found a good match between them for two halos. A comparison of some well known halos with X-ray temperature maps showed spatial coincidence of bright radio features with high temperature for three of them (Govoni et al., 2004).

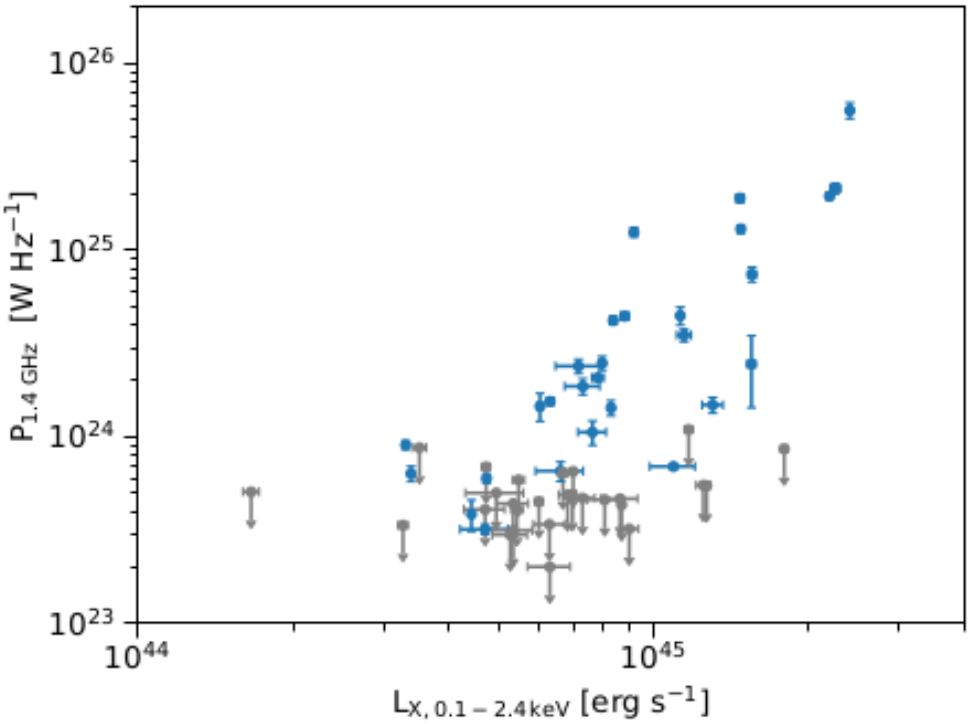

Figure 1.2: Cluster X-ray luminosity between 0.1 and 2.4 keV versus the halo radio power at 1.4 GHz. The image is taken from van Weeren et al. (2019). Blue dots indicate radio halos and grey dots indicate upper limits in radio power in clusters with non-detection of radio halos.

1.2.2 Integrated spectra of Halos

Observations of halos at multiple frequencies is important to distinguish between different models proposed for the origin of halos. The widely accepted model is the 'turbulent

re-acceleration model' according to which the turbulence injected during cluster mergers is believed to energize the synchrotron electrons. This is described in greater detail in a later section. An important consequence of this model is that electrons can only be accelerated upto a maximum energy (γ_{peak}), which will depend upon the balance between energy losses and acceleration efficiency. Beyond this, there will be a cutoff in the electron spectrum. The emission at the peak frequency (ν_{peak}) depends on $\gamma^2_{peak}B$.

Very few halos have been observed at more than three frequencies. As such, integrated spectra is available for only a few halos. Halos usually have steep spectra ($\alpha \leq -1$), which is indicative of old population of synchrotron electrons. The radio emitting electrons lose energy due to inverse compton and synchrotron losses. Therefore, their spectra becomes steeper with time and develops a break in frequency, which indicates the time since the last injection of synchrotron electrons. The highest frequency of observation, in most cases, is 1.4 GHz, and therefore the detection of break frequency has not been possible. A good example is the halo in the Coma cluster which has been studied over a wide range of frequencies from 0.3 to 4.8 GHz (Thierbach et al., 2003). The spectrum is found to be flatter between 0.3 and 1.4 GHz ($\alpha = -1.16$) and steepens to -2.28 between 1.4 and 4.8 GHz. High frequency steepening is observed in few other cases like A1914, A2319 and A3562 (Bacchi et al., 2003; Feretti et al., 1997; Giacintucci et al., 2005).

Some halos have even steeper spectrum like A521 and A697 (α in the range -1.8 to -2). These halos are almost invisible at 1.4 GHz. They were observed by high sensitive measurements from the GMRT at 153, 240, 325 and 610 MHz (Venturi et al., 2008; Brunetti et al., 2008; Macario et al., 2013). In fact, with the upcoming LOFAR survey (120−200 MHz) many more steep spectrum halos are expected to be discovered.

There are a few uncertainties involved in the measured values of integrated spectra due to errors involved in the estimation of flux densities of halos. For instance, the contribution of radio galaxies if present within the halo region, needs to be accurately subtracted. The sensitivity of measurements depend not only on the observing frequency, but also varies between different instruments due to their very different UV-coverages.

1.2.3 Spectral Index Images of Halos

Our knowledge of spectral index distribution in halos is limited to only a few of them. Spectral index images are available for about a dozen halos – A1656 (Giovannini et al., 1993), A665 and A2163 (Feretti et al., 2004), A3562 (Giacintucci et al., 2005), A2219 and A2744 (Orru' et al., 2007), A2255 (Pizzo and de Bruyn, 2009), A2256 (Kale and Dwarakanath, 2010), 1E 0657-56 (Shimwell et al., 2014), A520 (Vacca et al., 2014), RX J0603.3+4214 (van Weeren et al., 2012) and CIZA J2242.8+5301 (Hoang et al., 2017). They are mostly between 325 MHz and 1.4 GHz and with an arc-minute resolution. Examples of the spectral index image are shown in Figure 1.3. A review of the spectral index structures observed in these halos is given in Chapter 2 of this thesis.

According to the turbulent re-acceleraton model (see the section below for a theoretical description of the model), it is expected that flatter areas should be observed in the spectral index image in the regions currently under the influence of strong merger

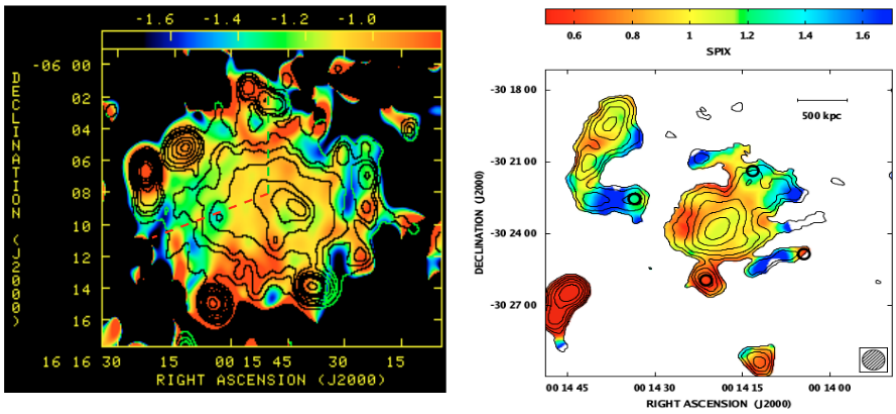

Figure 1.3: *Left*: Spectral index image of the halo A2163 between 325 and 1400 MHz at 60″×51″ resolution (Feretti et al., 2004). Contours are radio emission at 1.4 GHz. *Right*: Spectral index image of A2744 between 325 and 1400 MHz at 50″ resolution (Orru' et al., 2007). The contours show emission at 325 MHz. Black circles are point sources unrelated to the halo.

activity. Likewise, these regions should correlate with the X-ray images, as they reflect the morphology of the cluster merger. While a clear connection of spectral index image with the geometry of the merger has not been established in all them; still a few like A665 and A2163 and A2256 show some signatures of spectral flattening in regions under the influence of merger (Feretti et al., 2004; Kale and Dwarakanath, 2010).

1.2.4 Theoretical models proposed for the origin of Halos

Two models are proposed to explain the formation of halos based on the origin of relativistic electrons.

Primary electron model suggests that halo emission is due to re-acceleration of pre-existing population of electrons by the turbulence and shocks generated during cluster mergers (Brunetti et al., 2001; Brunetti, 2004; Petrosian, 2001; Fujita et al., 2003; Brunetti and Blasi, 2005; Brunetti et al., 2007; Petrosian and Bykov, 2008).

The problem of short radiative lifetime of electrons and Mpc extent of halos was first identified by Jaffe (1977), who suggested that electrons are accelerated *in-situ* throughout the cluster volume. Turbulence and shocks are expected to be present thoughout the cluster volume during a merging process and therefore short radiative lifetimes do not pose a problem.

Shock Acceleration: Shocks can be generated in the ICM by various methods.

Accretion shocks are generated several Mpc away from the cluster centre when matter from inter-galactic medium (IGM) accretes on the periphery of the cluster. IGM temperature is much lower than the ICM temperature, and therefore these shocks have high Mach numbers M ∼10−100 (Miniati et al., 2000), and can efficiently accelerate the cosmic rays.

Diffusive shock acceleration (DSA), being a first order Fermi process, is an efficient way to accelerate cosmic rays (Blandford and Eichler, 1987). Each time a particle diffuses across the shock front it gains a little energy. It will continue to do so until it is swept downstream. DSA has been invoked in various other astrophysical phenomena. For instance, bow shock in the lobes of radio galaxies as they pass through the IGM, or shocks generated by supernova explosion.

Merger shocks are generated in the interiors of galaxy clusters when a subgroup falls into the main cluster. These shocks are generally weak as the gas in the merging subgroups is already virialized and hot (T$\sim 10^7 - 10^8$ K) from the accretion of matter at the filaments where the clusters are formed (as per the hierarchical model of cluster formation). The Mach numbers are less than 4.

The significance of merger shocks in accelerating the particles in the case of halos is still debated. One reason is that shocks are a localized phenomena (relativistic electrons can travel only for a few hundred kpc before losing their energy), while halos occupy a larger volume. More importantly, merger shocks have been detected only in a few clusters and with low Mach number (eg. A520, 1E 0657-56; Markevitch et al. (2005, 2002)). Numerical simulations suggest that high Mach number shocks are rare within galaxy clusters and the energy stored in the form of cosmic rays is just few percent of thermal energy (Gabici and Blasi, 2003; Kang et al., 2012). Injection of particles from the thermal pool by weak merger shocks is in general difficult, especially for electrons as it is determined by the ratio p/q, where, p is the momentum of the particle ($=\sqrt{2mE}$) and q is its charge.

AGN shocks are observed when powerful AGNs push large bubbles into the ICM (Brüggen et al., 2007). They are usually observed at cluster centres and are weak like merger shocks.

Turbulent Acceleration: This is a Fermi-II process, which although less efficient than shock acceleration, is thought to be largely responsible for energizing the halos.

The gravitational binding energy released during a cluster merger is

$$E_{merger} = \frac{GM_1M_2}{d} \sim 10^{64} \text{ ergs}$$

for cluster masses of the order $10^{15}M_\odot$ and d $\sim$1 Mpc. Bulk of this energy goes in heating up the ICM via shock waves. The duration of a merger is typically a Gyr. Halos are expected to persist for a time duration of this order (Brunetti et al., 2009; Cassano et al., 2011). Numerical simulations show that cluster mergers can induce turbulence at a Mpc scale and the time during which they are effective is of the order of few 10^8 years. Up to $\sim$ 30% of thermal energy of ICM can be stored in the form of turbulent waves (Dolag et al., 2005; Cassano and Brunetti, 2005; Cassano et al., 2006; Vazza et al., 2006). If a fraction of 20$-$30% of the turbulence is in the form of compressible modes, then it can explain the observed occurrence of halos in clusters, and their scaling with the cluster mass. The probability of forming halos increased if more massive clusters were considered, because the available energy that can be channeled into turbulent waves increased.

Turbulence is injected into the ICM at length scales of $\sim 300-500$ kpc with velocity of turbulent eddies $\sim 500-1000$ km s^{-1} (Brunetti et al., 2007). The turbulence then cascades down to smaller scales, at which point it interacts with the particles (electrons, protons) and the re-acceleration takes place. Brunetti (2004) and Brunetti and Blasi (2005) considered interaction of Alfven waves for re-acceleration method. Alfven waves can interact with particles only at parsec scales, which would require significant cascading. Moreover, Alfven waves are damped by protons, and therefore it is required that very less energy ($\sim 5-10\%$ of thermal energy) be in protons, else the waves will be suppressed. Brunetti et al. (2007) considered magneto-sonic waves, whose scale of interaction with particles is of the order of kpc. They showed that if a small fraction of thermal energy in the form of turbulent modes, it was possible to efficiently re-accelerate relativistic electrons from $\gamma \sim 10^2 - 10^3$ to $\gamma \sim 10^4 - 10^5$. Under these circumstances, the electrons are capable of emitting in Mpc volume and at GHz frequencies in μG magnetic fields typical of clusters.

The time scale for the magneto-sonic waves to reach the length scales necessary for particle interaction is

$$\tau_{kk}(Gyr) \approx 0.6 \left(\frac{L_0}{300kpc}\right) \left(\frac{V_L}{10^3 kms^{-1}}\right)^{-1} \left(\frac{M_s}{0.5}\right)^{-1}$$

where, L_0 and V_L are length scale and velocity at the injection of turbulence, and M_s is the turbulent Mach number. The re-acceleration starts only after this time elapse. The re-acceleration timescale to accelerate electrons up to GeV energies is of the order $\sim 10^8$ years. The duration of re-acceleration period is constrained by the cluster-cluster crossing time and the turbulence cascading time mentioned above. These are not greater than a Gyr which is comparable to the lifetime of halos.

Observatioally, there is some indication of turbulence present in X-ray pressure maps of the ICM (Churazov et al., 2004; Schuecker et al., 2004). The support for turbulent re-acceleration model comes from the exclusive association of halos with mergers (Buote, 2001; Govoni et al., 2004). A high frequency cutoff in the integrated spectral index (as observed in A697, Macario et al. (2013) and A521, Brunetti et al. (2008)) is another important expectation of the model because the electrons are only accelerated upto a certain maximum energy which is decided by the balance between acceleration efficiency (percentage of turbulent energy input into the particles) and the losses incurred by the particles (synchrotron and inverse compton). The nature of spatial distribution in spectral index images (like flattening observed in merger induced areas and radial steepening elsewhere) are also in favour of the above model.

Lifetime of electrons in clusters and origin of seed electrons

The seed electrons for re-acceleration may be provided by AGN activity or galactic winds, supernova etc, and are expected to be present throughout the cluster volume. These electrons suffer various losses — synchrotron, inverse compton, coulomb and bremsstrahlung. The different loss mechanisms have different energy dependencies. This implies that electrons with different lorentz factor (γ) suffer different losses. For typical

cluster conditions of micro-gauss magnetic fields and electron number density of the order 10^{-3} cm^{-3}, inverse compton losses are dominant for $\gamma \geq 200$, and coulomb losses dominate for γ values less than 200 (Sarazin, 1999). Synchrotron losses contribute only for stronger magnetic fields ($B > 3\mu$G), while bremsstrahlung become significant only at higher densities than what is usually found in the cluster ICM. The electron lifetime is in Gyr (comparable to age of clusters), with peak $\gamma = 100-500$. The rapid losses suffered due to inverse compton (and synchrotron) make the electrons accumulate in the energy range $\gamma = 100-500$, where they survive for a very long time till they thermalize due to coulomb losses. In cluster cores where thermal density is more (coulomb losses more severe), the lifetime may be less than a Gyr. However, this implies that there is a reservoir of mildly relativistic electrons ($\gamma \sim 300$) already existing in the ICM that can provide the seed population necessary for re-acceleration. Cluster mergers provide the necessary fuel to re-accelerate these electrons.

Synchrotron and inverse compton (IC) losses, both of which have an energy loss rate depending on E^2, lie in our realm of interest.

$$\frac{dE}{dt} = -(\xi_{syn} + \xi_{IC})E^2 \tag{1.1}$$

where, $\xi_{syn} = 2/3c_2B^2$ for Jaffe-Perola (JP) model which assumes an isotropic distribution of electron pitch angles (Jaffe and Perola, 1973). Here constant $c_2 = 2e^4/3m_e^4c^7$ from Pacholczyk (1970). The electron pitch angles remain constant $\xi_{syn} = c_2B^2sin^2(\theta)$ in the Kardashev-Pacholczyk (KP) model. The JP model better describes the system in real cases. The inverse compton contribution is given by $\xi_{IC} = 2/3c_2B_{CMB}^2$; $B_{CMB} = 3.25(1+z)^2$. The IC loss rate dominates for the cluster redshifts and magnetic fields.

The energy losses cause the spectrum to steepen after some time t. The spectral 'break' frequency ν_{br} is proportional to $\frac{B}{([B^2 + B_{CMB}^2]t)^2}$. An exponential cutoff beyond the break frequency is predicted in the JP model, while in the KP model the spectra steepens to a power-law with a slope $(4/3)\alpha_{inj} - 1$ (α_{inj} is the injection spectral index). Apart form this, there are also other models – continuous injection (CI) where electrons are injected continuously (Pacholczyk, 1970); $KGJP$, $KGKP$ models where electrons are injected only for a fixed period of time (Komissarov and Gubanov, 1994).

Secondary electron model for the origin of halos proposes that secondary electrons are injected by inelastic nuclear collisions between the relativistic protons and thermal ions of intracluster medium. These electrons emit in the radio band in presence of magnetic field (Dennison, 1980; Blasi and Colafrancesco, 1999; Dolag and Enßlin, 2000). Clusters of galaxies are actually storehouse of protons because their energy losses are negligible (Sarazin, 1999). They can continuously produce electrons, distributed throughout the cluster volume. However, this would also mean that halos should be present in all clusters – which is contrary to observations. Also the spectral index images should be featureless with no correlation to the merger geometry. Moreover, emission of gamma rays and neutrions is predicted by this model. There is no observational evidence as yet

for the detection of gamma rays from clusters. All these arguments do not support the secondary model.

1.3 Radio Relics

Relics are extended radio structures similar to the halos, but usually located at the cluster periphery. Some properties that are common to both the halos and relics are low surface brightness, steep spectral index ($\alpha \leq -1$) and Mpc size. Relics differ most from the halos in their location, morphology and polarization properties. Relics are usually 20−40% polarized while halos are unpolarized down to 3−5%. Most relics have elongated, narrow arc-like shapes, with the axis roughly oriented perpendicular to the cluster center. These elongated relics are thought to be the tracers of outward going merger shocks. The spectral index images of such relics show a gradient with a steepening towards the cluster center. Sometimes relics occur in pairs and are seen on diametrically opposite directions to the cluster center, eg. A3376 (Bagchi et al., 2006). A few merging clusters are known to host both halos and relics, eg. A2744 (Orru' et al., 2007) and CL0217+70 (Brown et al., 2011).

The presence of relics signify the presence of magnetic field and relativistic electrons even in the cluster outskirts. Again, diffusive shock acceleration has been invoked to explain the origin of relics. But merger shocks are weak even in the cluster outskirts where the temperature is less (Vazza et al., 2009; Brüggen et al., 2012; Kang et al., 2012). Similar to the halos a pre-existing population of relativistic electrons is thought to be necessary for efficient boosting by low Mach number shocks. The most promising way to produce a population of mildly relativistic electrons is by dead lobes of radio galaxies. These lobes can be observed for a few Myr in the radio band after their central engine switches off, following which they will become invisible. Enßlin and Gopal-Krishna (2001) showed analytically that a relic may be a result of revival of fossil electrons from a dead AGN lobe by adiabatic compression of a merger shock. The model was used to explain the relic associated with the Coma cluster.

Apart from this, there is also a class of relics showing rounded morphology, eg. A2048 (Venturi et al., 2008) and A2255 (Clarke and Ensslin, 2006). Lack of an optical counterpart and the absence of any AGN nearby indicates that these sources are not dead radio lobes. They usually have steeper spectral index than elongated relics.

1.4 This thesis

The aim of this thesis is to look for structures in spectral index images of halos. We investigated the aspects regarding the origin of halos by constructing high resolution spectral index images made using the GMRT observations at low frequencies. We correlated the radio images with the optical and X-ray information of the clusters. A sample consisting of five clusters hosting halos were chosen for the current study. The archival GMRT data has also been re-analyzed and used wherever possible.

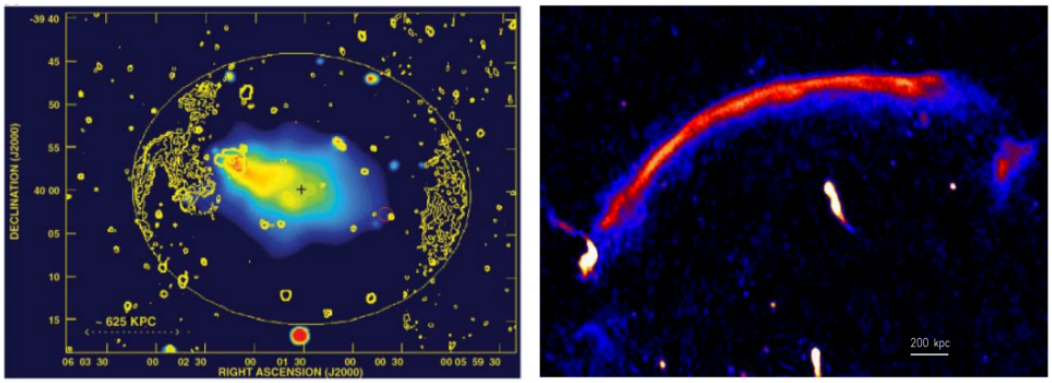

Figure 1.4: *Left*: Image of the relic in A3376 at 1.4 GHz (VLA) shown in yellow contours, overlaid on X-ray emission (ROSAT, 0.14−2 keV) shown in colour. Contour levels are at 0.12, 0.24, 0.48, 1 mJy/beam and a beam width of 20″. An elliptical fit to the relics is overlaid. The '+' marks the center of the ellipse and the red circles mark the positions of the two brightest cluster galaxies (Bagchi et al., 2006). *Right*: GMRT 610 MHz radio total intensity image of the relic in the cluster CIZA J2242.8+5301. The image has a resolution of 4.8″×3.9″ (van Weeren et al., 2010).

The organization of the thesis is as follows. In chapter two a literature review of the spectral index images of halos is provided. Chapter 3 describes the data selection, observations and methods of data reduction. Chapters 4−7 describe the results and discussion from the individual halos — A2163, A665, A2744, A520 and A773. We summarize and conclude in Chapter 8.

Throughout the thesis, ΛCDM cosmology with the parameters $\Omega_M = 0.3$, $\Omega_\Lambda = 0.7$ and $H_0 = 70$ km s^{-1} Mpc^{-1} is used.

Chapter 2

Spectral Index distribution in Halos – Literature Review

In this chapter we review the structures seen in the spectral index images of halos. Synchrotron emissivity depends on both the magnetic field and distribution of relativistic electrons. Spatially resolved spectral index images therefore carry both the information — energy distribution of synchrotron electrons and the variation of magnetic fields within the cluster ($\epsilon \propto \nu^{\alpha} B^{1-\alpha}$; where ϵ is the volume emissivity, ν, α and B are the frequency, spectral index and magnetic field, respectively). While these two cannot be separated, yet spectral index images are most important observational diagnostics available to understand the origin of halos. One can assume a constant distribution of the magnetic field throughout the cluster. A flat region in the spectral index image will then imply that electrons there have higher energy; possibly due to recent energization. The assumption that the magnetic field is constant is, however, not true. Simulations suggest that the magnetic field decreases with the cluster radius, roughly depending upon the thermal gas density (Dolag et al., 1999, 2005; Brüggen et al., 2005). Magnetic field is believed to increase during a merging process (Roettiger et al., 1999; Carilli and Taylor, 2002; Bonafede et al., 2010). In light of this, a spectral index image is expected to provide important clues about halos and re-acceleration model.

Both, high signal-to-noise ratio and high resolution (to identify structures within the halo) are essential to study the spatial variations in a halo. Resolution is also important to identify the presence of any contaminating discrete sources within the halo. Even then it is difficult to identify very faint sources within the halo. Synchrotron and inverse compton losses dominate and modify the electron spectrum at high frequencies ($>$ 400 MHz). It is the lower frequencies ($<$ 400 MHz) which bear the imprint of initial energization spectrum for a longer time. Also, halo emission is higher at low frequencies due to their very steep spectrum. Taking all these factors into account low frequency spectral index imaging becomes extremely important. However, obtaining sensitive images is a challenge at low frequencies due to radio frequency interference (RFI). Only ten halos have been observed at 150 MHz, which are A754 and A2256 (Kale and Dwarakanath, 2009, 2010), A2255 (Pizzo and de Bruyn, 2009), 1RXS J0603.3+4214 (van Weeren et al., 2012), A521 and A697 (Macario et al., 2013), A2034 (Shimwell et al.,

2016), CIZA J2242.8+5301 (Hoang et al., 2017), MACS J0717.5+3745 (Bonafede et al., 2018), A1758 (Botteon et al., 2018), A1132 (Wilber et al., 2018).

Spectral index images need to be constructed with instruments having similar *UV*-coverage and resolution. While these issues can be taken care of, the real limiting factor is the quality of the radio images itself. Any meaningful structures observed in spectral index images are expected to also correlate with the cluster dynamics, if our understanding of 'turbulent-acceleration model' is correct. Below a brief description of individual halos is provided.

The first spectral index image was constructed for the Coma cluster between 326 and 1380 MHz with a resolution of $130'' \times 80''$ (Giovannini et al., 1993). The image had a central 'plateau-like' region nearly $8'$ ($\sim$170 kpc) in size with almost a constant value of spectral index of -0.8, beyond which the spectrum steepened to -1.8. The size of the central 'plateau' region was approximately the size of the cluster core radius. The flatter spectral index in the cluster core was suggested to be due to higher density of optical galaxies in the inner regions of the cluster. The cluster also has two relics associated with it and a bridge of emission connecting the halo with one of the relics (Kim et al., 1989; Venturi et al., 1990; Deiss et al., 1997; Brown and Rudnick, 2011).

Giovannini et al. (1993) proposed a model for the origin of halo in Coma C, wherein the presence of a tailed radio galaxy NGC 4869 in the central region of the halo, was suggested to be supplying the seed synchrotron electrons and magnetic field required for the halo emission. From the total number of electrons within the tailed radio galaxy and the lifetime of radio emitting particles in the outermost region of the galaxy, an estimate of the time required for the electrons to diffuse out of its tail and form a halo was obtained. During this time duration the tailed source could complete nearly four orbits in the ICM. This model relies not only on the presence of one or more tailed radio galaxies within the cluster, but also them following a closed orbit around the cluster centre in order to fuel a halo. They further estimated the percentage of turbulent energy channeled into the non-thermal components, by assuming that the motion of galaxies through the cluster medium is the cause of the turbulent energy. The total energy input by the galaxy motion when compared with the synchrotron power of the halo, suggested that an efficiency of $\sim$1% was sufficient to convert from turbulent energy to the non-thermal component.

Another famous merging cluster hosting a halo is the 'Bullet Cluster' (Liang et al., 2000; Shimwell et al., 2016). Here a clear bow shock of Mach number 3 has been detected in the western region (Markevitch et al., 2002). The halo has a distinct 'edge' that is cospatial with the bow shock (Shimwell et al., 2014). In the direction of the merger the halo appeared to follow the path taken by the gas bullet. The 1.1$-$3.1 GHz spectral index image made using ATCA data has a series of resolutions ranging from $4''$ to $29''$. The image has variations across the halo, with a central value of -1.4. No clear trend is detected in the image. Although the halo morphology is similar to the X-ray emission, yet a point-to-point comparison of radio and spectral index images with the X-ray and weak-lensing mass reconstruction images did not reveal a strong correlation.

Feretti et al. (2004) carried out spectral index analyses of two halos — A665 and A2163 (Fig. 2.1). In both these halos it was observed that the flat spectrum values were

associated with regions under the influence of most recent merger activity, and a general radial steepening was found in regions not currently under the influence of merger. The 325−1400 MHz (68 arcsec × 59 arcsec resolution) spectral index image of A665 was 'clumpy' with almost constant flat values in the central region. Taking a cut across two directions in the halo, the authors showed that the spectral index was flat from centre to north-west direction – the region coincident with the asymmetric extended X-ray emission, indicating this region is strongly under the influence of merger. The spectral index in this region lied between −0.8 to −1. The spectrum steepened gradually from centre to south-east periphery of the halo ($\alpha = -1$ to -2). This radial decline in the region not presently under the influence of the merger was interpreted as due to the combined effect of radial decrease in magnetic field and the presence of high energy break in electron energies.

For A2163 (resolution 60 arcsec × 51 arcsec; Fig. 2.1) the western region of the halo was found to be flatter than the eastern one. A vertical region in the cluster center also showed flatter spectrum, with a clear evidence of spectral index flattening at the northern and southern edge of the halo. The profile along north-south direction was found to be flatter ($\alpha = -0.9$ to -1.1) than the south-east direction ($\alpha = -1$ to -1.6). The north-south region with a flat spectrum indicated an east-west merger geometry of the cluster; which was also supported by the X-ray brightness distribution. The 'clumpiness' in the spectral index images is expected in turbulent re-acceleration model. Both these halos showed that spectral index images can be good indicators of the cluster merger geometry.

The spectral index image of A2744 (325−1400 MHz; 50 arcsec resolution; Fig. 2.1) shows variations, with a prominent region of flat spectral index in the east and north-west (Orru' et al., 2007). The spectral index profile obtained from averaging surface brightness in ten concentric annuli of 25 arcsec width centered on halo peak, yielded a constant value of $\alpha \sim -1$ up to 1 Mpc from the cluster centre. The authors also obtained brightness and spectral index profiles in four quadrants in the halo and found that up to one core radius of the halo, all the four quadrants had nearly constant α of −1. Beyond this distance, the NW quadrant was found to be the steepest and SE the flattest. No association between spectral index features and optical and X-ray brightness features were found. However, a somewhat flat spectrum was found between NW group and cluster centre, which is likely the region affected by the merging between the main cluster and the group. Moreover, for the first time a comparison of the spectral index values and the gas temperature was performed. Using cells of 63 arcsec width it was shown that the highest gas temperature ($T \simeq 10$ keV) coincided with the flat spectrum region in the east of the radio halo ($\alpha \simeq -0.7$). Steep spectrum values were associated with cooler regions of the cluster. This result can be expected if a fraction of the gravitational energy which is dissipated during cluster merger and goes into heating up the plasma, is channeled into re-acceleration of relativistic particles and amplification of the magnetic field.

The spectral index image of A520 was presented by Vacca et al. (2014) using VLA archival observations at 325 and 1400 MHz. The authors constructed spectral index images with resolutions of 39 and 60 arcsec. The image had a 'clumpy' appearance at

both the resolutions. The pixel values had an asymmetric distribution with respect to the mean value, due to the cut imposed on the total intensity images for constructing the spectral index images. Further, the dispersion in the images were slightly higher than the mean value of the spectral index error image. This implies that while measurement errors did contribute to the fluctuations observed in the spectral index image; yet some amount was also intrinsic to the halo. The azimuthally averaged brightness distribution of the halo extracted from 60 arcsec images using concentric annuli of half-beam-width centered on the X-ray peak, was found to be almost constant up to 400 kpc from the cluster centre. The corresponding spectral index profile was also found to be flat. The flat nature of the halo was interpreted as due to a balance between magnetic field and the energy input into the halo from the centre to the periphery. The cluster hosts a bow shock similar to the 'Bullet cluster' which coincides with a radio 'edge'. A spectral index of ~ -1.2 was found at the location of the shock, as predicted by Markevitch et al. (2005); although no spectral index steepening was observed away from the shock front. The authors investigated for a correlation between the thermal and non-thermal properties of the cluster (similar to the case of A2744), by comparing the spectral index image with the X-ray temperature map. A certain agreement of flatter spectral index values with higher gas temperature (and vice versa) was found; however no clear point-to-point correlation was observed.

A2256 (Fig. 2.1) presents an interesting case as it has a relic that merges with the halo (Clarke and Ensslin, 2006; Kale and Dwarakanath, 2010; Clarke et al., 2011; van Weeren et al., 2012; Trasatti et al., 2015). The integrated spectral index of the halo at low frequencies was found to be steeper compared to that at high frequencies: $\alpha_{150}^{350} = -1.20 \pm 0.13$ and $\alpha_{350}^{1400} = -0.65 \pm 0.01$ (Kale and Dwarakanath, 2010); $\alpha_{63}^{351} = -1.5 \pm 0.1$ and $\alpha_{351}^{1369} = -1.1 \pm 0.1$ (van Weeren et al., 2012). Two epochs of merger producing two populations of electrons was suggested to be responsible for the low frequency spectral steepening. A line-of-sight merger between two groups generating shock wave and turbulence behind it is thought to be responsible for the diffuse halo emission and the relic. The spectral index image is available in both low (150−350 MHz) and high (350−1369 MHz) frequency range at a resolution of 67 arcsec. The image showed a steepening from north-west to south-east which was found to be consistent with the cluster merger geometry (Kale and Dwarakanath, 2010). The low frequency spectral steepening was inferred even from the two spectral index images, by comparing the values in small sectors of the size of the beam in NW-SE direction. A comparison of the spectral index image with the X-ray gas temperature indicated steeper spectrum to be associated with the hotter regions of the cluster. This is contrary to the correlation observed in A520 and A2744 and a mild correlation observed in a few other halos (Giovannini et al., 2009; Feretti et al., 2012). This anti-correlation can be understood by considering different cooling times of thermal and non-thermal plasma.

The cluster RX J0603.3+4214 hosts both a halo and a relic (van Weeren et al., 2016). Because of the morphology the relic is also known as the 'Toothbrush Relic' (van Weeren et al., 2012). An elongated halo is connected with the relic (Fig. 2.1). The relic shows a clear north-south gradient in the spectral index, consistent with the shock re-acceleration of fossil electrons and north-south geometry of the merger. The halo occupies the region

with highly disturbed X-ray gas. A low resolution spectral index image (31 arcsec × 24 arcsec) made between LOFAR 150 MHz and VLA 1.5 GHz revealed a very uniform distribution of spectral index across the halo, with uncertainties less than 0.1. The intrinsic scatter was found to be less than 0.04. The region between the halo and the relic showed strong steepening in the spectral index values. The re-flattening of the spectral index in the halo region suggests re-acceleration of the aged electrons in the downstream region of the relic by the turbulence. One of the possibilities suggested was that the large-scale turbulence responsible for the halo was generated by the passage of shock front. The timescale for the passage of shock, and decay of turbulence into smaller scales to accelerate the particles was found to be consistent with the halo model proposed by Brunetti et al. (2007), where particle acceleration takes place by compressive MHD turbulence. Another possibility suggested was that the weak shock (X-ray Mach number = 1.5) is not responsible for generating the turbulence. This was supported by the fact that no spectral steepening was observed in the southern portion of the halo where another shock front was detected.

Similar re-flattening of spectral index was observed in the halo in CIZA J2242.8+5301 which is bounded by two relics in the north and south (Hoang et al., 2017). The 35 arcsec spectral index made using LOFAR, GMRT and WSRT data spanning eight frequencies, showed steeper spectrum from the downstream region of the northern relic to the northern part of the halo; again suggestive of re-acceleration of electrons in the downstream region by merger induced turbulence. The presence of contaminating sources within the halo did not allow for any detailed deductions about the nature of the radio halo.

The halo in cluster A2255 differs from the usual morphology of halos. There are three polarizd bright filaments on the sides of the halo, that are nearly perpendicular to each other (Govoni et al., 2005; Pizzo and de Bruyn, 2009). The spectral index images were made with 163″×181″ resolution between 25 cm, 85 cm and 2m. It was found that steeper values of spectral index were at the cluster centre and flatter at the location of the filaments. This is rather unusual for halos, as they do not show polarised structures and spectral flattening at the edges. The results were interpreted as either due to superposition of distinct structures (relics) on the central halo, or that the halo is intrinsically peculiar. The cluster also hosts multiple relics. A 'bridge' of emission was detected between the halo and one of the relics.

The halo in MACS J0717.5 +3745 (Bonafede et al., 2009; van Weeren et al., 2009; Pandey-Pommier et al., 2013; van Weeren et al., 2017; Bonafede et al., 2018) has a central 'chair-like' structure within it (Fig. 2.1). The central 'filamentary' structure was identified previously as a relic (Edge et al., 2003), and subsequently a diffuse halo was found surrounding it (Bonafede et al., 2009). The nature of the 'filamentary' structure at the centre of the halo is still under debate – whether it is a peripheral relic appearing at the cluster centre due to projection; or it is a part of the halo. Similar to the case of A2255, the 'relic-filament' has been found to be polarized. However, no clear distinction could be made between the polarization properties of the halo and the filament – implying the structure may be a part of the halo. The high frequency spectral index image (1.365−4.885 GHz) did not reveal any discontinuity between the halo and the 'relic-filament', for example a steepening of spectral index across the relic as a result of shock

acceleration (Bonafede et al., 2009). There is also a head-tail radio galaxy embedded within this filamentary structure. Spectral index image between 235 and 610 MHz revealed a flat spectrum region within this filamentary structure; which is located between four merging galaxy subclusters and also has high temperature (Pandey-Pommier et al., 2013). Furthermore, a spectral index steepening from the filamentary structure towards the outer edges of the halo in the direction of the merging groups was also observed. The orientation of the major axis of the filament perpendicular to the merging axis, its flat spectral index, and coincidence with high ICM temperature was interpreted as due to large-scale shock wave generated during cluster merger.

The presence of discrete sources within the halo is a limiting factor in many spectral index images. Therefore, although a spectral index image is available for A2219 (325−1400 MHz; 56″ resolution), due to the blending of discrete sources at the centre of the halo, the image did not yield any information (Orru' et al., 2007). Even otherwise, no clear trend is detected in a few halos. For example, from the image of A3562 an average value of spectral index −1.5 was inferred, with 'knots' steepening up to −2.0 (Giacintucci et al., 2005).

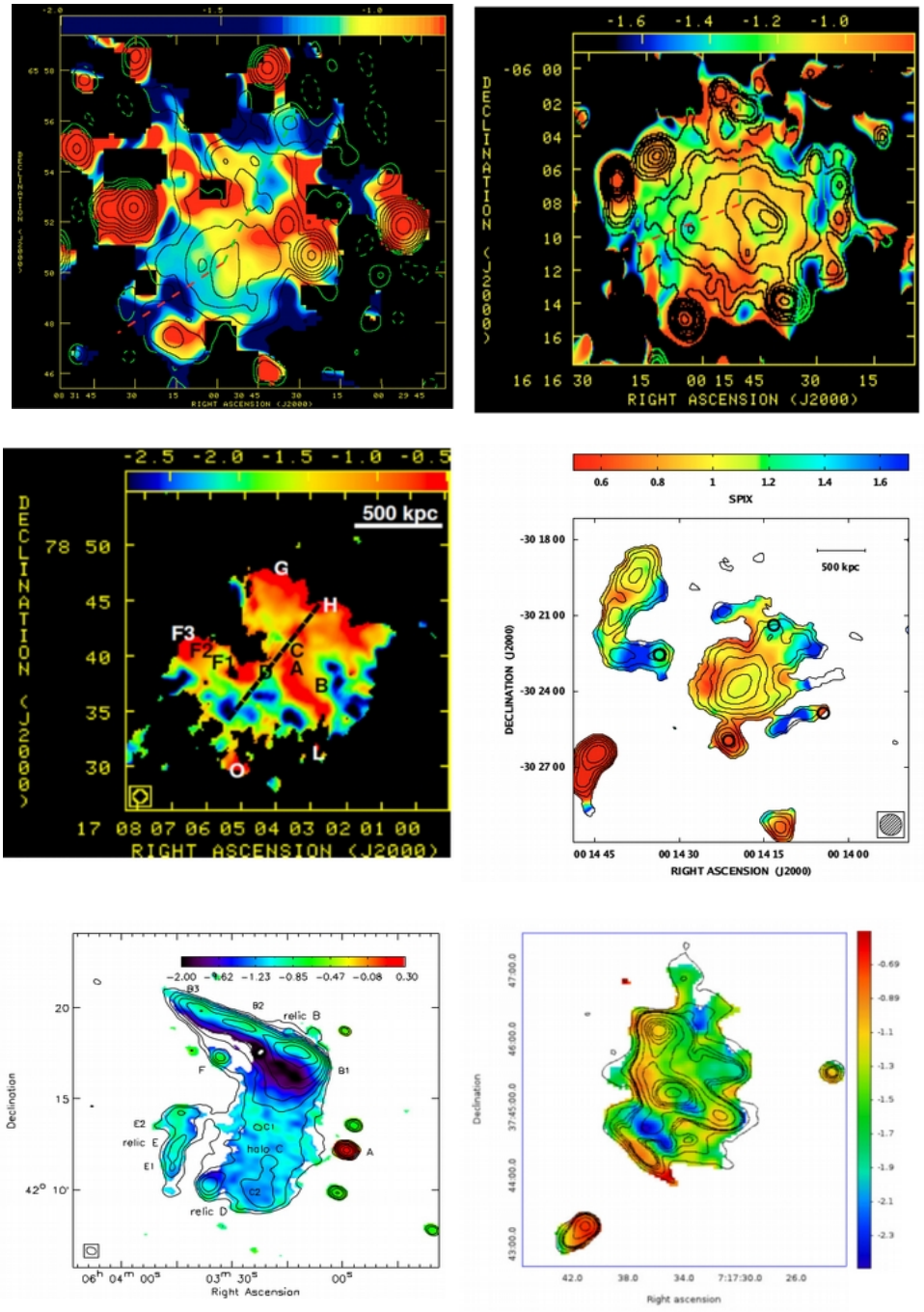

Figure 2.1: Spectral index images of A665 (*Top left*): 0.325−1.4 GHz, $68'' \times 59''$ resolution (Feretti et al., 2004); A2163 (*Top right*): 0.325−1.4 GHz, $60'' \times 51''$resolution (Feretti et al., 2004); A2256 (*Middle left*): 0.15−0.35 GHz, $67''$ resolution (Kale and Dwarakanath, 2010); A2744 (*Middle right*): 0.325−1.4 GHz, $50''$ resolution (Orru' et al., 2007); RX J0603.3+4214 (*Bottom left*): 0.15−1.5 GHz, $31'' \times 24''$ resolution (van Weeren et al., 2016); MACS J0717.5 +3745 (*Bottom right*): 0.235−0.61 GHz, $13.3'' \times 10.7''$ resolution (Pandey-Pommier et al., 2013).

Chapter 3

GMRT Observations and Data Reduction

The objects used in this study were observed using the Giant Metrewave Radio Telescope (GMRT, Swarup (1991)) as part of several programmes including Proj. Code 16_259 (A2163 and A2744; at 150, 325 and 610 MHz; 2009) and Proj. Code 27_070 (A665, A520 and A773; 150, 325 and 610 MHz; 2014−15) and also supplemented by data from the archives.

3.1 Cluster Sample

3.1.1 Source Selection

We selected the sources based on following criteria:

1. Halos with a size of at least 5 arcmin to obtain sufficient resolution elements across the halo. With a 150 MHz resolution of 23 arcsec we expect over 150 resolution elements across the source.

2. Availability of X-ray and optical images for details of cluster (merger) dynamics.

3. Surface brightness at 1400 MHz in excess of 0.5 μJy/arcsec^2, so that a spectral index = -1 would result in an observed surface brightness at GMRT-150 MHz of 3 mJy/beam.

4. Minimal number of confounding discrete sources superposed on the halo.

3.1.2 Cluster Properties

The properties of the clusters are given in Table 3.1.

Name	RA(J2000) (h m s)	DEC(J2000) (∘ ’ ")	z	kpc/arcsec
A2163	16:15:49.4	-6:08:60	0.203	3.338
A665	8:30:57.39	65:51:14.4	0.1818	3.059
A2744	00:14:19.5	-30:23:19	0.3080	4.536
A520	4:54:9.3	2:55:21	0.199	3.287
A773	09:17:59.4	51:42:23	0.22	3.552

Table 3.1: The columns are: 1)Cluster Name 2)Right Ascension 3)Declination 4)Redshift 5)arcsec to kpc conversion.

3.2 GMRT Observations

The observations were carried out in the following manner. Primary calibrators 3C 286, 3C 147 and 3C 48 (having high flux densities) were observed for around 15−20 minutes at the beginning and end of observations. The target source was observed for 25−30 minutes in each scan and phase calibrator was observed for 5 minutes between each target scan. Unresolved/point sources located as near to the target as possible were chosen as phase calibrators. The list of calibrators used for each cluster are given in Table 3.2. The data was acquired for every 2 seconds as opposed to 16 seconds which is the usual GMRT integration time. The high resolution data is required to get rid of the Radio Frequency Interference (RFI), described later. In the older mode of GMRT observations (before 2011) only one sideband of 8 MHz was observed at 150 MHz, while both the sidebands (USB and LSB) were observed at 325 and 610 MHz. Each sideband has 128 channels which gives a spectral resolution of 62.5 and 125 kHz at 150 and 325 MHz respectively. In the new mode of observations only one sideband of wider bandwidth (16 MHz at 150 and 32 MHz at 325 MHz) was observed, which consisted of 256 channels. All the observations used the GMRT full synthesis run which comprises 7 hours of observing time in each session. In most cases night time observations were preferred when data will be less affected by RFI. Two days were invested for observations at 150 MHz because at this frequency data is more severely affected by RFI. The details of the observations are given in Table 3.3. The archival data is marked by an asterisk (*).

The clusters A665 and A773 lie very close to each other in the sky plane. Hence, they were observed simultaneously with the same phase calibrator. Three nights were invested for observing these two clusters at 150 MHz. The clusters were observed for 15 minutes each on every scan and the phase calibrator was observed every 30 minutes for 5 minutes. The 325 MHz observations of the cluster A520 had to be repeated, as the phase calibrator was showing large variation in the phase, leading to difficulty in calibration of the target.

Name	Flux Cal	Phase Cal
A2163	3C 48/3C 286	3C 327.1
A2744	3C 48	0025−260
A665	3C 147/3C 286	0834+555
A520	3C 147	0521+166
A773	3C 147/3C 286	0834+555

Table 3.2: The columns are: 1) Cluster Name 2) Flux Calibrator observed at the beginning and end of observations 3) Phase Calibrator observed for five minutes between each target scan of 25−30 minutes.

Name	ν MHz	$\Delta\nu$ MHz	Date of Obs	Proj Code	On-Source Time hrs	Used BW MHz
A2163	153	8	22.5.2009	16_259	6.8	5.6
	153	8	24.5.2009	16_259	5.76	5.6
	332	16	3.6.2009	16_259	5.6	14.3
	617*	16	18.07.2002	02VKK01	3.39	14.4
A2744	153	8	25.8.2009	16_259	5.30	5.6
	153	8	27.8.2009	16_259	5.5	5.6
	332*	16	24.11.2006	11TVA01	4.7	14.6
	617	16	20.8.2009	16_259	4.38	14.4
A665	147	16	29.12.2014	27_070	2.28	14.6
	147	16	30.12.2014	27_070	3.4	14.6
	147	16	28.03.2015	27_070	3.6	14.6
	323*	32	7.01.2013	23_023	8	26
	610	32	29.10.2014	27_070	5.03	26
A520	147	16	29.12.2014	27_070	5.54	14.6
	147	16	30.12.2014	27_070	2.68	14.6
	240*	8	22.12.2008	15MAB01	4.1	5.3
	322	32	21.8.2015	27_070	4.5	27.34
	610*	16	24.01.2009	15MAB01	4.7	14.4
A773	147	16	29.12.2014	27_070	2.4	14.6
	147	16	30.12.2014	27_070	3.01	14.6
	147	16	28.03.2015	27_070	3.98	14.6
	323*	16	25.06.2005	08GBA01	4.8	14.4

Table 3.3: The columns are: 1)Cluster Name 2)Central Frequency of observation 3)Bandwidth 4)Date of Observation 5)GMRT Project Code 6)Time on target 7)Final used Bandwidth. *: GMRT archival Data.

3.3 Data Processing

3.3.1 Initial Flagging

The response of antennas fall off at the edges of frequency band. These channels with reduced sensitivity were discarded. Figure 3.1 shows the typical response of GMRT antennas for one sideband of 128 channels and a single polarization. For each antenna, the real part of the visibilities of each channel averaged over all the scans is plotted. The visibilities are scaled by a factor 1000 and weighted by median value of the entire band. We determined the usable bandwidth from a calibrator source and incorporated that range for further processing. The final bandwidth used at each frequency is mentioned in Table 3.3.

There are atleast two non-working antennas, on an average, in each GMRT observing session. Figure 3.2 shows an example plot to identify the non-working antennas. The amplitude of all 30 antennas used in the observations of A2163 is plotted for the phase-calibrator. The data is averaged over all the scans and both the polarizations. The baselines of each antenna is shown by colour scale. The baselines of non-working antennas show very low amplitude, while all the working antennas have almost a constant median amplitude.

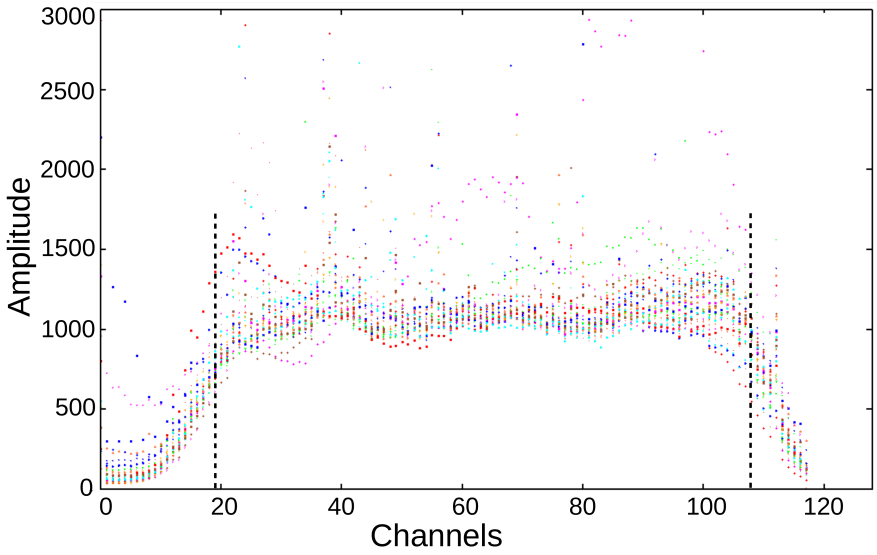

Figure 3.1: Bandshape of all the 30 GMRT antennas (of a single polarization), to identify the middle range of channels with nearly constant amplitude. Vertical dashed lines denote the lower and upper cutoff in channels used for processing. Different colours denote the 30 GMRT antennas.

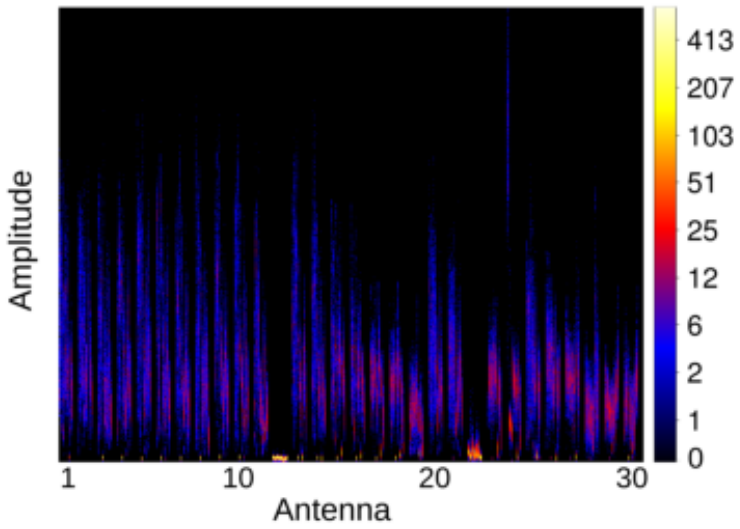

Figure 3.2: A plot to identify the non-working antennas during a GMRT observation. The median amplitude of all antennas is almost a constant while antennas showing very low amplitude are flagged. The colour scale shows the baselines corresponding to each antenna. All the baselines of antenna number 12 and 22 show very low amplitude, implying they were not working throughout the observations.

3.3.2 RFI removal in the raw data

The raw data at low frequencies are severely affected by Radio Frequency Interference (RFI) generated by different terrestrial signals. This is especially true for 150 MHz data which has been extensively used for this thesis. RFI can result in poor calibration solutions and therefore noisier image with ripples across the field. This is even more problematic when the target source has weak emission and lacks a definite structure, such as halos.

Initial RFI flagging was performed using the RfiX package (Athreya, 2009), which was applied individually to the flux and phase calibrators as well as the target source. This takes care of persistent and broadband RFI. Here persistent implies RFI that can corrupt data for tens of seconds or longer. Broadband refers to RFI affecting large portions of the observing band.

The algorithm works on correlator output from interferometer and makes use of fringe-stopping technique. An interferometer (which uses earth's rotation to track a source), compensates for the geometric delay between any two antennas by applying an additional delay which prevents the source from fringing at the phase centre. Due to earth's rotation, the delay introduced varies as a function of time and baseline. The fringe stop frequency is given by

$$\nu_F(t) = -\omega_E U_\lambda(t) cos\delta(t) \tag{3.1}$$

where ω_E is the angular velocity of the earth's rotation, $U_\lambda(t)$ is the instantaneous

spatial frequency component, and δ is the declination of the source at the phase centre. Any source of RFI that is stationary in space with respect to the interferometer, will affect a particular baseline with a constant amplitude and phase depending upon its location with respect to the two antennas. Due to fringe stopping, the RFI signal will be modulated at a rate equal to the fringe stop frequency. This will be true even in the presence of multiple sources of RFI having different amplitudes and phases, which will all add up vectorially. The resulting RFI signal will also fringe at the fringe-stop frequency.

The observed visibilities now become

$$V_{OBS} = V_{TRUE} + Ae^{i[2\pi\nu_F(t)t-\Phi]} + Noise \tag{3.2}$$

where $\nu_F(t)$ is again the fringe stop frequency, and A and Φ are the amplitude and phase of the RFI signal in the baseline. If the amplitude and phase of the RFI remain constant for a long enough time of the fringe period, then the observed data can be fitted for A and Φ, and V_{TRUE} can be estimated after subtracting the fit. The program does not lead to closure violations and the original visibilities are preserved.

Typical fringe fitting done by Rfix on visibilities (real and imaginary) is shown in Figure 3.3. The recovered visibilities after fringe subtraction is also shown. Figure 3.4 shows a comparison of rms values of raw data with the application of Rfix for a large number of five minute scans. After the application of Rfix the rms has decreased considerably in all the scans.

Rfix works best for smaller fringe periods so that the RFI remains more or less constant during the time and fitting can be achieved more effectively. It will fail for very rapidly changing RFI amplitude. Given these limitations, the algorithm may not work for very short baselines critical for imaging extended emission. These were tackled by different tools described later.

This technique can be applied to GMRT archival data also (having an integration time of 16 seconds). However, it works better for $2-4$ seconds integration time. Therefore we have used fresh observations at 150 MHz where RFI corrupts the data most.

At this stage basic clipping was done on the calibrators to remove some outlier points (very high or very low deviant points). This is normally achieved by AIPS task TVFLG. We have used an automated procedure which allows for quick and easier visualization as well as flagging of the deviant data points. Figure 3.5 shows the amplitude versus rms plot for the calibrators and the target source. The mean amplitude over the two polarizations, channels and time is plotted as a function of its rms. The calibrator sources are usually point sources. Therefore, we expect a compact structure in the plot. This is not true for the target sources. Clipping is done only for the calibrators. Very high or low amplitude and rms values are flagged.

Other ways in which data were examined was by looking at rms amplitude versus rms phase or UV-length. The data was then taken to Astronomical Image Processing System (AIPS; http://www.aips.nrao.edu/) from NRAO for further processing.

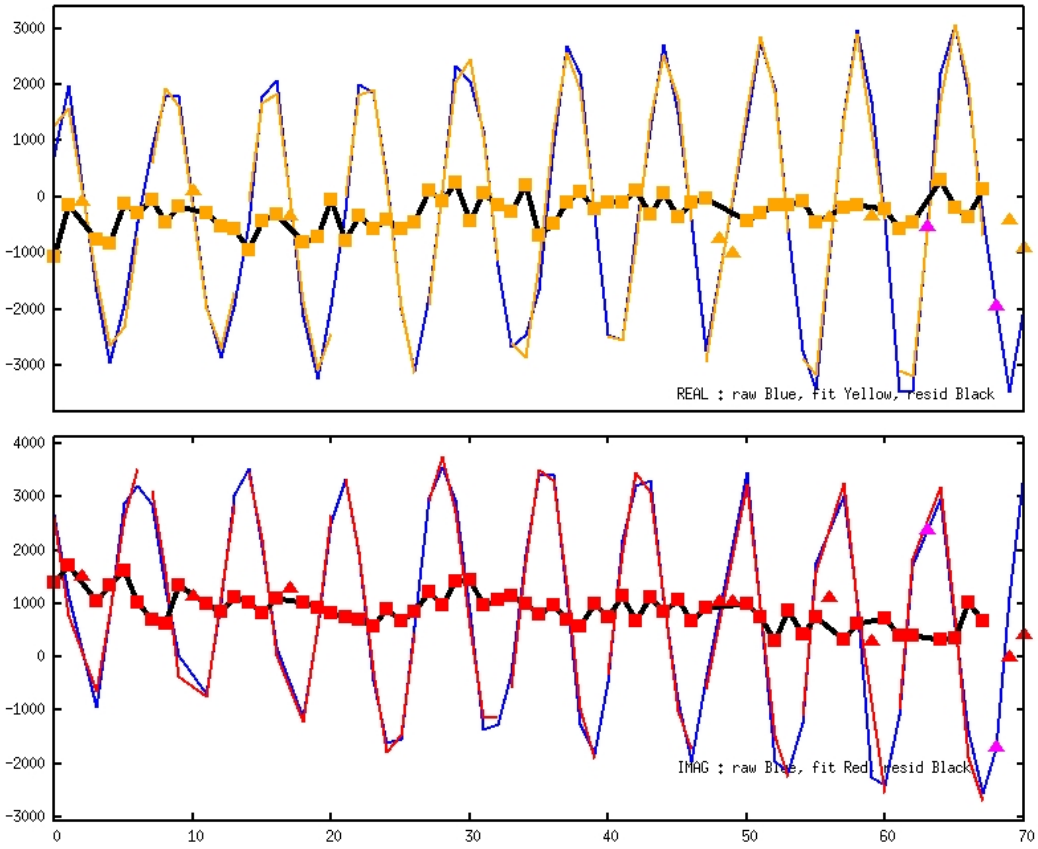

Figure 3.3: Fringe fitting done by Rfix on real and imaginary part of visibilities. Residuals after fringe subtraction, i.e. the true visibilities, are shown in black.

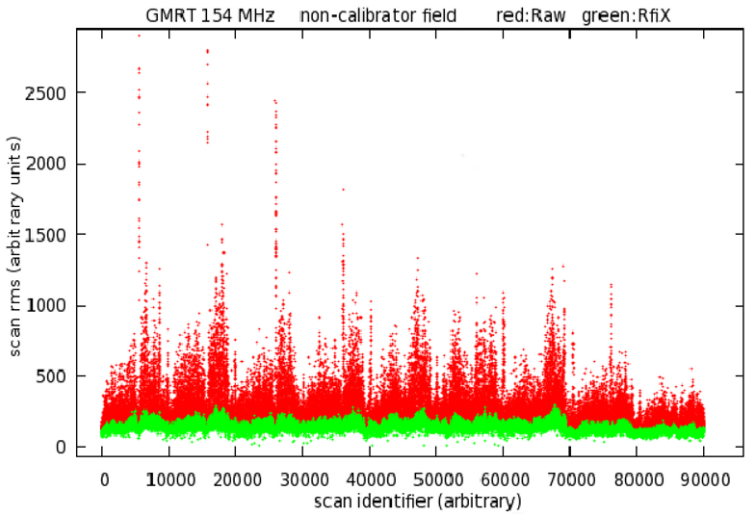

Figure 3.4: Decrease in rms values in each scan after the application of Rfix.

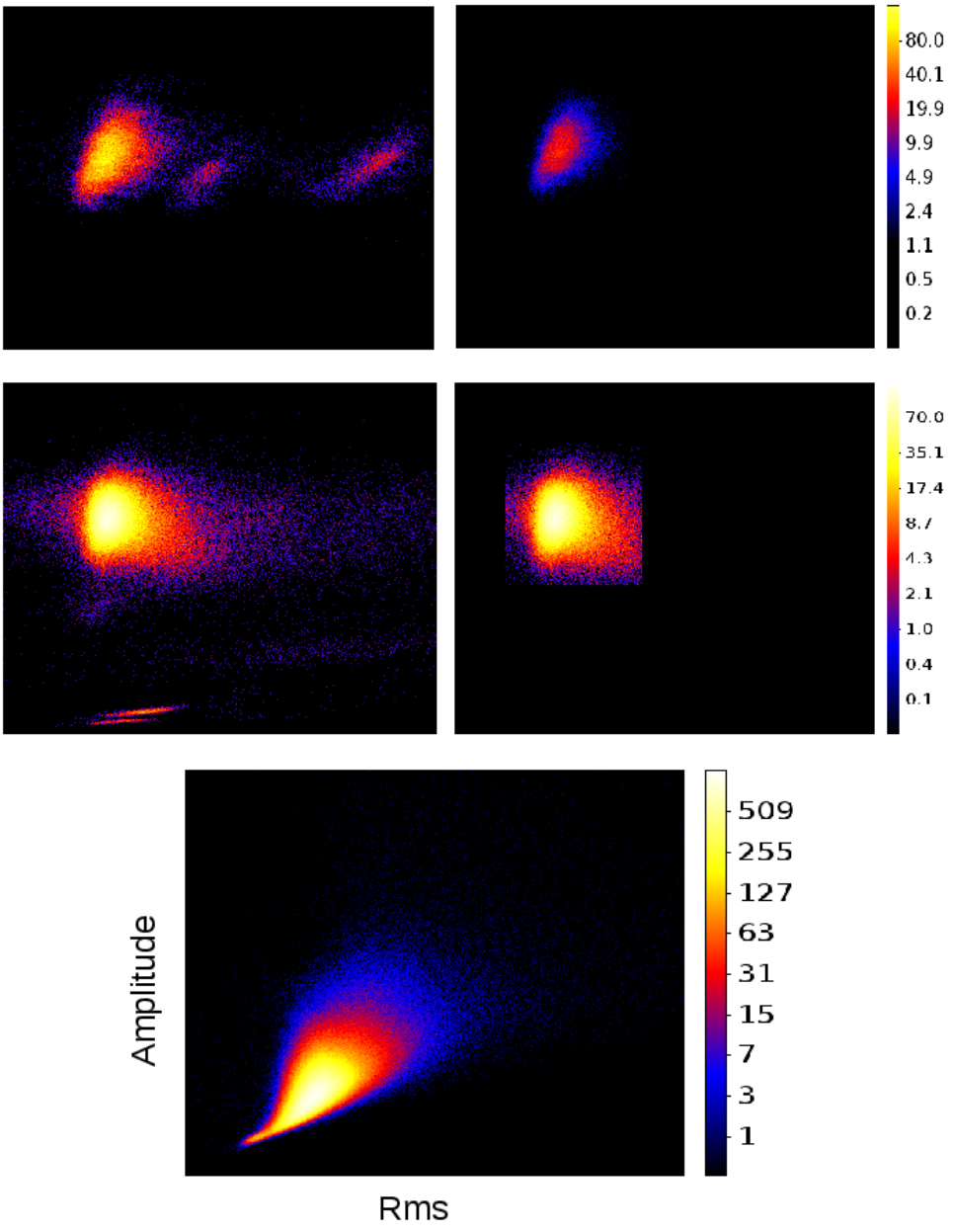

Figure 3.5: An example plot of Amplitude versus Rms used for flagging outliers. Pre-flagging visibilities are on the left and post-flagging visibilities, assuming a point source model, are on the right. Top and middle panels show the flux and phase calibrators, respectively. The bottom panel shows the target, for which no flagging was performed.

3.3.3 Calibration

Calibration is done to find antenna complex gain solutions which changes due to instrumental offsets or ionospheric changes. It is performed at various stages during data processing. This includes bandpass calibration, amplitude and phase calibration of the flux and phase calibrator, and finally self-calibration of the target field.

The response of antennas across the frequency band is obtained from bandpass calibrator which is usually the flux calibrator. This is achieved by tasks POSSM and BPASS in AIPS. The solutions were inspected and outlier channels were flagged. The solutions were smoothed with a sliding median window. The bandpass solutions were applied to the phase calibrator and the target.

The standard AIPS recipe for calibration includes first calculating the flux density of the flux calibrator using the task SETJY. The task CALIB is run to perform amplitude and phase calibration by supplying a clean component model of the flux calibrator. The model will be scaled to match the flux density information provided by SETJY. The secondary calibrators are also calibrated using CALIB. The flux density of the phase calibrator is retrieved by using the antenna gain solutions from the calibration process and the flux density of the primary calibrator. The task GETJY is used for this step. Finally, the antenna solutions from flux and phase calibrators are interpolated into a CL table using the task CLCAL.

We have adopted a different calibration process than the one mentioned above. We have calibrated the phase calibrator first. AIPS sets its flux density to unity by default. This is then used to calibrate the flux calibrator and its flux density is determined from SETJY. One round of imaging is done to determine its flux from IMFIT. The ratio of the flux densities determined from SETJY and IMFIT sets the flux density of the phase calibrator. This is the flux density scaling that is later on used to scale the target field. The flux scaling was set using Perley and Butler (2015).

Calibration solutions determined by the phase-calibrator were transferred to the target. The scale factor obtained through previous step was also applied. Calibration was done separately for different days of observations in the case of 150 MHz which were then combined using the task DBCON in AIPS.

Calibrators are generally chosen such that they are strong point sources over a wide range of UV-lengths. In addition, phase calibrators have to be as near to the target source as possible. The phase calibrator 3C 327.1 chosen for the cluster A2163 was a point source only between 1 and 4 kλ. Therefore, running CALIB on the entire UV-range resulted in many failed solutions. Calibrating within the limited UV-range and giving lesser weight to the data outside this range (setting WTUV to 0.1 in CALIB) resulted in very few failed solutions.

3.3.4 Data Averaging

The initial few steps of RFI removal and data editing were done on high resolution data which was required for identifying RFI and subtracting out from the visibility data. In order to speed up the imaging and self-calibration process, we averaged the target data

in time and channel to reduce its size. Each 5 channels and 14 seconds in time were averaged. The final spectral resolution is 312.5 kHz at 150 MHz and 625 kHz at 325 MHz respectively. The averaged data were then used for imaging.

Averaging data lead to distortions in the image, known as 'bandwidth' and 'time average' smearing. Bandwidth smearing is due to finite observing bandwidth of the interferometer. The antenna co-ordinates (U,V) vary as a function of frequency, but they are recorded only for the central frequency of observation. The true and recorded co-ordinates are related by

$$(U,\, V) = \left(\frac{\nu_0 U_\nu}{\nu}, \frac{\nu_0 V_\nu}{\nu}\right)$$

where, ν_0 is the central frequency of observation and U_ν and V_ν are the co-ordinates at frequency ν. The effect on the image plane upon fourier transform, is to smear a point source at a location (l, m), radially by a length $(\Delta\nu/\nu_0)\sqrt{l^2+m^2}$ and a decrease in the source strength. To reduce its effect, the bandwidth is divided into narrow channels (such that they will not be affected by smearing), and the co-ordinates are calculated for each channel separately.

As we average every five channels, we can estimate the reduction in peak intensity of the point source at the edge of the primary beam. The reduction in peak intensity for a square bandpass and circular gaussian beam is given by

$$R_{\Delta\nu} = \frac{\sqrt{\pi}}{2\sqrt{ln2}\beta_{max}} erf(\sqrt{ln2}\beta_{max})$$

$$\beta_{max} = \frac{\Delta\nu B_{max}}{\nu 2\sqrt{ln2} D}$$

Here, $R_{\Delta\nu}$ is the fractional reduction in peak intensity, B_{max} is the largest baseline length in metres and D is the diametre of the antenna. The reduction at the edge of the primary beam with averaged channel width of 312.5 kHz at 150 MHz and 625 kHz at 325 MHz is less than 10%.

Time average smearing is due to averaging and recording the data in order to reduce its size. Again, as the antenna co-ordinates change with time due to the earth's rotation, averaging data will give wrong estimations of the U,V values depending upon the integration time. In the image plane, this will lead to rotation of the sources at a rate equal to earth's rotational speed. A point source away from the phase centre would now get smeared in azimuthal direction. The default integration time of GMRT is 16 seconds. We requested for 2 seconds integration time, which upon averaging have 14 seconds of data. The archival data were therefore not averaged in time during analysis.

3.3.5 Imaging and self-calibration

We have used circular beam for imaging, with approximate resolution of 23, 12 and 6 arcsec at 150, 325 and 610 MHz, respectively. The pixel size is 4.5, 2 and 1 arcsec at

the three frequencies. Various rounds of phase self-calibration (Cornwell and Fomalont, 1989) and imaging (Schwab, 1984) were performed in AIPS using the tasks CALIB and IMAGR. Wide-field imaging was performed using facets. A total of 37, 43 and 55 overlapping facets of size 1024 × 1024 pixels spanning the primary beam were used at 150, 325 and 610 MHz. Tighter boxes (256 × 256 pixels) were put around strong sources. The number of small boxes depend upon how deep we clean the image (noise and detection threshold for point sources). Subsequent rounds of imaging and self-calibration result in more number of sources given as input model for self-calibration. The total number of facets used in the last round of imaging for each cluster are given in Table 3.4.

The smaller facets containing strong sources were cleaned first and then the bigger facets. This process has an advantage because all the strong sources will be centered at the phase centre which will result in lesser residuals elsewhere (due to them) at the time of cleaning. On the other hand, a strong source at the edge of a large facet will result in improper cleaning, even though one may save time using bigger facets. We have used 3−8 thousand iterations for cleaning strong sources, and more than 30000 iterations for cleaning the full field. Channel-by-channel calibration was also performed after a few rounds of channel averaged calibrations, which improves the solutions to a large extent if the initial model is correct.

In a few cases, many ripples were seen across the image after the first round of imaging the entire field. Carrying out self-calibration on this data resulted in large-scale rejection of data (more than 50−60%). Ripples are usually due to a few baselines that show very high amplitude (up to 50−100 Jy). These baselines were identified and flagged.

Name	150 MHz	325 MHz	610 MHz
A2163	87	78	80
A2744	89	64	61
A665	78	58	77
A520	105	63	-
A773	68	64	-

Table 3.4: The columns are: Cluster Name (Col. 1), total number of facets used at 150 MHz (Col. 2), 325 MHz (Col. 3) and 610 MHz (Col. 4). The total number of facets includes 37, 43 and 55 big facets of size 1024×1024 pixels each at the three frequencies, and the rest are smaller facets of size 256×256 pixels centered on strong sources.

3.3.6 Residual flagging for additional RFI removal

As mentioned before, the procedure mentioned for initial RFI removal does not take care of very strong RFI signals that are intermittently present in time or frequency band. This may cause ripples in the image which leads to wrong estimation of halo properties such as size and flux densities.

The flagging routines used here were applied on residual visibilities (Sekhar and Athreya, 2018). After atleast five rounds of imaging and self-calibration, the residuals of the UV-data were obtained by subtracting out the clean components of all the sources in the field using the task UVSUB.

RFI present for short duration of time appear as very high points in the residual visibility data, which cause ripples in the image. The algorithm GRIDFLAG grids the residual UV-data with a default size of each grid as $10\times10\lambda$. The median value of the visibilities falling into each grid is calculated and plotted as annular strips for calculating RFI threshold as a function of UV-distance. RFI affected data (which is seen as high points in the residual visibility plane) is identified by comparing the median values of UV-grid with the neighbouring grids. Sigma clipping is done to flag away the high points.

The flagging procedure was applied to all the clusters. Figures 3.6 and 3.7 show its usage for two clusters at different frequencies. The amplitude in the visibility plane before and after the application of the program are plotted. As can be seen in the figures very high points are significantly suppressed.

An important point to be mentioned here is that the residual file usually contains a significant amount of diffuse emission from the halo. The flagging routines were applied typically to baselines greater than $3k\lambda$ to not flag away the lower UV-coverage critical for halo emission. Still, at some point it was required to get rid of ripples contributed by lower baselines. Multi-scale imaging was done using the AIPS task IMAGR by giving at least three gaussians. The choice of parameters depend upon the observing frequency and size of the halo. These multi-scale images were then subtracted from the UV-data to get rid of the residual emission from the halo. The file was thereby used to carefully flag at lower baselines. Although, the AIPS implementation of multi-scale CLEAN is not very sophisticated, yet subtracting out the multi-scale images resulted in mimimum halo emission in the residuals.

3.3.7 Generating the final Image

The flags from previous step were transferred to the first UV-file, and imaging and self-cal loop was repeated. The whole procedure of imaging, self-calibration and residual flagging loop was repeated several times until a good image was obtained. In the last round, amplitude calibration was performed and primary beam correction was applied using the AIPS task PBCOR (Lal, 2013).

Only the central facets containing the halo were used for making spectral index image, by subtracting out the clean components of all other sources from the field. Final images of the halos have a noise range of $0.7-1.3$ mJy/beam at 150 MHz ($23''$ resolution), $60-100\mu$Jy/beam at 325 MHz ($12''$ resolution) and $40-70\mu$Jy/beam at 610 MHz ($6''$ resolution). Figure 3.8 and 3.9 show the noise histogram in the final images containing the halos.

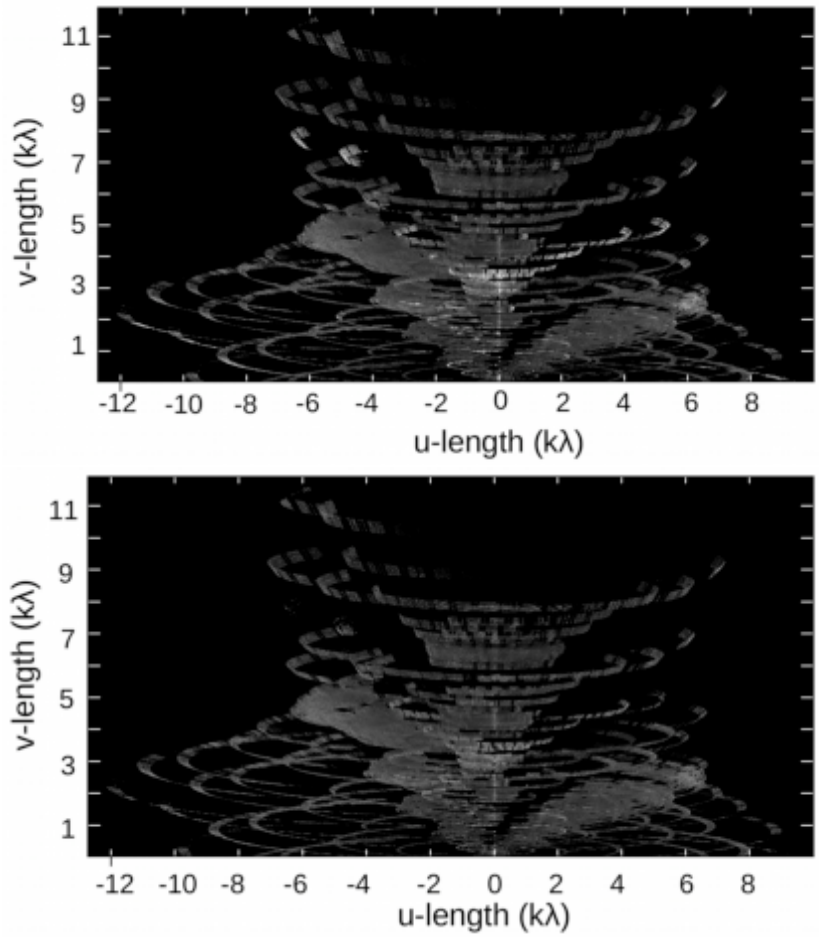

Figure 3.6: The UV-grid plot of the residual visibilities of halo A2163 at 153 MHz, before (*Top*) and after (*Bottom*) the application of GRIDFLAG. The median flux density in a grid size of $10\lambda \times 10\lambda$ is shown. The high points in the figure correspond to RFI, and are removed by sigma clipping.

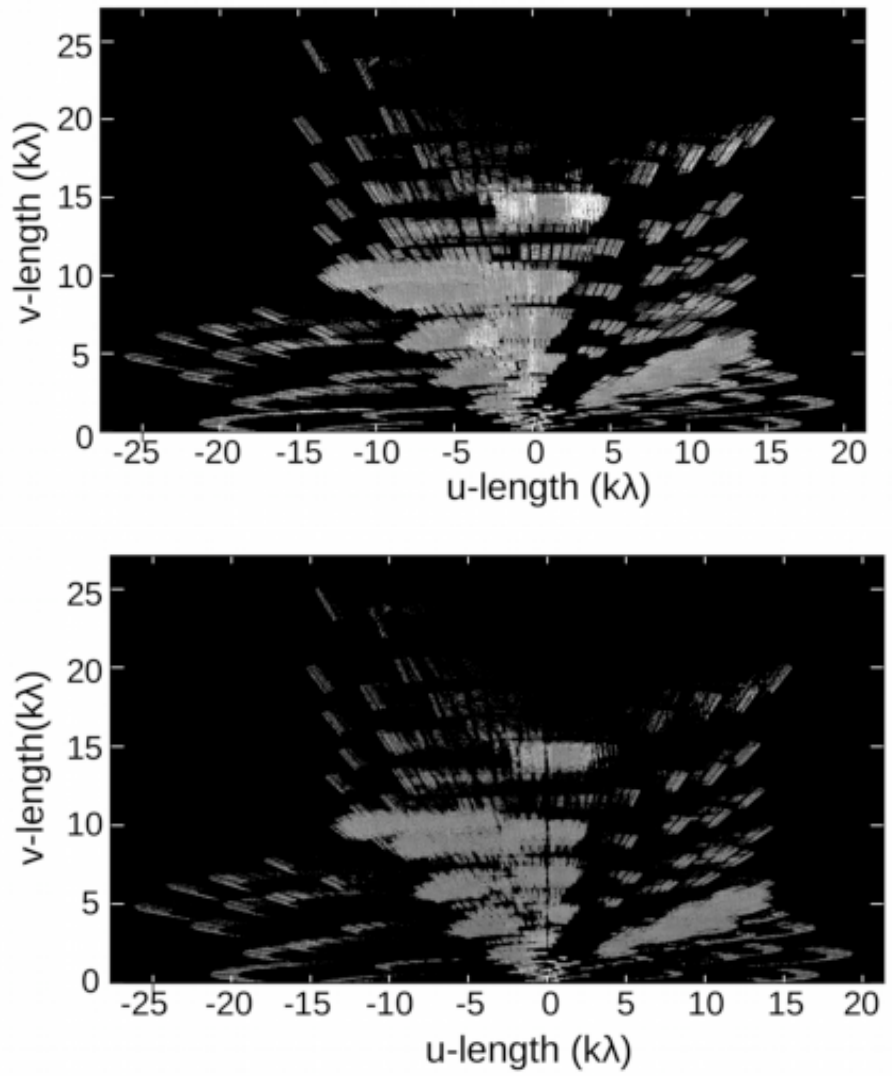

Figure 3.7: Same as Figure 3.6 for the halo A520 at 325 MHz, before (*Top*) and after (*Bottom*) the application of GRIDFLAG. The grid size is $20\lambda \times 20\lambda$. The vertical line through the centre and other high points are removed through the flagging routine.

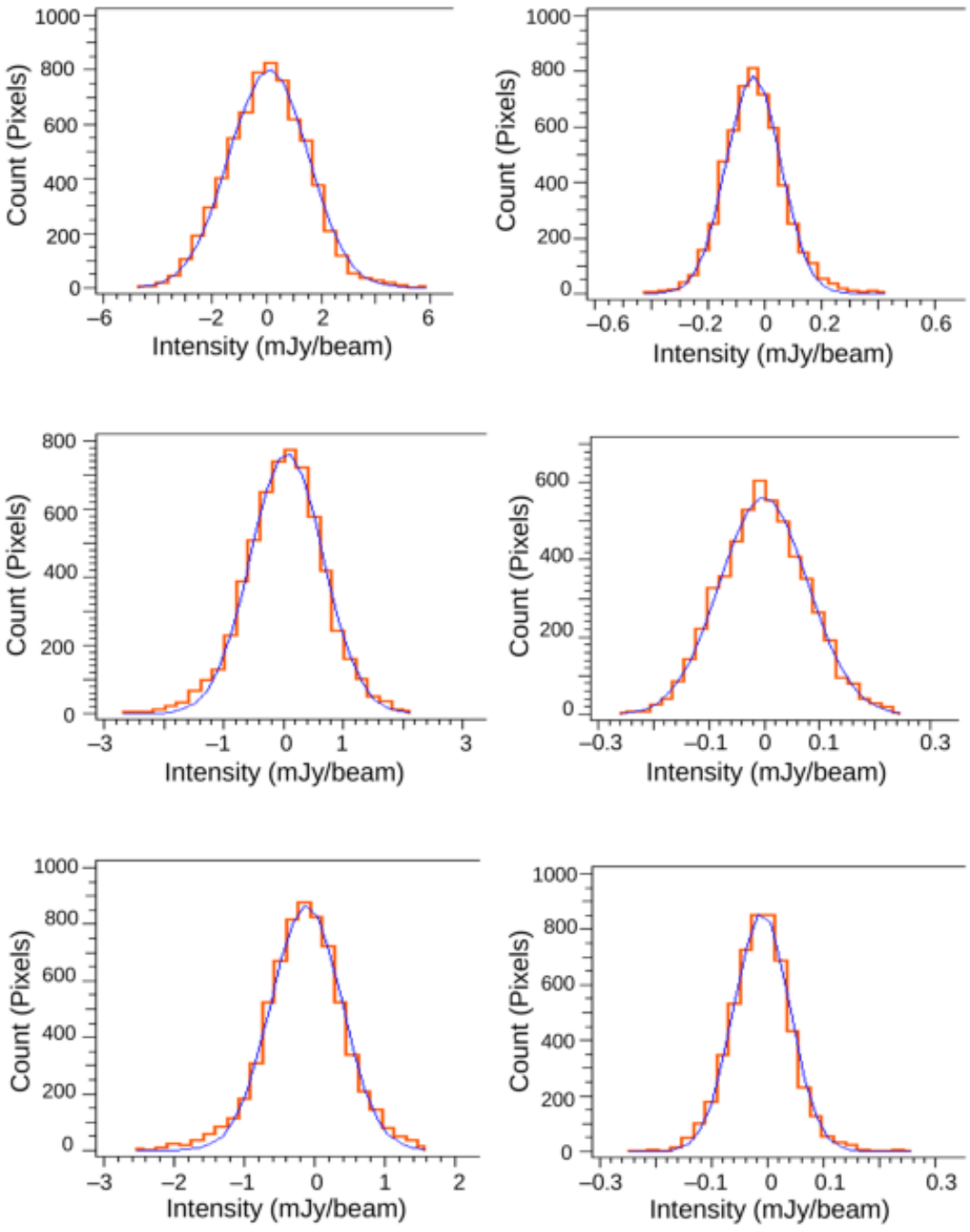

Figure 3.8: Histogram showing image rms at 150 MHz (*Left*) and 325 MHz (*Right*) for the halos A2163, A2744 and A520 from top to bottom.

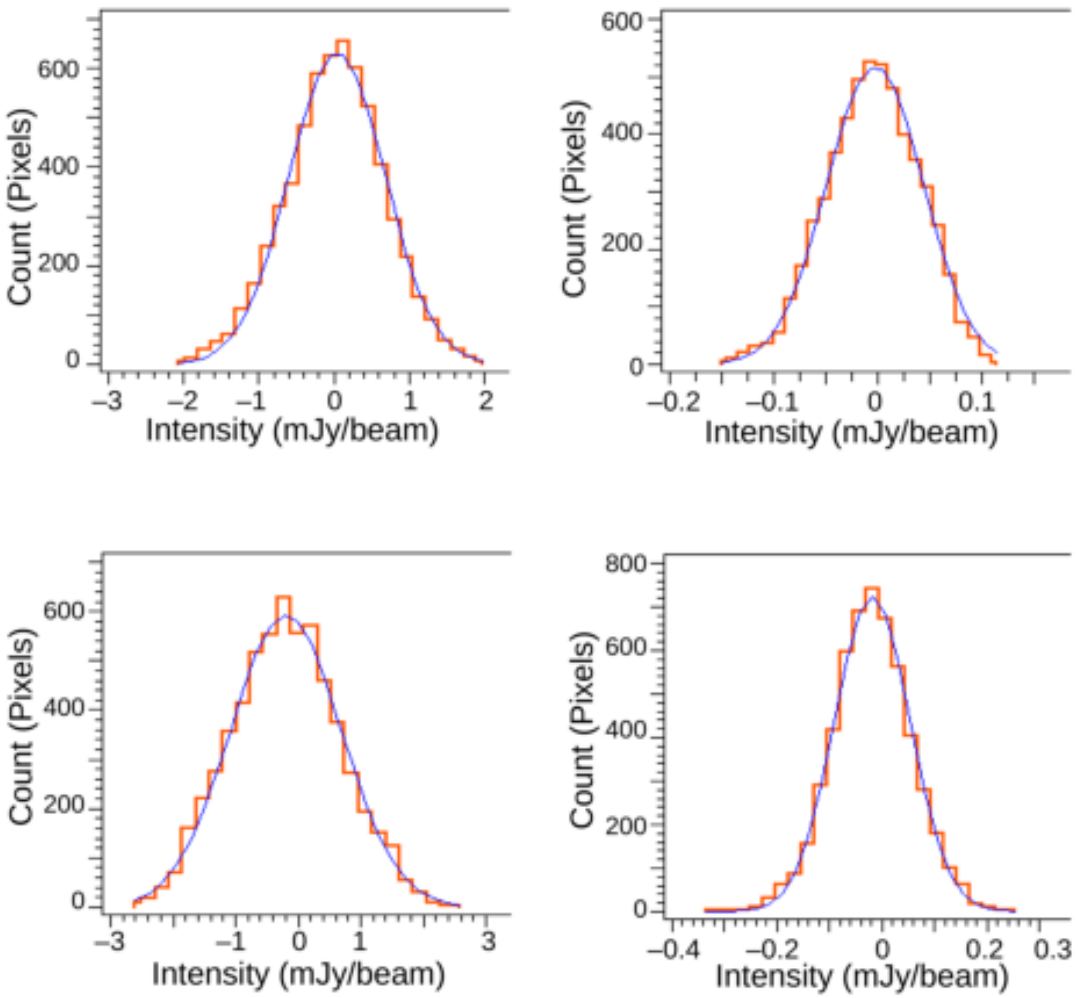

Figure 3.9: Same as Figure 3.8 for the halos A665 (*Top*) and A773 (*Bottom*).

3.3.8 Imaging of GMRT archival data

The GMRT archival data were also imaged using similar techniques. In a few cases the archival data did not yield image of sufficient quality to construct the spectral index images, especially at 610 MHz where halo emission is also comparatively less. This could be due to longer integration time of 16.94 seconds. The problem is aggravated due to lack of lower baselines at 610 MHz, necessary for the imaging of diffuse large scale emission. The high resolution archival data served the purpose of identifying the locations of point sources within the halo. Hence they have been used as complementary to our main observations. The archival data at 325 MHz has been effectively used for constructing the spectral index images, as the halo emission is higher at this frequency.

3.4 Imaging Extended Emission: Some Issues

The shorter baseline UV-coverage of the interferometer plays a very important role in imaging of extended emission. This varies between frequency of observation and telescopes. At lower frequencies the short spacing has a better coverage. For example, there is a lack of baselines less than 20λ (= 40 metre) for GMRT at 150 MHz. This is due to finite distance between the antennas. The visibility $V(0,0)$ which corresponds to the total flux of the sky upon fourier transform is not measured by an interferometer. This introduces a negative 'bowl' in the instrument response function, which when convolved with the extended emission at the centre results in negative brightness around it. Therefore, estimation of the halo flux density becomes difficult. The issue of missing short spacings of antennas has been a long standing problem. The background estimation can be performed with a single dish telescope with equivalent sensitivity and coverage to the interferometer at that frequency. Deconvolution algorithms such as CLEAN (Högbom, 1974; Clark, 1980) can only partially alleviate the problem. Multi-resolution clean which cleans the source with multiple gaussians can better recover the flux from extended emission. The AIPS implementation of the multi-resolution clean was used to remove the residual extended emission before taking the UV-file for flagging. These images were not used for making spectral index images as they were found to be noisier.

There are also various data weighting schemes available such as 'uniform and natural'. These weights are applied to the data before taking them for fourier transform. The UV-data is gridded before the fourier transform and the weighting factor is proportional to the number of UV-points falling in a gridded cell. In the case of uniform weighting, the weight is inversely proportional to the number of samples in a given cell. This will give lesser weight to short baselines as there are larger number of shorter baselines compared to the longer ones in an interferometric array. The result is reduced sensitivity to extended emission but the image gains in resolution. For natural weighting, higher weights are given to higher UV-density and therefore this mode is preferred for imaging extended emission, where resolution can be compromised to some extent. This is also the default mode of imaging in AIPS. The ROBUST parameter in the AIPS task IMAGR, introduced by Briggs (http://www.aoc.nrao.edu/dissertations/dbriggs/) con-

trols the data weighting options. In addition, UV-tapering can also be used to suppress the contribution of longer baselines by using a gaussian weighting function. All these weighting schemes were tried and it was found that the best possible image of the halo was with ROBUST=0, which gives a trade-off between resolution and sensitivity.

The loss of halo flux density and structure was further explored by making images with variable lower UV-cutoffs. The effect is illustrated in Figure 3.10, where a halo from our sample (A2163) is imaged at 150 MHz with no UV-limit, and lower UV-cutoff = 100λ, 200λ and 300λ. The halo occupies the central part of the image along with a sharp feature at its centre, which we call the *ridge* (Chapter 4 of the thesis). The largest linear size of the halo is $10'$ in east-west direction. At 100λ (which is also approximately the minimum short baseline length at 325 MHz), the halo structure remains nearly unchanged. At 200λ, the halo size is reduced by nearly $4'$ in east-west direction and the flux density decreases by half. Evidently, at 300λ only the bright central *ridge* is visible. Beyond this, even the *ridge* loses structure. This implies that the lower UV-cutoff we have used for making the spectral index images (=50−100 λ) is perhaps safe with regard to halo structure and flux density.

The presence of very strong sources near to the halo is another major concern. The deconvolution procedure often leaves the shape of the synthesized (dirty) beam across it causing large negative and positive sidelobes which may extend out to the halo. The shape of the dirty beam depends upon the UV-coverage, which in turn depends upon the location of the source. The sidelobe levels are decided by the gaps in the UV-coverage. We have encountered such a problem for the halo A665 (a high declination cluster), which had a very strong source nearly 15 arcmin from the halo. The flux density of the source is approximately 1168, 716 and 410 mJy at 150, 325 and 610 MHz. Figure 3.11 shows the effect of the sidelobes of the dirty beam due to the source on the halo. The effect is more severe at 610 MHz because of the faintness of the halo at this frequency. We tried 'peeling' of the source at 325 and 610 MHz by first obtaining the residual UV-file after subtracting out all the sources. Only the facets containing the point source to the left of the halo were added, and the UV-file was calibrated and imaged in this direction. This gives better calibration solution for the source in this direction. The image was then subtracted from the UV-file which leaves better residuals for the source. The CALIB solutions were inverted using the task CLINV and next point source added. The procedure was repeated. However, peeling did not help in this case. Several rounds of imaging and flagging resulted in slight improvement at 610 MHz, while at 150 and 325 MHz we could manage to get rid of the ripples at the centre. Imaging of just the halo resulted in further improvement of the image.

We have observed a decrease in the flux density of the halo when the resolution of the final UV-file containing only the halo facets, is lowered in order to make the spectral index images. For instance, at 325 MHz, when the resolution of the image is changed from 10 arcsec (its native resolution) to 23 arcsec (resolution at 150 MHz), then the halo flux reduced by as much as 50−100 mJy in some cases. This is not due to any lower UV-cutoff given for imaging. As a check, we imaged the full field at lower resolution and yet the problem persisted. As an alternative to imaging, we re-gridded and convolved the 325 MHz image. This procedure is mentioned in greater detail under the section

'Spectral Index Imaging' and did not result in the loss of flux density.

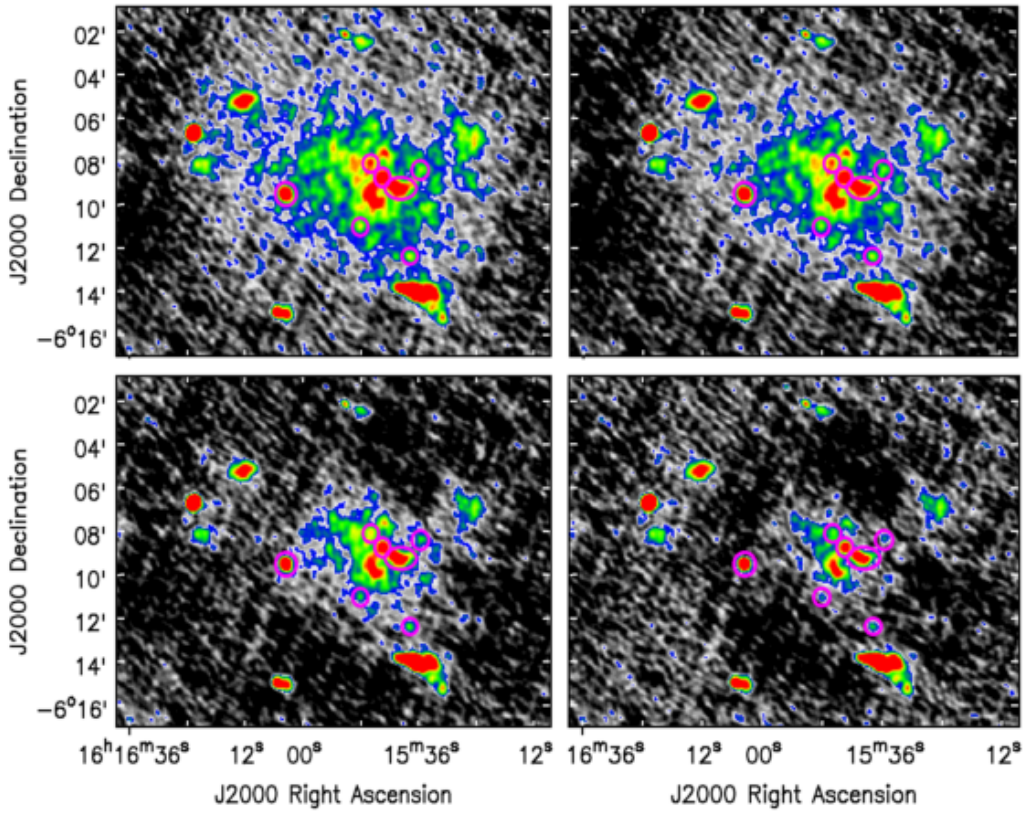

Figure 3.10: The halo of A2163 at 150 MHz with no UV-cutoff (*Top left*), lower UV-cutoff = 100λ (*Top right*), 200λ (*Bottom left*) and 300λ (*Bottom right*). The halo starts losing structure beyond 200λ. Pink ellipses denote point sources identified by 610 MHz image (Chapter 4).

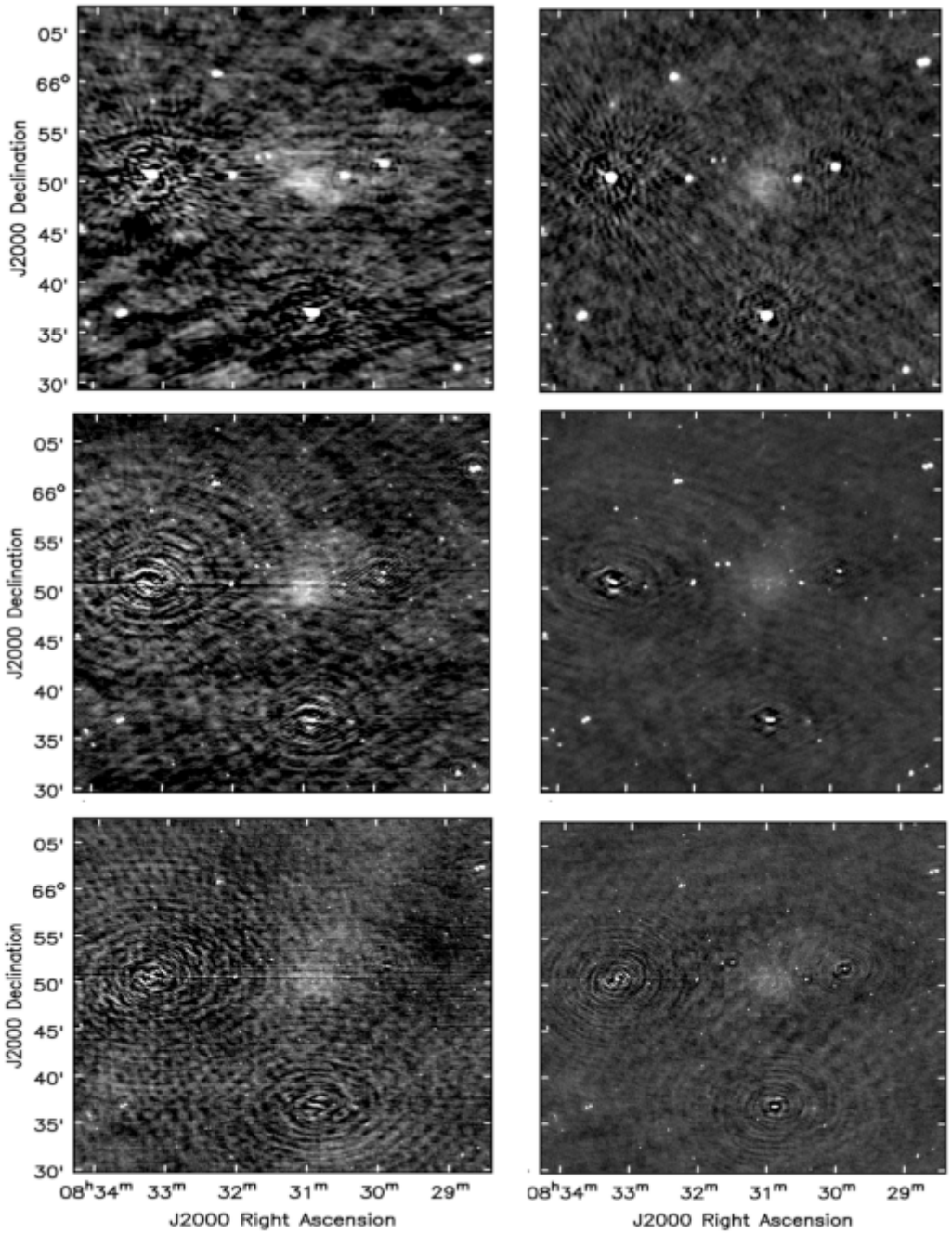

Figure 3.11: The cluster A665 has a strong source nearly 15′ east of the halo, which caused large scale ripples to extend till the halo. The top, middle and bottom panels are 150, 325 and 610 MHz images. Left panels denote the images after the first self-calibration, while right panels are imaged after applying flagging routines and self-calibration. The ripples have reduced in intensity in all the three cases.

3.5 Flux Density Scale

Despite the flux density scaling carried out by the flux calibrator, there are usually discrepancies in the flux densities of the observed sources in the field in comparison to those available in literature. This is usually a small multiplicative correction factor which may have resulted from various factors such as errors in self-calibration, beam shape, etc. The correction factor for each individual cluster at each frequency was determined and applied to the final image.

3.5.1 Source Extraction

We used the software Python Blob Detector and Source Finder (PyBDSF) (Mohan and Rafferty, 2015) to locate the sources in our field. The primary beam corrected full field image was given as input to the algorithm.

PyBDSF uses FITS Stokes I images (or CASA images) to first generate noise and mean images. A threshold for detecting sources is set, which can also be specified by the user. It then fits multiple gaussians to contiguous islands of emission based on those parameters. In its default mode, a threshold of 3σ is used to define the island boundary and 5σ to detect sources. Gaussians within a given island are grouped together into sources. The software indicates whether single or multiple gaussians were used to decompose a source. Also, extended emission is excluded from gaussian fitting by default, which eliminates the halo at the centre. However, if the halo has strong condensed structures within it, such as we see in the case of A2163 (Chapter 4), then those structures are fitted as well. This does not affect our purpose as we eventually use only the point sources of the field for flux density comparison. An example image of the fitting done by PyBDSF is shown in Figure 3.12 for the cluster A2163 at 325 MHz. A residual image after subtracting out the gaussian model from the original image is also shown.

3.5.2 Catalogs used for Source Matching

The catalogs generated by PyBDSF at the frequencies 150 and 325 MHz for each halo is compared with the TIFR GMRT Sky Survey (TGSS) (Intema et al., 2017) at 147.5 MHz and NRAO VLA Sky Survey (NVSS) (Condon et al., 1998) at 1400 MHz.

TGSS-Alternate Data Release 1 has a beam size of $25'' \times 25''$ and median noise of 3.5 mJy/beam. The catalog covers 36 900 deg^2 of the sky between -53° and $+90^\circ$ declination, which is 90 percent of the total sky. The median detection threshold for sources is 24.5 mJy/beam. The standard deviation of positional offset of sources is less than 2 arcsec in right ascension and declination and the flux density error is around 10%. The primary beam parameters were independently derived for the survey using known flux calibrators like 3C 48, 3C 147, 3C 286 etc. Except for 3C 286 (which needed a scaling by a factor 1.55), the primary beam model derived was found to be a good match for all the calibrators.

The NVSS survey has a beam size of $45'' \times 45''$ and the sensitivity is 0.45 mJy/beam (Condon et al., 1998). The survey covers the entire sky north of the declination -40

degrees. The uncertainties in right ascension and declination are less than 1 arcsec for point sources stronger than 15 mJy and 7 arcsec for the faint sources (Flux density = 2.5 mJy which is the detection threshold).

3.5.3 Catalog Matching

The four catalogs (our 150 and 325 MHz data, TGSS and NVSS) were matched using TOPCAT (Taylor, 2005), and sources with positional coincidence less than 10″ (HPBW at 325 MHz) were selected. This resulted in around 50−100 common sources. Point sources were extracted from this list by selecting only those sources whose deconvolved major axis is smaller than the HPBW of the synthesized beam. We used the higher resolution 325 MHz beam size for this step i.e deconvolved major axis $\leq 10''$. A further elimination was performed by discarding those sources whose flux density is below 10σ in TGSS or NVSS survey.

3.5.4 Estimation of Flux Density and Positional Errors

The percentage difference in flux density calculation is found by $\frac{S_{obs} - S_{exp}}{S_{exp}} \times 100$. Robust sigma clipping was done to eliminate the outliers. The multiplication factor was estimated based on the ratio $\frac{S_{obs}}{S_{exp}}$ and applied throughout the data. This includes just increasing or lowering the final image by this factor. In most cases the factor was less than 5%. The scatter in flux densities after applying this correction factor is shown in Figures 3.13 to 3.17 for all the clusters. The list of the sources used and their measured flux densities at 150 and 325 MHz are given in the Appendix.

We also compared the source positions with the TGSS values. These are again shown in Figures 3.13 to 3.17. In most cases the mean values and standard deviations of positional coincidence lie well within the pixel size (=4.5 and 2 arcsec at 150 and 325 MHz respectively). The scatter is more at 150 MHz perhaps due to larger errors in phase self-calibration at this frequency. For the case of A665 and A773, the scatter at 150 MHz is higher (= 15″ and 8.9″). But this is also within the beam size of 23″. We also find a systematic offset between RA and DEC at both the frequencies of A520, which may be again due to calibration errors.

For consistency purpose we have used only TGSS and NVSS catalogs for all the clusters, although for example WENSS survey at 327 MHz (Rengelink et al., 1997) was available for the cluster A665. We have refrained from using VLSS survey at 74 MHz due to its much bigger beam size and higher noise. Also few sources may show a turnover in spectral index between 150 and 74 MHz. In fact, turning of spectral index poses a problem especially at 610 MHz, where in general 15−20 sources are found to match with the TGSS and NVSS catalogs because of its much smaller primary beam size (∼1 deg). The sources having extremely flat spectrum or a turnover between 610 and 150 MHz would lead to erroneous estimation of flux density values at 610 MHz. These sources were manually checked and eliminated if necessary. Only for the case of A2744, the 610

MHz data was useful to derive halo properties. In other cases the 610 MHz image is used just as an indicator for point sources and therefore an accurate flux density scaling is not an issue.

We have calculated the spectral index for the sources used in flux density scale estimation. The mean value is approximately between -0.73 to -0.78 for each halo, which is again consistent with the typical values of spectral indices of radio galaxies (Mahony et al., 2016). The information is provided in the Appendix.

Comparison of the positions of the above selected sources in our 150 and 325 MHz data is shown in Figure 3.18 for all the five clusters. Ideally the positional offsets in RA and DEC should be centered around zero. All the clusters show a slight deviation of mean values, which are well within the pixel size. The positional offsets have not been corrected for. The RA of A665 and A773 show a very large scatter (standard deviation $16''$ and $10''$ respectively). A possible reason for this could be that the observations at 150 MHz were carried on three different days. The phase centre of the observations were slightly different on all the three days, although less than an arcsec. This created a problem while combining the data of all the three days before imaging. Therefore, the AIPS task UVFIX was used to adjust the phase centres of all the days to a common phase reference. This may have caused larger variations in positions of sources between 150 and 325 MHz. We explored the variations in RA offsets as a function of radial distance from the phase centre. Although the number of sources are less, we can see that within a degree the offset is less than 10 arcsec. So the effect at halo would be less severe.

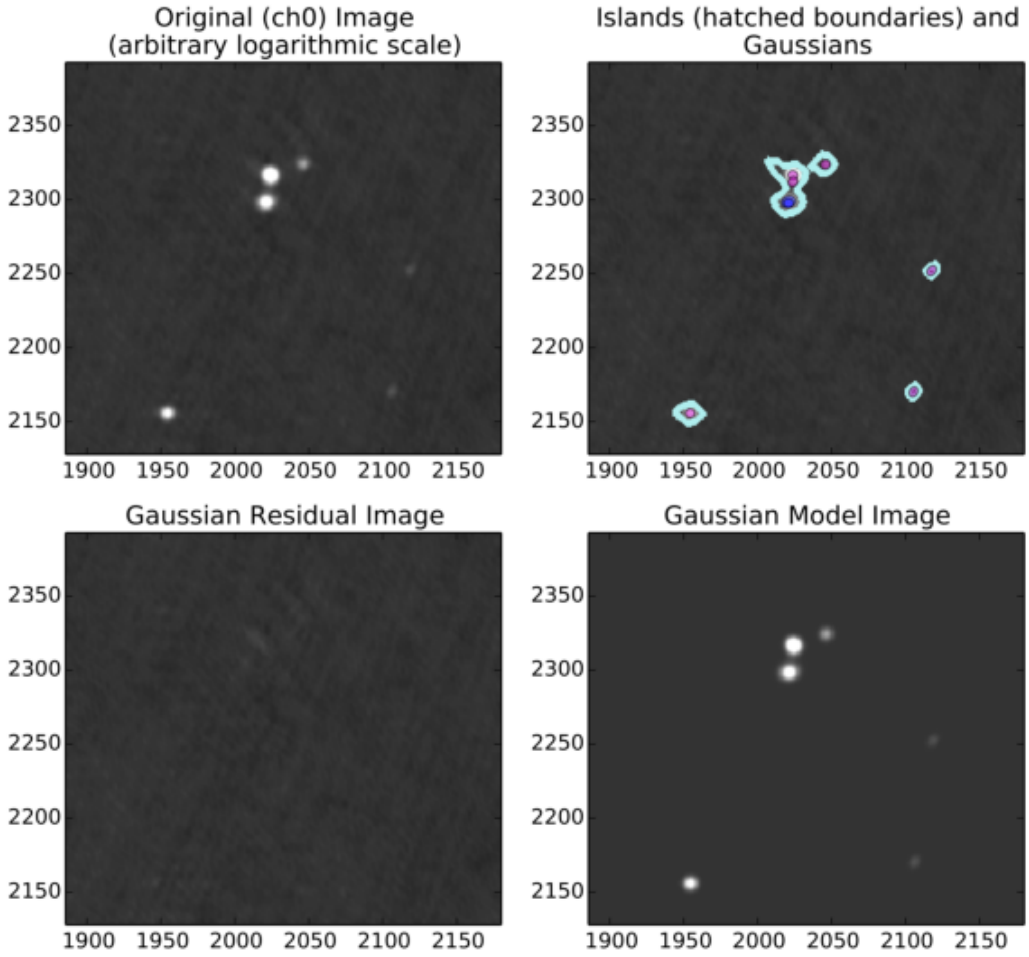

Figure 3.12: A section of PyBDSF fit results for the cluster A2163 at 325 MHz. The island boundaries which have identified emission are denoted by cyan. Gaussians fitted into the islands are shown by ellipses. The size of ellipses corresponds to FWHM of gaussians. Gaussians that have been grouped together into a single source are shown with the same color. For a likely double radio galaxy shown here, two pink gaussians are grouped into the upper lobe, while the blue gaussians form the lower lobe.

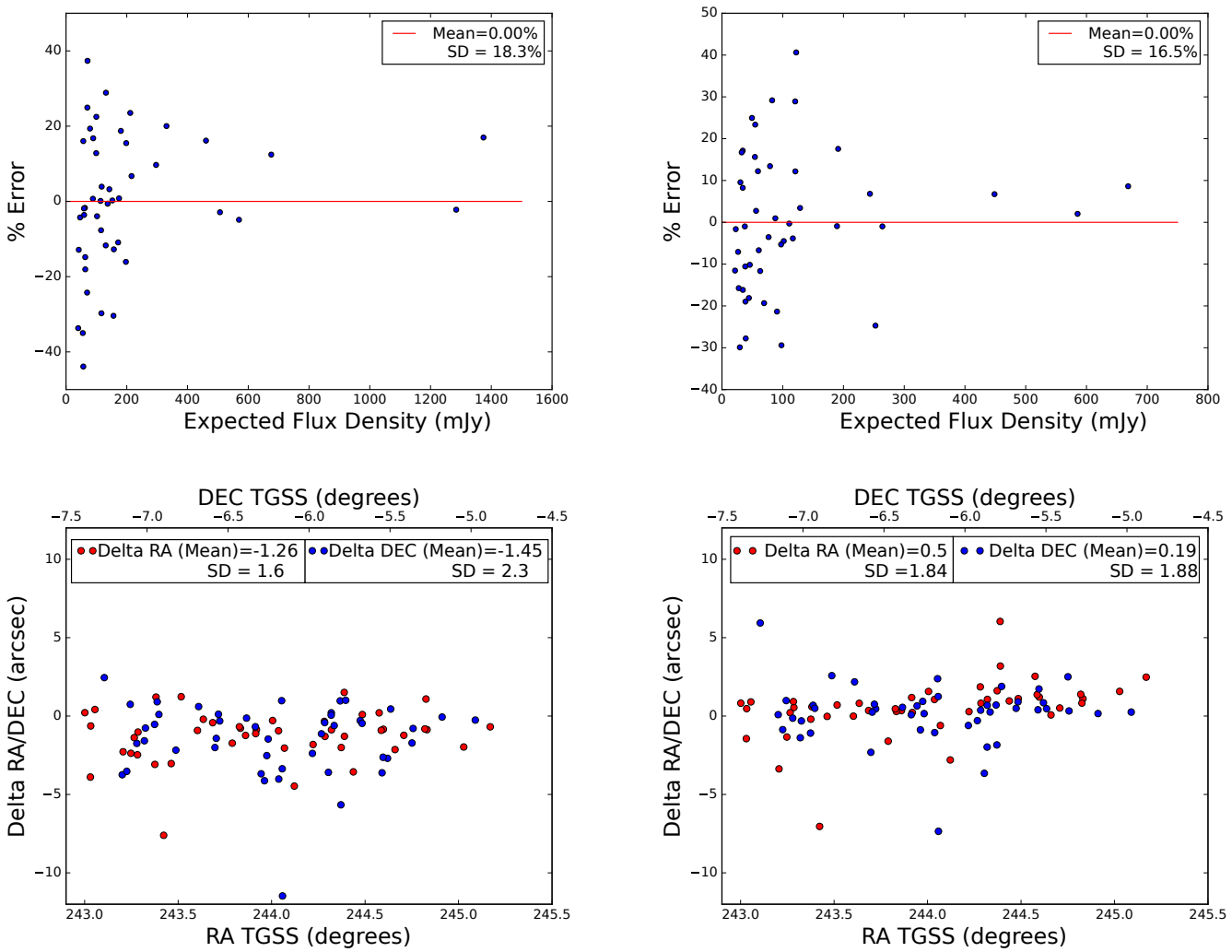

Figure 3.13: A2163: Percentage error in flux densities at 153 MHz (*Top left*) and 332 MHz (*Top right*). SD denotes the standard deviation (here and in all subsequent images). Positional coincidence of the sources at 153 MHz (*Bottom left*) and 332 MHz (*Bottom right*) w.r.t to the TGSS survey. The mean values of differences in RA and DEC lie well within a pixel size in each case.

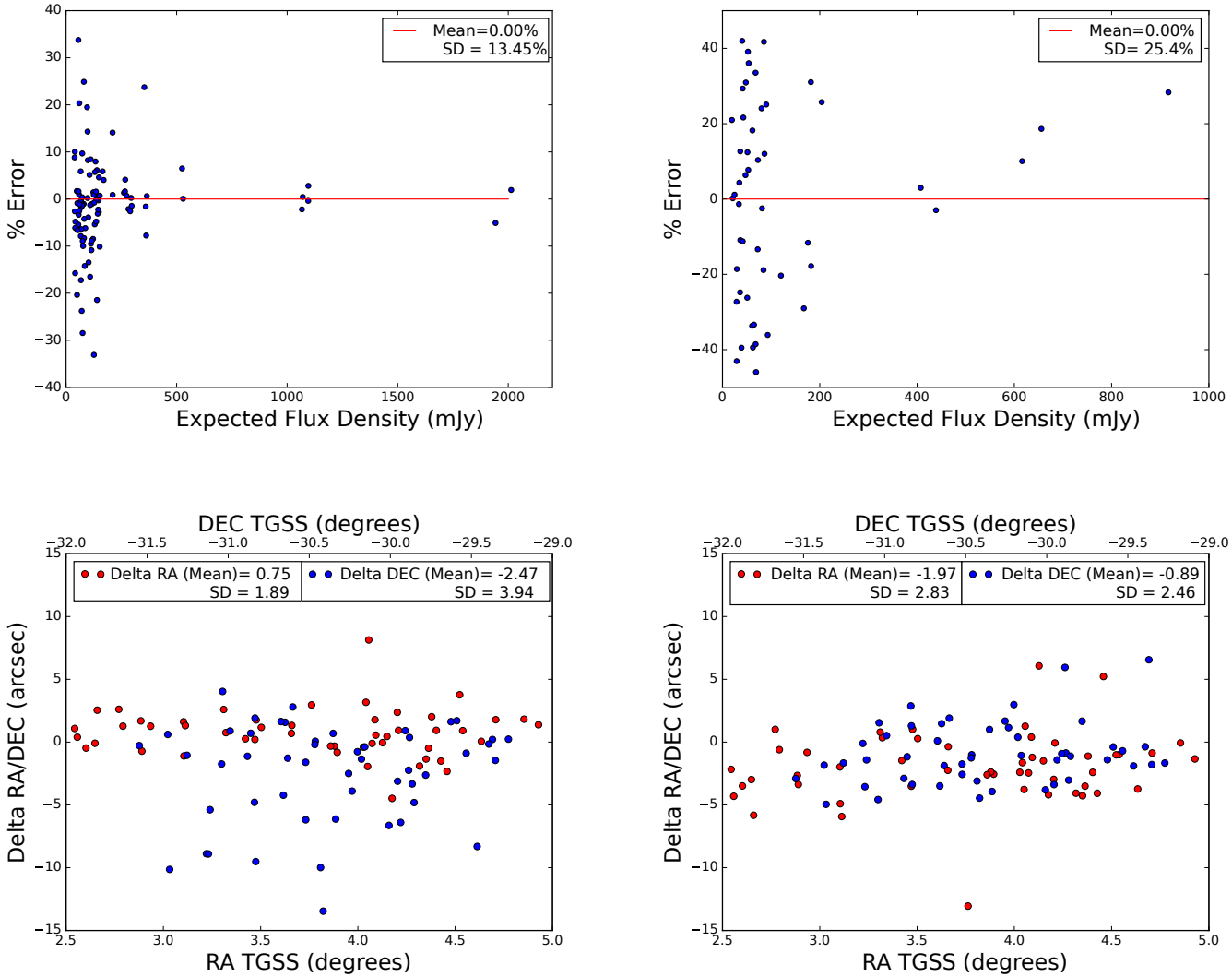

Figure 3.14: Same as Figure 3.13 for the cluster A2744.

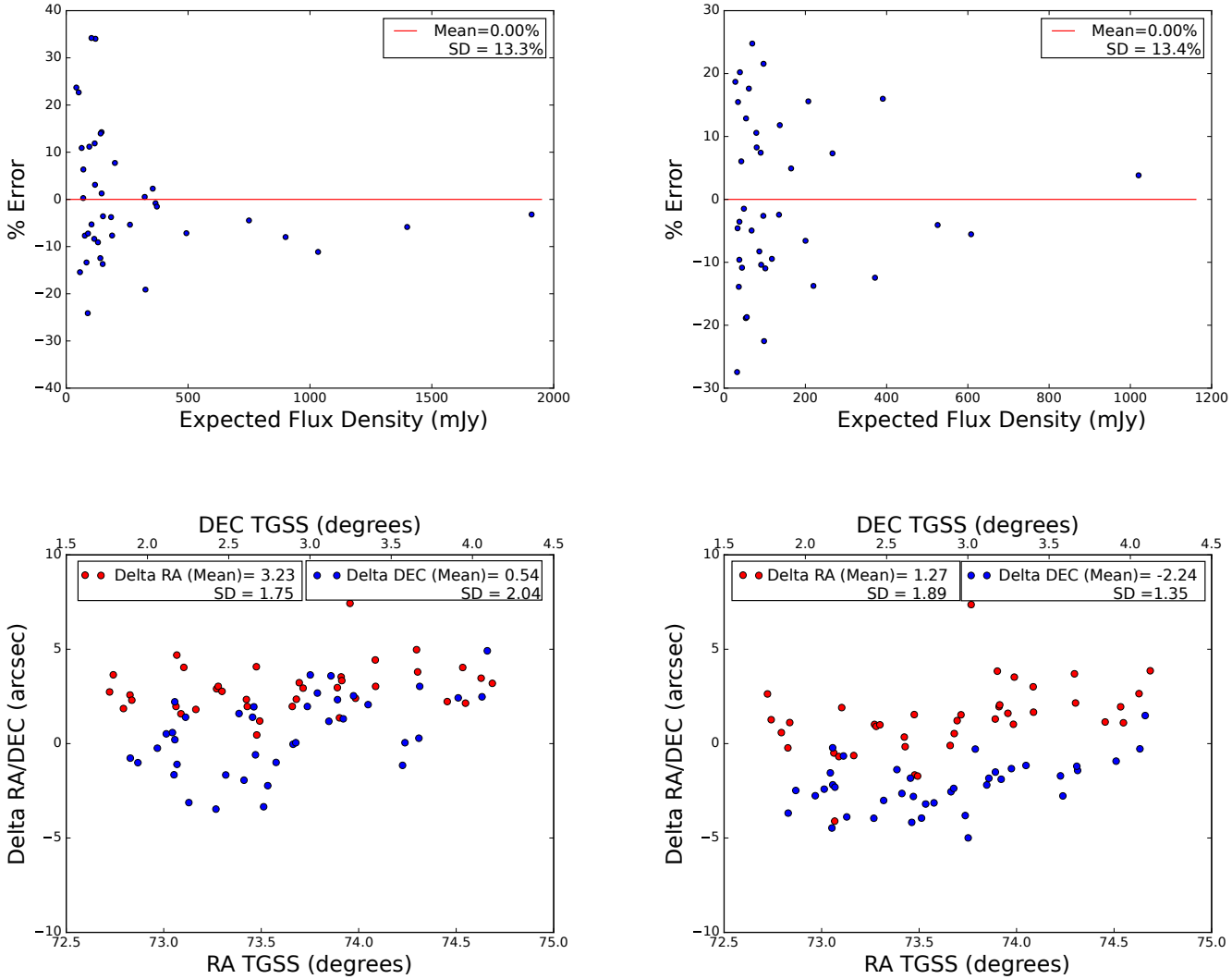

Figure 3.15: Same as Figure 3.13 for the cluster A520.

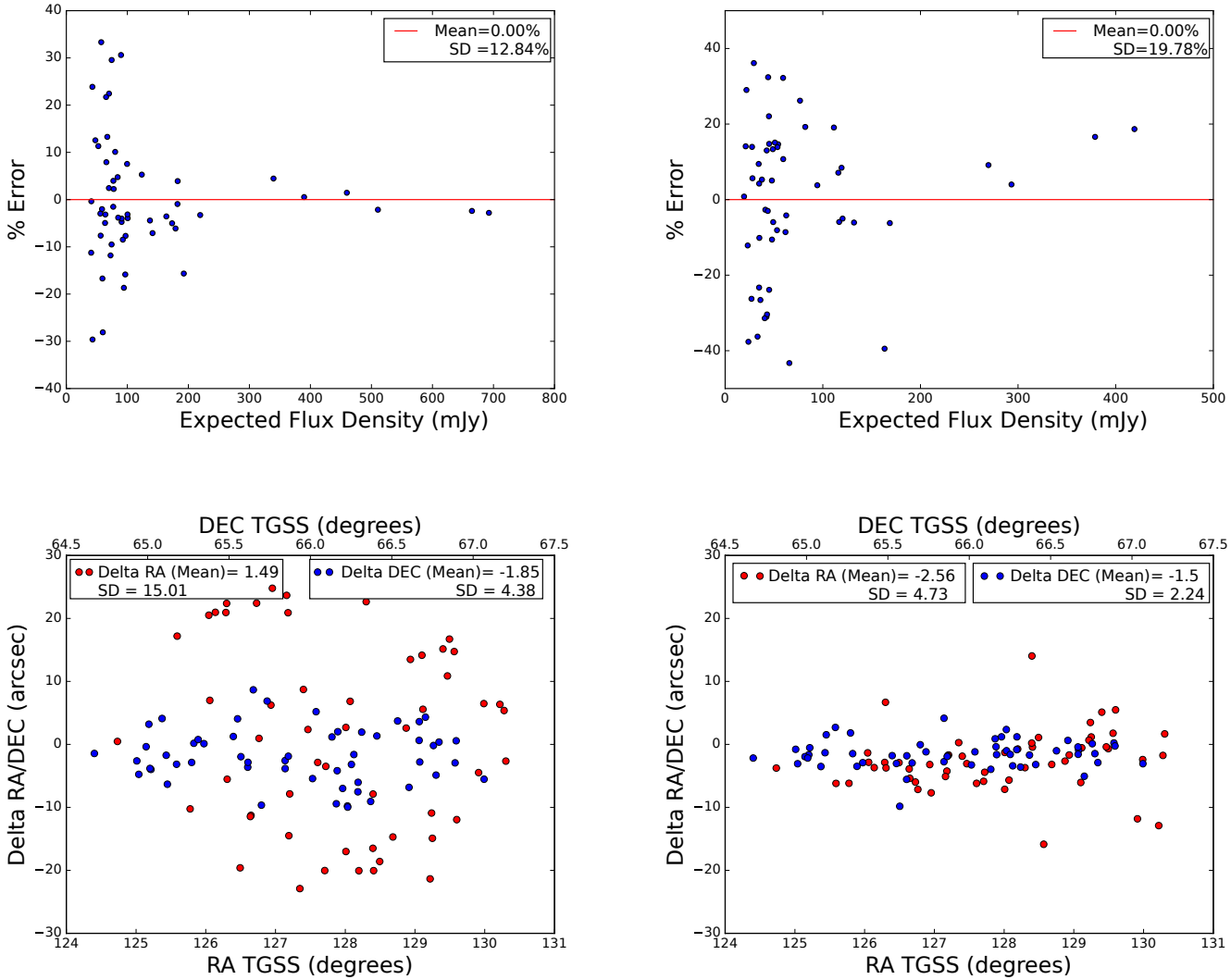

Figure 3.16: Same as Figure 3.13 for the cluster A665.

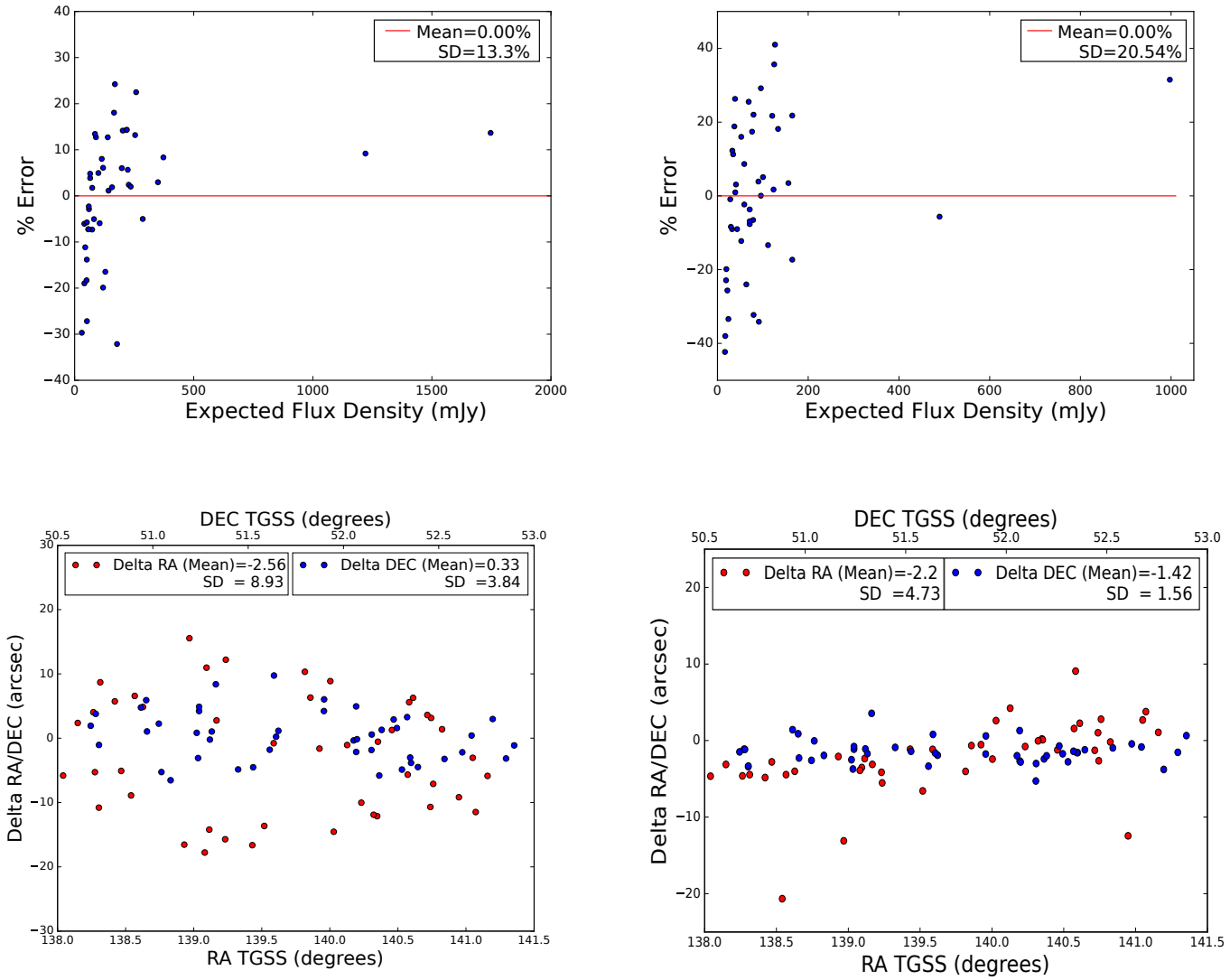

Figure 3.17: Same as Figure 3.13 for the cluster A773.

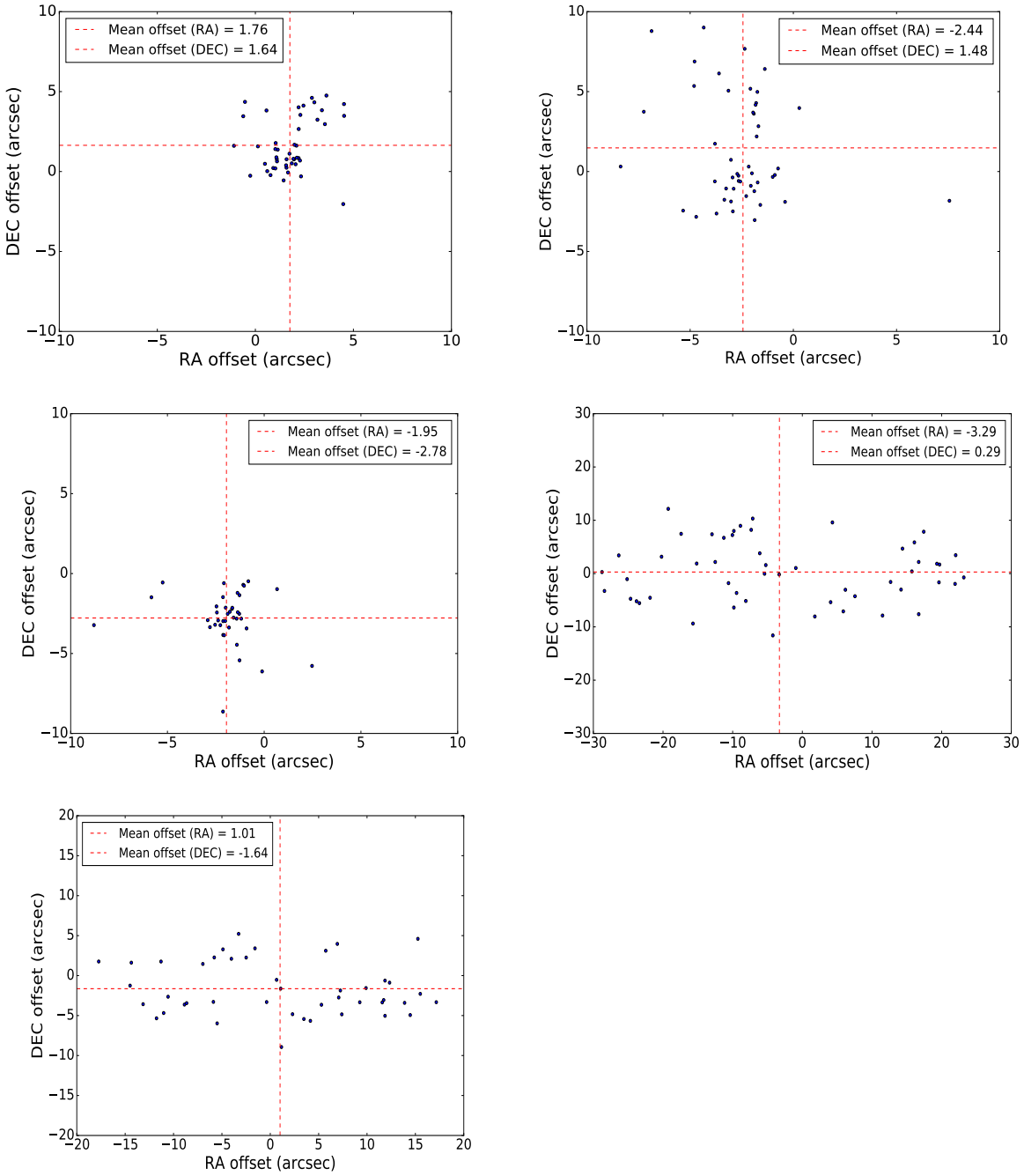

Figure 3.18: Positional coincidence of the sources at 150 MHz and 325 MHz for the clusters A2163 (*Top left*), A2744 (*Top right*), A520 (*Middle left*), A665 (*Middle right*) and A773 (*Bottom*)

.

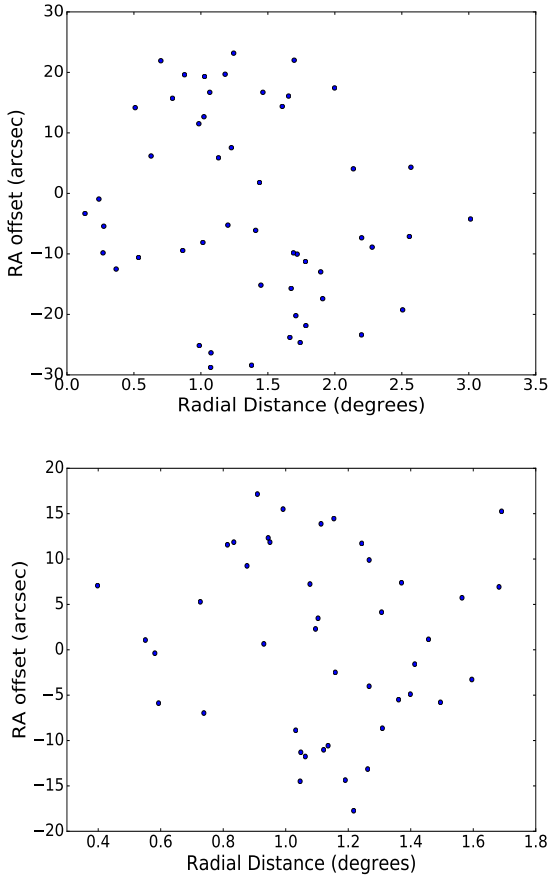

Figure 3.19: Offsets in RA plotted as a function of radial distance for the clusters A665 (*Top*) and A773 (*Bottom*). The offsets are less than 10 arcsec for sources less than a degree in both the cases.

3.6 Spectral Index Imaging

To make the spectral index image it is required to match the resolution, cell size and UV-range of the two frequencies. Low resolution image of halo at 325 MHz was constructed to bring it to the resolution of 150 MHz (23 arsec) or both the frequencies were re-imaged to a common resolution. Primary beam correction of the image was performed. The images at the two frequencies were aligned to a common phase reference using the task OHGEO (if required). The AIPS task COMB was used to make the spectral index images by pixel-pixel comparison of the fluxes at the two frequencies and blanking the pixels below 2 (or 3) sigma at both the frequencies. Giving a sigma cutoff may introduce a bias towards steep spectrum values at the edges of the halo, because the spectral index images are largely determined by the image with a higher noise (150 MHz image). Therefore, weak emission at the edges of the halo may get rejected.

As mentioned earlier, the process of imaging at a lower resolution resulted in loss of flux density across the halo. This loss was not due to any lower cutoff in UV-length. In fact, the lower UV-length cutoff is determined by the 325 MHz itself. Even when full field was imaged at lower resolution the flux was not recovered. Therefore, instead of imaging, the central facet was re-gridded to match the pixel size of 150 MHz (4.5 arcsec). The image was then convolved with the beam size of 150 MHz. This process recovered the entire flux density of the halo. Interestingly, the spectral index images constructed by imaging and by re-gridding/convolving are similar in their basic features (although the pixel values differ). This is shown for the case of A2163 and A665 (Chapters 4 and 5).

Clusters of galaxies generally have many radio galaxies within them (or seen in projection). These have to be excluded before constructing the spectral index images. One way is to make a high resolution image of just the radio galaxies, by excluding shorter baselines less than 3 or 4 kλ, and then subtract this high resolution image from the UV-data to make an image of the halo. However, this resulted in partial subtraction of flux from the radio galaxies and also removed some flux from the halo. Therefore, we chose to mask the pixels at the location of radio galaxies prior to making the spectral index image.

We checked to see if there is any gradient introduced in the spectral index image as a result of offsets in source positions. Again, taking the example of the halo A2163, we introduced a shift in RA position by $\pm10''$, $\pm20''$, $\pm30''$ and $\pm40''$ (because we see larger offsets in RA compared to DEC, as in the cluster A665 and A773). We then re-constructed the spectral index images. The result is shown in Figures 3.20 and 3.21. A number of point sources and tailed radio galaxies aid in identifying the gradient in the spectral index images. The effect of RA shift is obvious on radio galaxies right from $\pm10''$, but its not trivial to identify the same in a halo.

The spectral index images are further compared with the optical and X-ray images of the cluster. In the following chapters the results obtained for individual halos are presented.

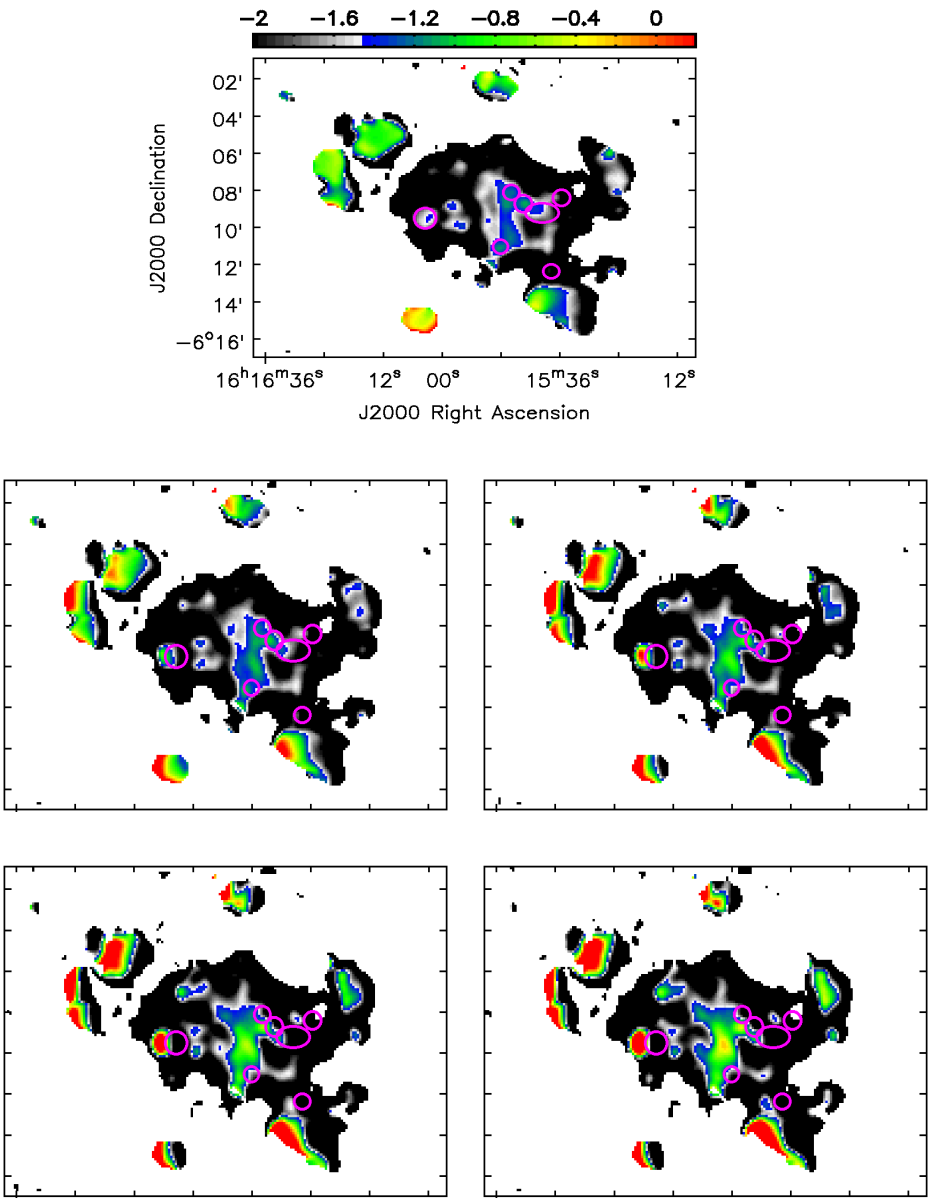

Figure 3.20: Effect of shifting images in RA on spectral index image of halo A2163 made between 150 and 325 MHz with 40″ resolution. The top image is made without any shift. Spectral index images made after applying 10″ shift in RA at 325 MHz (*Middle left*), 20″ (*Middle right*), 30″ (*Bottom left*) and 40″ (*Bottom right*). Pink ellipses mark the original positions of radio galaxies as seen at 610 MHz.

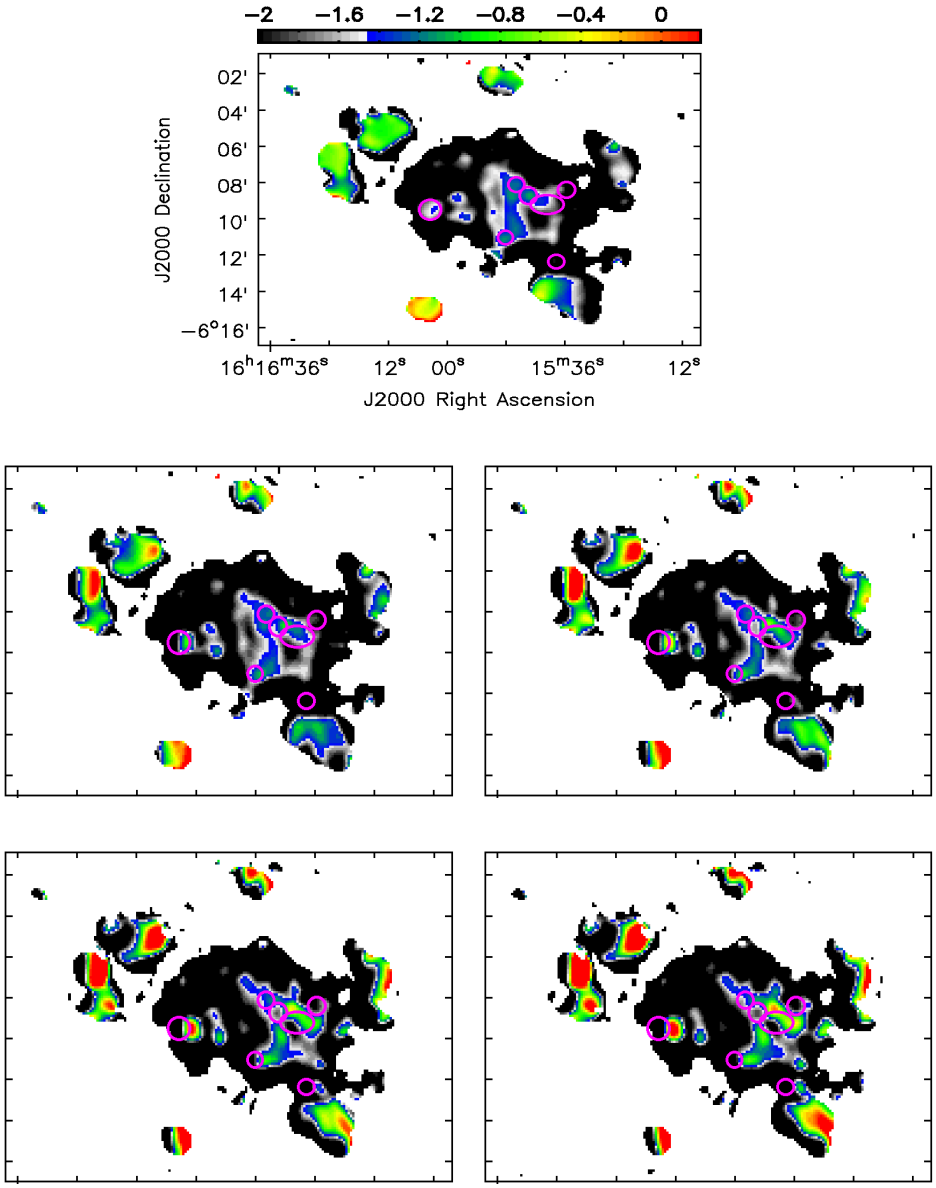

Figure 3.21: Same as Figure 3.20 but with applying $-10''$ shift in RA at 325 MHz (*Middle left*), $-20''$ (*Middle right*), $-30''$ (*Bottom left*) and $-40''$ (*Bottom right*).

Chapter 4

Re-energisation of Radio Halo Electrons in the Merging Galaxy Cluster A2163

The galaxy cluster Abell 2163 hosts one of the biggest and most luminous halos known (Feretti et al., 2001, 2004; Govoni et al., 2004). The presence of diffuse radio emission was first reported by Herbig and Birkinshaw (1994). The radio emission at 20 cm displays a very regular shape, slightly elongated in the E-W direction, with a total extent of ∼11.5 arcmin, corresponding to ∼2.3 Mpc (Feretti et al., 2001, 2004). The authors also constructed a spectral index image between 325 and 1400 MHz.

We targeted A2163 with the GMRT at 153 and 332 MHz to obtain spectral index images which improved upon previous images in sensitivity and resolution by factors of several. These observations show for the first time a well-defined subcomponent, uncontaminated by confounding superposed active radio sources, in the halo A2163, and a clear link between the geometry of a cluster merger and re-energisation of halo synchrotron electrons in an individual source.

4.1 Radio Observations and Data Reduction

We observed A2163 using the GMRT under the project code 16_259. Imaging was carried out by methods described in Chapter 3. After correcting for the flux densities, we estimated from the strongest sources that the scale may be too high by ∼10 per cent at 153 MHz and by ∼3 per cent at 332 MHz, which would have steepened the true spectral index by ∼0.09. The final image noise reached are 1.2 mJy/beam (22″ resolution) at 153 MHz and 0.1 mJy/beam (12″ resolution) at 332 MHz.

GMRT archival data of A2163 at 617 MHz (Proj. Code 02VKK01, observed on 2002-07-18) was processed in the same manner. RFI excision was less effective for this data which was recorded with 16.7 s integration but RFI is less of an issue at this frequency. The final image noise and resolution are 75 μJy/beam and 6 arcsec resolution.

4.2 Results

4.2.1 Radio Images

The 153 MHz Stokes I image (Figure 4.1a) is dominated by the diffuse emission of the radio halo. It is ovoid with size 14 arcmin × 8 arcmin (2.8 Mpc × 1.6 Mpc) and elongated along the east-west direction. The bright spots of emission marked on the image with a "+" on and around the halo are unrelated to it and are radio galaxies in the cluster which were masked while determining the halo properties. Estimates of halo properties are confounded by the presence of superposed cluster radio galaxies. Such sources often show a flatter-spectrum compact component in them. The high resolution 617 MHz image, in which the flatter-spectrum compact component is expected to be more prominent, was used to identify such radio galaxies within the halo (Figure 4.1c).

The Central *Ridge*

We report the presence of a well-demarcated linear structure, the *ridge*, at the centre of the halo in A2163. This elongate 4 arcmin × 1 arcmin (800 kpc × 200 kpc) sized structure is circumscribed by a black contour in the 332 MHz image (Figure 4.1b) and constitutes the brightest part of the halo (see Figure 4.2). Its surface brightness at 332 MHz is ∼4 times higher than the halo median value and its integrated flux density is ∼27 per cent of the total for the halo. This structure is prominent and detected at a very significant level at this frequency. The *ridge* is less prominent in the lower resolution 153 MHz image but even there the brightest part of the *ridge* is visible as a prominent central condensation (Figure 4.1a).

The *ridge* is also visible in the high resolution 617 MHz image (Figure 4.1c). In fact, it is the only halo feature visible at 617 MHz. The lack of a bright compact feature at any frequency, especially in the high resolution 617 MHz image, confirms that the linear *ridge* is not an active radio galaxy.

As elaborated in the rest of this section, this *ridge*, which has been detected in Stokes I images at all three frequencies at multiple resolutions, is also prominent in spectral index images made in multiple ways, and persists even in images with extreme background modification. All these strongly suggest that the structure is real.

4.2.2 Flux density of the Halo

We estimated halo flux densities, $S_{153} = 2356$ mJy and $S_{332} = 467$ mJy after subtracting the contribution from the interloper radio galaxies. The flux densities of the radio galaxies were determined by the task IMFIT. Only for the tailed radio source, the flux density was determined by IMSTAT. The integrated spectral index of the halo is estimated to be -2.09, which would put this at the extreme edge of the spectral index distribution of halos (Brunetti et al., 2008; Dallacasa et al., 2009; Macario et al., 2010; Macario et al., 2013). Previous observations have reported $\alpha_{325}^{1400} = -1.18$ value (Feretti et al., 2004). We also obtain a spectral index of $\alpha_{153}^{325} = -1.3$ using our 153 MHz measurement and the 325 MHz value of Feretti et al. (2004). This suggests that the discrepancy lies in the

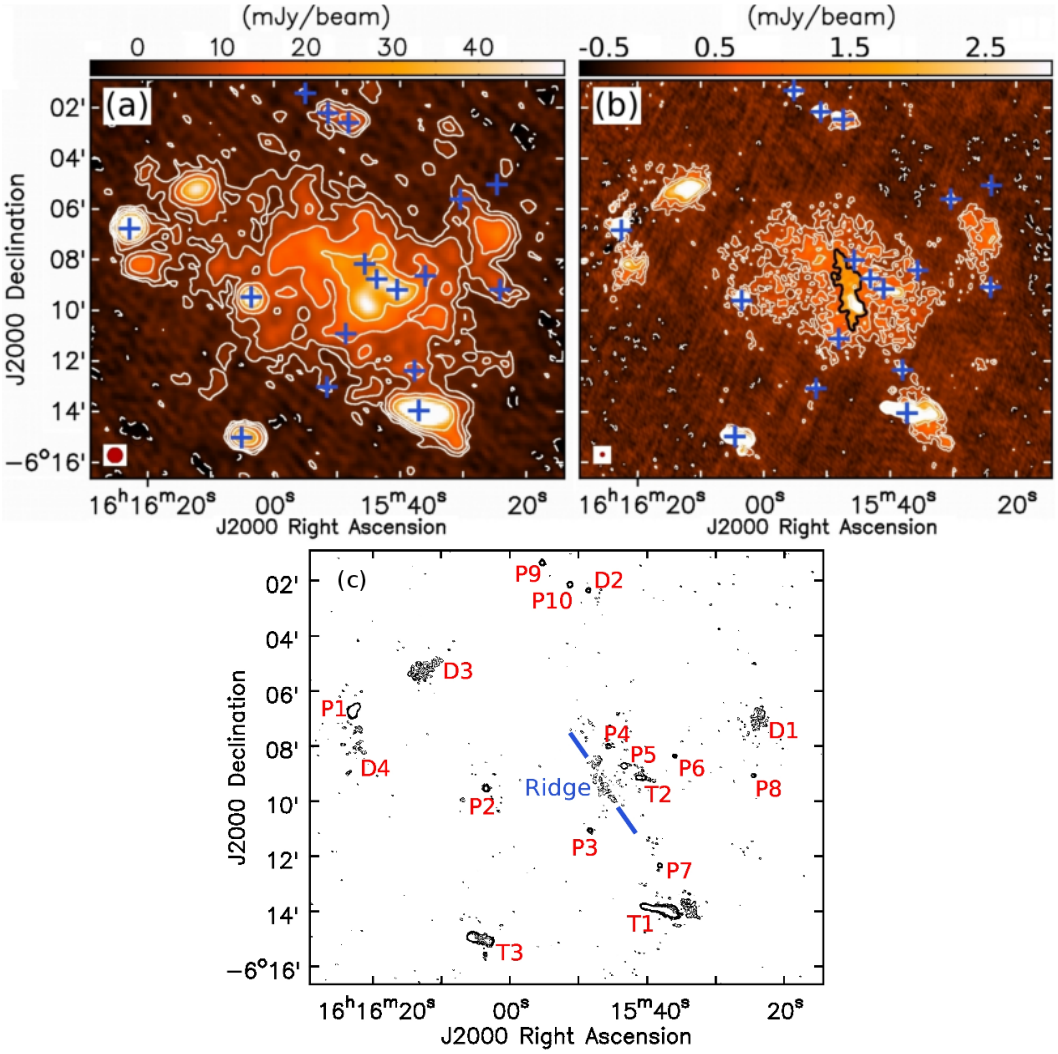

Figure 4.1: Images of the radio halo in the cluster A2163: **(a)** 153 MHz Stokes I (resolution 35 arcsec; 1st contour level 3 mJy/beam), **(b)** 332 MHz Stokes I (12 arcsec; 0.3 mJy/beam). Contour levels differ by a multiplicative factor 2 in both the images. The size of the beam is shown as a red disc in the lower left corner of the images. Cluster radio galaxies are indicated by "+". The central *ridge* is outlined in black (1.2 mJy/beam contour) in **(b)**. **(c)** 617 MHz (resolution 6 arcsec; image noise 70 μJy/beam; 1st contour level 0.21 mJy/beam). The diffuse halo is largely resolved out and only its brightest central component, the *ridge*, is visible. This image was used to identify and mask cluster radio galaxies unrelated to the halo while estimating its properties at 153 and 332 MHz. These objects are labeled P1−P10 (compact sources), D1−D4 (diffuse sources) (Feretti et al., 2004) and T1−T3 (head-tail sources) (Feretti et al., 2004).

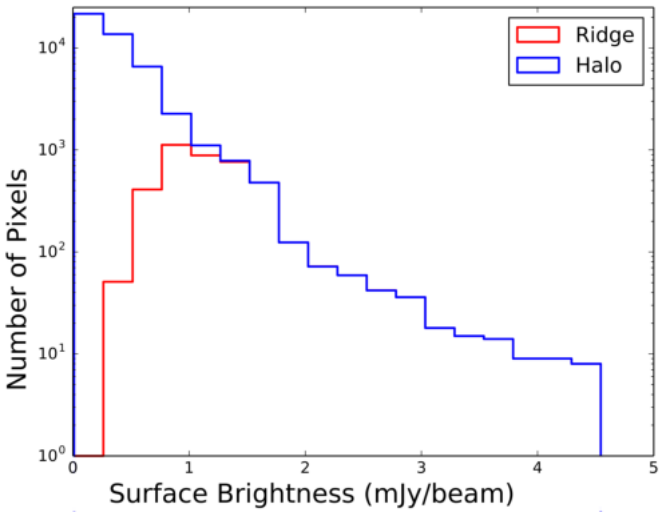

Figure 4.2: Distribution of surface brightness at 332 MHz in the radio halo A2163. The *ridge* (in red) is the brightest region in the entire halo (in blue).

two different 325 MHz flux density measurements, 467 mJy (our image) and 861 mJy (Feretti et al., 2004). We discuss this issue in detail below:

(a) Flux density scales can differ by up to 20% between telescopes and could explain a substantial part of the difference. We anchored our flux density scale at both 153 and 332 MHz to the wide area TGSS-ADR1 survey and NVSS surveys. Therefore, our spectral index values should suffer from a smaller systematic offset than even our flux density values. Indeed, this is confirmed by the detection of flat spectrum ($\alpha > -0.5$) cores in the many active FR I radio sources seen in the vicinity of the halo, and an average spectral index for the field of -0.74. Furthermore, the flux density that Feretti et al. (2004) mention for the source D3 (= 82 mJy), which they suggest is a relic, is very similar to our measurement at 332 MHz (= 95 mJy).
(b) With a factor of 5 higher resolution we can separate out halo contamination from superposed radio galaxies to a much better degree. This could explain $50-100$ mJy of the observed difference.
(c) The area of the halo at 325 MHz in the previously published image (Feretti et al., 2004) is larger than in our 332-MHz image by about 50%, but it matches with that seen in our 153-MHz image. Therefore, we believe over-resolution in our 332 MHz image is the most likely source of the discrepancy. The UV-length histogram shows poor sampling below 500λ which corresponds to a scale of $\sim$7 arcmin. Conversely, the flux density, and hence the spectral index, in the central regions of the halo are not affected. The high resolution ($15''$) 1.4 GHz image of the halo (Feretti et al., 2001) looks very similar to our 332 MHz image.
(d) Estimating the flux densities of very large diffuse sources like a radio halo is a tricky exercise. A non-zero (positive or negative) background, even if barely discernible visually, will change the flux density by a large amount. For example, a background change of

just 100 μJy/beam (= rms noise) will change the integrated flux density by 125 mJy over the $\sim$ 50,000 pixels that the halo occupies. We note that the rms noise in the previously published image (Feretti et al., 2004) was 400 μJy/beam, and a background pedestal of 100 μJy/beam would not have been easily discernible.

The *ridge*, which is considerably smaller than the halo and therefore should not have any over-resolution issues, has a flux density of about 405 mJy, 126 mJy and 33 mJy at 153, 332 and 617 MHz respectively.

4.2.3 Spectral Index Images

We limited the visibilities to the same UV-length range of $70-9000\lambda$ at both 153 and 332 MHz to obtain matched resolution (35 arcsec; pixel size 7 arcsec) images. These images were smoothed with a 40 arcsec beam and combined using the AIPS task COMB to get the spectral index image and its error image (Figure 4.3). The image noise at this resolution was 1.3 mJy/beam and 0.17 mJy/beam at 153 and 332 MHz respectively. We blanked pixels with flux density below 2σ at either frequency to minimize spurious spectral index values. We also avoided contamination of the halo spectral index by masking pixels in the vicinity of the superposed radio galaxies based on their structure and location on the 617 MHz image (Figure 4.1c).

The *ridge* is most prominent in the spectral index image (Figure 4.3) as the region with the flattest spectrum in the halo: $\alpha_{ridge} > -1.4$. As in the Stokes I images, the *ridge* lacks a compact flat spectrum nuclear component ($\alpha > -0.5$) visible in the other active radio galaxies in the cluster, and therefore, it is clearly not active radio AGN. This structure is consistent with the region of flatter spectral index previously reported (Feretti et al., 2004). The distribution of spectral index values for the halo and the *ridge* is shown in Figure 4.4. The median spectral indices for the halo and the *ridge* are -2.26 and -1.28, respectively.

This *ridge* is the first detection of a "well-delineated, central, flatter-spectrum" component within a radio halo. The radial reduction of both surface brightness (readily discernible in Figure 4.1) and spectral index (Figure 4.5) suggest that the re-energisation happened most recently at the centre.

It is also clear from the 332-MHz image (Figure 4.1b), spectral index images (Figure 4.3), and from the 617-MHz image (Figure 4.1c) that the *ridge* is not the extended emission from the nearby radio galaxies.

We confirmed that the spectral index structure that we present here are not affected by the flux density issues by changing the background by as much as 2σ: ± 2.6 mJy/beam at 153 MHz and ± 0.34 mJy/beam at 332 MHz (Figure 4.6). This corresponds to changing the overall flux density in the 332 MHz image by 425 mJy, which is equal to the observed discrepancy between our measurement and that of Feretti et al. (2004). The flat spectrum *ridge* persists in all these images in spite of the substantial change.

Matching the UV-range at different frequencies reduces the number of visibilities in each, resulting in an increase in artifacts since imaging and deconvolution are highly non-linear operations. We investigated such a possibility (of data pathology) by achieving matched resolution, not only by UV-length limits, but by post-imaging regridding and

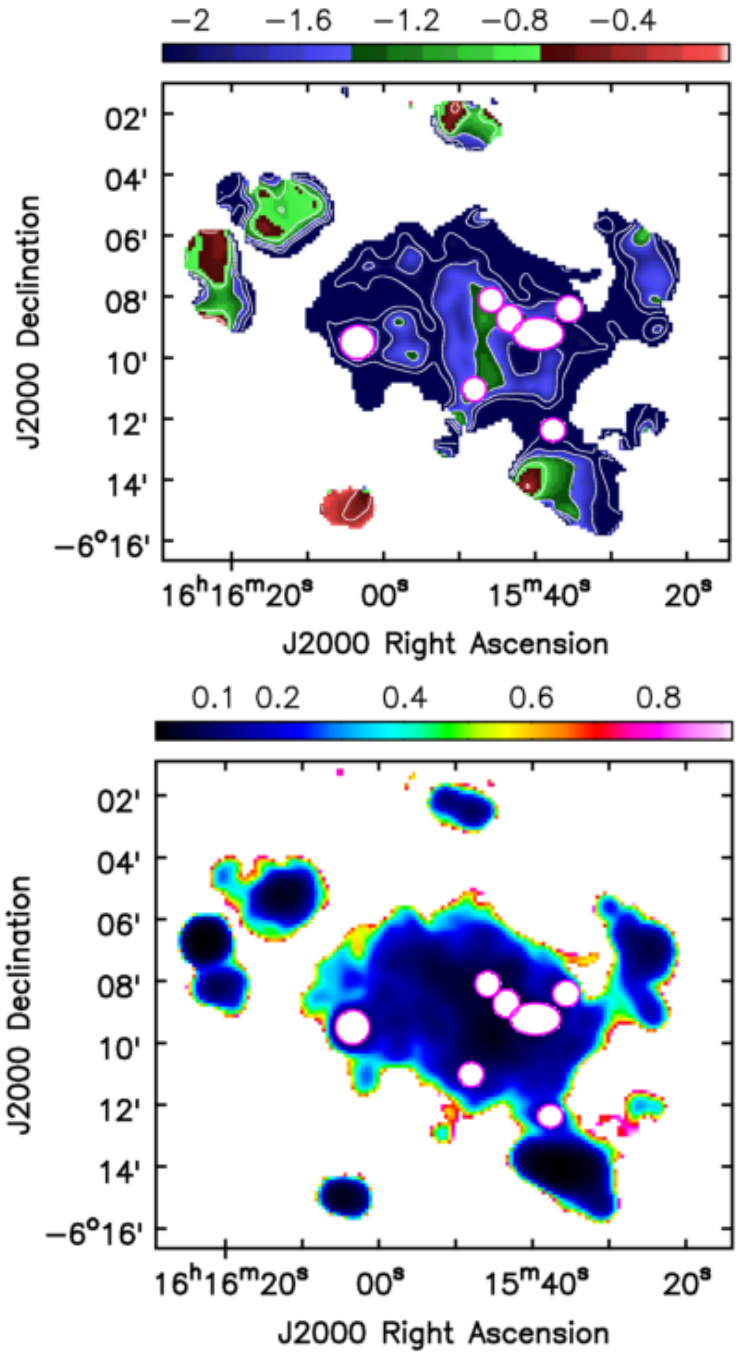

Figure 4.3: Spectral index image of the radio halo A2163 between 153 and 332 MHz at 40 arcsec resolution (*Top*). The first contour level is -2.4 and the central *ridge* is $\alpha > -1.4$ (shaded green). *Bottom*: Spectral index error image. The errors are ≤ 0.05 at the *ridge* and ≤ 0.25 over most of the halo. The pink ellipses are the masks at the locations of the radio galaxies in both the images.

smoothing to the desired resolution. Thus, we generated a 40 arcsec spectral index image by regridding and smoothing the full data (12 arcsec resolution) 332-MHz and (22 arcsec resolution) 153-MHz images (Figure 4.7). This regridded 40-arcsec image is very similar to the 40-arcsec matched UV-range image 4.3. We also generated a high resolution 22 arcsec resolution spectral index image by regridding the 12-arcsec 332-MHz image to the resolution of the 22-arcsec 153-MHz image (Figure 4.7). This high resolution spectral index image is noisier but similar in its key features to its considerably lower resolution counterparts.

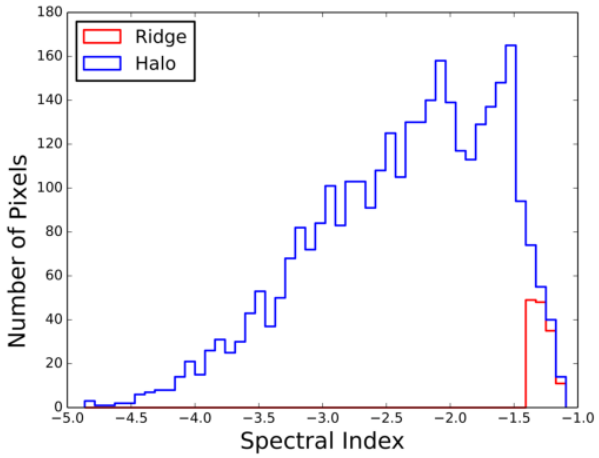

Figure 4.4: Distribution of spectral index α_{332}^{153} in the radio halo. The *ridge* (in red) is the flattest region in the entire halo (in blue).

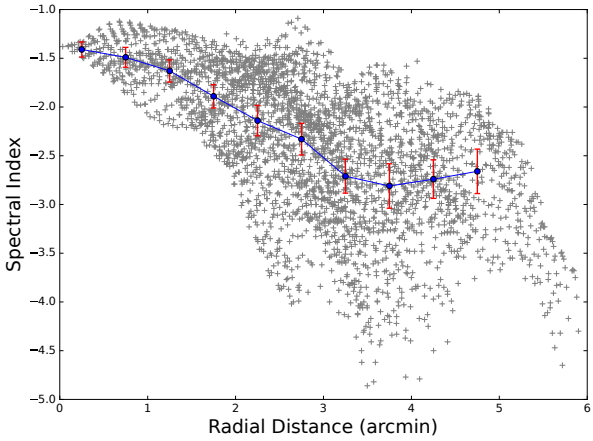

Figure 4.5: Radial distribution of spectral index α_{332}^{153} in the radio halo. The grey points represent individual pixels. The blue dots and the red bars are the mean values and standard errors in each successive 30 arcsec shell from the centroid.

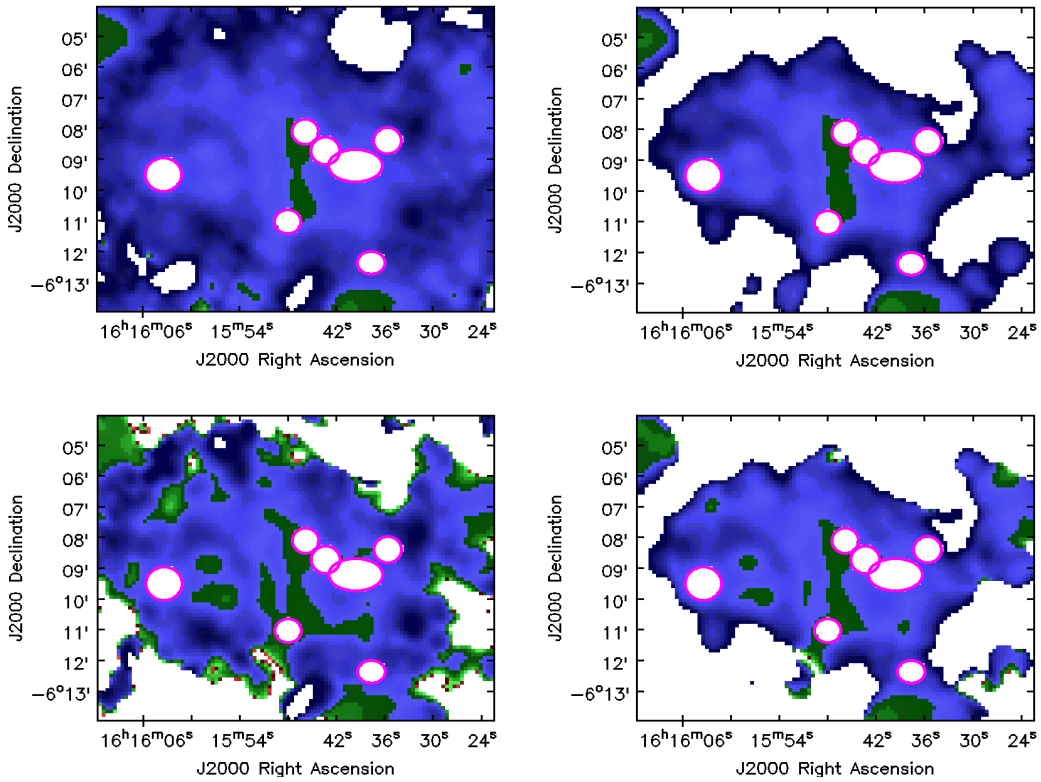

Figure 4.6: Spectral index α_{332}^{153} images at 40 arcsec resolution obtained by changing the halo background by $\pm 2\sigma$ at 153 MHz (=2.6 mJy/beam) and at 332 MHz (=0.34 mJy/beam). *Top Left*: (153 MHz, $+2\sigma$; 332 MHz, $+2\sigma$), *Top Right*: (153 MHz, $+2\sigma$; 332 MHz, -2σ), *Bottom Left*: (153 MHz, -2σ; 332 MHz, $+2\sigma$) and *Bottom Right*: (153 MHz, -2σ; 332 MHz, -2σ). The presence of the *ridge* even in these *extreme* images suggests that it is not an artefact due to improper background estimation.

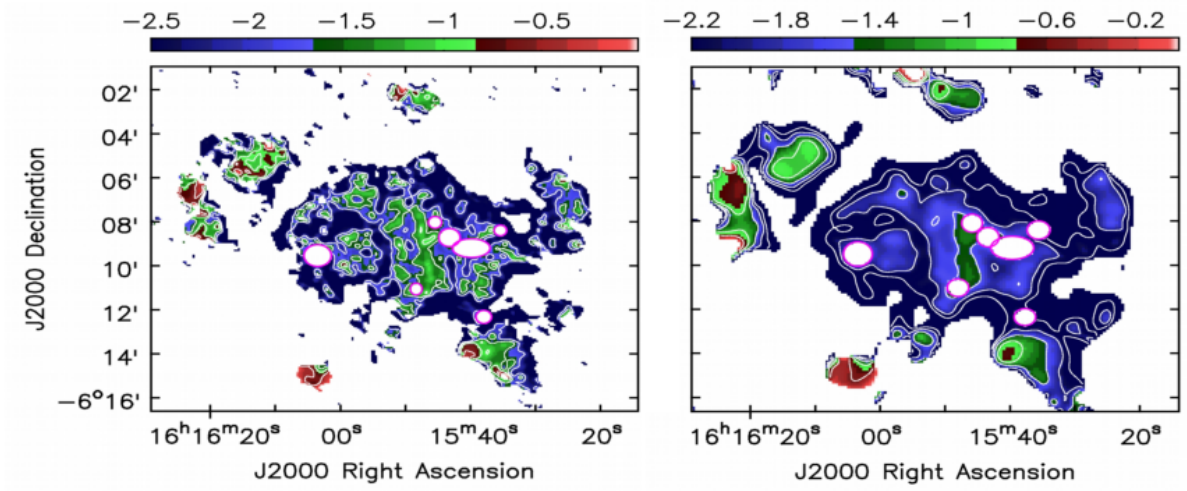

Figure 4.7: Spectral index α_{332}^{153} images made by regridding and smoothing the highest resolution 153- and 332-MHz images. *Left*: 22-arcsec resolution image (contours at α = −2, −1.5, −1, −0.5). *Right*: 40-arcsec resolution image (contours at α = −2.5, −2, −1.5, −1, −0.5). The central *ridge* is prominent in both these images. The overall spectral index structure is similar to the spectral index image in Figure 4.3 which was made by constraining the visibilities to the same UV-range at both frequencies.

4.2.4 Comparison with optical and X-ray

Previous studies of Abell 2163 had shown that the peak of the X-ray emission approximately coincided with the radio centroid, but the resolution was insufficient for further investigation of the radio structure or its link to the X-ray (Govoni et al., 2004). Maurogordato et al. (2008) carried out the optical study of the cluster and identified 361 galaxies as cluster members. They detected a prominent central bimodal structure in the density distribution of galaxies, along with other smaller peaks away from the centre. The authors concluded that the central structure has undergone a recent merger ($t \sim$ 0.5 Gyr) in east-west or NE-SW direction. X-ray temperature maps show a cool, dense and compact core in the central region of the cluster (Govoni et al., 2004; Bourdin et al., 2011). Bourdin et al. (2011) inferred a westward motion of the compact core situated very close, but separated from one of the central optical density peaks. The passing core is lagging behind the optical peak possibly due to ram pressure stripping. They further showed that the gas behind the crossing 'bullet' is adiabatically compressed due to shock heating. They also concluded a merger geometry in E-W direction.

Figure 4.8 shows the position of the *ridge* with respect to the optical and X-ray images of the cluster. The *ridge* is located at the point of merger, in between the two optical subclusters (Maurogordato et al., 2008) and also the peaks in the excess X-ray emission arising from the cluster merger (i.e. the residue after subtracting the smooth radial cluster X-ray component) (Bourdin et al., 2011). The *ridge* is also perpendicular to the axis of the merger (E-W), defined by the optical subclusters and the X-ray peaks.

We confirmed that the emission in the *ridge* is not from an active radio source from

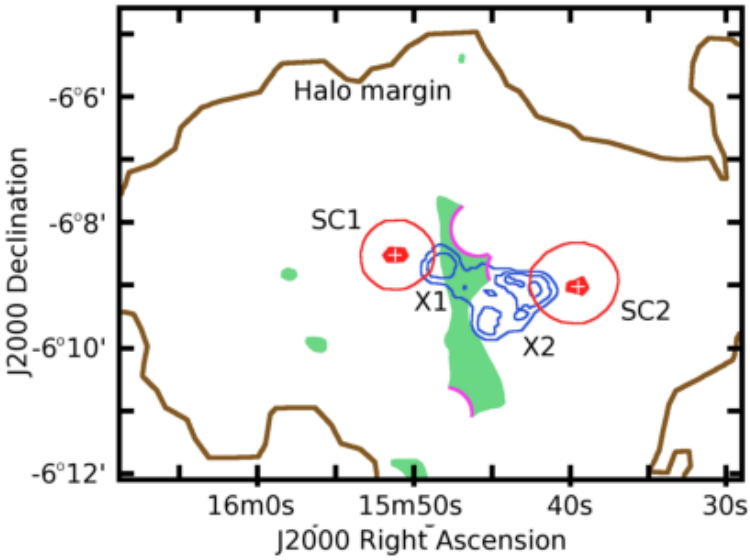

Figure 4.8: Optical−Radio−X-ray overlay. The central *ridge* (green) lies between and perpendicular to the merging optical subcluster peaks SC1 and SC2 (red contours) and to the excess X-ray emission X1 and X2 (blue contours). This configuration is consistent with the halo being powered by a shock front (i.e the *ridge*) generated by the merging subclusters. Cluster radio galaxies are masked by pink-edged ellipses.

the absence of any flatter spectrum core ($\alpha \sim -0.5$) at the locations of optical galaxies in the DSS image. The left panel of Figure 4.9 shows the DSS image and the radio contours of the *ridge* overlaid on it. Green and white contours are plotted from 332 and 617 MHz respectively. Optical galaxies that are located at the cluster redshift ($0.18 \leq z \leq 0.22$) are denoted by black circles. The same galaxies are marked on the 22 arcsec resolution spectral index image in figure 4.9 (right panel). Surrounding radio galaxies have their tentative optical counterparts near to their cores.

4.2.5 Minimum energy estimates

The minimum energy density required by a synchrotron source, which approximately corresponds to equipartition of energy between relativistic particles and magnetic field, can be related to the observed parameters (see Govoni and Feretti (2004) and Appendix at the end of this Chapter).

Using average source depth $d = 1000$ kpc (the minor axis of the halo), $z = 0.203$, and surface brightness $I = 10$ μJy/arcsec^2 at 153 MHz, we derive for $\alpha = -1.3$ calculated between our 153 MHz and previous 325 MHz data (or $\alpha = -2.09$ using only our data) luminosity L $= 2.9 \times 10^{42}$ (or 7.8×10^{42}) erg s^{-1}, (minimum) energy density u_{min} $= 3.8 \times 10^{-14}$ (or 9.2×10^{-14}) erg cm^{-3}, magnetic field B $= 0.68$ (or 0.99) μG and (minimum) energy of the synchrotron reservoir $U_{min} = 2.6 \times 10^{60}$ (or 6.3×10^{60}) ergs. The number of synchrotron electrons with critical frequency between 10 MHz and 10 GHz is estimated to be 3×10^{62} (or 10.8×10^{62}).

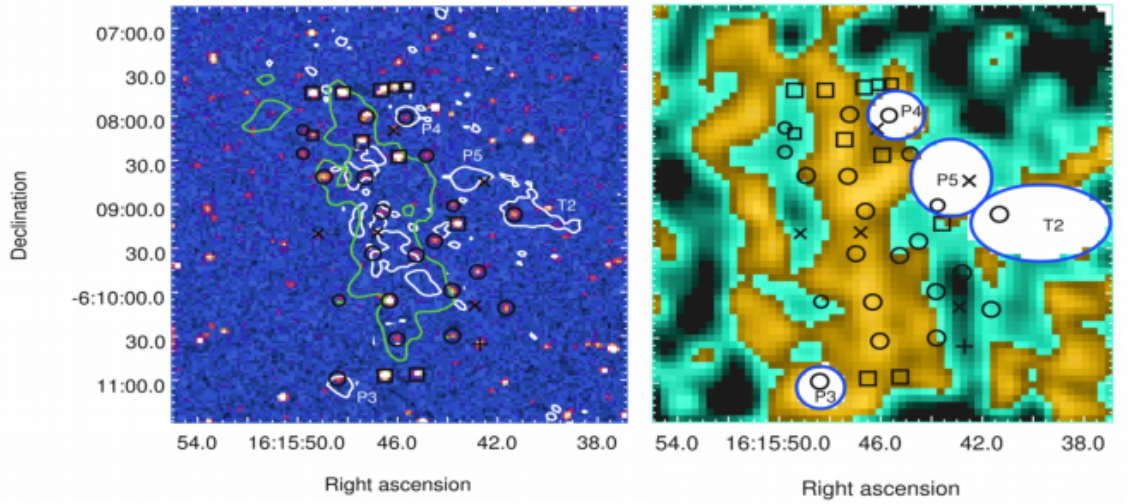

Figure 4.9: *Left*: Radio contours of the *ridge* at 332 MHz (green) and 617 MHz (white) overlaid on the optical DSS image. Optical galaxies in the vicinity of the *ridge* are marked — black circles are cluster galaxies, square boxes have no redshift information available. Galaxies located at a different redshift are denoted by '+' sign while '×' indicates objects not identified by NED. *Right*: Same optical galaxies marked on the 22 arcsec resolution spectral index image showing the *ridge*. P3−P5 and T2 are same as marked in Figure 4.1c.

4.3 Discussion

4.3.1 Energising a Halo

The lack of any obvious energy source, indeed the lack of any definite structure, in these amorphous objects — unlike for example the presence of compact radio cores and radio jets which are visible in most radio galaxies (Kellermann and Owen, 1988) — has made it difficult to identify the physical process(es) responsible for the halo emission (Feretti et al., 2012). The aim of our observing proposal was to look for one or more (compact?) regions of flat spectral index in the halo which could serve as candidate location(s) for energisation of synchrotron electrons. We propose that the *ridge* is one such, or perhaps the most significant, candidate location. From its shape, spectral index (flattest value for the halo), location and orientation vis-a-vis the optical and X-ray geometries, the *ridge* is consistent with being the shock front in the intracluster medium through which the merger is energising the halo.

The infusion of energy is likely a one-time event at the time of merger and the synchrotron spectral index should subsequently steepen with time. If the energisation only occurred in the *ridge* then the gradient of spectral index towards the periphery, due to the aging of energised electrons as they stream outwards, is a measure of the time since halo formation. However, diffusion or bulk movement of energised electrons to the edges of the halo is expected to be much slower than the radiative loss timescale

(Sarazin, 1999).

The spectral index of synchrotron electrons energised by a Fermi 1st order process at a shock front is related to its Mach number (Blandford and Eichler, 1987). The flattest spectral index in the halo, in the central *ridge* ($\alpha \sim -1.12$ to -1.4), is considerably steeper than the $\alpha \geq -0.5$ typically seen in the cores of radio galaxies (Kellermann and Owen, 1988). Possibly, the initial $\alpha = -0.5$ may have steepened to the observed steeper value due to age. On the other hand, cluster merger velocities are only a few 1000 $\mathrm{km\,s^{-1}}$ (Sarazin, 2002) compared to radio galaxy hotspots where synchrotron jets collide at bulk speeds close to the speed of light (Lorentz $\gamma > 5$) (Marscher, 2006). Therefore, Mach numbers of cluster merger shocks should be much smaller and halos may simply start out with a steeper spectral index. In this case, the estimated Mach number $M \sim 2.85$ at the *ridge* (see the subsection on 'Width of the *Ridge*'). The energisation of synchrotron electrons up to the periphery of the halo may be due to turbulence injected in the intracluster medium due to the cluster merger. Energisation due to turbulence being a second order process is less efficient than shock acceleration which is a first order process. However, as shown in later subsection 'Width of the *Ridge*', the shock accelerated electrons can travel only up to few hundred kpc before losing energy, and therefore the bulk of the diffuse halo emission is more likely due to turbulence.

4.3.2 Is the *Ridge* a Relic?

Relics are usually observed at the edge of halos and are almost always tangential in extent and polarized (Orru' et al., 2007; Ferrari et al., 2008; Feretti et al., 2012; Hoang et al., 2017). Even while being on the periphery relics can appear to associate with halos in a complex manner due to projection effects (Pizzo and de Bruyn, 2009; Rajpurohit et al., 2018). A ridge-like structure has been observed at the centre of the halo in MACS J0717.5+3745. But its nature is still unclear, largely because of the head-tail source superposed on it: it has been identified as a relic in projection (Bonafede et al., 2009; van Weeren et al., 2009, 2017; Bonafede et al., 2018); it has also been suggested that the entire structure may be a wide-angle tail radio source (van Weeren et al., 2009); it has also been considered as a filamentary structure associated with the halo and unrelated to the relic phenomenon (Bonafede et al., 2009; Pandey-Pommier et al., 2013).

We note that our *ridge* is definitely not an active radio source given the absence of a flat spectrum component. We would prefer to go with the circumstantial evidence of its location between the two optical substructures and the excess X-ray emission at the centre. Since one expects the merging substructures and the excess X-ray to be at the centre, and not the periphery, we suggest that the *ridge* is also at the centre of the merger. However, one can only rule out the possibility of it being a (peripheral) relic through polarization studies.

4.3.3 Width of the *Ridge*

Assuming that the *ridge* is a result of shock acceleration of relativistic electrons at the merger site, the width of the *ridge* can be estimated by multiplying the lifetime

of electrons accelerated by shock and the downstream velocity of gas. The lifetime of ultrarelativistic electrons, which suffer both inverse Compton (IC) and synchrotron energy losses can be related to their magnetic field, redshift and frequency of observation (Sarazin, 1999; Markevitch et al., 2005). The following equations describe the relations:

$$t_{loss} = 2400\gamma^{-1}\left(B_{\mu G}^2 + 10.52(1+z)^4\right)^{-1} \quad \text{Gyr} \tag{4.1}$$

The lorentz factor γ of the electrons contributing most to emission at a frequency is given by

$$\gamma_{peak} \approx 10^4(\nu_{GHz}^{1/2} B_{\mu G}^{-1/2}) \tag{4.2}$$

Using cluster $z = 0.203$ and $B = 1\mu$G (assumed typical value for clusters), the lifetime of electrons at 153, 332, 617 and 1400 MHz are 266, 181, 133 and 88 Myr respectively.

The downstream velocity of gas in the rest frame of shock is obtained from shock jump conditions and can be expressed entirely in terms of Mach number and hence the spectral index (Landau and Lifshitz, 1959; Brunetti et al., 2008).

$$v_{ds} = c_{us}\frac{M^2+3}{4M} \tag{4.3}$$

where, M is the Mach number of the shock and c_{us} is the speed of sound upstream of the shock and is given by

$$c_{us} \approx 1700\sqrt{\frac{16M^2}{(5M^2-1)(M^2+3)}} \quad \text{km/s} \tag{4.4}$$

The Mach number of the shock may be related to the injection spectral index of synchrotron emission through (Blandford and Eichler, 1987)

$$M = \sqrt{\frac{2\alpha_{inj}-3}{2\alpha_{inj}+1}} \tag{4.5}$$

Here, α_{inj} is related to the power-law energy distribution of synchrotron electrons

$$dN(E)/dE \propto E^{-\delta_{inj}} \tag{4.6}$$

$dN(E)$ is the number of electrons within energy range E and $E + dE$, and $\alpha_{inj} = -(\delta_{inj} - 1)/2$. But the electrons suffer severe losses due to inverse compton and synchrotron, as they are advected downstream of shock front. The effect is their 'volume integrated' spectrum steepens by half $\alpha = \alpha_{inj} - 1/2$, if we do not have sufficient resolution.

The average spectral index ($\alpha = -1.28$) of the *ridge* yields $\alpha_{inj} = -0.78$, $M \sim 2.85$ and downstream velocity of approximately 900 km/s. From these we calculate that the width of the *ridge* should be 245, 166, 122 and 81 kpc at the four frequencies between 153 and 1400 MHz. We do not have images of sufficient quality to define the width of the *ridge* in a formal manner at different frequencies (e.g. as the half power width in

excess of the mean halo brightness). But this calculation does explain why the previous low resolution observations (Feretti et al., 2004), which had a linear resolution of 200 kpc, could not have detected the *ridge* on the α_{1400}^{325} image.

4.3.4 Origin of particles and fields

Accelerating electrons from the thermal pool in the intracluster medium would be difficult for the low Mach number shocks in merging clusters, though they may succeed in boosting the energy of a pre-existing population of relativistic electrons (Lorentz $\gamma \sim 100$) to detectable regimes (Sarazin, 1999). The most promising candidates for such a population are the relativistic electrons in the dead radio lobes of active galactic nuclei. Such radio lobes become invisible a few million years after their central engine switches off. Enßlin and Gopal-Krishna (2001) showed analytically that the merger shock induced adiabatic compression of a dead lobe could result in emission from a relic. The model was used to successfully explain the relic in the Coma cluster, which has a radio galaxy connected to it (Giovannini et al., 1991). Recent observations have linked the relic in Abell 3411−3412 to a re-acceleration of old electrons in the lobes of a coincident radio galaxy (van Weeren et al., 2017).

It has also been shown that the synchrotron magnetic field in the lobes of a radio galaxy like Cygnus A, if diffused out into the intracluster medium, can provide sufficient seed fields to explain the observed Faraday rotation in clusters (Tribble, 1994). It was suggested that an orbiting head-tail radio galaxy near the centre may be the source of synchrotron electrons of the halo in the Coma cluster. Below we propose a model to account for the synchrotron emitting particles and magnetic field necessary for the origin of halos.

The halo region of A2163 contains more than 15 visible radio galaxies, some of which show a compact (i.e active) hotspot/core. Others which do not show a compact component may have recently had their jets turned off. There is considerable evidence that radio galaxies cycle through multiple on-off phases (Schoenmakers et al., 2000) with a generational gap of about 200 Myr (Kaiser et al., 2000). This yields enough time for 40 episodes of radio activity in A2163 during the 8.5 Gyr between z $\sim$ 3, when substantial radio galaxy activity began in the Universe (Miley and De Breuck, 2008), and z = 0.25 (epoch of merger in A2163 Maurogordato et al. (2008)).

The several diffuse sources of emission (e.g. D1 and D3 in Figure 4.1) may be the fading remnants of recently dead radio galaxies. The emission from a synchrotron electron shifts downward in both frequency and luminosity with time. We estimate that these objects, which are 2−5 times the detection limit, will become invisible in 17−36 Myr (see the discussion below on the 'Timescale of disappearance of dead radio lobes', similar to other estimates (Kaiser et al., 2000). The energy of 217−342 MHz synchrotron electrons, which are what will reach the 153-MHz threshold, will only reduce by factor $\sim$10−100 over 1−8 Gyr. The shock (or turbulence) from a merger would only have to increase their energy by this amount (and not many orders of magnitude) for the lobes to become visible again. Radio galaxies which have slipped below the detection limit in the last 20−200 Myr will only need to have their particle/field energies increased by

less than a factor 2 to become visible again. Perhaps, even the weak shocks of cluster mergers are capable of doing this. We propose that a halo may be a collection of a large number of dead radio lobes re-energised by a cluster merger.

Timescale of disappearance of dead radio lobes

Let S_{153} be the current surface brightness of a fading radio lobe at 153 MHz and α be its spectral index. Let the detection threshold on the 153-MHz image be S_{TH}. In this model a population of electrons of initial energy E_0 while emitting radiation will move to lower values along both axes in the (luminosity or) flux density – frequency plane (Figure 4.10). The line BC represents the current spectrum of the radio lobe, and the points A, B, and C are known. The point D(S, ν) – to be calculated – lies on the line BC and is the current position of the electron population which will move along the locus DA over time – to be calculated – before falling below the detection threshold S_{TH} at 153 MHz.

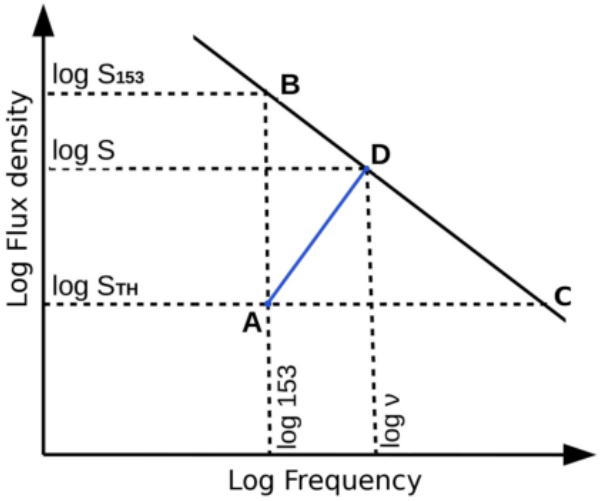

Figure 4.10: Time evolution of an electron on the Frequency–Flux density plane. The line BC is the current spectrum with spectral index α. Point D represents the population of electrons currently emitting with the critical frequency ν which will evolve to go below the detection threshold (S_{TH}) at 153 MHz at A. The slope of AD must be 1. The radio galaxies in A2163 will take 17−36 Myr to traverse from D ($\nu = 217 - 342$ MHz) to A after the central engine switches off.

The time dependence of the electron energy (Moffet, 1975)

$$E(t) = E_0 \left(1 + t/t_{1/2}\right)^{-1} \tag{4.7}$$

where, E_0 is the initial electron energy in GeV, $t_{1/2} = 8.352/(B_{eff}^2 E_0)$ Gyr is the time taken to reduce the electron energy to half the initial value, and B_{eff} is the effective magnetic field in μG considering also the contribution of Inverse Compton losses to the cosmic microwave background photons at that redshift ($B_{CMB} = 3.25(1+z)^2 = 4.7$ μG).

The critical frequency (ν_c) at which a synchrotron electron radiates most of its energy is given by

$$E = \sqrt{\nu_c / 16.08B} \quad \text{GeV} \tag{4.8}$$

where, B is the synchrotron magnetic field.

Since for a synchrotron source luminosity (flux density) and critical frequency are both proportional to E^2, the locus of the electron population on the flux density – frequency plane will have a unit slope. D lies at the intersection of the two lines defined by

$$\log S - \log S_{TH} = \log\nu - \log 153 \tag{4.9}$$

$$\log S_{153} - \log S = \alpha \ (\log 153 - \log\nu) \tag{4.10}$$

Using $S_{153} = 6-15$ mJy/beam for some of the radio lobes, $S_{TH} = 3$ mJy/beam (3σ), $\alpha = -1.0$, synchrotron $B = 1\mu$G, effective $B_{eff} \sim 5$ μG, we obtain $\nu = 217-342$ MHz, t = 17−36 Myr for the lobe to go below the detection threshold on our image after the central engine is switched off. Though, even after 200 Myr the electrons will still retain more than half the energy. The reduction in energy is only by factor 10 in 1 Gyr.

The number of synchrotron electrons in the lobes of active radio galaxies in A2163 is about 10^{61}, and in the halo $\sim 3 \times 10^{62}$ (from 'Minimum Energy calculation'). Therefore, the activity of about 30 radio galaxies over the lifetime of the cluster will suffice to populate the intracluster medium with the required number of energised synchrotron electrons, and perhaps magnetic fields too. This number of radio galaxies is much smaller than the product of the number of objects currently visible in A2163 and the 40 generations of radio activity possible since z = 3. Furthermore, the minimum energy supposition may well be inappropriate and the total energy in the lobes of a radio galaxy may be an order of magnitude or more higher (Beck and Krause, 2005), which would work in the direction of our suggestion. We have already argued that the *ridge* is not the lobe of an *active* radio galaxy. In the light of the discussion here the issue of whether it is the remnant of a dead radio galaxy is moot. Curiously, the higher resolution spectral index map that we have of A2163 (Figure 4.7) shows a blotchy pattern expected of the halo being a collection of dead radio galaxy lobes, though, a better quality higher resolution image is necessary for a more secure claim. We note that this model for the origin of a halo is a straight-forward extension of other observations which suggest that merger-induced re-acceleration in the dead lobes of single radio sources result in radio relic sources (Enßlin and Gopal-Krishna, 2001; Giacintucci et al., 2008; van Weeren et al., 2010, 2012, 2017). A similar model was proposed to explain the origin of radio halo observed in A2255 (Feretti et al., 1997).

Halos should only occur in clusters which can support/host many radio galaxies, which would explain why they only occur in a small fraction of clusters. This would also require halos to occur predominantly at lower redshifts where many generations of radio galaxies have had enough time to spew sufficient synchrotron electrons and magnetic fields into the intracluster medium.

4.4 Conclusions

Sensitive low frequency images obtained using the GMRT have shown a clearly demarcated substructure in a radio halo, with no superposed active radio sources to confound the interpretation. The spectral index, shape and location of this *ridge* of radio emission in the halo in the galaxy cluster A2163 is consistent with it being the site of the principal shock-front at which synchrotron electrons are being re-energised by a cluster merger. Based on estimates from our images we propose that a radio halo may well be the collective reincarnation of the lobes of long dead radio galaxies triggered by a cluster merger. The improved resolution and sensitivity of future low frequency observations (e.g. LOFAR, uGMRT, and SKA) should be able to confirm this.

Appendix: Minimum Energy calculation

The total number of electrons N in a synchrotron source can be calculated from equipartition energy estimate. The total energy of a synchrotron source is due to energy stored in relativistic particles: electrons with energy U_{el}, protons with U_{pr}, and the energy in magnetic fields U_B.

$$U_{tot} = U_{el} + U_{pr} + U_B \tag{4.11}$$

We will assume that the energy stored in heavier particles is a multiplicative factor of energy of electrons, i.e,

$$U_{pr} = kU_{el} \tag{4.12}$$

We have taken k to be 1 in our calculations which is a usual assumption for galaxy clusters.

The condition of minimum energy is obtained when the contributions of the magnetic field and the relativistic particles are approximately equal:

$$U_B = \frac{3}{4}(1+k)U_{el} \tag{4.13}$$

Therefore,

$$U_{tot}(min) = \frac{7}{4}(1+k)U_{el} \tag{4.14}$$

Equipartition of energy gives us an estimate of the minimum energy density of the synchrotron source from the observable quantities such as frequency ν, spectral index α and surface bightness I:

$$u_{min}[\frac{erg}{cm^{-3}}] = \xi(-\alpha, \nu_1, \nu_2)(1+k)^{4/7}\nu^{-4\alpha/7}(1+z)^{(12-4\alpha)/7}I^{4/7}d^{-4/7} \tag{4.15}$$

and the magnetic field as

$$B = \left(\frac{24\pi}{7}u_{min}\right)^{1/2} \tag{4.16}$$

For fixed cutoff frequencies ν_1, ν_2, spectral index α and assuming a certain source depth d we can estimate the source volume which will give the (minimum) total energy of the source ($U_{tot}(min) = u_{min} \times V$) (Govoni and Feretti, 2004). The energy stored in the electrons is (for $k = 1$)

$$U_{el} = \frac{2}{7}U_{tot}(min) \tag{4.17}$$

From the electron energy, total number of electrons can be estimated as follows. We will assume a power law distribution of electrons with density

$$n(E) = n_0 E^{-\gamma} \tag{4.18}$$

between energies E_1 and E_2. γ is related to the electron spectral index α as $\gamma = 1-2\alpha$. The electron energy density u_{el} is then

$$u_{el} = \int_{E_1}^{E_2} n(E)EdE \tag{4.19}$$

Taking $N_0 = n_0 V$, where V is the source volume, the total electron energy U_{el} is given by

$$U_{el} = N_0\left(\frac{E_2^{2-\gamma} - E_1^{2-\gamma}}{2-\gamma}\right) \tag{4.20}$$

Expressing U_{el} in terms of cutoff frequencies ν_1 and ν_2, where energy is related to critical frequency by $E = \sqrt{\nu_c/C_1 B}$. Here C_1 is a constant with value = 16.08 when mgnetic field B is expressed in μG and energy E in GeV.

$$U_{el} = \frac{N_0}{2\alpha+1}\frac{(\nu_2^{\alpha+1/2} - \nu_1^{\alpha+1/2})}{(C_1 B)^{\alpha+1/2}} \tag{4.21}$$

We take the cutoff frequencies as 10 MHz and 10 GHz. The energy stored in electrons U_{el} (obtained from equipartition estimate) gives us N_0 and finally N is given by

$$N = \frac{N_0}{2\alpha}\frac{(\nu_2^{\alpha} - \nu_1^{\alpha})}{(C_1 B)^{\alpha}} \tag{4.22}$$

The equipartition values are estimated assuming a lower and higher cutoff in frequency which ultimately depend upon electron energy. A more reasonable assumption is taking a lower and higher cutoff in energies (Brunetti et al., 1997; Beck and Krause,

2005) and assuming the Lorentz factors $\gamma_{min} \ll \gamma_{max}$. The revised equipartition estimate of the magnetic field is given by

$$B'_{eq} \sim 1.1 \gamma_{min}^{(1+2\alpha)/(3-\alpha)} B_{eq}^{7/(6-2\alpha)} \tag{4.23}$$

where, B_{eq} is the equipartition magnetic field. A $\gamma_{min} = 100$ is usually assumed.

Chapter 5

Spectral Index Imaging of A665

The presence of diffuse extended radio emission at the centre of the cluster A665 was first indicated by Moffet and Birkinshaw (1989). This was subsequently confirmed by Jones and Saunders (1996). Further observations of the cluster were carried out by Giovannini and Feretti (2000) at 1.4 GHz and Feretti et al. (2004) at 325 MHz, who reported a halo 1.8 Mpc in size with an extension in SE-NW direction. The latter authors also presented a spectral index image between 325 MHz and 1.4 GHz.

The cluster has been studied extensively in X-ray (Markevitch and Vikhlinin, 2001; Govoni et al., 2004; Million and Allen, 2009; Dasadia et al., 2016). There is no recent optical study of the cluster. The dynamical analysis of the cluster was carried out by Gómez et al. (2000) and by Geller and Beers (1982) before that.

The spectral index image presented here is made using our GMRT observations at 147 MHz and GMRT archival data at 323 MHz, which was re-analyzed for this project.

5.1 Results

5.1.1 Radio Images

Figures 5.1 and 5.2 show the radio images of the halo at 147 MHz (25 arcsec resolution) and 323 MHz (11 and 25 arcsec resolution). The halo is $5' \times 3'$ ($\sim$ 918 kpc $\times$ 550 kpc) in size at 147 MHz, slightly assymetric with a very sharp edge in the south-east. We used the 608 MHz high resolution (6 arcsec) image to identify the compact radio sources within the halo (Figure 5.3). These sources are marked with numerical labels 1$-$14 in Figure 5.3 and by a "+" sign in Figures 5.1 and 5.2.

The halo appears bigger and more symmetric at 323 MHz, and with the absence of the south-eastern edge. There is a higher intensity 'plateau-like' horizontal structure in the north, which is less obvious in the 147 MHz image. On the other hand the brightest structure in the 147 MHz image lies to the south of the plateau in the 323 MHz image. The full extent of the halo is nearly 1.1 Mpc (= 6 arcmin) in the low resolution image. We believe that some of the halo emission visible at 323 MHz (extending up to sources marked as 8$-$10 in Figure 5.3) has been lost at 147 MHz. This cannot be due to

resolution and therefore poor data is the most likely culprit. Further sensitive images are required to confirm the presence of emission in this region.

We also observed the halo at 608 MHz (P.C 27_070). However, the final image could not be used for determining halo properties due to its lower sensitivity to extended emission. The image is shown in Figure 5.3. The halo appears fragmented at this frequency, being affected by ripples from a strong, partially resolved nearby source, approximately 15 arcmin to the east. The flux density of the contaminating source is ∼400 mJy at 608 MHz. The 'dirty beam' from this location extends out to the halo, which has posed a serious problem while imaging, at all the frequencies, as discussed in Chapter 3. At 608 MHz in particular, the halo size is much less than that at 147 and 323 MHz. Even the low resolution image made at 608 MHz suffered from similar artefacts. 'Peeling' the source did not result in any significant improvement of the image. Therefore, the 608 MHz image has only been used to identify the point sources in and around the halo.

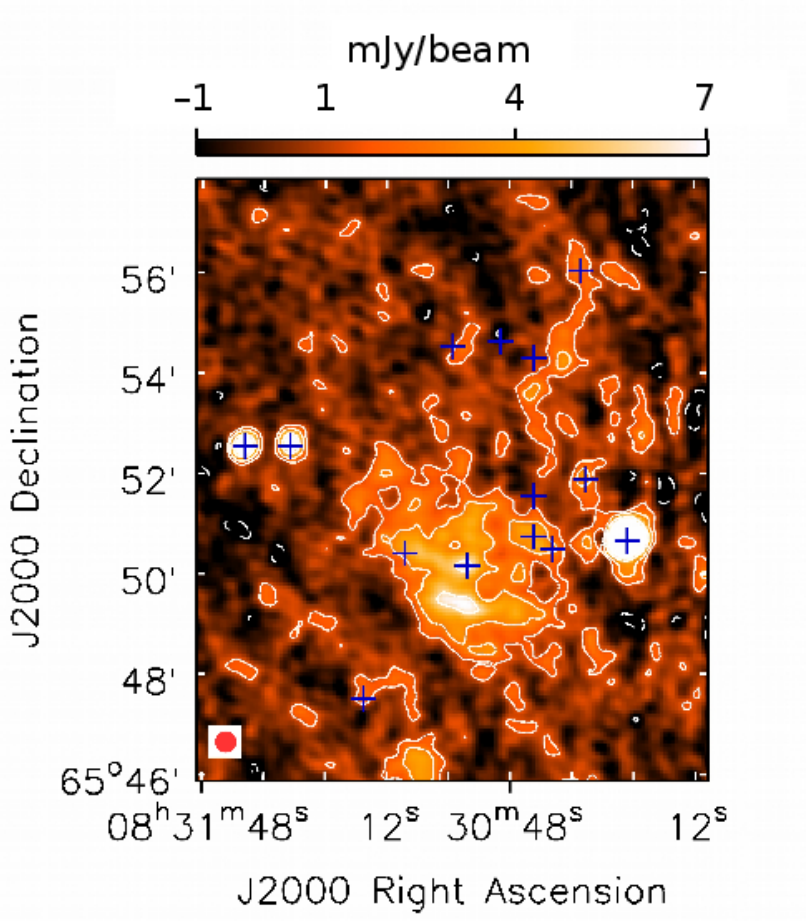

Figure 5.1: 147 MHz image of the halo A665 at 25″ resolution. Contours start at 1.5 mJy/beam (=2σ) and then scale by a factor 2. The "+" sign indicates the positions of the point sources some of which are only visible at higher resolution images at 323 and 608 MHz (Figures 5.2 5.3). The dashed contour in the image is −1.5 mJy/beam.

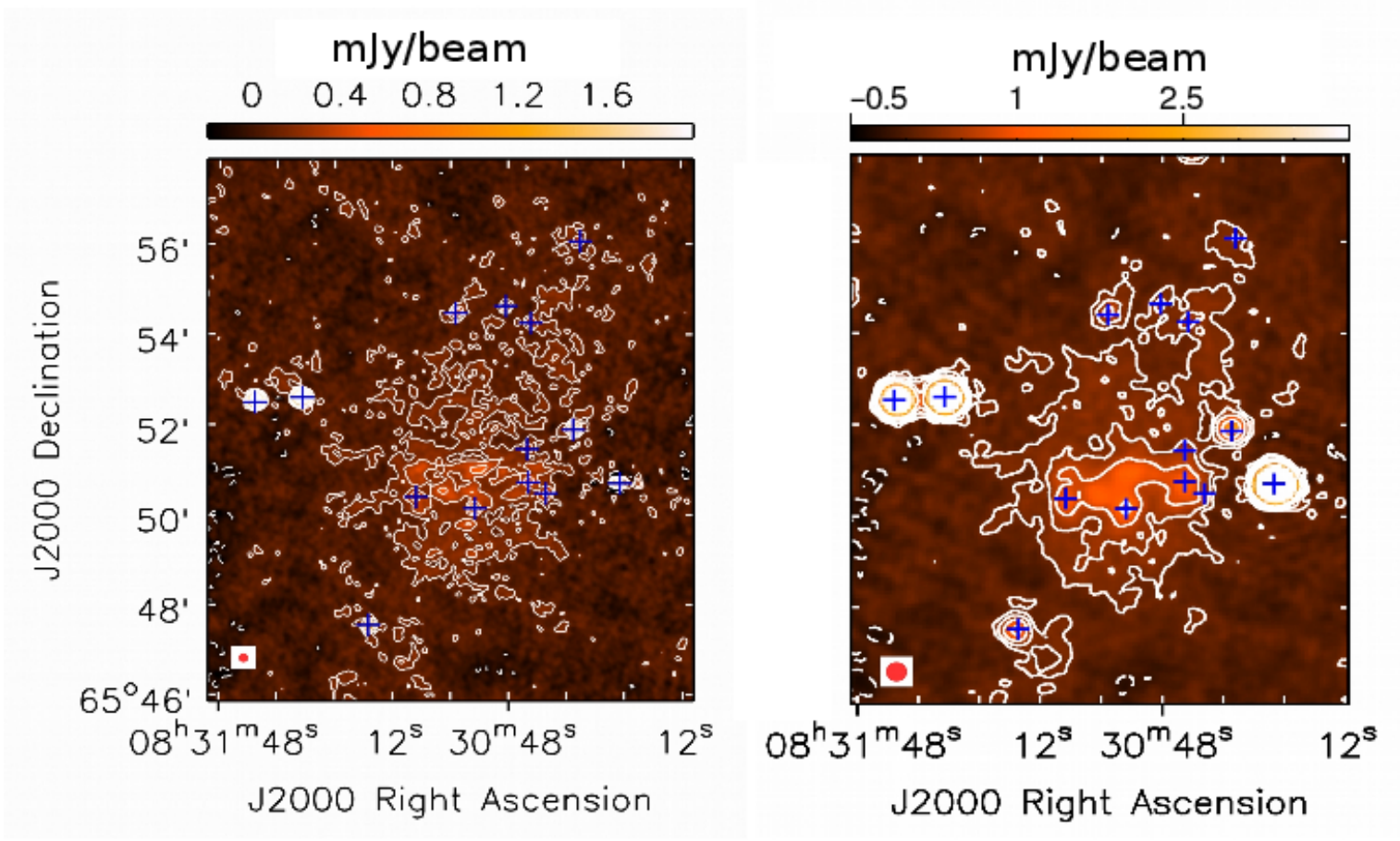

Figure 5.2: Radio stokes I images of the halo at 323 MHz – 11″ (*Left*) and 25″ (*Right*). Contours start at 0.12 mJy/beam (=3σ) and 0.18 mJy/beam (=3σ) in the two images and then scale by a factor of 2. The -3σ level is shown as dashed contours. The "+" sign indicates the positions of the point sources. Beam size is indicated by solid red circle at the bottom left corner in each image.

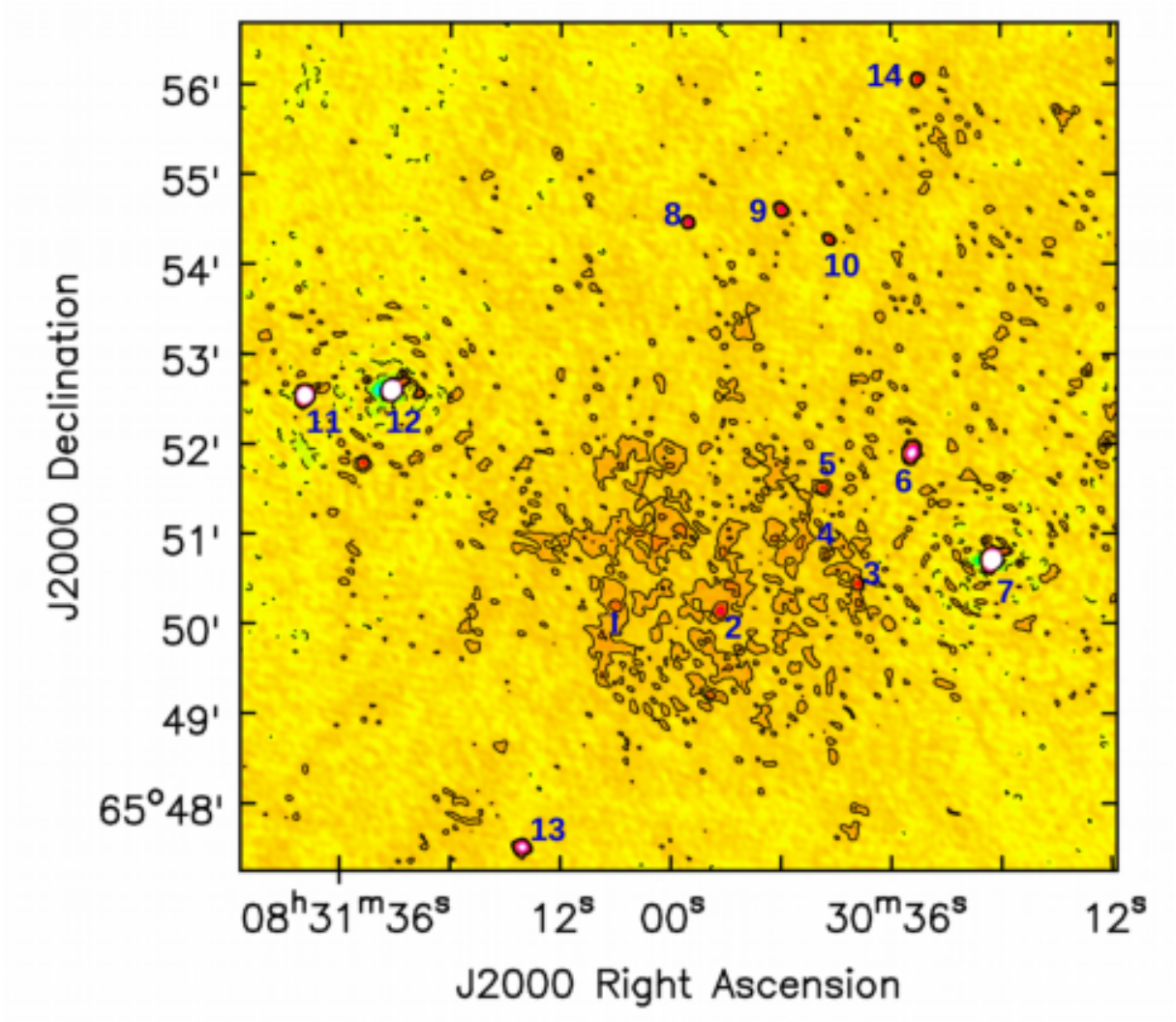

Figure 5.3: 608 MHz image of the halo at 6″ resolution. Contour level is $+3\sigma = 0.03$ mJy/beam. The halo appears fragmented at this frequency. The positions of the point sources are numbered 1−14.

5.1.2 Flux Density of the Halo and Integrated Spectral Index

The estimated flux density of the halo is 146 mJy at 323 MHz. This excludes the point sources identified within the halo and includes the full extent of the halo. The combined flux density of the point sources within the halo (sources 1−5) is around 3 mJy at 323 MHz. This was obtained by the task IMFIT of AIPS. As many of these point sources are extremely faint or invisible at 147 MHz, therefore accurate estimation of their flux densities is difficult. The flux densities in the tentative positions of the point sources adds up to nearly 15 mJy. But this also includes the background emission due to the halo. Assuming a spectral index of −0.75 for these sources, the contribution at 147 MHz

is less than 6 mJy. Assuming the contribution to be atleast 6 mJy at 147 MHz, the flux density of the halo is 303 mJy. Including the same area of integration at 323 MHz as that of 147 MHz yields a flux density of 113 mJy. The image sensitivity is 0.7 mJy/beam and 40 μJy/beam at 147 and 323 MHz, respectively. The details of the halo are given in Table 5.1.

ν (MHz)	UV-range (kλ)	Resolution ($''$)	S (mJy)	LLS (Mpc)	rms (mJy/beam)
147	0−13.5	25	303	0.9	0.7
323	0−27	11	146	1.1	0.04

Table 5.1: The columns are: 1)Central frequency of observation 2) UV-range in kilolambda 3)Restoring beam in arcsec 4)Flux Density of the halo, after the subtraction of discrete sources 5)Largest Linear Size of the halo 6)Noise in the image.

The flux density reported earlier at 325 MHz by Feretti et al. (2004) is 197 mJy, which is nearly 50 mJy higher than the value estimated by us. The discrepancy in flux densities could be due to various reasons. We have encountered a similar situation for the case of A2163 (Chapter 4), where we have highlighted the various factors that can explain the observed discrepancy. The loss of flux density may be attributed to different UV-coverage of the telescopes, non-zero background contribution, blend of discrete sources and larger area of integration. We have already checked the flux scaling for the field by comparing the point sources in our field with NVSS and TGSS catalogs (Chapter 3). The point sources within the halo are very weak. Different areas of integration and contribution from the background seems to be the most likely cause for the observed difference in the flux density of the halo. Moreover, our 323 MHz image is nearly ten times more sensitive than the previous image.

From the flux densities estimated over same area at both the frequencies, the integrated value of the spectral index is −1.25. Allowing for a 10% error in the flux densities, this would amount to an error of 0.18 in the measured value of spectral index. This is steeper than the value estimated by Feretti et al. (2004) between 325 and 1400 MHz, which was −1.04.

5.1.3 Spectral Index Images

Figure 5.4 shows the spectral index image between 147 and 323 MHz and the corresponding error image. The resolution is 25 arcsec. Pixels below 2σ are blanked at both the frequencies. The positions of the point sources within the halo are masked and denoted by pink ellipses in the image. The outer contour is the 2σ contour at 147 MHz.

The spectral index image shows that the northern part of the halo is flatter than the southern part. The northern flat spectrum structure approximately 1 arcmin wide and 4 arcmin long (∼183 kpc×730 kpc) has a mean spectral index around −1.89 and the southern part of the halo has a mean value of −3.0. The error in the spectral index

values in the central part of the halo is ∼0.2, while at the edges it is around 0.5. The northern part of the halo showing flatter spectrum is a result of higher emission at 323 MHz.

We measured a higher flux density for the halo in the high resolution 323 MHz compared to the value in the lower resolution image made at the same frequency (using different UV cutoff). This discrepancy was a factor of 2 when the same region was used to measure the integrated flux density in both the images. It is the usual practice to construct spectral index images using matched UV-range, and hence matched resolution images, at both the frequencies. However, because of the above issue we also created a spectral index image using the full resolution (11 arcsec) 323 MHz data but regridded and convolved to match the 147 MHz image (4.5 arcsec pixel, 23 arcsec resolution).

The spectral index images made in two different ways are shown in Figure 5.4 (matched UV) and Figure 5.5 (regridded image). Even though the values of the spectral indices are very different in the two images, there is a high degree of correspondence between structures in them. The mean values of the spectral index in the northern and southern half are -1.15 and -1.67, respectively.

Figure 5.6 shows a pixel-by-pixel comparison of the spectral index values obtained by the two different methods. The tight correlation reflects the high degree of correspondence between the two. Figure 5.7 shows the difference in the spectral index values of the northern and southern parts of the halo.

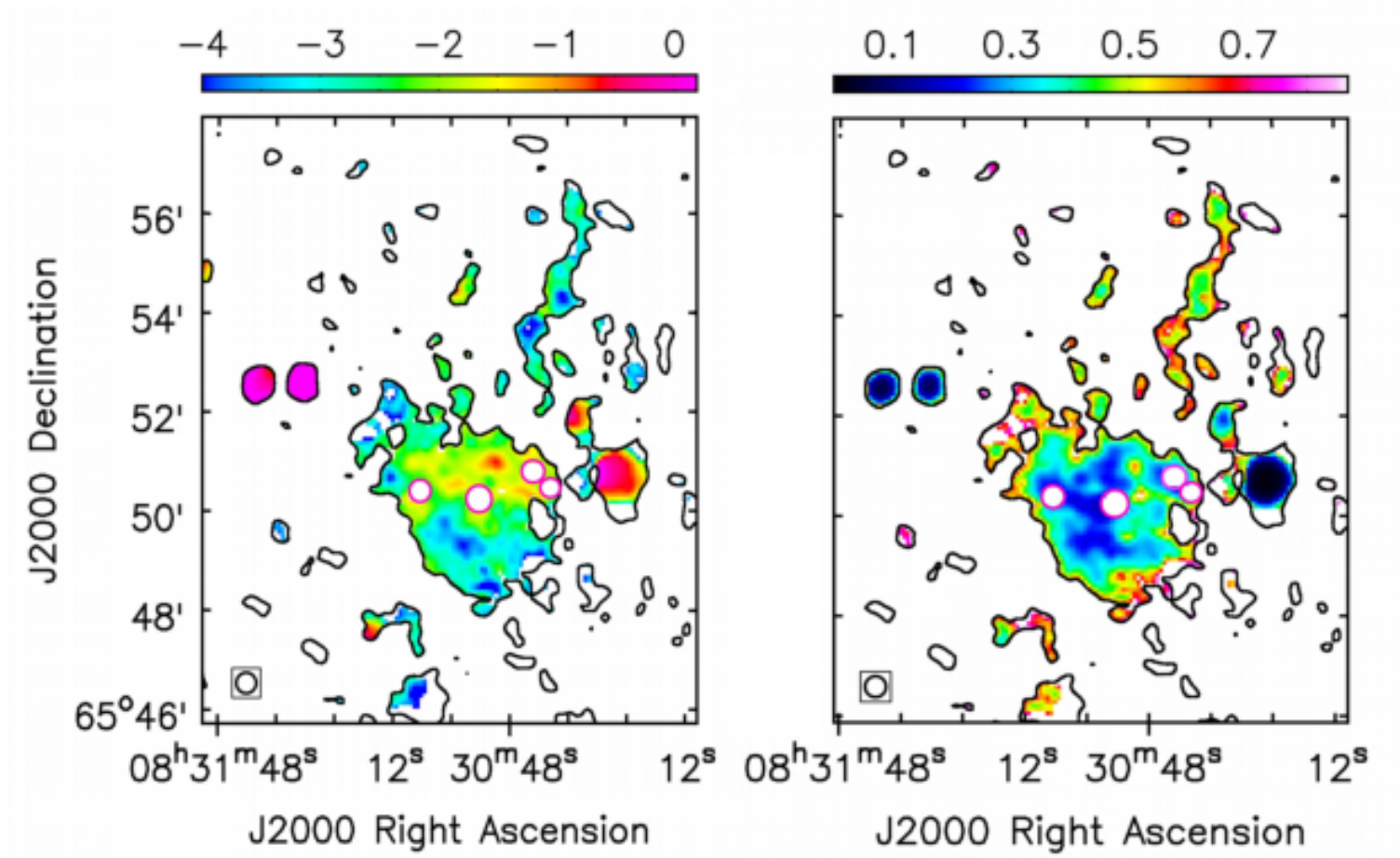

Figure 5.4: Spectral index image made between 147 and 323 MHz at 25 arcsec resolution (*left*) and its error image (*right*). The contour enclosing the halo in both the images is $+2\sigma$ level (= 1.5 mJy/beam) at 147 MHz. The point sources within the halo are masked and the same are indicated by pink ellipses in both the images. Beam size is indicated on the bottom left corner in both the images.

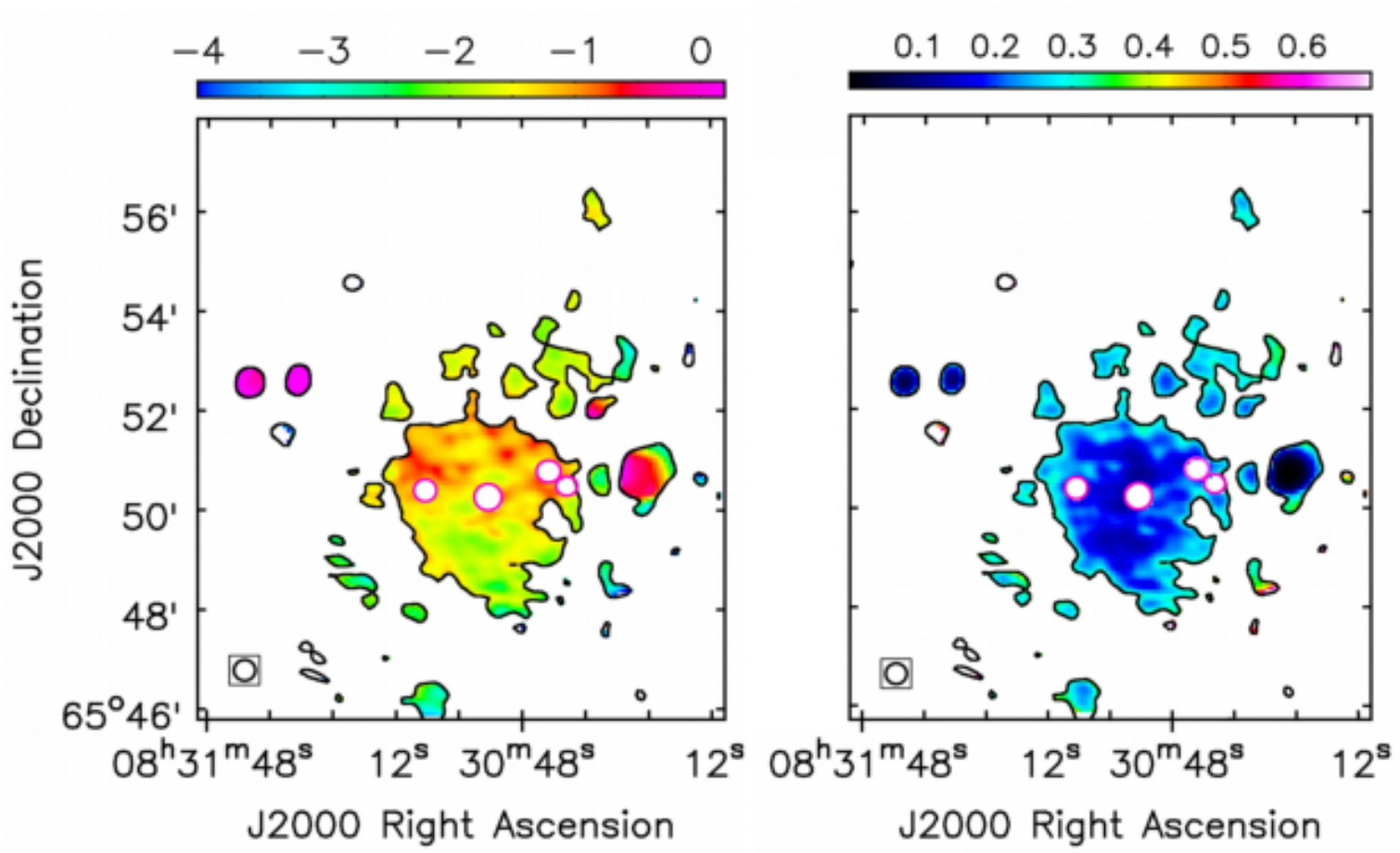

Figure 5.5: Spectral index image between 147 and 323 MHz made by regridding and convolving the 323 MHz (11 arcsec) image to match the resolution of 147 MHz-25 arcsec (*left*), and its error image (*right*). The contour enclosing the halo in both the images is $+4\sigma$ level (= 2.8 mJy/beam) at 147 MHz.

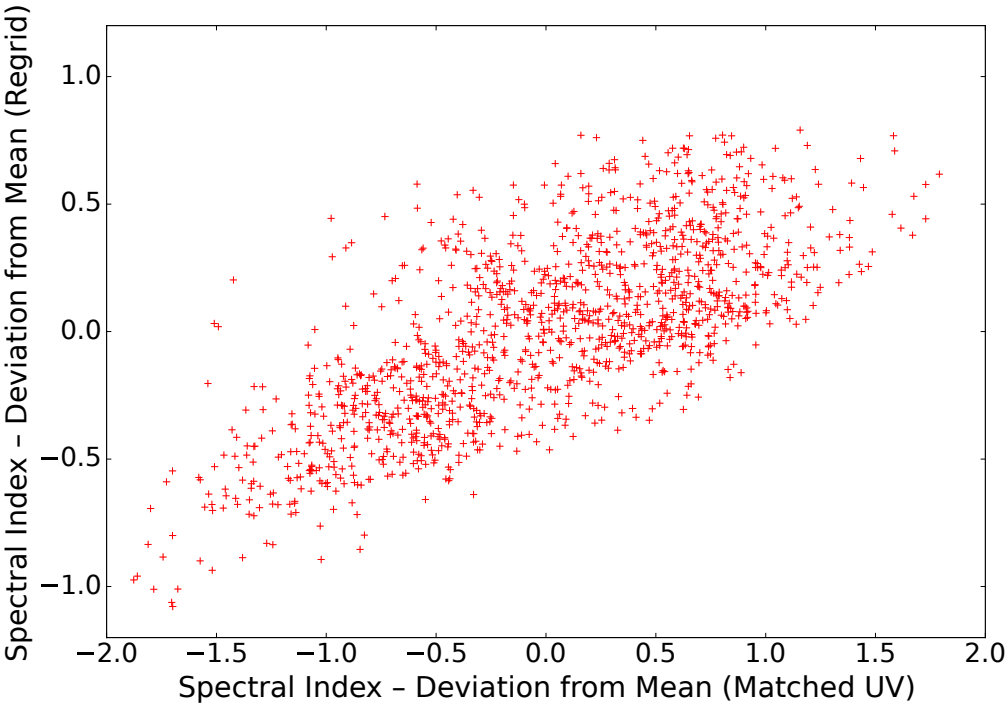

Figure 5.6: Comparison of the pixel values of the (mean subtracted) spectral index of the halo, obtained by making images in two different ways – matched UV, and regridding and convolving (see text). The plot shows a tight correspondence between the two images (correlation coefficient = 0.72).

5.1.4 Equipartition values

Assuming equipartition of energy between relativistic particles and magnetic field, we derived the minimum energy density = 2.5 × 10^{-14} erg cm^{-3}, B_{eq}= 0.52 μG and a luminosity of 9.5 × 10^{41} erg s^{-1}. These were calculated using a source depth of 700 kpc, surface brightness of 4.76 μJy/arcsec^2 at 147 MHz, spectral index −1.26 and cutoff frequencies 10 MHz and 10 GHz.

Assuming a lower and higher cutoff in energies (Brunetti et al., 1997; Beck and Krause, 2005) and assuming the Lorentz factors $\gamma_{min}(= 100) \ll \gamma_{max}$ yields a somewhat different estimate of 1.45 μG for the magentic field.

Vacca et al. (2010) carried out power spectrum study of the magnetic field in A665 using polarization observations at 1.4 GHz and simulations. They obtained a central magnetic field of 1.3 μG. They showed that the halo brightness profile can be reproduced by assuming a decrease in magnetic field with thermal gas density; with an average magnetic field of 0.75 μG in the cluster. The equipartition magnetic field value obtained by Feretti et al. (2004) was 0.55 μG and minimum energy density of 2.8 × 10^{-14} erg cm^{-3}. Our observations conform to these estimated values.

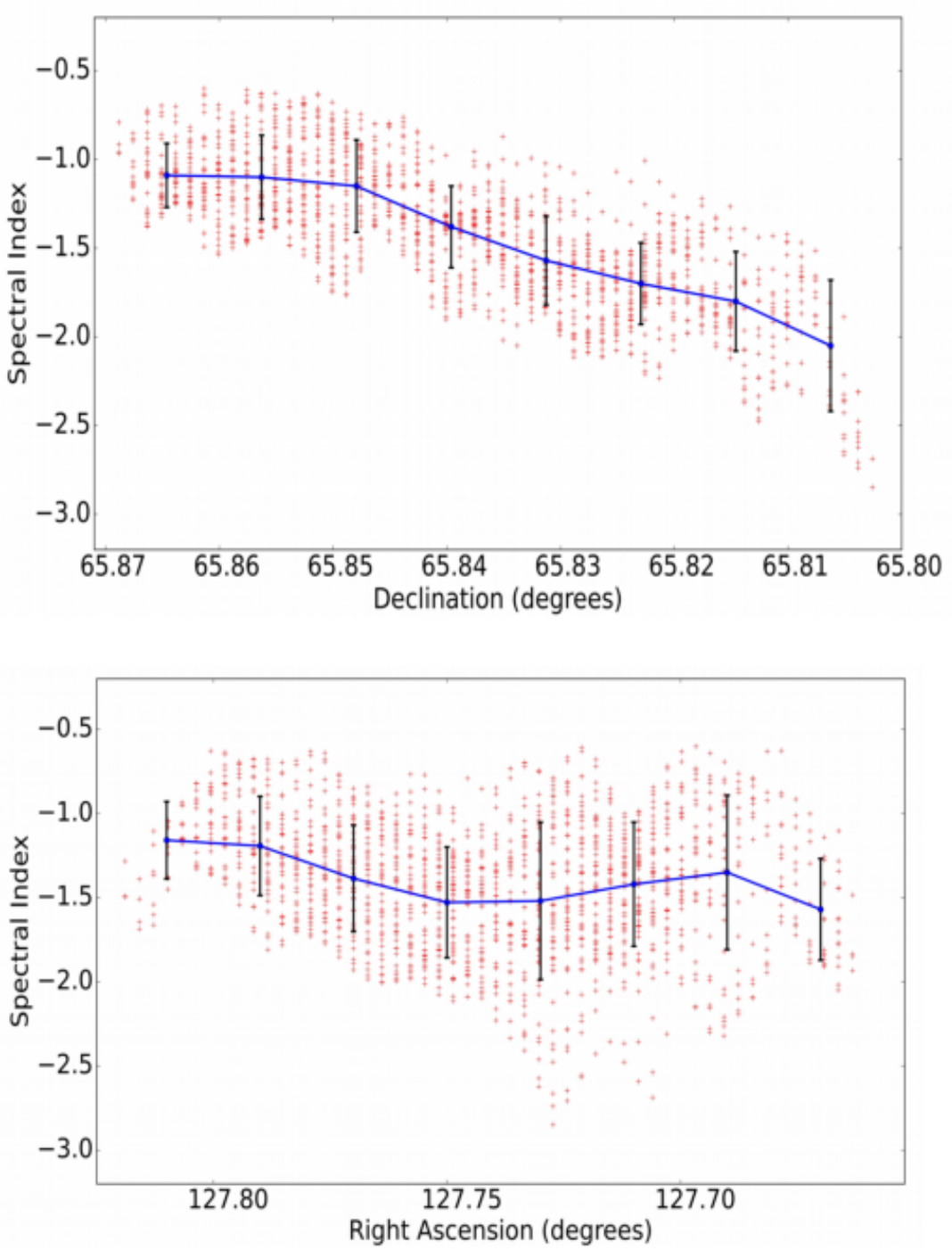

Figure 5.7: Pixel values of spectral index of the halo as a function of Declination (*top*) and Right Ascension (*bottom*). The images have been constructed by re-gridding the 323 MHz image (see text). The mean values in 30 arcsec intervals are over-plotted. The top panel shows a smooth steepening of the spectral index values from northern to southern part of the halo, while it is almost constant along the RA axis.

5.1.5 Comparison of Spectral Index Image with Optical and X-ray

Figure 5.8 shows an overlay of the radio contours at 323 MHz on the optical DSS image. The halo fills the optically dense region. Particularly, the flatter spectrum region in the halo coincides with the dense optical peak at the centre. We also show the overlay of the X-ray brightness contours, obtained from the archival *XMM-Newton* data (Obs. ID: 0109890501), on the spectral index image. The halo only partially covers the X-ray emission. The halo extends beyond the southern compact core while much of the X-ray emission extends to north-west. With our present sensitivity at 147 MHz, we do not see any halo emission in the north-west extension of the X-ray emission, while at 323 MHz some emission is visible in the north-west. The flattest spectrum region lies just above the southern compact core.

5.2 Discussion

X-ray analyses of this cluster have been carried out by Jones and Saunders (1996); Gómez et al. (2000); Markevitch and Vikhlinin (2001); Govoni et al. (2004) and more recently by Dasadia et al. (2016). The X-ray brightness image reveals a very bright and compact core in south, along with a tail of much lower brightness extension fanning out to the north-west. These studies suggest that the cluster has recently experienced a two-body merger along the north-south direction. The images have been interpreted in terms of the compact core in the south being associated with a subcluster falling in from the north. They suggest that the lack of a second compact core indicates that the main cluster in the north has likely been disrupted by the merger.

Gómez et al. (2000) found no evidence of non-gaussianity along the line-of-sight from the study of velocity distribution of 77 confirmed cluster members. This may be a result of a merger in the plane of the sky. But the two-dimensional spatial distribution of central galaxies have also failed to reveal any substructure. It was concluded from the optical data that the cluster is in a fairly relaxed state. In order to explain the apparently contrary results from optical and X-ray, the authors carried out N-body simulations of head-on cluster merger and concluded that the substructure in the X-ray can be explained by two similar mass subclusters (mass ratio 1:1 or 1:2) seen close to the time of core crossing, (which is also consistent with the observed velocity distribution of the galaxies for a certain range of viewing angle). Moreover, both the optical and X-ray distribution show elongation in the same NW-SE direction. The X-ray core shows a mild offset of 1 arcmin from the galaxy density peak.

The central concentration of galaxies in the DSS image (Figure 5.8), which according to the previous interpretation contains both the subclusters at the point of merger, coincides with the flatter spectrum central plateau in the 323 MHz image. If so, the gas in this region would be shock heated and energized by the fast moving core. This would be consistent with the region, the plateau, having the flattest spectral index of the whole halo. Our spectral index image is limited by the 147 MHz image which does not extend

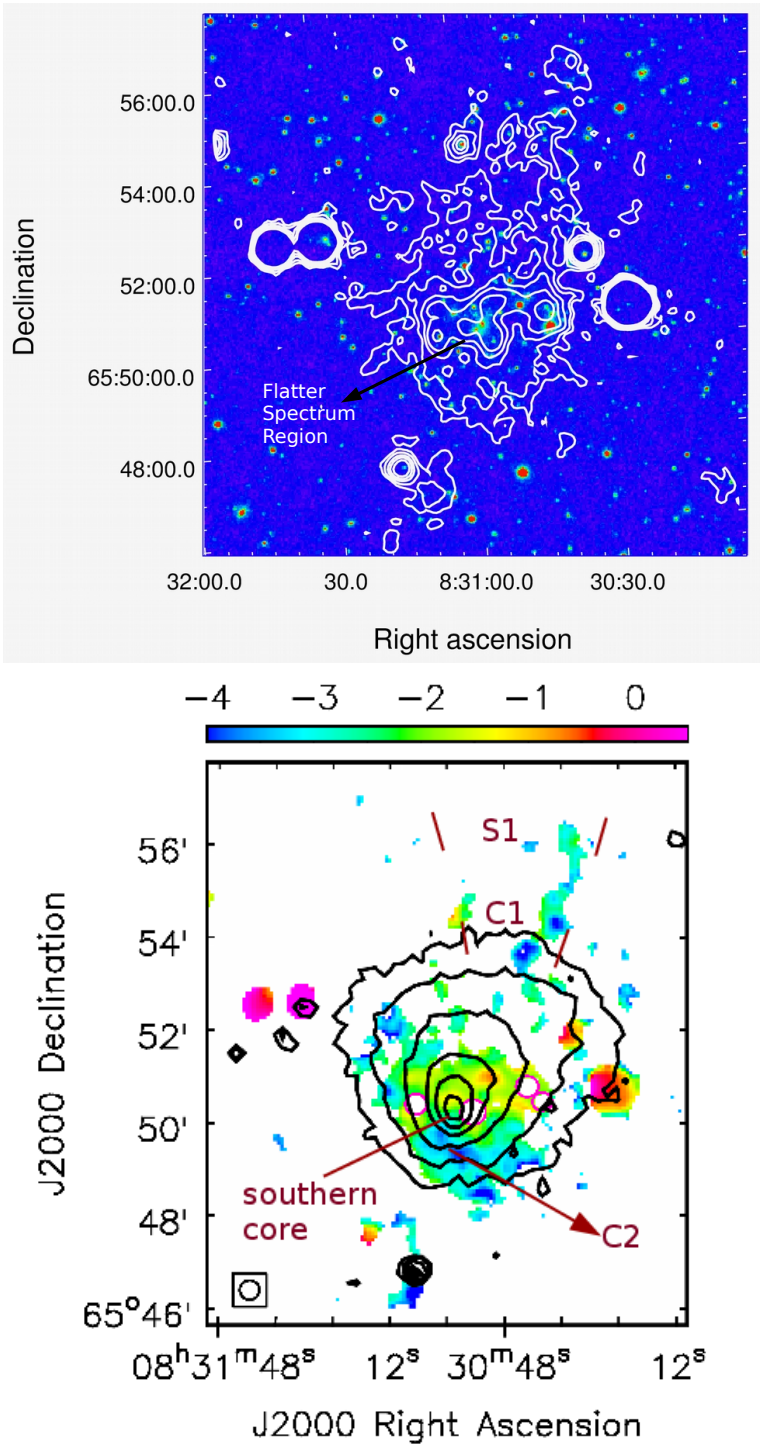

Figure 5.8: Radio–Optical–X-ray comparison. *Top*: Radio contours at 323 MHz (25″ resolution) overlaid on optical DSS image (in colour). The contour levels are 0.18, 0.3, 0.5, 0.7 and 1 mJy/b. The flat spectrum region in the halo coincides with the high galaxy density region. *Bottom*: X-ray brightness contours on the spectral index image. The contours are taken from *XMM-Newton* archival data. The flat spectrum region of the halo lies just above the X-ray core. S1, C1 and C2 are the tentative positions of shock front and the the two cold fronts detected by Dasadia et al. (2016). No relic is observed at the position of the shock front.

further north. It will be interesting to look for spectral index features beyond what we currently observe.

Markevitch and Vikhlinin (2001) suggested a shock front at the leading edge of the southern core. But this has now been classified as a cold front by Dasadia et al. (2016). Cold fronts are also surface discontinuities like shock fronts, which develop when the gas in the cool core of the merging subcluster comes into contact with the surrounding intracluster gas. Cold fronts differ from shocks in that increase in density across the front is accompanied by corresponding decrease in temperature. There is also no significant increase in pressure and entropy across the front. The location of the cold front is marked as 'C2' in the Figure 5.8 and is taken from Dasadia et al. (2016). No spectral index flattening is observed at this location. The previous 325−1400 MHz spectral index image of Feretti et al. (2004) also did not reveal any spectral flattening at this location. 'C1' marks another cold front while 'S1' is a shock front of Mach number 3. A665 is the second cluster (after the Bullet cluster) where a high Mach number shock front is observed. We do not detect a relic at this location though such a possibility has been suggested before (Dasadia et al., 2016). Unavailability of seed electrons in this region could explain the non-detection of relic in this location.

The halo in A665 is similar to the case of A2163 (Chapter 4) where a 'flat spectrum ridge' was observed between two subclusters that have recently crossed each other. The spectral index image presented here is consistent with the merger geometry as deduced from the X-ray, i.e., a merger occurring in the north-south direction along the plane of the sky would be expected to yield a horizontal flat spectrum region between them such as we see in Figure 5.8. However, in the case of A2163, the intensity images also showed a distinct increase in surface brightness; which is absent in the 147 MHz image and only a slight increase at 323 MHz. More sensitive observations of halos and spectral index images may reveal that such features are present in many of these objects.

Chapter 6

The Radio Halo and Relic in A2744

The cluster A2744 hosts both a halo and a relic and has been observed previously with the VLA at 1.4 GHz (Giovannini et al., 1999; Govoni et al., 2001), and at 325 MHz with both the VLA (Orru' et al., 2007) and the GMRT (Giacintucci, 2011). Previous spectral index images for this halo are available in Orru' et al. (2007), between 325 and 1400 MHz and Pearce et al. (2017) between 1 and 4 GHz. We present here radio images from new observations at 153 and 617 MHz and from archival data at 332 MHz.

6.1 Results

6.1.1 Radio Images of A2744

Figure 6.1 shows the radio image of A2744 at 153 MHz with 23 arcsec resolution. It has a noise of 0.7 mJy/beam. The halo is regular in shape, and with an extent of $8'$ $\times$ $6'$ ($\sim$2.17 Mpc$\times$1.6 Mpc) the halo is larger than what was observed earlier at 332 MHz (Figure 6.2 and Orru' et al. (2007); Giacintucci (2011)). There are only two radio galaxies, marked S1 and S2, near the halo. S2 may be a member of the galaxy cluster and likely a head-tail radio source (617 MHz images in Figure 6.2). S1 was identified as a background object by Boschin et al. (2006), from optical observations.

Figure 6.2 shows both the high ($12''$) and low ($23''$) resolution images made at 332 MHz. The low resolution image was used to make the 153$-$332 MHz spectral index image. The halo has a size of $6' \times 4'$ (1.6 Mpc$\times$1.08 Mpc) at 332 MHz. We detect more of the halo at this frequency than is visible in the VLA image of Orru' et al. (2007). Unlike in the 153 MHz image, where the halo extends all the way to the relic, here they appear separate with a "bridge" of emission connecting them. This "bridge" is also reported in a previous study (Giacintucci, 2011).

At 617 MHz the halo is less than half the size at 153 MHz (Figure 6.2) — about $3' \times 3'$ (0.82 Mpc $\times$ 0.82 Mpc). This reduction in extent is to be expected given their steep spectral index. A part of the emission is also visible below the source S1.

The galaxy cluster also hosts a relic, to the north-east of the halo, which is approximately $6' \times 2'$ in size (1.6 Mpc $\times$0 .54 Mpc) at 153 and 332 MHz, and about $5' \times 1'$ in

size (1.3 Mpc × 0.27 Mpc) at 617 MHz.

6.1.2 Flux Densities and Integrated Spectral Index

We measured flux densities of 792, 363 and 71 mJy at the three frequencies (excluding the discrete sources S1 and S2). At 332 MHz the flux densities measured for the halo and the relic are higher than those obtained by Orru' et al. (2007) and comparable to Giacintucci (2011). The relic has flux densities of 230, 120 and 49 mJy, respectively. The details of the observed flux densities, source size and rms noise of each image are given in Table 6.1.

From the integrated flux values, we estimated an average halo spectral index of −1.0 between 153 and 332 MHz, and −2.63 between 332 and 617 MHz. The much steeper value of spectral index between 332 and 617 MHz could be due to the loss of flux density due to resolving out of the halo in the peripheral regions. Limiting the measurements to the same area at both frequencies yielded a value of −1.6. The flux density of the halo measured at 1.4 GHz is 57.1 mJy (Govoni et al., 2001). This gives an integrated spectral index of −1.28 between 332 and 1400 MHz for the halo, to be compared with −1.0 (Orru' et al., 2007). However, as also noted by Giacintucci (2011), the 332 MHz GMRT halo flux density is significantly higher than that of VLA (Orru' et al., 2007) even while comparing within the same area. It is to be noted that our flux density is anchored to the TGSS-NVSS scale using point sources in the field of view.

For the relic, the spectrum is approximately linear between 153 MHz and 1.4 GHz, with a spectral index of −1.17. This is similar to the value of −1.1 obtained by Orru' et al. (2007) between 325 and 1400 MHz.

The spectral index values are given in Table 6.2 for the halo and the relic.

ν (MHz)	UV-range (kλ)	Resolution ($''$)	S(H) (mJy)	LLS(H) (Mpc)	S(R) (mJy)	LLS(R) (Mpc)	rms (mJy/beam)
153	0−13	23	792	2.17	230	1.6	0.75
332	0−27	12	363	1.6	120	1.6	0.08
617	0−50	6	71	0.8	49	1.3	0.04

Table 6.1: The columns are: 1)Frequency of observation 2) UV-range in kilolambda 3)Restoring beam in arcsec 4)Flux Density of the halo, after subtraction of discrete sources 5)Largest Linear Size of the halo 6)Flux Density of the relic 7)Largest Linear Size of the relic 8)Noise in the image.

	α_{332}^{153}	α_{617}^{332}	α_{1400}^{617}	α_{1400}^{332}
Halo	−1	−2.63	−0.26	−1.28
Relic	−0.84	−1.44	−1.21	−1.31

Table 6.2: Spectral index values for the halo and relic in A2744 between frequencies 153 to 1400 MHz.

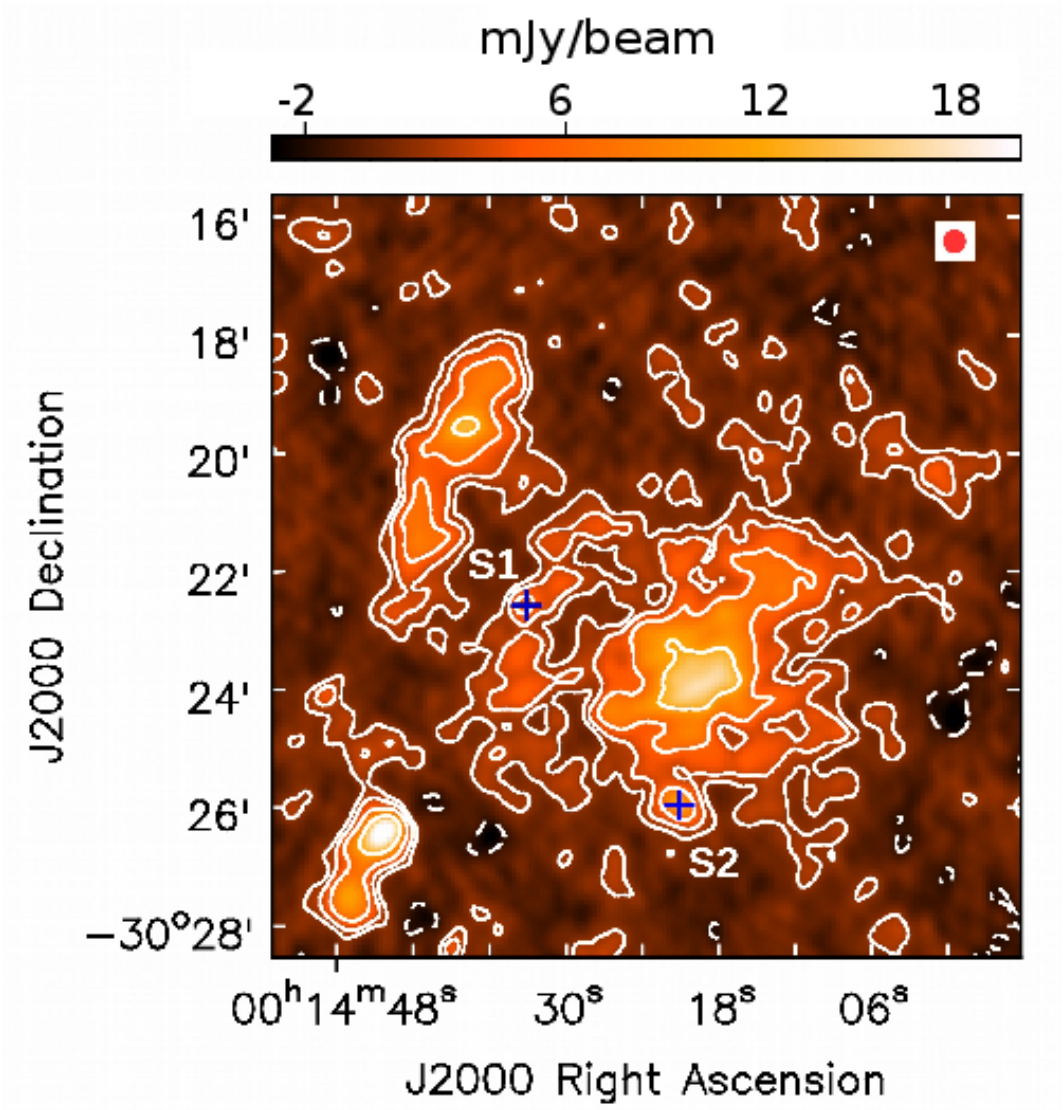

Figure 6.1: Radio stokes I image of the cluster A2744 at 153 MHz, showing the central halo and the north-eastern relic. The contours start at $+2\sigma = 1.5$ mJy/beam and then scale by a factor of 2. The beam has a resolution of $23'' \times 23''$ and is shown on top right corner of the image. The dashed contours represent -2σ level. S1 and S2 are two radio galaxies with active nuceli. S2 is a member galaxy of the cluster while S1 is a background object.

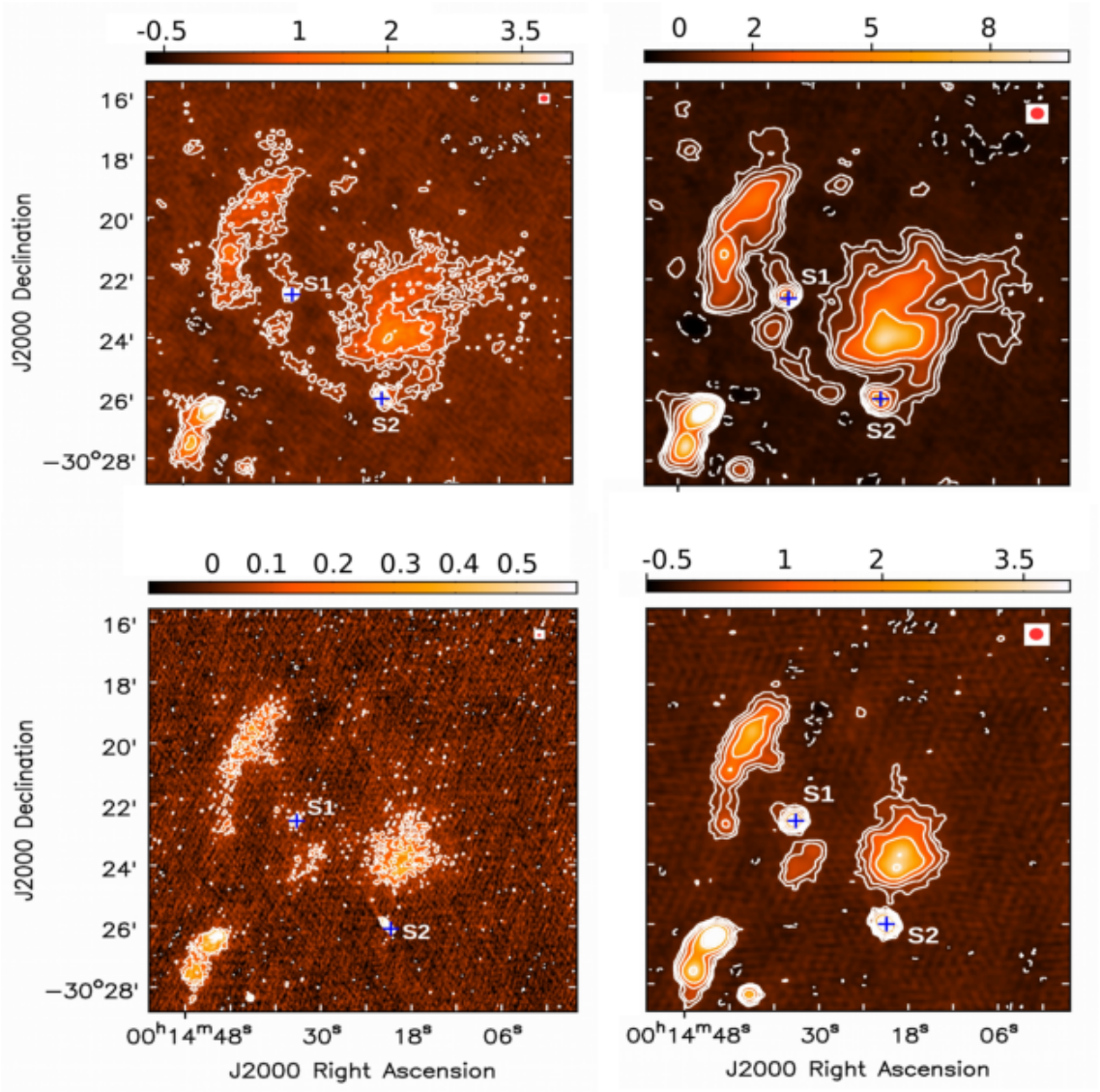

Figure 6.2: 332 and 617 MHz image of the halo A2744. *Top left*: 332 MHz image with a circular beam of 12″ resolution using the GMRT archival data. *Top right*: Low resolution (23″ × 23″) image of the halo at 332 MHz. The first contour is 0.24 mJy/beam (=3σ) and 0.3 mJy/beam (=3σ) in the two images and then scale by 2. 617 MHz image of the halo made at 6″ resolution (*Bottom left*) and 23″ resolution (*Bottom right*). Contour levels start at +3σ = 0.12 and 0.21 mJy/beam in the two images and then scale by 2. The −3σ level is shown as dashed contours in all the images and the colour scale is marked in mJy/beam. The source S2 appears as a head-tail source at high resolution.

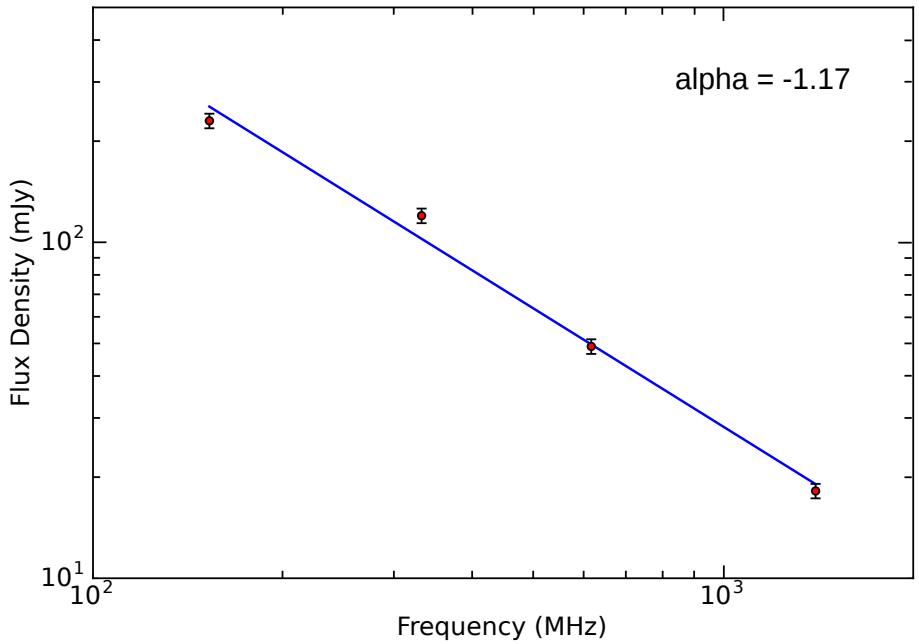

Figure 6.3: Integrated spectra of relic between 153−1400 MHz. A single power law slope of −1.17 fits the values.

6.1.3 Brightness distribution of Halo

The halo in A2744 shows a regular, centrally-peaked structure unlike the halo in A665. Figure 6.4 shows the average radial surface brightness profile in 8 concentric rings each of 25″ width, centred on the peak of the halo at 153 MHz (RA = 00h14m20.1s; DEC = −30d24′03″), up to the extent of the halo in the 23 arcsec resolution 617 MHz image. The discrete sources S1 and S2 were masked before calculating the brightness profiles. The error bars include both the calibration error (∼10%) and the image noise, added in quadrature.

The surface brightness falls of gradually from the peak to the periphery at all the frequencies. The brightness evens out beyond 510 kpc, which is approximately equal to the cluster core radius of 115″ (Govoni et al., 2001).

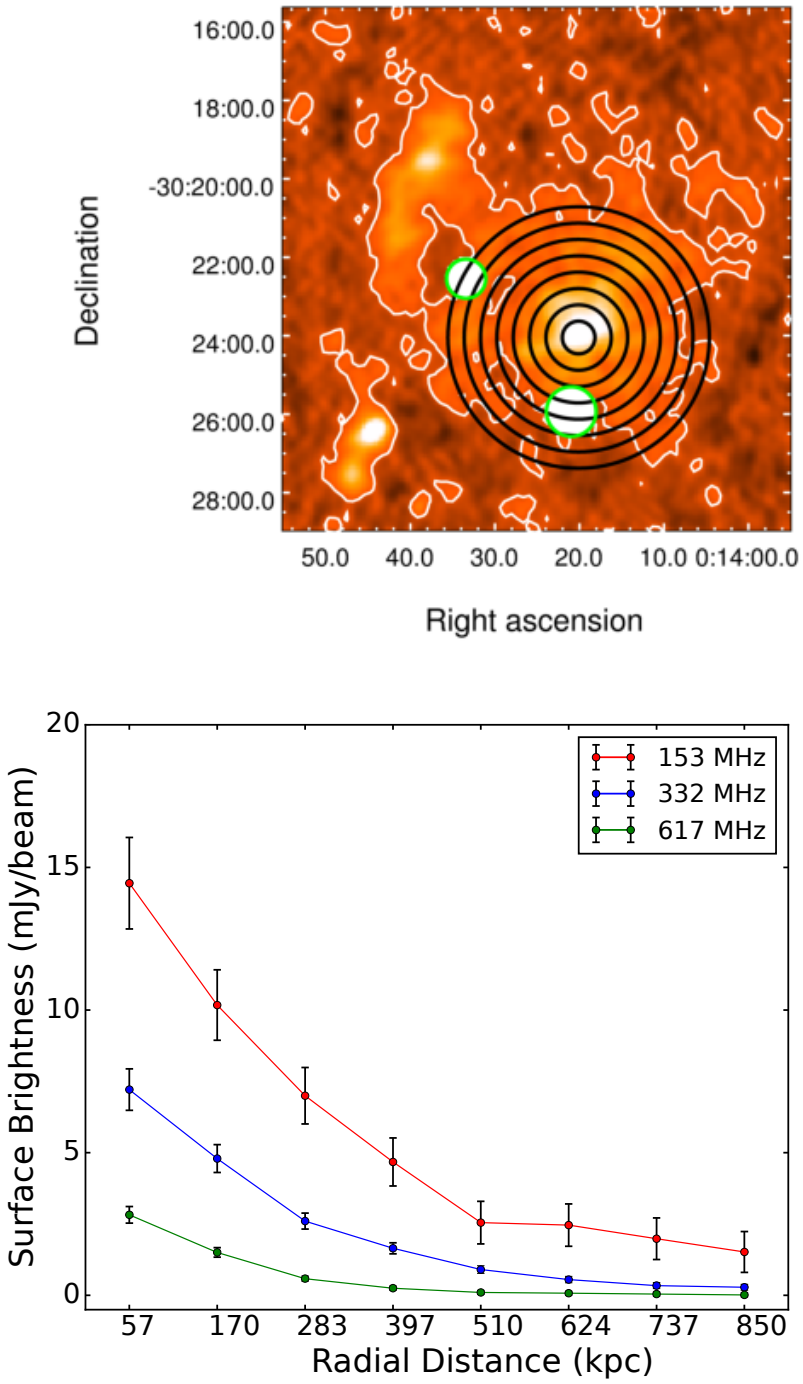

Figure 6.4: Radial brightness profile of the halo. *Top*: Concentric rings (black) of width 25 arcsec each centered on the halo peak at 153 MHz, that were used to extract the surface brightness profile at each frequency. Green circles denote the positions of discrete sources that were masked before obtaining the profiles. White contour denotes 1 mJy/b level. *Bottom*: Brightness as a function of radial distance from the central peak. The points are marked on the median of each ring. The halo shows a smooth decline in radial brightness at each frequency.

6.1.4 Spectral Index Images

Spectral index images were made between 153 and −332 MHz, 332 and −610 MHz and 153 and −610 MHz. We used images with a cell-size of 4.5″ and a UV-range of 130λ−13kλ at all frequencies for this purpose, which yielded images with a resolution of 23 arcsec, which is the native resolution at 153 MHz. The lower cutoff in UV-range was decided by the 617 MHz data while the higher cutoff is from the longest baseline at 153 MHz. The spectral index images are shown in Figure 6.5 and 6.6.

The 153−332 MHz spectral index image in Figure 6.5 shows two north-south structures of flat spectral index. The northern region with some pixels showing positive spectral index, consists of two separate components spanning ∼1.5 arcmin (mean $\alpha \sim -0.15$ and −0.2 for the two visible components). The inverted spectrum at these locations in the 332−617 MHz spectral index image (Figure 6.6), suggests the possibility of low frequency spectral turn-over due to synchrotron self-absorption or the presence of thermal plasma. The southern structure, which extends in south-west region, has a mean spectral index of about −0.8. The two are connected by a region of flattish spectral index of about −0.95. There is another isolated compact region of positive spectral index to the north-west. The radio 'bridge' between the halo and the relic has an average $\alpha \sim -1.7$.

Comparing the spectral index images between low and high frequencies, shows that images made with 153 MHz are similar (flat regions in north-south direction and south-west), although the 153−617 MHz image lacks the extent of halo as well as the detail. The image between 332 and 617 MHz shows a more regular structure, with a slight tilt of the central flat spectrum towards the north-west.

The relic seems to consist of two components along a north-south line. The southern part of the relic has a flatter spectrum ($\alpha \sim -0.86$) compared to the northern part ($\alpha \sim -1.35$) in the 153−332 MHz spectral index image (Figure 6.5). This is also seen in greater detail in spectral index images which use the 617 MHz data (Figure 6.6). The spectral index starts out with a flat spectrum ($\alpha \sim -0.7$) in a compact region at the southern tip of the relic, and gradually steepens to a value ~ -2 till about 2 arcmin to the north. This gradient changes sign further northwards with the spectral index increasing to a value −1.25 in the northern component. This northern component also shows a gradient in spectral index in the transverse direction, i.e. along the radial line connecting it to the halo centre. The steepening of the spectral index towards the halo centre is seen in the 153−617 and 332−617 spectral index images, and is also reported by (Orru' et al., 2007).

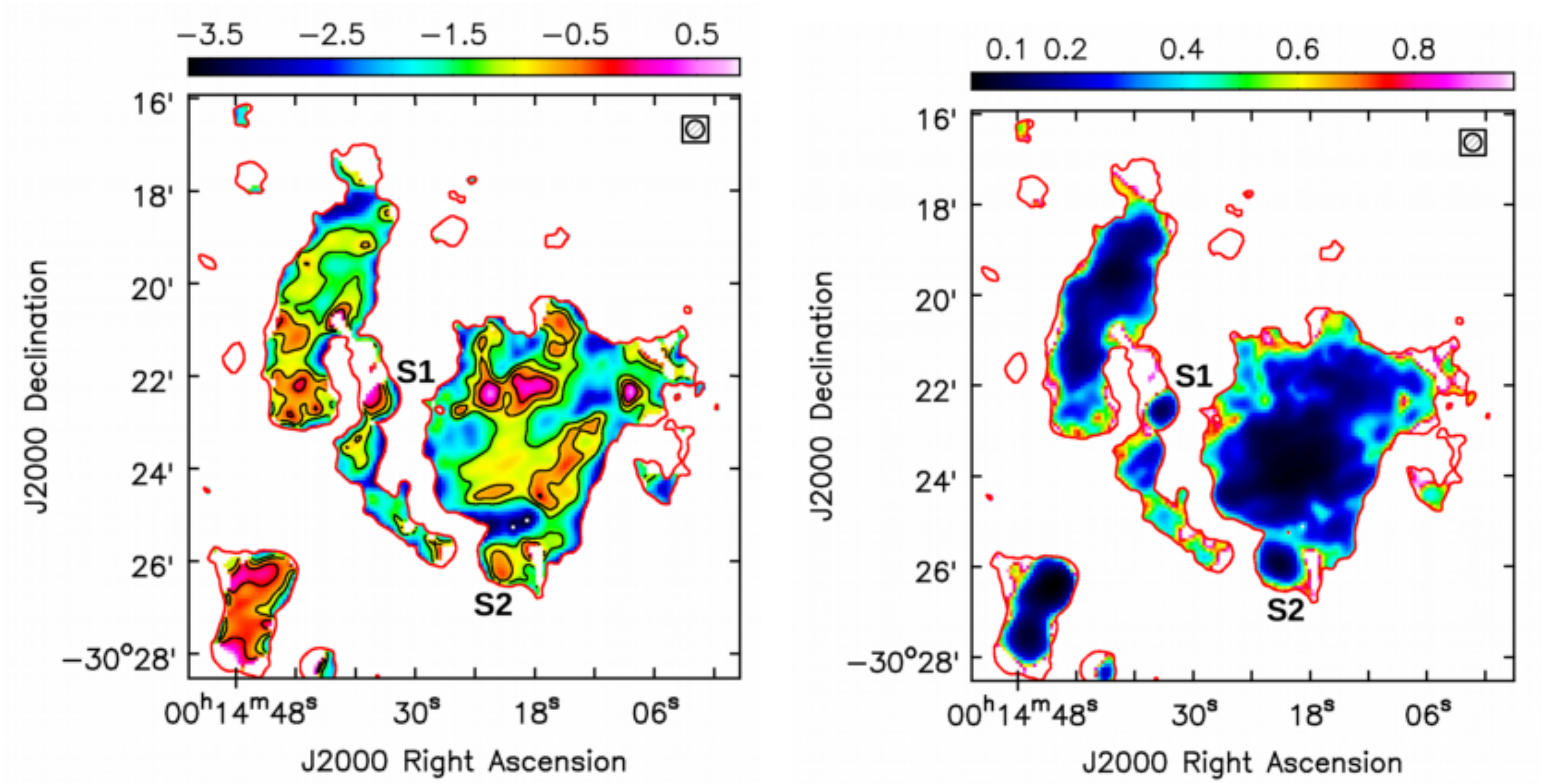

Figure 6.5: Spectral index image between 153 and 332 MHz made with 23″ resolution (*Left*). The black contours represent the spectral index values at −1.25, −0.75, and −0.25. *Right*: Spectral index error image. Errors are less than 0.1 in the inner regions of halo and relic and around 0.2 in most places. The outermost red contour in both the images denotes the 3σ contour from the low resolution image of 332 MHz (= 0.3 mJy/b).

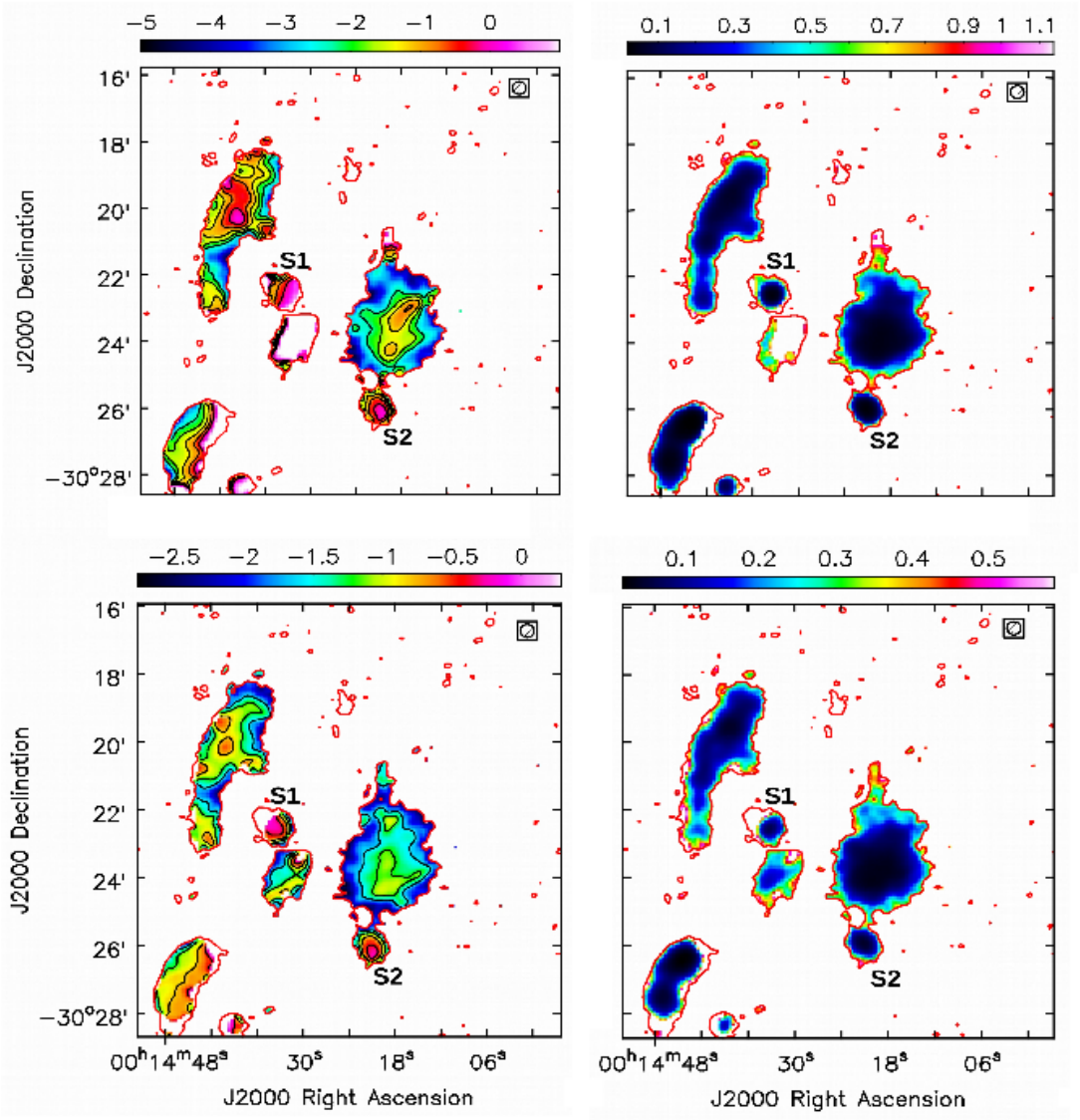

Figure 6.6: Spectral index image between – 332 and 617 MHz (*Top left*); 153 and 617 MHz (*Bottom left*). The right panels have equivalent error images. The resolution is 23″ in all the images. Black contour levels are −2.25, −1.75, −1.25, −0.75 and −0.25 (*Top left*) and −1.6, −1.2, −0.8 and −0.4 (*Bottom left*). Red outer contours denote the 617 MHz contour at 2σ (= 0.16 mJy/b) in all the images.

6.1.5 Comparison with Optical and X-ray

Optical

Figure 6.7 shows radio 153 MHz contours overlaid on the optical DSS image. The radio peak coincides with the optical density peak at the centre. In Figure 6.8 2-dimensional density contours of (optical) galaxies (Orru' et al., 2007) are plotted on the 153−332 MHz spectral index image. The density contours were made from optical spectrosopic and photometric observations of 102 cluster galaxies by Boschin et al. (2006). The optical density contours clearly show the presence of multiple subgroups, somewhat associated with the spectral index structures. Boschin et al. (2006) detected two major peaks in the 2D distribution of galaxies — one at the centre and one nearly 2.5′ north of it. The contours show the two major peaks in the north (NP) and centre (CP), and other peaks in the south-west (SWP) and to the north-west (NWP).

X-ray

Figure 6.8 shows Chandra X-ray brightness contours from Kempner and David (2004) overlaid on the 153−332 MHz spectral index image. The X-ray structure includes a global peak at the centre (XC) and significant compact peaks in the north, south and north-west (XN, XS and XNW).

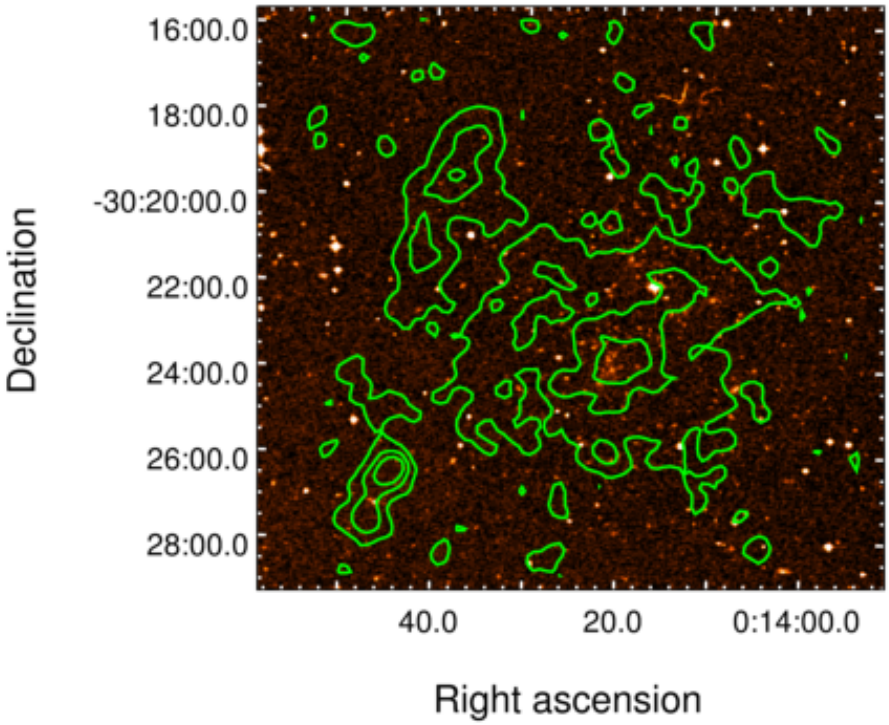

Figure 6.7: Radio contours at 153 MHz overlaid on the optical DSS plate. The contours are 1.5, 6 and 12 mJy/beam. The radio peak coincides with the optical density peak at the centre.

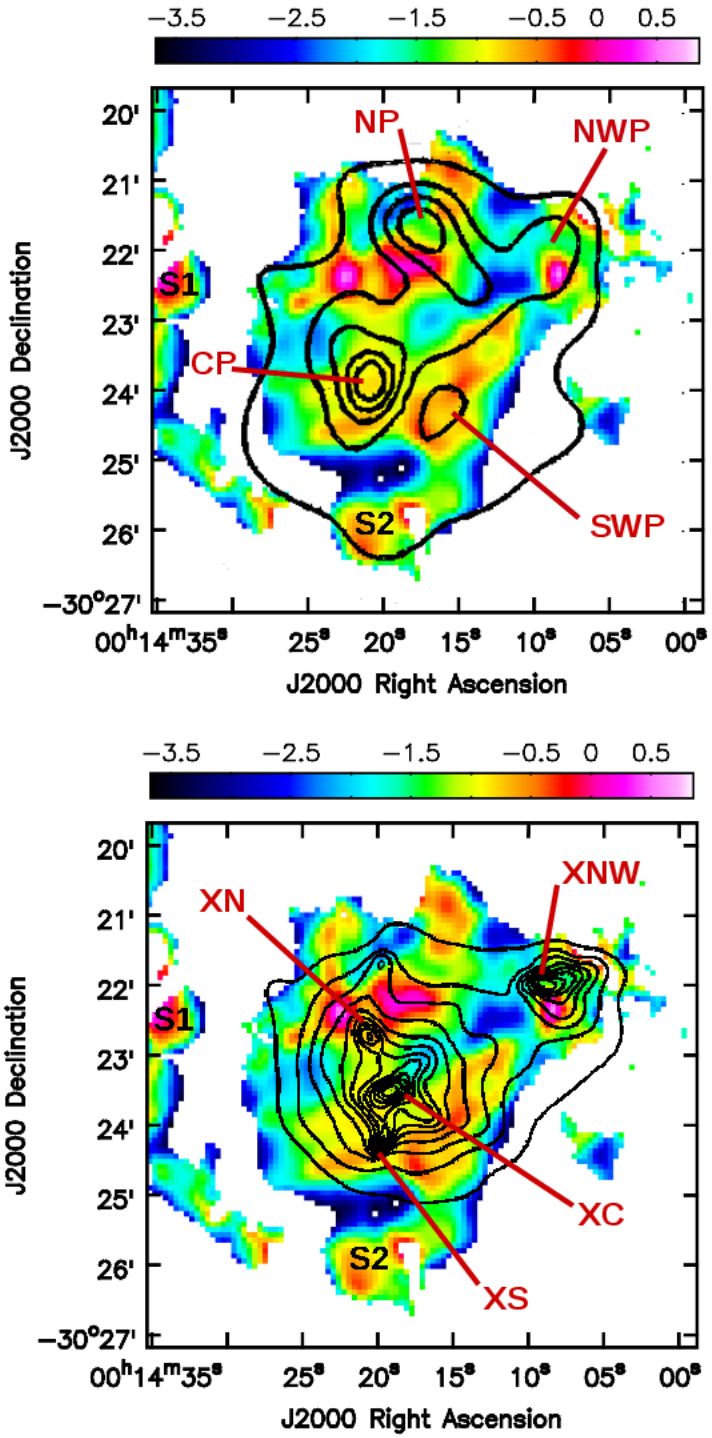

Figure 6.8: Colour map shows the spectral index image of the halo between 153 and 332 MHz. Overlaid are optical contours (*Top*) and X-ray contours (*Bottom*). The contours for both the images are taken from Orru' et al. (2007).

6.1.6 Transverse Gradient in the Relic

Eckert et al. (2016) detected a shock front approximately 1.5 Mpc away from the cluster centre, coinciding with the position of the relic. Such a process should lead to a gradient in the spectral index across the relic. We investigated this using a series of narrow rectangular boxes of dimensions $200'' \times 15''$ across the shocked section of the relic (Figure 6.9). The profile of mean surface brightness across the boxes is shown in Figure 6.9. We see a smooth increase and decrease in the intensity from inner to outer edge of the relic, at all the three frequencies (radial distances are calculated from the halo centroid at 153 MHz).

The spectral index across these boxes is shown in Figure 6.10. Since poor registration of images at different frequencies would lead to a gradient in spectral index we measured this effect using point sources in the vicinity of the halo-relic. The mean offset between the images was much lower than the size of a pixel (4.5 arcsec) in the spectral index images.

6.1.7 Equipartition Values

Using equipartition criteria, minimum energy density of 1.9×10^{-14} erg cm^{-3}, magnetic field of 0.46 μG and luminosity of 10.7×10^{42} erg s^{-1} is derived for the halo assuming a depth of 1500 kpc, measured surface brightness of 5.1 μJy/arcsec^2 at 153 MHz and spectral index of -1.01 between 153 and 332 MHz. For the relic, the derived quantities are 2.7×10^{-14}, 0.54 μG and 1.38×10^{42} erg s^{-1} (assuming a source depth of 1000 kpc, measured surface brightness of 5.4 μJy/arcsec^2 at 153 MHz and spectral index of -1.17 obtained from fit value). If instead cutoff in energy is assumed with γ_{min}=100, a magnetic field of 1 and 1.4 μG for the halo and the relic is obtained.

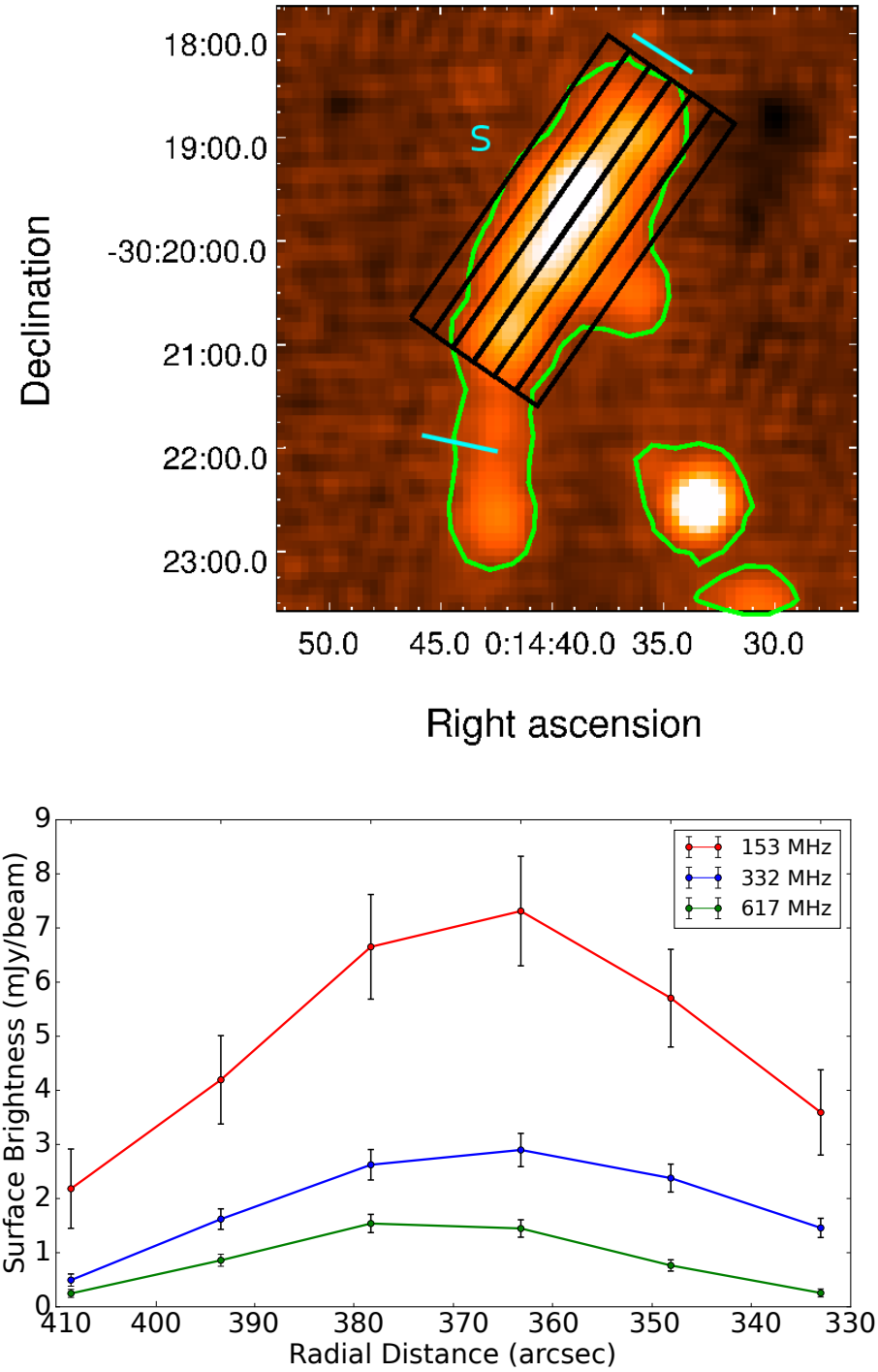

Figure 6.9: 617 MHz low resolution (23 arcsec) image of the relic (*Top*) showing the regions used to extract the brightness (Black boxes). Each box is $200'' \times 15''$ size oriented at 55 degrees angle. Green contour level is 0.21 mJy/beam. The cyan lines indicate the region used to extract shock jump conditions (Eckert et al., 2016). *Bottom*: Surface brightness profile of the relic at all the three frequencies. Error bars include 10 per cent assumed flux density uncertainty and image noise. The distances are calculated from the halo centroid at 153 MHz (RA: 00h14m18.48s; DEC: -30d23′21.5″).

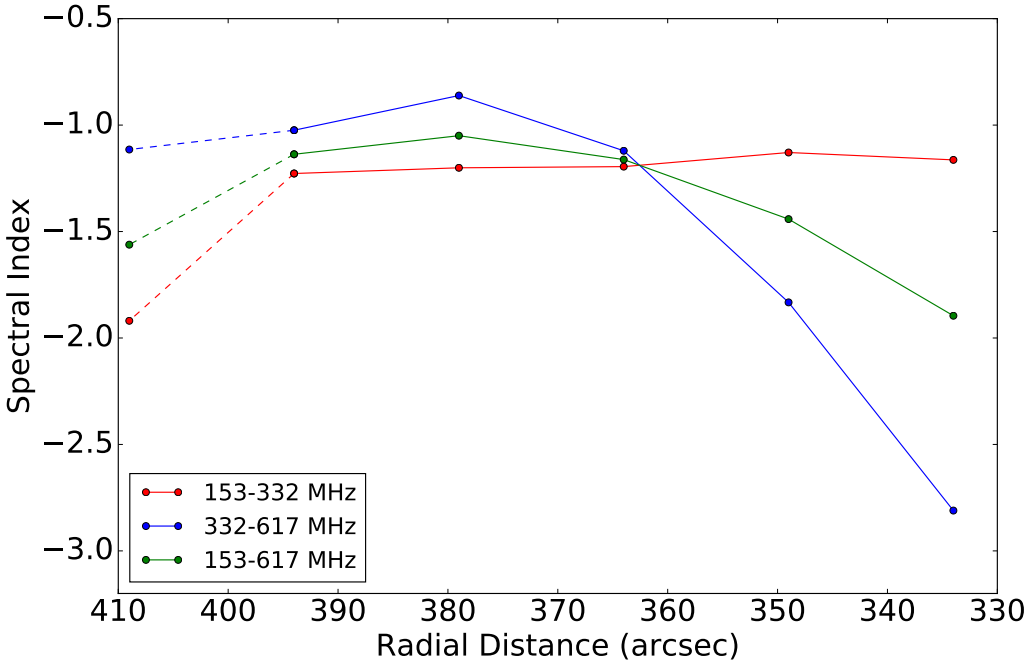

Figure 6.10: Spectral index trend of the relic between different frequencies. The boxes used to extract the profiles are same as in Figure 6.9. The dashed line in all the plots represent the outer relic edge. Radial distance is calculated from the halo centroid. The spectral steepening towards the cluster centre is visible in the plots made with the 617 MHz image.

6.2 Discussion

6.2.1 The Relic

Shock acceleration of electrons from thermal plasma is possible via DSA mechanism (Ensslin et al., 1998; Roettiger et al., 1999; Hoeft and Brüggen, 2007). Cluster merger shocks are generally weak, even in the cluster outskirts where temperature is less (Ryu et al., 2003; Vazza et al., 2009;). Simulations suggest that such weak shocks are inefficient to accelerate electrons from the thermal pool (Kang et al., 2012; Pinzke et al., 2013). On the other hand, a pre-existing population of mildly relativistic electrons may be effectively re-accelerated by weak shocks to the levels needed to explain the observed relic brightness.

X-ray observations with *XMM-Newton* and *Suzaku* detected a weak shock front of Mach number 1.7 (velocity of 2000−2800 km/s) at the location of the relic (Eckert et al., 2016). The pre- and post-shock gas temperatures were estimated to be about 4.6 and 12.3 keV, respectively. The expected spectral index corresponding to the X-ray Mach number should be a good approximation to the value of the spectral index at injection of the synchrotron electrons, for plane-parallel shocks. The Mach number of the shock in the relic from the radio spectral index $\alpha = -1.17$ is 2, which is a little higher but consistent with X-ray Mach number. On the other hand, we know that the telescope resolution is much coarser than the width of the shock front, and therefore the smoothed out observed emission from the vicinity of the shock front would in general have a spectral index that is steeper than the injection spectral index by about 0.5. Therefore, radio observations suggests $\alpha_{inj} = -0.67$ which corresponds to a Mach number of 3.6, which is much higher than the X-ray value. The derived X-ray Mach number of 1.7 would actually require the integrated relic spectral index to be as steep as -2.0, which is much higher than the typical value for these sources. Eckert et al. (2016) favoured the re-acceleration of fossil electrons by the passage of shock front over DSA of fresh electron population for the relic in A2744. We confirm the discrepancy that they highlighted between the Mach numbers from the X-ray and the radio observations. Such a discrepancy is also observed in other relics, for instance in the 'Toothbrush' relic (Ogrean et al., 2013; van Weeren et al., 2016), and may be a result of mixture of Mach numbers of shocks (Skillman et al., 2013). The radio derived Mach number would then be more sensitive to high Mach number (Hoeft and Brüggen, 2007). Another possibility is the re-acceleration of pre-existing population of electrons by the shock front.

Enßlin and Gopal-Krishna (2001) discussed the possibility of adiabatic compression of fossil radio plasma as a mechanism for relic emission. This is a five step model consisting of: 1) injection by a radio galaxy, 2) expansion of the radio cocoon when it becomes undetectable, 3) the "lurking"-phase when pressure equilibrium is reached and the volume of the cocoon remains constant, 4) adiabatic compression of the cocoon when the radio emission is boosted so it becomes visible again. The break frequency shifts to higher frequencies during this time, and finally 5) the radio emission fades away due to synchrotron and IC losses.

Even fossil radio plasma as old as 2 Gyr can be revived by adiabatic compression

from cluster shocks. The change in the break frequency from the adiabatic compression is (Giacintucci et al., 2008)

$$\frac{\nu_b^{post}}{\nu_b^{pre}} \approx \frac{5M^2 - 1}{4}$$

For the shock with Mach number 1.7, the break frequency would shift by a factor 3. Adopting a value of 100 MHz as the break frequency of fossil radio plasma, it should result in a break frequency in the re-energised plasma (i.e. the relic) at about 300 MHz, which is not observed. A spectral break beyond 1.4 GHz, which is the highest frequency for which we have data, would need a Mach number greater than 3.4. This is consistent with the previous discussion wherein the radio spectral index suggests a much higher Mach number of ∼3.6 than the X-ray value. A curved integrated radio spectrum is predicted in this case, showing a steepening at high frequency. We do not have high frequency observations to distinguish which process is at work.

Figure 6.10 shows that along the (radially) outer edge of the relic the 153−332 MHz and 332−617 MHz spectral indices are much closer to each other than on the inner edge. This suggests that the electrons on the inner edge are older. This is consistent with the relic being formed by a radially outward travelling shock; in such a situation the acceleration happens at the front, and therefore the outer edge should have a flatter and a more linear spectrum across the frequency range. The synchrotron radiation on the inner edge would arise from electrons swept downstream; these older electrons should have a steeper spectrum, especially at the higher frequencies.

At cluster periphery, where relics are generally located finding a seed population of high energy electrons is a problem. Old lobes of dead radio galaxies may supply the seed population, which may get re-energised by shock. However, the link between the radio source associated with an AGN and a relic has been observed in a few cases. An example of a relic which appears to be connected to a radio galaxy is PLCKG287.0+32.9 (Bonafede et al., 2014). The association is also confirmed by spectral index images. However, no optical counterpart was found at the position of the radio galaxy core. van Weeren et al. (2017) detected a cluster AGN whose radio lobes were connected to the relic in Abell 3411-3412. The spectral index image showed a clear steepening from the nucleus outwards till the edge of the relic, beyond which the spectral index flattened again. In addition, a steepening of spectral index across the relic towards the cluster centre, expected from shock acceleration, was also observed. This study provided a direct evidence of an AGN supplying seed electron population for a relic. Yet another example is the relic in the Coma cluster which also had an associated AGN located nearby (Giovannini et al., 1991).

The transverse gradient in the spectral index as well as the pattern of spectral index along the relic in A2744 is similar to that expected when radio lobes are involved in the formation of a relic (Figures 6.6 and 6.10). However, the DSS optical image does not reveal an AGN in that location, nor do the radio images identify the core with any degree of certainty. As the relic is located in the cluster outskirts, this region is not covered by Subaru (Medezinski et al., 2016). New and deeper observations in the radio and optical will be required to detect the radio source host galaxy if such is responsible

for the creation of the relic.

We can estimate the shock acceleration efficiency in the section of the relic where shock front is strongly detected. We make use of the shock parameters and radio luminosity. The acceleration efficiency (η) is defined as the fraction of kinetic energy flux across shocks (ΔF_{KE}) that is dissipated into the acceleration of electrons. The flux of kinetic energy dissipated in the shock is given by (Finoguenov et al., 2010)

$$\Delta F_{KE} = \frac{1}{2}\rho_1 V_{sh}^3 \left(1 - \frac{1}{C^2}\right)$$

where, ρ_1 is the pre-shock mass density of the gas, V_{sh} is the shock velocity and C is the compression ratio of the shock. We obtain ρ_1 from pre-shock electron density n_1 = 9.5×10^{-5} cm^{-3} and assuming a mean molecular mass of 0.6, V_{sh} = 2000 km/s and C = 1.9 (Eckert et al., 2016). This gives ΔF_{KE} = 2.7 ×10^{-4} erg cm^{-2} s^{-1}. Assuming the area of the shock to be a circle with diameter equal to the length of the relic where shock front is strongly detected (= 1 Mpc), gives 0.8 Mpc^2. The rate of dissipation of energy at the shock front is given by dE_{KE}/dt = 1.98×10^{45} erg s^{-1}.

We obtain the luminosity of the relic from equipartition values. We adopt 1.4 μG magnetic field and an IC contribution of B_{CMB} = 5.56 μG. The synchrotron and IC luminosities are related by $L_{IC} = L_{syn}\,(B_{CMB}/B)^2$. This gives a total luminosity of 6.8×10^{43} erg s^{-1} for $\alpha_{inj} = -0.67$. Therefore, an acceleration efficiency $\left(\eta = \frac{L_{tot}}{dE_{KE}/dt}\right)$ of 3.4% is obtained. Electron acceleration efficiency by weak merger shocks is not yet fully understood, yet, less than a few percent of the shock energy flux is expected to be transferred to freshly injected CR protons from thermal pool (Brunetti and Jones, 2014). The efficiency is less than 1% for fresh injection of electrons. The required efficiency will increase even further for smaller magnetic field values. The high acceleration efficiency required indicates that DSA is not a viable option. Our estimates are consistent with some other estimates for relics (Botteon et al., 2016; van Weeren et al., 2016), and favour re-acceleration by shock.

The 'bridge' of emission connecting the halo and the relic may be attributed to the turbulence generated behind an outward moving shock. Simulations suggest that turbulence is generated in the post-shock region (Paul et al., 2011). Similar bridge is observed between the Coma cluster radio halo and relic (Brown and Rudnick, 2011). A radio bridge is also seen in A3667 connecting the NW relic to the cluster centre. This bridge of unpolarized synchrotron emission was also found to be coincident with a diffuse X-ray tail, and is thought to be related to the post-shock turbulence trailing the outward going relic shock (Carretti et al., 2013).

6.2.2 The Halo

Halos usually display a variety of morphologies – some are centrally peaked, like Coma (Brown and Rudnick, 2011), while some show assymetric or "clumpy" distribution, e.g. RXC J2003.5−2323 (Giacintucci et al., 2009). The different morphologies may be a result

of different merging scenario or stages of individual clusters, distribution of magnetic field, etc. Here, we see a smooth radial decline in the intensity of the halo (Figure 6.4). The peak of the halo emission is at the optical galaxy density peak (Figure 6.8). This is similar to the situation in the case of A2163 and A665 (Chapter 4 and 5).

Optical spectroscopy revealed two central groups of galaxies in the cluster, with a mass ratio of 3:1 and mean velocity difference ~ 4000 km s^{-1} (Boschin et al., 2006). The main group is distributed over the entire cluster, and smaller one is mainly concentrated to the south and south-west. The authors proposed a merging scenario in which the cores of the two groups have crossed each other. The merging axis is roughly along the N-S direction. There is also a minor substructure in north-west which is apparently moving from west to east. Owers et al. (2011) using deeper Chandra data and a larger spectroscopic sample, associated the main galaxy group with the northern peak detected in 2D optical analysis (NP). The peak at the centre is due to the apparent superposition of the main group and the secondary group (S/SW subcluster detected in 1D) as a result of projection i.e superposition of corresponding NP and SWP in 2D. They also proposed a merging scenario where two substructures have undergone a violent core passage and are now moving away from each other roughly along north-south direction with a large LOS component.

X-ray observations show the presence of two compact cores, associated with the galaxy groups to the north and the south, as well as a central, much higher peak (Kempner and David, 2004; Owers et al., 2011). This also suggests a north-south motion of the two galaxy groups after core passage. The X-ray peak at the centre may be due to the stripped gas of the two merging subclusters. This usually happens as the gas forms a collisional system and is dragged behind the galaxy motion. A possible shock front with Mach number 1.41 southeast of the southern compact core was suggested by Owers et al. (2011), which also coincides with a radio edge in the halo Giacintucci (2011).

The north-western substructure (NWP) is moving in N/NE direction and is believed to be an interloper (Owers et al., 2011).

Unlike in the case of A2163, the spectral index image for A2744 lacks a central dominant feature. However, we find a northern and a southern ridge of flatter spectral index corresponding to the northern and southern galaxy groups which have been implicated in the cluster merger in A2744. There is also a narrow ridge of flatter spectral index which links these two radio structures. This is at the location of the central peak, which as we have discussed is the superposition of the northern and southern galaxy groups, and may have been the site of the merger before the groups moved away from there to their present position. The north-western interloper also has a flat spectrum structure associated with it. However, we do not see an exact coincidence between the radio spectral index and optical structures. But such offsets between the radio and the optical has been noticed before (Feretti et al., 2010), and may be an indication of a system which has yet to dynamically relax.

This association of flat spectrum regions with optical and X-ray structures was not reported in Orru' et al. (2007) or Pearce et al. (2017). Although, Orru' et al. (2007) did point-to-point comparison of the spectral index image with the X-ray temperature image and found that flatter spectral index is associated with higher temperature values and

vice versa. However, Pearce et al. (2017) did not find evidence of correlation between flatter spectral index features and ICM temperature in their high frequency study.

According to turbulent re-acceleration model, spectral index features should be varying according to variations in magnetic field and turbulent energy dissipated across the halo. In optically over-dense regions, perhaps the motion of group of galaxies give rise to greater energy being dissipated via turbulence or shocks; and therefore, a connection between flatter spectrum regions and location of galaxy groups is observed. The morphological connection in our observations support the idea that a fraction of the gravitational energy, which is dissipated during merging process is converted into re-acceleration of relativistic particles and amplification of the magnetic field.

Chapter 7

Spectral index imaging of Radio Halo A520 and A773

The cluster A520 lies at a redshift of 0.199 (1″= 3.287 kpc). The first detection of diffuse emission at the centre of the cluster was by Giovannini et al. (1999) from the NVSS survey. This was later confirmed by Govoni et al. (2001) using deeper VLA observations at 1.4 GHz. A radio halo showing NE-SW extension with a maximum size of 1.4 Mpc along this direction was observed. The halo was found to be elongated in the same direction as the central X-ray emission. Vacca et al. (2014) constructed a spectral index image of the halo using VLA observations at 325 and 1400 MHz.

The presence of a radio halo in A773 was suggested by Giovannini et al. (1999) based on the NVSS image. It was later confirmed by Govoni et al. (2001) at 1.4 GHz. They reported a halo of size 6′ (1.6 Mpc) at the cluster centre. The X-ray image of the cluster shows an elongated core, possibly due to two peaks (Rizza et al., 1998).

7.1 Results – A520

7.1.1 Radio Images

I present the total intensity and spectral index images from GMRT observations at 147 and 322 MHz. We also attempted to image the archival GMRT data observed at 240 and 610 MHz (P.C 15MAB01). Even after several rounds of imaging and calibration, the image did not improve much and therefore not presented here.

Figures 7.1 and 7.2 show the total intensity images at 147 and 322 MHz. The central diffuse region is the halo. It is surrounded by many radio galaxies of which the strongest are two narrow angle tailed (NAT) sources to the east (marked D and E), and another source to the North (marked C) – possibly a head-tail source. Another radio source B, possibly a double-lobed source, is also superposed on the halo.

At 147 MHz (22″ resolution), the maximum size of the halo is 6 arcmin (1.18 Mpc) along the NE-SW direction. The width of the halo is approximately 3 arcmin (592 kpc) along E-W direction. The halo has a sharp ‘edge’ in the south-west, which is coincident

with a 'bow-shock' (Govoni et al., 2004; Markevitch et al., 2005; Wang et al., 2018). A ridge of high intensity, which is in fact one of the two brightest regions of the halo, starts just behind this 'edge' and extends for about 1.5 arcmin. The other bright region is located in the north-eastern region (between the sources marked C and D). There is a possibility of a counter shock in the north-east region (Wang et al., 2016). Unlike in the case of A2744 and A2163, the halo is not peaked at the centre. In fact, the surface brightness at the centre is lower than the rest of the halo.

At 323 MHz, the largest extent of the halo is 5 arcmin (986 kpc) in NE-SW direction. This is considerably bigger than the previous image at this frequency (Vacca et al., 2014). The features described in the 147 MHz image are also visible at this frequency.

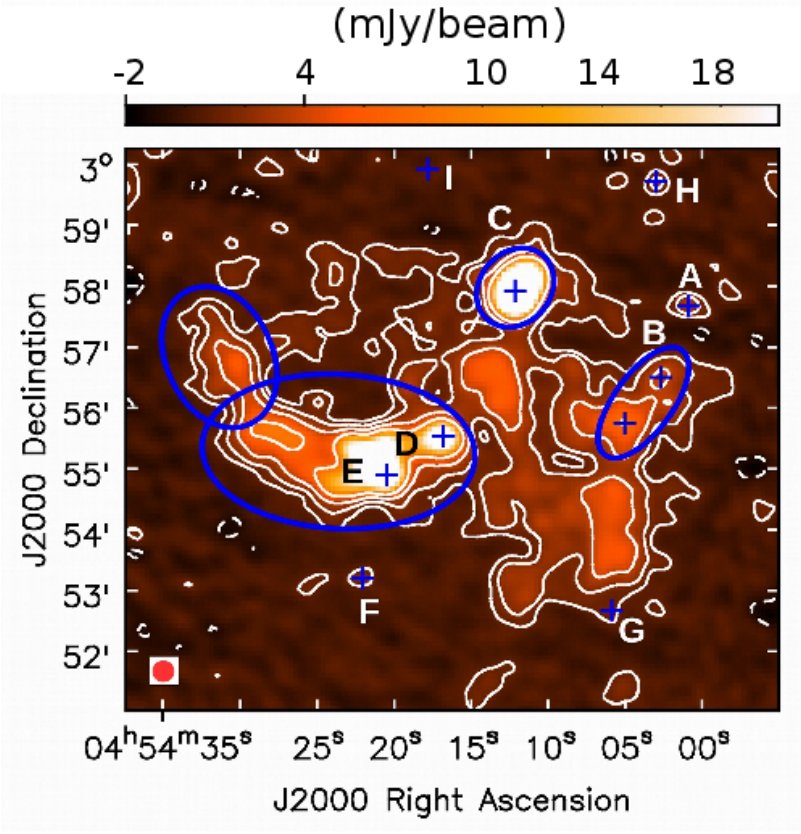

Figure 7.1: 147 MHz image of the halo A520. Contours start at 0.9 mJy/beam and then scale by a factor of 2. The beam size is 22 arcsec. Unrelated discrete sources are marked A−I.

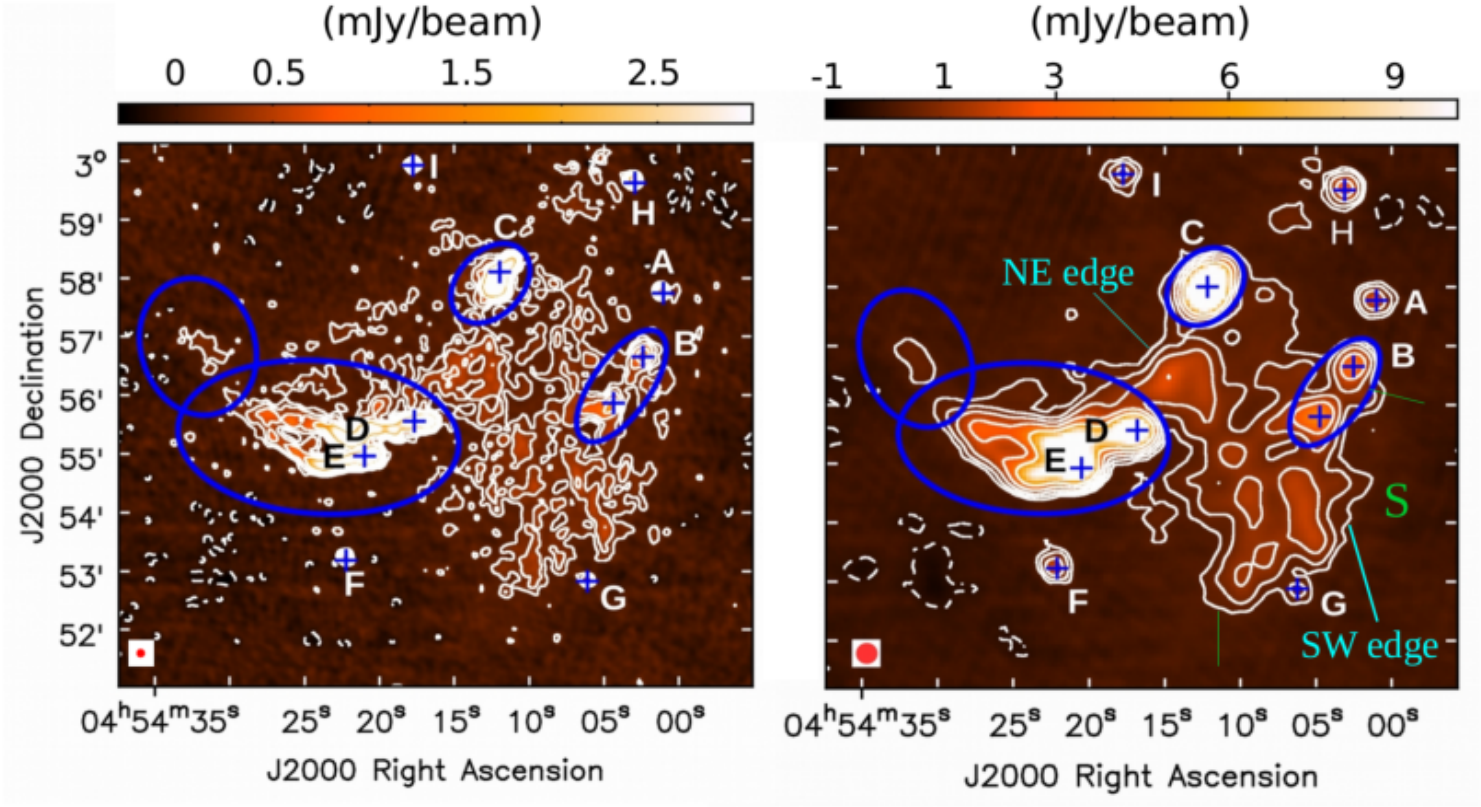

Figure 7.2: 322 MHz image of the halo made at its own resolution of 9″ (*Left*) and with 22″ (*Right*). Contours start at 0.15 mJy/beam (=3σ) and 0.3 mJy/beam (=3σ) and scale by a factor of 2. The −3σ level is shown as dashed contours. Unrelated discrete sources are marked A−I. Green lines mark the region where shock front 'S' is detected (Markevitch et al., 2005; Wang et al., 2018).

7.1.2 Flux Density and Integrated Spectral Index

The flux density of the halo is 217 mJy and 119 mJy at 147 and 322 MHz respectively, excluding all the embedded discrete sources. The flux density measured at 322 MHz is higher than that measured previously (= 85 mJy; Vacca et al. (2014)), which is due to a larger area of halo emission in our image. Table 7.1 summarizes the details of the halo. The integrated spectral index calculated within the same area at the two frequencies is -0.76, which is much flatter compared to the usual values of the spectral index for the halos. The spectral index estimated between 325 and 1400 MHz is -1.12 (Vacca et al., 2014).

ν (MHz)	UV-range (kλ)	Resolution ($''$)	S (mJy)	LLS (Mpc)	rms (mJy/beam)
147	0−13	22	217	1.18	0.4
322	0−27	9	119	0.98	0.05

Table 7.1: The columns are: 1)Central frequency of observation 2)UV-range in kilo-lambda 3)Restoring beam in arcsec 4)Flux Density of the halo, after subtraction of discrete sources 5)Largest Linear Size of the halo 8)Noise in the image.

7.1.3 Brightness Profile of the halo: The SW and NE radio 'edge'

We extracted the brightness profile of the halo along the NE-SW extent, avoiding the neighbouring radio galaxies, using boxes of length $1.5'$ and width equal to beam size, and oriented at 70 degrees (Figure 7.3). The profile clearly shows the brightness peaks near the NE and SW edges. These peaks are much more prominent at 147 MHz.

The SW edge of the halo which is coincident with a shock front, has been extensively studied (Markevitch et al., 2005; Wang et al., 2016, 2018). The radio edge visible in our images coincides with the region with the highest shock Mach number of 2.5 for the halo Wang et al. (2018).

Figure 7.4 shows the profile along a horizontal cross-section of the halo which includes the south-western peak. It shows that the intensity falls from the highest in the halo to almost the lowest within one beam width.

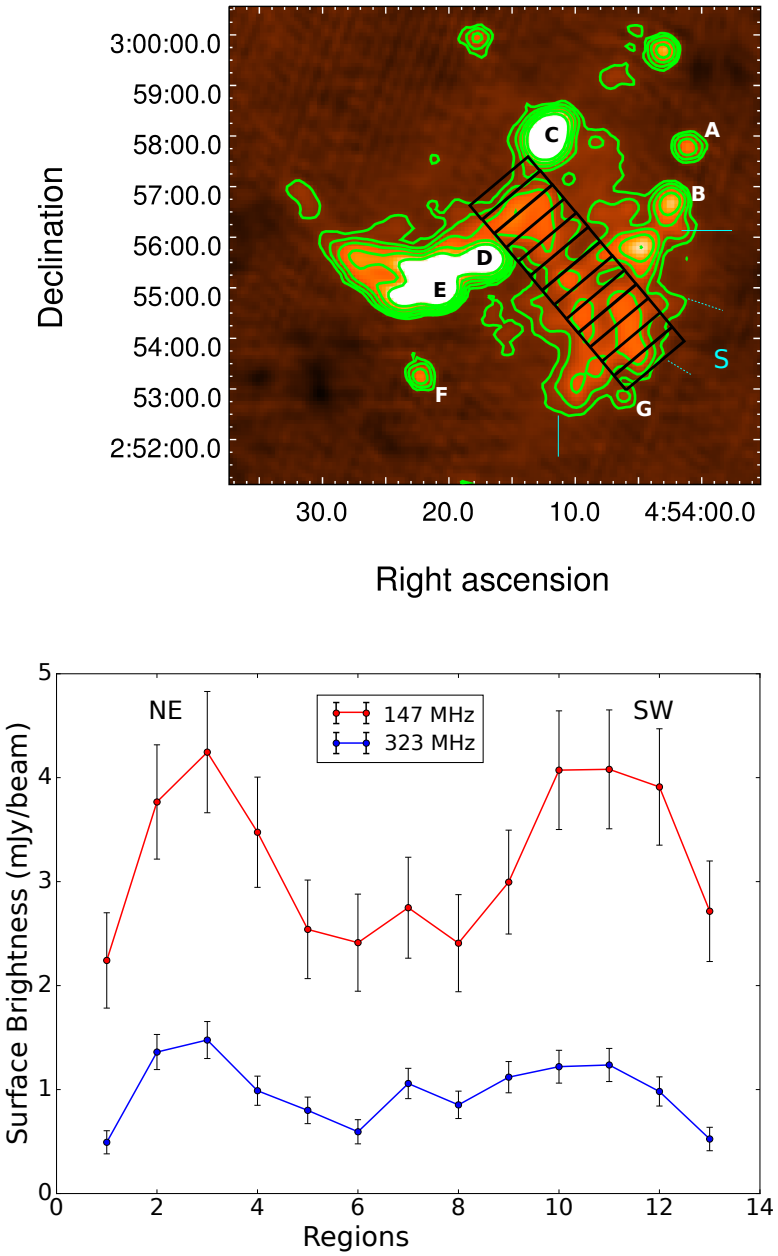

Figure 7.3: 323 MHz-22 arcsec resolution image of A520 showing the regions used to extract the brightness profile of the halo (*Top*), and the profile (*Bottom*). The green contours are same as in Figure 7.2. The north-east and south-west edges of halo are clearly peaked at both the frequencies, especially at 147 MHz. Cyan lines mark the region where shock front is detected; dashed cyan lines mark the region where the shock jump was highest (Markevitch et al., 2005; Wang et al., 2018).

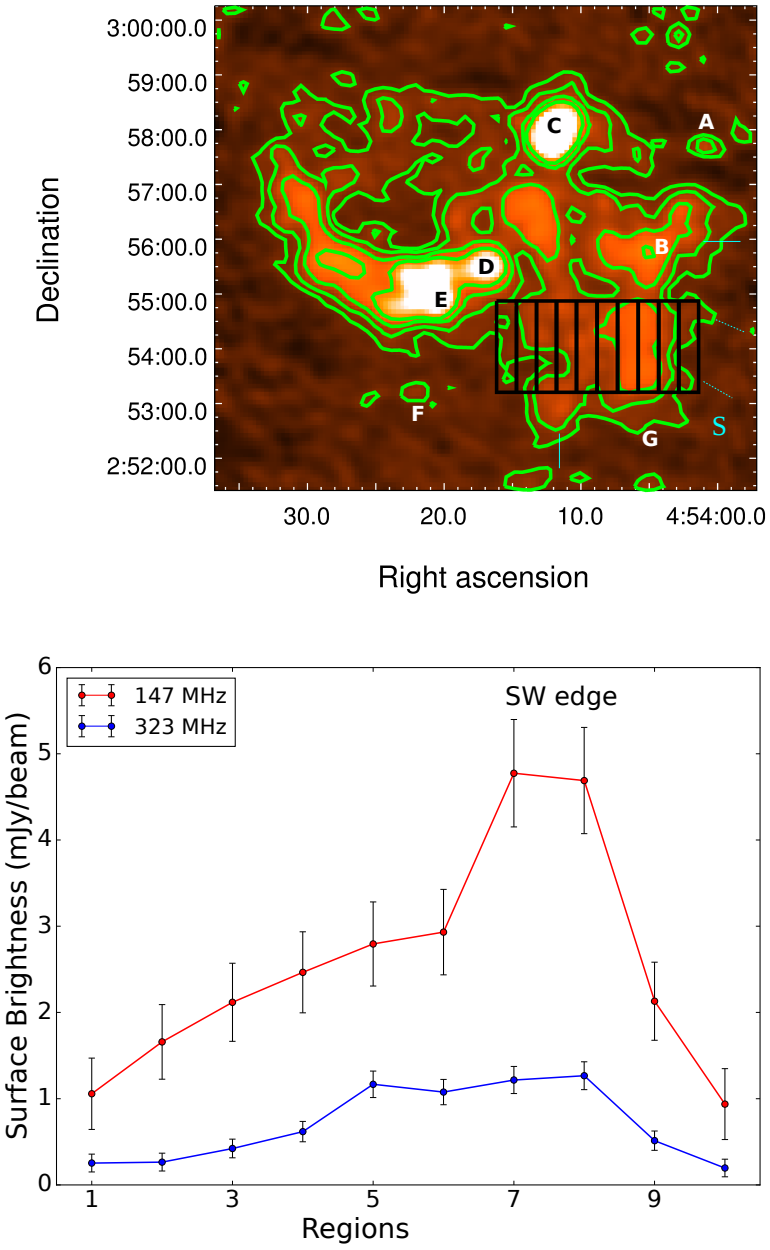

Figure 7.4: 147 MHz-22 arcsec resolution image of A520 showing the regions used to extract the brightness profile of the halo in the horizontal direction (*Top*), and the profile (*Bottom*). The green contours are same as in Figure 7.1. The peak near the south-west edge is clearly visible at 147 MHz. Cyan lines mark the region where shock front is detected; dashed cyan lines mark the region where the shock jump was highest (Markevitch et al., 2005; Wang et al., 2018).

7.1.4 Spectral Index Image of halo

Figure 7.5 shows the 147−322 MHz spectral index image made with 22″ resolution and 4.5″ cell-size. Pixels below 2σ at both the frequencies were blanked before constructing the image. The discrete sources adjacent to the halo are not masked.

The spectral index image shows narrow filaments of flat spectrum regions running across the halo. The spectral indices of these filaments are in the range −1.0 to −1.4. The south-western 'edge' seen in radio images (and coincident with the shock front) does not have an equivalent flat spectrum structure in the spectral index image. It has an average spectral index of -1.75 ± 0.3. The elongated south-western brightness peak has a corresponding "flatter" spectrum filament associated with it, though its spectral index is not the flattest in the halo.

Figure 7.6 shows the spectral index profiles along the (boxed) regions shown in Figures 7.3 and 7.4. The NE region shows a spectral index flattening ($\alpha = -1.3$), while no flattening is observed in the SW bright region ($\alpha = -1.6$). The gradient in spectral index expected from two outward going shocks and from two peaks observed in the radio images, is not obvious in the spectral index image.

7.1.5 Equipartition values

Using the equipartition criteria, we estimated a minimum energy density of 1.1×10^{-14} erg cm^{-3}, magnetic field of 0.35 μG and luminosity of 6.1×10^{41} erg s^{-1} for the halo, assuming a depth of 700 kpc, measured surface brightness of 2 μJy/arcsec^2 at 147 MHz and spectral index of −0.76. Assuming a cutoff in electron energy (γ_{min}=100) instead of critical frequency, yields a magnetic field of 0.57 μG.

7.1.6 Comparison with Optical and X-ray

Figure 7.7 shows the Chandra X-ray brightness contours (Chandra archive ObsID 9430) superposed on the 147−322 MHz spectral index and 322 MHz total intensity images, respectively. The letters on the image show the location of the individual radio sources, as mentioned before. The 323 MHz radio contours are overlaid on the DSS image. The numbers show the location of the peaks in optical galaxy density (Girardi et al., 2008). The optical peaks are also confirmed by weak-lensing analysis of the cluster (Mahdavi et al., 2007; Okabe and Umetsu, 2008; Jee et al., 2012; Clowe et al., 2012).

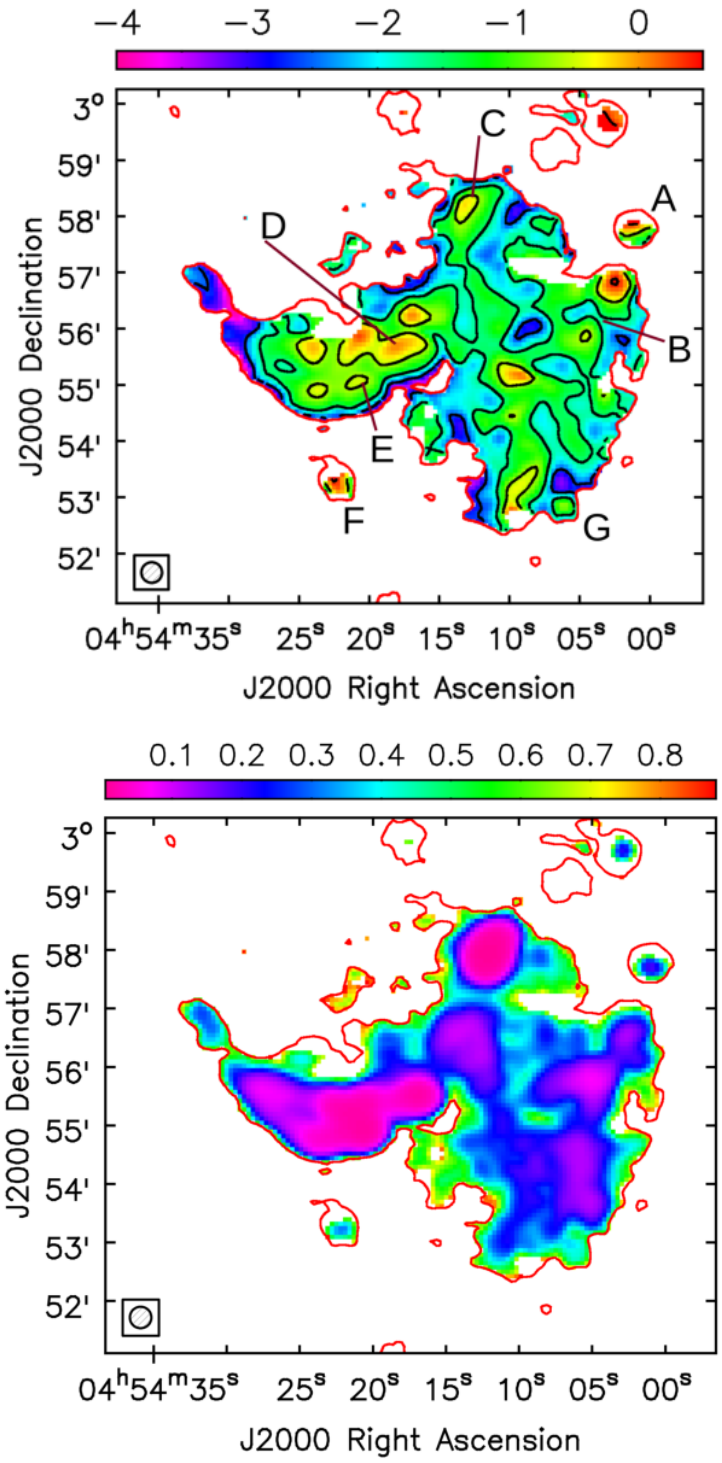

Figure 7.5: Spectral index image of the halo between 147 and 322 MHz (*Top*). The discrete sources are marked A−I. Sources B−E and G lie adjacent to the halo and are not masked. The spectral index of NAT sources D and E show a gradient as expected. Black contours denote the spectral index values at −2.6, −1.6, −0.6 and 0.4. *Bottom*: Spectral index error image. The NE and SW peaks of halo have errors less than 0.1. Outer red contour in both the images denotes the 2σ level at 322 MHz (= 0.2 mJy/b).

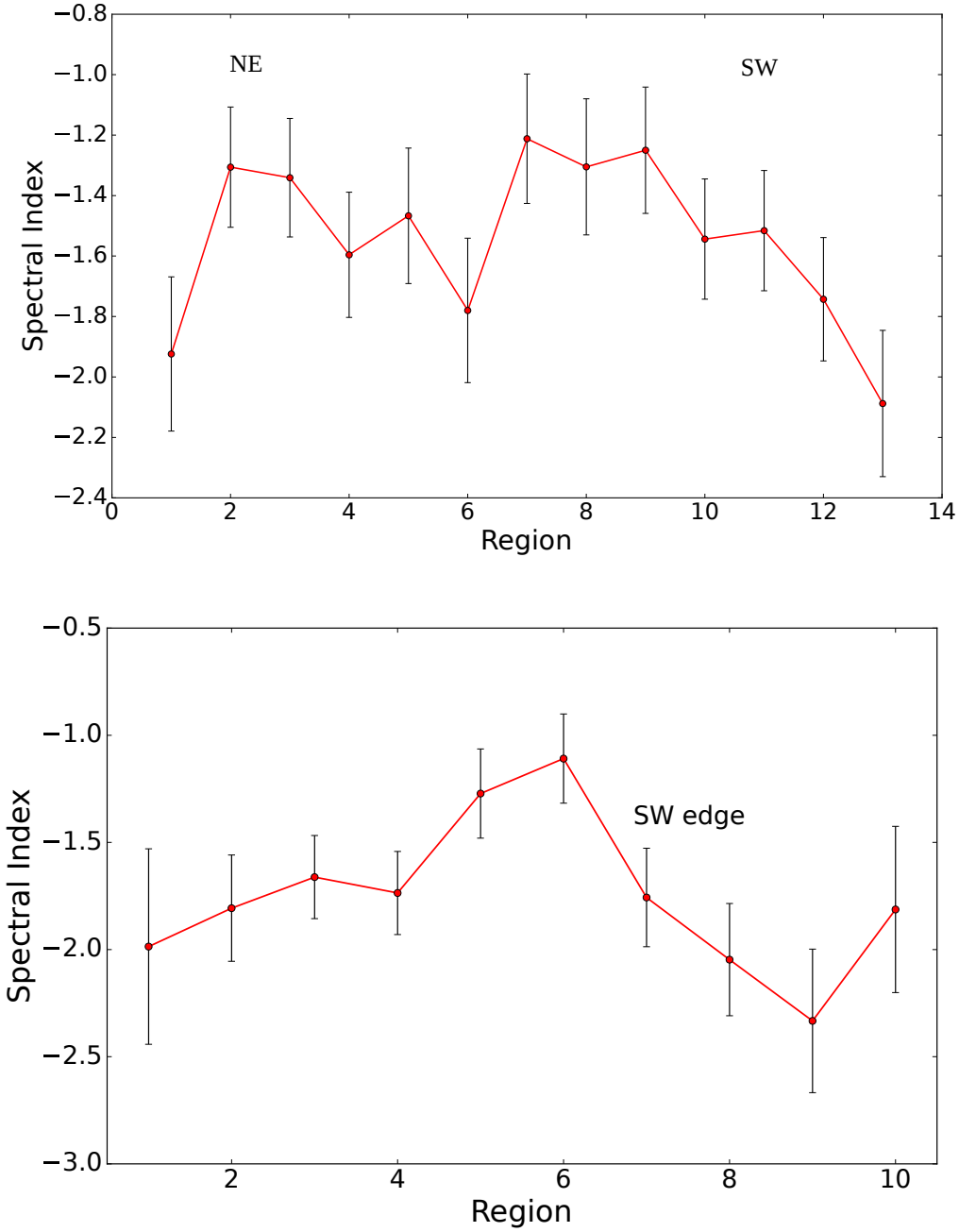

Figure 7.6: Spectral index profiles obtained from regions shown in Figures 7.3 and 7.4. No significant spectral flattening is observed in the south-west region where shock is detected. The north-east region shows slight spectral flattening compared to the surroundings.

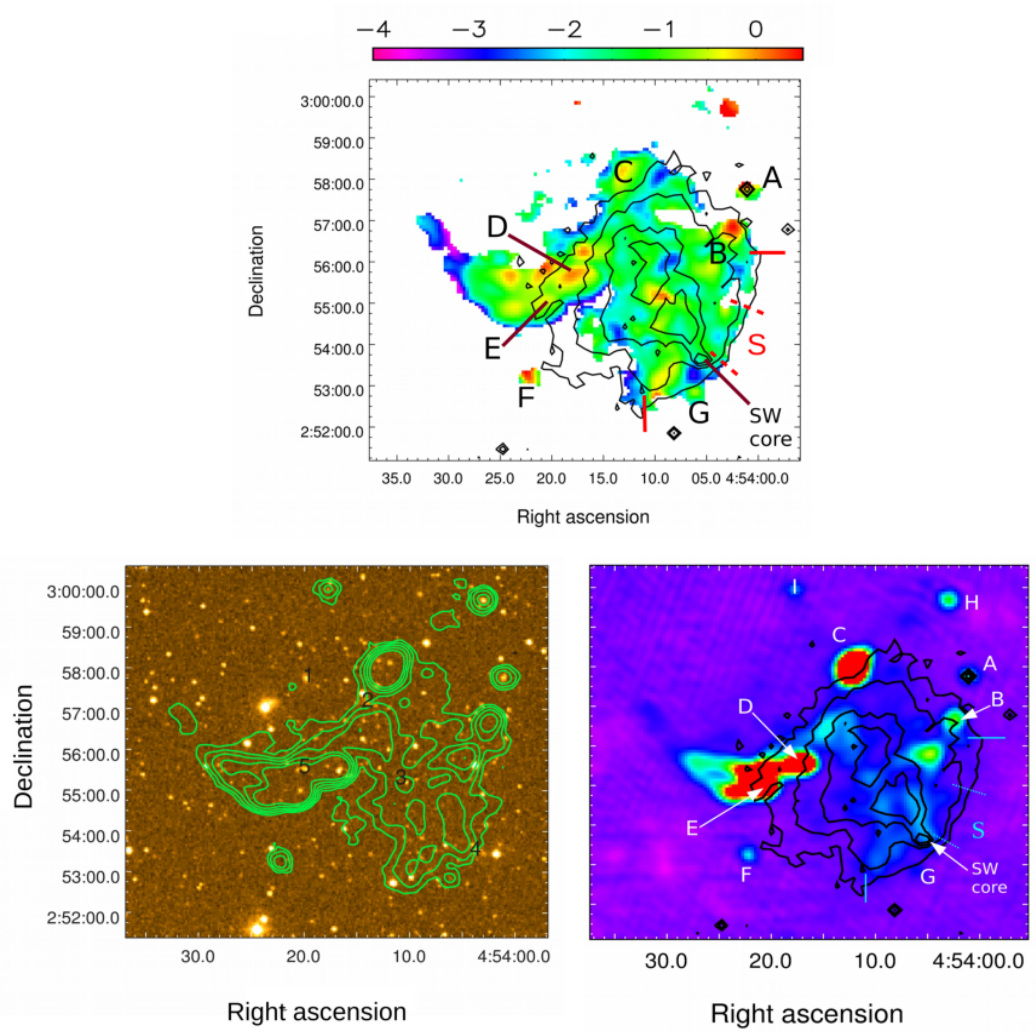

Figure 7.7: Spectral index image with *Chandra* X-ray contours overlaid (*Top*). The shock front detected is marked as 'S'. No significant spectral index flattening is observed in the region where strongest jump is detected (marked with red dashed line). Radio contours at 323 MHz overlaid on the optical DSS image of A520 (*Bottom left*). The contours are same as in Figure 7.2. Numbers 1−5 mark the important peaks found in weak-lensing analysis of the cluster (Mahdavi et al., 2007). Numbers 1,2,4 and 5 also have equivalent optical density groups associated with them. *Bottom right*: *Chandra* X-ray brightness contours overlaid on the 323 MHz image. The brightest region of the halo in the south-west lies approximately 200 kpc behind the shock front. It coincides with the trail of gas left behind by the passing SW compact core.

7.2 Results – A773

7.2.1 Radio Images

We observed A773 with the GMRT at 147 MHz and analyzed the archival data at 332 MHz and dual band 240-610 MHz. We could make an image only with the 332 MHz data. The 240−610 MHz data was too poor for an image.

The 147 and 332 MHz images are shown in Figure 7.8. The noise in the images are 0.4 and 0.08 mJy/beam at 147 and 332 MHz. Twelve radio galaxies, marked with a "+" symbol, crowd the region of the halo making it very difficult to derive the actual parameters of the halo. At 147 MHz only the brightest portions of the halo are visible. Even at the sensitivity level reached at this frequency, the halo appears to have less emission compared to other halos in our sample. It is $6' \times 4'$ in size (1.27 Mpc $\times$ 0.85 Mpc) and has the largest extent along the NE-SW direction.

The peak of the halo emission is in the north and two narrow 'filamentary' extensions south-west from it. The halo peak has a very bright point source 1.5 arcmin away to the east. However, none of the images show a connection between the two. The two 'filamentary' extensions may be halo features. The sharp edge of the contours in the south-east may be analogous to the 'radio edge' due to shock acceleration in A520. A hint of the halo peak and filaments was visible in the previous 15 arcsec resolution 1.4 GHz image (Govoni et al., 2001).

The flux densities of the halo (excluding the point sources) are 146 and 63 mJy at 147 and 332 MHz, respectively. This gives an integrated spectral index of -1.03.

7.2.2 Spectral index image and comparison with Optical/X-ray

Figure 7.9 shows the spectral index image between 147 and 332 MHz. The radio images were smoothed by 30 arcsec gaussian beam, and the point sources overlapping with the halo are marked by dotted circles. The spectral index image is limited by the 147 MHz image, which has lesser halo emission. Optical and X-ray peaks are marked on the image.

The halo has flat region of $\alpha = -0.73 \pm 0.37$ in the northern region. This flat region does not coincide with the halo peak. The halo peak has a mean spectral index of -1.19 ± 0.2. The spectral index in the south-eastern filament/extension of the halo is $\alpha = -0.8 \pm 0.46$.

The 2D optical analysis by Barrena et al. (2007) detected two peaks separated by nearly $2'$ in E-W direction. These are marked by crosses and labelled EP (eastern peak) and WP (western peak) on Figure 7.9. Figure 7.10 shows the overlay of radio contours at 332 MHz on the optical DSS image of the cluster. The halo peak coincides with WP. There is no discernible increase in radio emission at EP.

The X-ray brightness shows two peaks lying very close to each other (Rizza et al., 1998). These are marked as XP1 and XP2 and denoted by '+' on the image (Figure 7.9). Of the two peaks, the NE one (XP1) lies closer to the western optical peak (WP) as well as the halo peak.

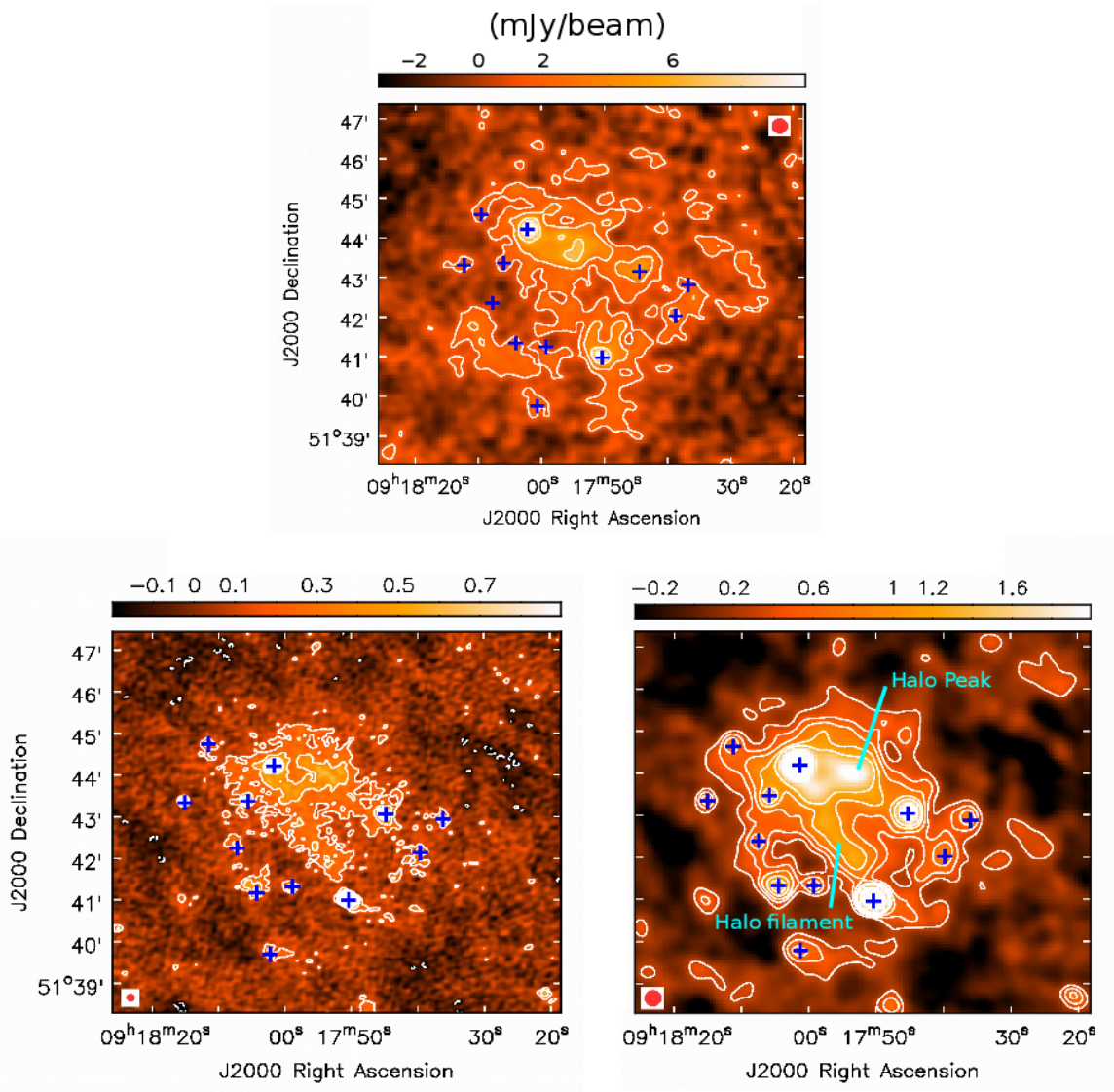

Figure 7.8: *Top*: 147 MHz image of the halo made at 23″ resolution. Contours start at $+3\sigma = 0.12$ mJy/beam. '+' sign denotes the positions of point sources, some of which are invisible at this frequency at our sensitivity and have been located using 332 MHz image (*Bottom*). The bottom left image has a resolution of 11″, first contour: 0.24 mJy/beam (=3σ); right image has 23″ resolution, first contour level at 0.3 mJy/beam (=3σ). Contours scale by 2 in all the images.

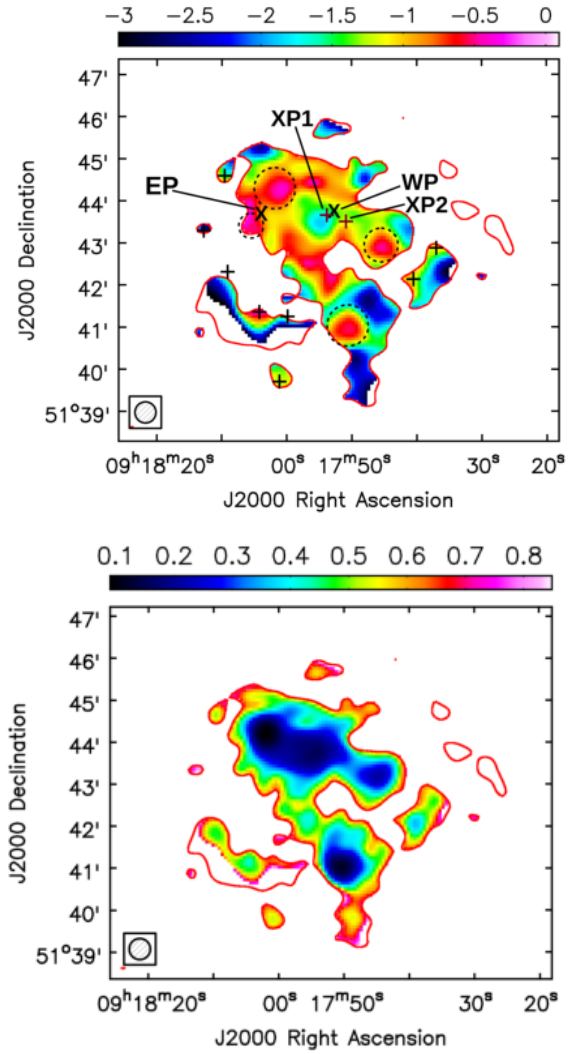

Figure 7.9: *Top*: Spectral index image between 147 and 332 MHz. The image has a resolution of 30 arcsec. EP and WP are 2 optical peaks and XP1 and XP2 (denoted by brown coloured '+' on the image) are two X-ray peaks. *Bottom*: Spectral index error image. Black dotted circles and '+' denote the positions of radio sources within and around the halo. The outer red contour denotes 2.4 mJy/beam in both the images ($= 2\sigma$ in the smoothed 147 MHz image).

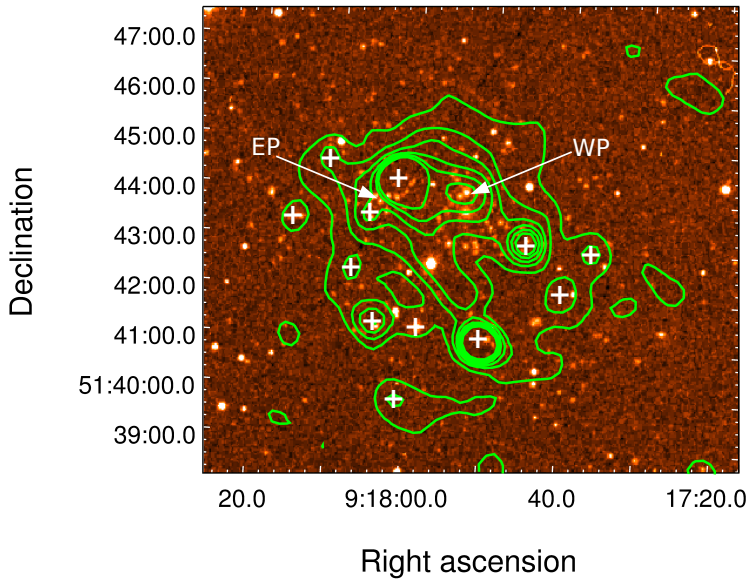

Figure 7.10: Radio contours at 332 MHz-30″ image overlaid on the optical DSS image. The bright halo peak coincides with the western optical peak. The first radio contour is 0.5 mJy/beam and then increases by 0.5 mJy/beam.

7.3 Discussion

7.3.1 A520 – Cluster Dynamics

This cluster is also known as the 'train wreck' cluster (Mahdavi et al., 2007). Optical results by Girardi et al. (2008) suggest that the cluster formation is taking place at the crossing of three filaments — one in the NE-SW direction, one in the E-W direction, and one aligned close to the line-of-sight. The optical group '4' has crossed the groups 1 and 2 from north-east and is moving towards the south-west (Figure 7.7). The east-west merger involves the group marked as '5' in the image. The minor optical group '3' is falling into the main cluster along the line-of-sight.

In the weak-lensing mass reconstruction of the cluster, the authors (Mahdavi et al., 2007; Jee et al., 2012) detected a massive dark core coinciding with the peak X-ray emission at the centre but devoid of bright galaxies (peak 3 in the Figure 7.7). This is unusual because both cold dark matter and galaxies form collisionless systems. This peak devoid of galaxies is not significantly detected by Okabe and Umetsu (2008); Clowe et al. (2012).

From high resolution *Chandra* data Govoni et al. (2004) showed a dense, cool and compact core south-west of the center, which has passed the main cluster from north-east, leaving behind a cool bright trail along with a strip of shock-heated gas. We confirm that the halo radio emission traces the X-ray brightness and is elongated in the same NE-SW direction (Figure 7.7). The bright halo region in the south-west coincides with the trail of gas left behind by the passing south-west compact core, suggesting a

connection between thermal and non-thermal components of the cluster. Vacca et al. (2014) carried out a comparison of spectral index image and X-ray gas temperature and found that higher temperature gas has flatter spectral index values, although no point-to-point correlation was found. The fast moving core in south-west will generate turbulence behind it, which may be powering the halo.

7.3.2 A520 – The Radio 'Edge'

Govoni et al. (2004) first hinted at the possibility of a bow shock in front of the south-western core, which was later confirmed by Markevitch et al. (2005). Markevitch et al. (2005), and later Wang et al. (2018) used this region as a test bed to distinguish between shock acceleration and adiabatic compression. They predicted that the spectral index of the halo in this region should be -1.2 if the edge is produced by shock acceleration. Subsequently, the spectral index should steepen away from the shock as is observed in the case of some relics (van Weeren et al., 2012). Vacca et al. (2014) detected a spectral index of -1.25 behind the shock front in the images made between 325 and 1400 MHz at 39 arcsec resolution. We measure a spectral index immediately behind the shock front (marked as red dotted line in Figure 7.7) as -1.75. The 1σ error is 0.3. The injection spectral index expected from a shock with Mach number 2.5 is ~ -0.9, and for unresolved region in the image α should be -1.4 ($= \alpha_{inj} - 0.5$). The expected value of the spectral index lies midway between our estimate and that of Vacca et al. (2014). Neither our images nor those of Vacca et al. (2014) detect any gradient in spectral index away from the shock front.

While the entire halo may not be a result of shock acceleration, as the relativistic electrons can only travel upto a few hundred kpc before they lose their energies due to inverse compton and synchrotron losses; but the 'edge' and the 'brightening' observed in the halo may be explained by shock acceleration (or re-acceleration). Markevitch et al. (2005) and Wang et al. (2018) suggested an alternative explanation of adiabatic compression of magnetic field and pre-existing electrons by the shock front, similar to the model for relics by Ensslin et al. (1998). This model predicts a reduction in radio emission just across (i.e ahead) of the shock by a factor which can be estimated from the shock compression ratio. For a power law distribution of electrons $\frac{dN}{d\gamma} \propto N_0 \gamma^{-\delta}$, the increase in magnetic field strength due to compression is $B \propto x^{2/3}$, where x is gas density jump at shock. The increase in radio intensity is predicted to be $I_\nu \propto x^{(2/3)\delta+1}$. The pre-shock radio emission is predicted to be fainter by a factor of 16 (or 9) for $\alpha = -1.25$ (or -0.75) in the region where shock jump was highest ($x = 2.7$). Using VLA data at 1.4 GHz, the authors discarded the adiabatic compression model at 2σ confidence. However, as noted by them, the presence of a 'negative bowl' ahead of the radio-edge may have hampered the results. We also do not detect significant emission in front of the shock front (at 3σ level). This implies that adiabatic compression may not have produced the radio edge, although as noted by Wang et al. (2018), both shock acceleration and compression may be at work here.

Our high resolution images show that the bright radio feature does not lie immedi-

ately behind the shock front (region N1+N2 from Wang et al. (2018)). It lies roughly 200 kpc behind the front and is not perfectly aligned with it. A slight spectral index flattening is observed in the NE edge. There is a possibility of a 'reverse' shock at this location, but no significant temperature jump was detected (Wang et al., 2016). The non-detection of the shock front may also be due to unfavourable viewing angle.

The halo in A520 differs from other halos as it is not centrally peaked like most other halos. The brightest structures in the halo lie towards the periphery. The integrated spectrum of the halo is also flatter, while halos are known to be steep spectrum objects. It is at the cross-roads of many merging groups. It has also been suggested that the halo may in fact be a relic seen in projection (Govoni et al., 2001). This can be tested by polarization studies as relics show up to 30−40% polarization, unlike halos. Another possibility is that the bright structures observed to the north-east and the south-west may be relics projected onto the halo (Rajpurohit et al., 2018). The halo in A520 demonstrates the many complexities involved in understanding these objects.

7.3.3 A773

Barrena et al. (2007) suggest multiple mergers for the cluster — an older merger in N-S direction and a more recent one involving the eastern group, as also suggested by Govoni et al. (2004).

Based on the optical image and X-ray temperature map, Govoni et al. (2004) suggested that the eastern group is exiting the main merger site leaving behind a shock heated region. There is no X-ray peak associated with the eastern group, which may be because the group has shed its gas due to ram pressure stripping.

Due to the small size of the halo, the large number of confounding radio galaxies within it and the poor nature of the 147 MHz image, we are unable to interpret the spectral index structures in any reliable manner. Govoni et al. (2004) noted that the halo does not follow the X-ray brightness or the temperature distribution of the ICM. It occupies the cooler region between the two optical subclusters, and does not extend into the shock heated region behind the western optical peak (T $\sim$ 11−12 keV). However, we have detected a much larger halo that extends well beyond the western optical and X-ray peaks.

As in other halos in our sample the peak of the halo emission coincides with a peak in galaxy density. However, we do not see an equivalent high intensity halo emission in the eastern group of A773. This may be due to a paucity of electrons and/or magnetic field in this peripheral region. The suggestion by Govoni et al. (2004) that this subcluster has been stripped of gas would tie in with the lack of a halo peak. On the other hand, the region is confounded by the presence of two radio galaxies which makes the determination of halo emission difficult.

The lower of the two filaments is located at the radio 'edge'. This is similar to the case of A520 and we should also expect an X-ray edge here if it is due to shock acceleration. No such shock front has been detected in the X-ray. This may also be due to an unfavourable orientation of the shock. If this filamentary structure is a result of an outward going shock, then the mean value of the spectral index suggests a shock with

Mach number nearly 3, typical of cluster shocks. A better 147 MHz image would greatly help. The lack of emission behind this 'edge' at 147 MHz does not allow for a detailed study (for example a steepening away from the edge). The bright optical source (RA 09:17:56, DEC 51:42:15) located within the lower filament has no redshift information available in NED, and therefore we cannot comment on its association with the filament.

The clumps and filaments in the halo in A773 is similar to those in RXC J2003.5−2323 (Giacintucci et al., 2009). The clumpy morphology of the latter halo was attributed to the distribution of both relativistic electrons and magnetic field. In A2255 the surface brightness of the halo increases from the centre towards the filaments at the edges (Govoni et al., 2005; Pizzo and de Bruyn, 2009). The authors noted that the filaments could be relics seen in projection near the cluster centre, which was also later suggested by Pizzo et al. (2011) through rotation measure study of the cluster. In A773 the filaments are not as bright as in A2255, and from the radio contours they appear to be a part of the halo; perhaps brightened up due to tracing the outward going merger shocks.

Chapter 8

Summary and Conclusion

8.1 Summary

Radio halos have remained mysterious objects ever since their discovery, owing to their diffuse nature and difficulties associated with imaging them. In comparison there has been some advancement in our understanding of relics, in recent times, perhaps due to their more definite structure, association with shocks, and spectral gradients. Halos, on the other hand, are thought to be powered by both shocks and turbulence, and occupy much larger volumes in the interiors of galaxy clusters. We therefore expect much complex morphologies and structures in the spectral index images of halos. Detecting turbulence is a challenge and has not been currently achieved with X-ray telescopes. Flat spectrum structures correlating with the merger geometry is a strong evidence of re-acceleration model for the origin of halos. In this thesis, we have been able to identify energization sites lying close to merging subgroups, in three out of five halos in our sample.

The major result of this work is the detection of a 'sharply-defined' structure located at the centre of the halo A2163. The significant detection of this *ridge* in the total intensity images at three frequencies, and in the spectral index image as the flattest region, indicates that energization happened most recently in this region. This region also lies between two merging subclusters, which is a strong evidence that cluster mergers power halos. While most of the diffuse part of the halo may be a result of re-acceleration due to cluster-wide turbulence injected during a merger, the linear structure such as the *ridge* may be a result of shock (re-)acceleration closer to the merger site.

We detect a similar flat spectrum feature in the halo A665, in a region expected to be dominated by recent merger activity. However, in this case only the 323 MHz image revealed a bright *ridge*-like feature at the location of the flatter spectrum region. The lack of a bright halo structure in the 147 MHz image may be due to smaller size of the halo, less power than A2163 and/or bad data. Nevertheless, both these halos highlight the possibility that similar structures may be detected in more number of halos. A favourable merging geometry in these clusters may have also aided us in detecting these structures.

We detected flat spectrum areas in the image of A2744 that are coincident with optically overdense regions and the merger axis. The connection between flat spectral index features and galaxy groups has not been reported earlier for this halo. For A520, we confirm the coincidence of the south-west radio 'edge' with the cluster bow-shock. The radio edge also shows an increase in surface brightness. We also detected another edge in the north-east, which may be coincident with a reverse shock. The spectral index image does not provide much clues about the halo, which we think may be due to multiple mergers taking place. The south-west edge does not show significant spectral flattening, or a gradient away from it as is expected from shock re-acceleration. For A773, the small size, less flux density and the presence of a number of contaminating radio galaxies in the neighbourhood of the halo, did not allow for any detailed study. Although, we do detect a radio edge similar to the case of A520. The presence of a shock front at this location needs to be verified by future studies. The different structures seen in the spectral index images for different halos may be linked to the different evolutionary stages of the halo. The halo in A520 and A773 may still be in the formative stages, which may explain the lack of dominant features in the images.

We have also outlined a likely scenario to explain the origin of magnetic field and seed electrons required for halo formation, based on the presence of a number of radio galaxies in and around the halo A2163. We propose that a halo may be a collection of dead radio lobes that are invisible due to sensitivity limits, until they are re-energised by a cluster merger. We make use of the premise that radio galaxies show recurrent (or interrupted) jet activity and that the reduction in energy of particles after the jet engine switches off is only marginal, so that even weak cluster shocks and turbulence can re-energise them. In this model, it is imperative that cluster hosts a number of AGNs. The number of radio galaxies required to explain halos is within range of the number of radio jet activities possible since the formation history of radio galaxies at z=3.

In our sample we have a single cluster hosting a relic, i.e A2744. A shock front is also detected at this location. The spectral index image of the relic shows a steepening away from the shock, which is typical for relics. More interesting is the gradient we observe in the lateral direction. The relic shows a progressive steepening from a compact flat region ($\alpha \sim -0.7$) at the southern tip of the relic. The spectrum becomes flat again in the region where shock front is detected (where a radial steepening is also observed). We think the trend that we observe is because of an AGN lobe supplying seed electrons to the relic. From the spectral index values, we favour re-acceleration of fossil electrons by the passage of shock front, rather than DSA from the thermal pool. However, we need deeper optical and radio images to establish the presence of an AGN and optical galaxy in the expected region on the relic.

We have observed the coincidence of the halo peak with optically overdense regions for three halos in our sample – A665, A2744 and A773. For A2163, the bright *ridge* lies between two optical groups. In literature, the bright features in the Coma cluster halo was found to have a correspondance with the surface mass density derived by weak lensing study (Brown and Rudnick, 2011). Further, the relic source 1253+275 in the Coma cluster lies just outside of a 'wall' of infalling group of galaxies (Brown and Rudnick, 2011). The origin of the relic is thought to be the 'infall shock' generated by

the 'wall' of galaxies. An infall shock as defined by Brown and Rudnick (2011) is caused by a dense group of galaxies with its own intragroup medium penetrating the ICM in the early stages of a merging event. This may account for increased radio emission coinciding or lying in the vicinity of dense optical groups in four of our halos.

8.2 Conclusion and Future Work

There are many questions regarding these giant radio sources that remain to be answered. The obvious puzzle is the origin of vast reservoir of synchrotron electrons. Future studies of halos would include:

1)Observing and detecting more number of these sources to derive their statistical properties. This would include observing them at higher redshifts, which will help in constraining their origin. At present most halos have been detected till the redshift 0.35, with only a handful of them beyond that (A851 at z = 0.4069, Giovannini et al. (2009); CL 0016+16 and MACS J0717.5+3745 both at z = 0.55, Giovannini and Feretti (2000); Bonafede et al. (2009); El Gordo at z = 0.87, Lindner et al. (2014)). Absence of halos at higher redshift could be related to the evolution of clusters – possibly mergers have to be in an advanced stages to power these objects. Alternatively, as we have proposed in Chapter 4, halos can result only after sufficient radio activity has taken place.

Ultra-steep spectrum radio halos is another avenue that needs to be explored. An important expectation of the re-acceleration model is a large population of steep spectrum halos, which are a result of minor cluster mergers that are more common than major mergers. These halos are visible only at lower frequencies (< 600 MHz), and therefore a low frequency survey is expected to increase their number count considerably. Future observations with LOFAR, LWA and SKA will be able to detect these sources.

2)Observing halos at multiple frequencies to constrain their integrated spectra. Some halos with high frequency observations, show a spectral break in favour of the re-acceleration model.

3)Obtaining spectral index images with the necessary resolution. Our small sample has helped in identifying a definite energisation site in few of them. Clearly, secondary model cannot explain the correlation of the spectral index image with the cluster merger geometry. A larger sample of clusters hosting powerful halos may shed light on energization process, its link with cluster mergers and efficiency of acceleration.

4)Although halos follow a generally good correlation between radio power and X-ray luminosity of the clusters, there are a few exceptions that have higher radio power than expected. Halos are generally associated with massive clusters (high X-ray luminosity), but in a few cases it has been found that clusters having low X-ray luminosity also host halos, eg: A1213, A523 and CL 0217+70 (Giovannini et al., 2009; Giovannini et al., 2011; Brown et al., 2011). These halos which do not follow the above correlation present

an interesting class of halos. Moreover, there are clusters which are well-known merging systems but do not host halos, perhaps a threshold in mass could explain the absence of halos.

The next generation of telescopes like LOFAR, SKA and uGMRT are expected to answer some of these long standing questions.

LOFAR has already become operational, with as many as 50 antennas and baselines ranging from 100m−1000km, offering few arcsec resolution. The survey between 10 MHz−240 MHz is expected to discover a large number of halos. The phase 1 survey between 120−190 MHz, expected to reach a sensitivity of 0.1 mJy/beam, will be able to detect nearly 400 halos up to a redshift of 0.6 (Cassano et al., 2010). Nearly half of these halos are expected to have extremely steep spectrum ($\alpha < -1.9$), visible only at low frequencies (< 600 MHz). Discovering steep spectrum halos will be a big step in the direction of electron re-acceleration model.

ASKAP will have 36 12-metre antennas, a resolution of $10''-30''$, and expected rms sensitivity of 10 μJy/beam for a 12 hour observation period. The planned EMU (Evolutionary Map of the Universe) radio continuum survey of the Southeren Sky at 1.3 GHz will provide both the resolution and sensitivity for detecting diffuse sources (Norris et al., 2011).

Finally, the upgraded GMRT (uGMRT) has already started operating. It offers a wider bandwidth ranging from 100−400 MHz in the frequency ranges 120−240, 250−500, 550−850 and 1060−1460 MHz. With the increased UV-coverage and sensitivity we can better recover extended sources and study them in greater detail.

Appendix

List of sources used in Flux density scaling estimation

The columns in each table are 1)Source name according to IAU convention 2) Right Ascension of the source 3) Declination of the source 4) Flux density of the source from TGSS catalog 5) Flux density at 153 (or 147) MHz in our field 6) Flux Density at 332 (or 322) MHz in our field 7) Flux density from NVSS catalog 8) Spectral index of the source measured between 153 (or 147) MHz and 332 (or 322) MHz in our field. The mean spectral index is −0.74, −0.75, −0.7, −0.78, −0.77 for the clusters A2163, A665, A2744, A520 and A773, respectively.

A2163

Source Name	RA (h m s)	DEC (d m s)	S_{147} mJy	S_{153} mJy	S_{332} mJy	S_{1400} mJy	α_{332}^{153}
J162040.6−061630	16:20:40.66	−06:16:30.36	132.4	115.5	97.1	63.7	−0.22
J162006.6−061113	16:20:06.62	−06:11:13.56	71.4	52.6	31.3	13.0	−0.67
J161919.5−061952	16:19:19.46	−06:19:51.96	159.4	153.0	56.6	10.9	−1.28
J161918.1−054828	16:19:18.14	−05:48:28.08	43.2	36.6	22.4	7.3	−0.63
J161916.6−055524	16:19:16.68	−05:55:23.88	57.2	35.9	24.7	6.8	−0.49
J161849.6−052127	16:18:49.68	−05:21:27.72	202.0	165.4	112.2	44.1	−0.50
j161838.4−070730	16:18:38.40	−07:07:29.64	222.7	230.3	110.4	32.1	−0.95
J161823.4−070035	16:18:23.40	−07:00:34.92	302.7	325.2	224.8	84.7	−0.48
J161820.7−062309	16:18:20.71	−06:23:08.88	1333.3	1256.2	597.2	135.9	−0.96
J161818.1−063450	16:18:18.07	−06:34:50.52	105.1	98.1	57.7	18.5	−0.68
J161756.4−070059	16:17:56.45	−07:00:59.04	72.0	97.2	61.8	25.4	−0.58
J161744.9−052152	16:17:44.90	−05:21:51.84	58.8	31.9	23.2	7.2	−0.41
J161733.4−055147	16:17:33.41	−05:51:47.16	523.8	492.1	190.2	69.3	−1.23
J161733.2−071550	16:17:33.22	−07:15:49.68	81.8	94.4	28.3	10.6	−1.56
J161729.3−064918	16:17:29.35	−06:49:18.48	58.4	66.0	37.9	11.5	−0.71
J161716.8−055411	16:17:16.82	−05:54:11.16	590.7	541.7	261.5	63.3	−0.94
J161708.5−055042	16:17:08.50	−05:50:41.64	174.0	152.9	133.1	75.3	−0.18
J161707.6−053257	16:17:07.66	−05:32:57.48	64.9	51.9	34.2	15.0	−0.54
J161653.2−061507	16:16:53.16	−06:15:07.56	120.3	121.9	55.9	26.1	−1.01
J161629.1−055249	16:16:29.11	−05:52:49.44	41.2	26.5	19.0	6.8	−0.43
J161616.4−065711	16:16:16.44	−06:57:11.52	202.9	228.9	135.6	48.2	−0.68

Source Name	RA (h m s)	DEC (d m s)	S_{147} mJy	S_{153} mJy	S_{332} mJy	S_{1400} mJy	α_{332}^{153}
J161608.8−063421	16:16:08.81	−06:34:21.00	63.8	61.2	37.3	14.8	−0.64
J161601.2−045825	16:16:01.25	−04:58:24.96	91.4	89.1	36.3	12.3	−1.16
J161540.4−054103	16:15:40.42	−05:41:03.48	102.3	122.2	66.5	22.5	−0.79
J161539.5−053056	16:15:39.55	−05:30:55.80	115.3	113.7	106.7	45.7	−0.08
J161526.5−070612	16:15:26.50	−07:06:12.24	183.9	214.4	171.9	59.2	−0.29
J161519.9−054626	16:15:19.87	−05:46:25.68	91.6	104.5	62.7	21.4	−0.66
J161518.6−054021	16:15:18.62	−05:40:21.00	139.2	136.2	69.1	52.5	−0.87
J161509.4−064053	16:15:09.41	−06:40:53.04	339.6	396.9	187.6	67.2	−0.97
J161444.3−065614	16:14:44.30	−06:56:13.92	217.2	261.2	155.4	42.4	−0.67
J161432.3−061009	16:14:32.30	−06:10:08.76	60.7	58.0	37.1	12.4	−0.58
J161424.7−051043	16:14:24.74	−05:10:42.96	118.7	106.5	55.6	20.4	−0.84
J161403.8−053235	16:14:03.86	−05:32:35.52	159.8	108.8	92.2	40.4	−0.21
J161351.0−061744	16:13:51.07	−06:17:44.52	134.7	169.5	89.8	30.8	−0.82
J161341.4−054811	16:13:41.38	−05:48:11.16	161.6	137.4	71.3	32.5	−0.85
J161331.5−061539	16:13:31.54	−06:15:38.88	120.7	81.8	67.6	13.5	−0.25
J161330.1−060955	16:13:30.10	−06:09:55.44	146.9	147.3	74.1	24.3	−0.89
J161308.4−065536	16:13:08.40	−06:55:36.12	1422.1	1607.7	726.2	175.3	−1.03
J161307.7−070910	16:13:07.75	−07:09:10.08	180.4	176.0	88.7	24.5	−0.89
J161303.5−063304	16:13:03.55	−06:33:04.32	72.7	87.8	40.1	9.0	−1.01
J161259.3−055846	16:12:59.35	−05:58:45.84	47.2	44.3	33.3	13.9	−0.37
J161249.3−070347	16:12:49.27	−07:03:46.80	65.6	53.9	20.6	7.1	−1.24
J161213.1−055145	16:12:13.15	−05:51:45.36	475.0	535.3	260.2	74.5	−0.93
J161207.7−063333	16:12:07.70	−06:33:33.12	688.9	759.7	478.8	209.6	−0.60
J161207.3−060949	16:12:07.27	−06:09:49.32	61.1	57.4	28.8	12.4	−0.89
J161200.1−052946	16:12:00.17	−05:29:45.96	103.1	112.1	41.2	10.9	−1.29

A665

Source Name	RA (h m s)	DEC (d m s)	S_{147} (TGSS) mJy	S_{147} mJy	S_{322} mJy	S_{1400} mJy	α_{322}^{147}
J084112.5+654156	08:41:12.53	65:41:55.68	510.6	499.7	305.0	103.7	−0.63
J084106.5+660933	08:41:06.54	66:09:33.12	63.5	60.4	19.9	5.4	−1.42
J084052.1+661341	08:40:52.08	66:13:40.80	123.7	130.2	37.3	20.1	−1.60
J083956.8+661346	08:39:56.76	66:13:45.59	94.3	76.7	78.4	24.9	+0.03
J083938.9+661154	08:39:38.86	66:11:53.70	59.8	43.0	21.2	11.0	−0.91
J083823.5+650716	08:38:23.52	65:07:16.39	70.0	85.7	62.2	33.7	−0.41
J083814.8+662213	08:38:14.83	66:22:12.72	67.2	76.1	29.5	5.4	−1.21
J083758.5+663622	08:37:58.51	66:36:22.10	69.8	71.5	40.1	15.3	−0.74
J083751.6+661730	08:37:51.58	66:17:30.26	90.6	86.3	61.0	20.0	−0.44
J083736.1+661735	08:37:36.14	66:17:34.51	59.2	49.3	26.7	12.8	−0.79
J083659.8+651038	08:36:59.77	65:10:37.92	80.1	88.2	56.5	38.0	−0.57
J083651.9+650111	08:36:51.89	65:01:11.28	173.3	164.6	97.9	30.2	−0.66

Source Name	RA (h m s)	DEC (d m s)	S_{147} (TGSS) mJy	S_{147} mJy	S_{322} mJy	S_{1400} mJy	α_{322}^{147}
J083656.8+651613	08:36:56.84	65:16:13.08	192.5	162.4	114.2	49.8	−0.45
J083627.2+660952	08:36:27.17	66:09:52.27	179.0	168.0	124.1	51.3	−0.39
J083623.7+665320	08:36:23.72	66:53:20.47	76.9	75.7	29.2	13.8	−1.22
J083544.1+664020	08:35:44.11	66:40:19.99	163.9	158.1	123.9	87.9	−0.31
J083529.5+661507	08:35:29.47	66:15:07.27	41.0	40.9	24.0	6.0	−0.68
J083443.9+653422	08:34:43.87	65:34:22.40	65.2	79.4	26.5	11.9	−1.40
J083358.4+645644	08:33:58.42	64:56:43.87	99.6	107.1	42.9	12.2	−1.17
J083416.2+670402	08:34:16.19	67:04:01.56	339.5	354.7	98.9	41.4	−1.63
J083337.5+651701	08:33:37.55	65:17:01.46	137.1	131.0	96.8	25.8	−0.39
J083335.0+650051	08:33:35.01	65:00:50.76	692.5	673.1	497.4	163.6	−0.39
J083335.5+653654	08:33:35.54	65:36:53.96	89.7	117.2	34.3	12.4	−1.57
J083311.8+664619	08:33:11.80	66:46:19.13	100.6	96.6	55.3	12.6	−0.71
J083246.9+645560	08:32:46.87	64:55:59.99	97.1	89.6	50.3	12.7	−0.74
J083216.8+660047	08:32:16.83	66:00:47.41	57.2	76.3	36.3	13.7	−0.95
J083202.2+650650	08:32:02.23	65:06:50.00	65.6	70.8	48.1	18.9	−0.49
J083202.0+655041	08:32:02.00	65:50:41.39	52.5	58.4	14.8	5.4	−1.75
J083052.9+653659	08:30:52.94	65:36:58.68	664.7	648.7	441.8	132.1	−0.49
J083049.3+652045	08:30:49.31	65:20:44.52	90.8	87.1	65.8	26.9	−0.36
J083025.1+655041	08:30:25.12	65:50:40.70	85.0	81.8	58.2	12.8	−0.43
J082951.5+655151	08:29:51.48	65:51:51.19	182.5	189.7	132.6	44.1	−0.46
J082935.9+661602	08:29:35.93	66:16:01.56	43.0	30.3	20.3	7.2	−0.51
J082923.7+644020	08:29:23.66	64:40:20.50	389.7	391.8	158.2	35.1	−1.16
J082848.8+653135	08:28:48.82	65:31:34.61	42.7	52.9	28.2	6.2	−0.81
J082843.1+664005	08:28:43.05	66:40:05.38	84.1	88.1	54.7	13.8	−0.61
J082845.9+645926	08:28:45.89	64:59:25.55	459.7	466.4	294.3	99.2	−0.59
J082838.2+664522	08:28:38.17	66:45:21.96	77.1	80.2	46.3	21.2	−0.70
J082749.1+665345	08:27:49.07	66:53:44.59	40.7	36.1	19.5	4.8	−0.79
J082744.1+661006	08:27:44.15	66:10:05.95	47.6	53.6	40.0	11.9	−0.37
J082703.2+660757	08:27:03.16	66:07:57.00	56.3	52.0	31.4	7.2	−0.65
J082654.7+664726	08:26:54.70	66:47:25.84	64.0	62.0	31.5	11.3	−0.87
J082635.7+653309	08:26:35.70	65:33:08.71	96.6	81.3	48.8	17.3	−0.65
J082633.3+651836	08:26:33.29	65:18:36.36	182.2	180.5	129.2	53.8	−0.43
J082558.2+650518	08:25:58.21	65:05:18.24	58.5	57.3	39.7	16.5	−0.47
J082511.7+664225	08:25:11.74	66:42:24.66	74.3	96.3	29.8	15.3	−1.50
J082509.2+664009	08:25:09.15	66:40:08.51	100.3	97.1	59.9	25.8	−0.62
J082513.6+654403	08:25:13.55	65:44:02.76	55.8	54.1	37.6	13.8	−0.47
J082432.9+663210	08:24:32.91	66:32:09.53	92.6	84.8	58.6	16.6	−0.47
J082410.5+662430	08:24:10.52	66:24:29.92	74.2	67.2	51.7	17.7	−0.33
J082413.9+660205	08:24:13.91	66:02:04.88	141.3	131.3	97.8	29.6	−0.38
J082306.1+650026	08:23:06.15	65:00:26.35	219.4	212.2	109.9	35.8	−0.84
J082221.4+661855	08:22:21.44	66:18:54.86	72.5	63.9	42.4	16.9	−0.53
J081856.0+653856	08:18:55.97	65:38:56.44	77.6	79.3	27.8	12.0	−1.34

Source Name	RA (h m s)	DEC (d m s)	S_{147} mJy	S_{153} mJy	S_{332} mJy	S_{1400} mJy	α_{332}^{153}
J001942.7−303121	00:19:42.73	−30:31:20.60	360.4	334.3	419.8	507.0	+0.29
J001924.9−295254	00:19:24.92	−29:52:54.37	73.2	80.2	62.7	71.0	−0.32
J001850.0−303758	00:18:50.03	−30:37:58.40	108.9	111.5	72.7	22.4	−0.55
J001832.2−301041	00:18:32.24	−30:10:41.45	73.1	54.0	32.6	10.8	−0.65
J001809.4−303119	00:18:09.35	−30:31:18.52	86.8	72.4	50.3	16.2	−0.47
J001805.6−302548	00:18:05.57	−30:25:47.93	77.0	53.6	36.8	13.9	−0.48
J001749.9−295428	00:17:49.93	−29:54:27.97	125.3	111.6	37.3	24.0	−1.41
J001742.3−305005	00:17:42.31	−30:50:04.78	2013.3	1843.4	1176.1	227.9	−0.58
J001736.7−305252	00:17:36.67	−30:52:51.71	60.8	71.9	53.8	21.3	−0.37
J001731.0−301408	00:17:31.01	−30:14:07.73	100.3	111.3	72.9	16.6	−0.55
J001727.2−303934	00:17:27.20	−30:39:34.13	82.0	100.5	73.3	25.6	−0.41
J001724.1−310204	00:17:24.14	−31:02:04.16	170.0	174.8	112.6	29.2	−0.57
J001716.0−295154	00:17:16.04	−29:51:53.93	56.9	52.7	27.3	16.3	−0.85
J001650.1−292108	00:16:50.12	−29:21:08.50	296.8	282.3	155.2	69.4	−0.77
J001648.6−312223	00:16:48.64	−31:22:23.12	365.3	437.8	238.2	52.9	−0.78
J001642.2−310642	00:16:42.17	−31:06:42.26	129.8	84.3	41.9	21.8	−0.90
J001635.8−295112	00:16:35.84	−29:51:12.20	42.0	34.8	21.1	15.0	−0.65
J001630.4−295315	00:16:30.43	−29:53:14.64	145.1	148.0	40.4	13.1	−1.67
J001621.0−292753	00:16:21.00	−29:27:52.60	81.3	78.8	37.5	22.2	−0.96
J001622.1−302013	00:16:22.09	−30:20:13.49	41.3	43.9	23.5	5.1	−0.81
J001617.6−305018	00:16:17.59	−30:50:18.10	136.3	134.8	120.7	37.1	−0.14
J001613.4−310803	00:16:13.38	−31:08:03.48	115.3	120.5	57.8	12.3	−0.95
J001610.0−310718	00:16:09.97	−31:07:18.41	74.9	71.5	33.4	8.3	−0.98
J001612.0−301526	00:16:12.01	−30:15:26.06	60.0	59.2	41.2	15.2	−0.47
J001606.8−303855	00:16:06.76	−30:38:54.96	134.9	138.2	90.9	20.3	−0.54
J001534.5−295611	00:15:34.50	−29:56:10.50	68.8	61.4	36.2	10.3	−0.68
J001531.0−303606	00:15:30.99	−30:36:05.58	1095.8	1075.2	777.6	264.2	−0.42
J001526.4−304027	00:15:26.40	−30:40:27.23	56.5	74.5	57.7	22.7	−0.33
J001502.9−292212	00:15:02.87	−29:22:12.11	97.1	113.7	37.9	28.7	−1.42
J001438.5−300030	00:14:38.52	−30:00:30.13	52.0	51.1	25.1	6.7	−0.92
J001438.0−305918	00:14:37.98	−30:59:17.92	210.6	240.0	256.4	192.8	+0.09
J001400.8−292334	00:14:00.80	−29:23:34.22	136.4	143.8	79.3	32.6	−0.77
J001354.5−293156	00:13:54.48	−29:31:55.96	50.8	39.5	24.1	11.4	−0.64
J001353.0−313253	00:13:52.98	−31:32:53.34	147.1	143.6	96.7	33.6	−0.51
J001341.2−300927	00:13:41.24	−30:09:27.04	1095.2	1043.3	677.9	222.5	−0.56
J001317.1−291618	00:13:17.15	−29:16:17.72	294.1	276.3	95.8	24.7	−1.37
J001314.5−294655	00:13:14.48	−29:46:54.77	39.6	41.9	21.2	7.0	−0.88
J001227.1−301210	00:12:27.13	−30:12:10.08	127.6	125.5	43.1	19.5	−1.38
J001225.3−311515	00:12:25.28	−31:15:15.34	116.9	102.0	80.4	31.6	−0.31
J001224.9−304948	00:12:24.92	−30:49:47.89	112.3	90.6	57.0	14.0	−0.60

Source Name	RA (h m s)	DEC (d m s)	S_{147} mJy	S_{153} mJy	S_{332} mJy	S_{1400} mJy	α_{332}^{153}
J001144.3−312140	00:11:44.30	−31:21:40.10	151.9	155.3	59.4	39.0	−1.24
J001132.3−302452	00:11:32.29	−30:24:51.84	101.8	106.5	63.0	12.8	−0.68
J001133.6−295719	00:11:33.57	−29:57:18.76	143.2	109.8	68.4	33.0	−0.61
J001110.2−293733	00:11:10.17	−29:37:33.31	266.5	265.4	149.7	92.9	−0.74
J001105.1−293524	00:11:05.08	−29:35:23.68	48.5	44.4	16.6	11.9	−1.27
J001038.4−302110	00:10:38.41	−30:21:10.44	273.7	278.6	118.7	70.0	−1.10
J001035.7−302747	00:10:35.69	−30:27:46.76	529.3	558.8	425.9	315.3	−0.35
J001024.6−305139	00:10:24.57	−30:51:39.42	152.4	143.9	99.7	25.9	−0.47
J001013.9−310227	00:10:13.88	−31:02:26.74	69.2	55.8	23.6	14.2	−1.11
J001010.6−302757	00:10:10.64	−30:27:56.99	67.6	70.1	52.2	19.2	−0.38

A520

Source Name	RA (h m s)	DEC (d m s)	S_{147} (TGSS) mJy	S_{147} mJy	S_{322} mJy	S_{1400} mJy	α_{322}^{147}
J045844.5+024425	04:58:44.47	02:44:24.72	371.9	366.3	189.7	82.0	−0.84
J045830.7+022516	04:58:30.67	02:25:16.32	899.9	828.1	325.2	70.5	−1.19
J045811.5+021517	04:58:11.47	02:15:16.92	150.9	145.5	64.3	15.0	−1.04
J045808.0+024254	04:58:07.99	02:42:53.64	83.2	72.1	33.8	8.3	−0.97
J045749.0+023539	04:57:48.98	02:35:39.12	89.5	83.0	31.2	6.6	−1.25
J045712.6+024729	04:57:12.55	02:47:29.04	1398.9	1317.1	574.2	127.1	−1.06
J045711.2+022854	04:57:11.21	02:28:54.48	149.6	129.1	79.5	31.1	−0.62
J045620.8+025446	04:56:20.81	02:54:46.08	1033.3	918.3	504.2	147.7	−0.76
J045620.4+033505	04:56:20.40	03:35:04.56	70.2	74.7	36.3	11.7	−0.92
J045557.2+033412	04:55:57.17	03:34:11.64	130.3	118.5	86.7	32.1	−0.40
J045556.0+021054	04:55:56.04	02:10:54.48	355.1	363.2	131.8	22.0	−1.29
J045549.3+034013	04:55:49.27	03:40:13.44	103.5	138.9	71.8	22.6	−0.84
J045539.2+025346	04:55:39.19	02:53:45.96	1909.4	1848.2	1059.4	314.5	−0.71
J045536.3+025902	04:55:36.26	02:59:02.04	141.1	160.8	90.4	54.7	−0.73
J045538.4+040332	04:55:38.40	04:03:31.68	69.7	69.9	46.8	13.0	−0.51
J045533.7+023953	04:55:33.70	02:39:52.56	188.3	173.9	94.0	27.5	−0.78
J045504.1+040528	04:55:04.08	04:05:28.32	51.2	62.8	23.2	13.2	−1.27
J045451.6+034031	04:54:51.58	03:40:31.08	492.9	457.6	286.3	84.2	−0.60
J045446.8+030245	04:54:46.78	03:02:44.52	63.4	70.3	39.6	10.8	−0.73
J045443.2+030659	04:54:43.25	03:06:59.04	103.9	98.4	47.9	11.7	−0.92
J045438.3+031605	04:54:38.26	03:16:04.80	144.9	165.5	118.0	45.7	−0.43
J045358.2+015339	04:53:58.18	01:53:39.48	114.9	105.3	45.4	14.4	−1.07
J045354.5+031010	04:53:54.50	03:10:09.84	41.4	51.2	32.8	12.9	−0.57
J045354.0+031218	04:53:54.02	03:12:18.36	94.6	105.2	60.9	18.8	−0.70
J045341.8+020913	04:53:41.81	02:09:12.96	366.5	363.5	187.1	64.4	−0.85
J045342.8+015628	04:53:42.84	01:56:28.32	88.3	67.0	39.2	11.9	−0.68
J045311.7+021007	04:53:11.74	02:10:06.96	145.3	147.1	96.7	36.6	−0.53

Source Name	RA (h m s)	DEC (d m s)	S_{147} (TGSS) mJy	S_{147} mJy	S_{322} mJy	S_{1400} mJy	α_{322}^{147}
J045307.2+023349	04:53:07.15	02:33:48.60	120.0	160.9	86.5	24.7	−0.79
J045305.1+020339	04:53:05.09	02:03:38.88	322.0	323.7	173.0	46.9	−0.80
J045239.5+021005	04:52:39.53	02:10:05.16	56.3	47.6	31.6	12.2	−0.52
J045224.7+030006	04:52:24.74	03:00:06.48	116.9	130.8	43.4	12.3	−1.41
J045221.2+023848	04:52:21.22	02:38:48.48	199.8	215.2	153.2	67.5	−0.43
J045216.1+032128	04:52:16.10	03:21:28.08	118.2	121.9	81.8	56.1	−0.51
J045215.1+021405	04:52:15.12	02:14:04.56	261.5	247.5	106.5	26.2	−1.07
J045120.8+020949	04:51:20.76	02:09:48.60	76.4	70.5	44.8	13.9	−0.58
J045118.5+035445	04:51:18.48	03:54:44.64	139.9	122.5	87.7	27.3	−0.43
J045110.5+030745	04:51:10.46	03:07:45.12	749.8	716.3	453.2	114.9	−0.58
J045057.9+020658	04:50:57.94	02:06:57.60	325.1	263.0	239.6	89.0	−0.12
J045053.4+023917	04:50:53.40	02:39:17.28	184.1	177.2	76.2	30.3	−1.07

A773

Source Name	RA (h m s)	DEC (d m s)	S_{147} (TGSS) mJy	S_{147} mJy	S_{322} mJy	S_{1400} mJy	α_{322}^{147}
J092438.0+512651	09:24:37.97	51:26:50.71	339.7	349.8	164.8	77.4	−0.92
J092417.1+510535	09:24:17.11	51:05:34.84	50.4	40.8	21.9	11.3	−0.77
J092411.9+513134	09:24:11.87	51:31:34.18	1118.4	1221.1	489.5	132.8	−1.12
J092347.5+510242	09:23:47.47	51:02:42.25	301.1	286.0	91.2	34.9	−1.40
J092317.8+521116	09:23:17.81	52:11:15.97	176.9	202.0	100.4	32.0	−0.86
J092302.2+513647	09:23:02.24	51:36:46.87	112.6	119.5	95.7	71.7	−0.27
J092257.2+513931	09:22:57.17	51:39:30.56	189.6	216.7	156.3	101.0	−0.40
J092258.5+523147	09:22:58.49	52:31:47.28	123.4	139.1	78.5	42.4	−0.70
J092251.8+522326	09:22:51.79	52:23:25.69	191.7	219.2	90.2	21.3	−1.09
J092226.7+521824	09:22:26.72	52:18:24.37	62.6	65.0	40.8	17.5	−0.57
J092219.8+515354	09:22:19.78	51:53:54.31	262.2	177.9	111.5	36.4	−0.57
J092217.2+513847	09:22:17.21	51:38:47.11	61.6	57.1	52.4	56.6	−0.11
J092149.4+522116	09:21:49.42	52:21:16.45	224.4	254.0	133.6	33.5	−0.79
J092123.4+511757	09:21:23.38	51:17:57.12	154.3	128.9	71.1	22.4	−0.73
J092124.7+520401	09:21:24.73	52:04:00.66	62.1	65.1	37.2	9.3	−0.69
J092117.1+511414	09:21:17.14	51:14:14.14	43.3	40.7	28.2	13.5	−0.45
J092055.5+511348	09:20:55.48	51:13:48.04	140.8	142.4	63.6	33.2	−0.99
J092030.5+520359	09:20:30.48	52:03:59.18	62.0	60.2	39.3	17.0	−0.53
J092006.8+505809	09:20:06.80	50:58:09.41	61.3	50.1	32.3	13.5	−0.54
J092000.8+523725	09:20:00.81	52:37:24.74	186.7	197.9	71.0	14.2	−1.26
J091941.7+520311	09:19:41.72	52:03:11.48	140.1	165.4	95.7	23.9	−0.67
J091925.7+522060	09:19:25.72	52:20:59.78	343.9	372.6	164.8	25.9	−1.00
J091915.9+525110	09:19:15.93	52:51:10.30	85.5	81.2	43.3	16.8	−0.77
J091821.0+521649	09:18:20.95	52:16:49.40	210.7	258.1	120.6	26.0	−0.93
J091804.4+511833	09:18:04.36	51:18:32.65	221.9	227.3	123.5	41.7	−0.75

Source Name	RA (h m s)	DEC (d m s)	S_{147} (TGSS) mJy	S_{147} mJy	S_{322} mJy	S_{1400} mJy	α_{322}^{147}
J091743.3+504302	09:17:43.33	50:43:01.56	105.4	113.9	59.1	22.6	−0.81
J091656.6+525344	09:16:56.57	52:53:44.30	59.3	51.1	17.2	7.2	−1.34
J091655.5+505614	09:16:55.47	50:56:13.92	149.0	119.4	71.0	23.2	−0.64
J091640.2+521202	09:16:40.21	52:12:01.51	154.2	157.1	79.4	14.1	−0.84
J091627.4+505754	09:16:27.38	50:57:54.22	79.4	89.5	59.0	27.7	−0.51
J091622.6+524020	09:16:22.56	52:40:19.56	42.8	30.1	19.6	9.0	−0.53
J091619.5+504025	09:16:19.45	50:40:25.25	75.4	85.5	68.8	31.1	−0.27
J091552.4+524658	09:15:52.41	52:46:58.48	79.3	73.5	16.5	4.7	−1.83
J091543.4+504201	09:15:43.35	50:42:00.97	60.9	59.5	29.6	10.5	−0.86
J091430.5+521548	09:14:30.50	52:15:47.88	136.2	169.2	126.8	43.1	−0.35
J091416.0+522003	09:14:16.02	52:20:02.62	62.6	58.1	38.7	8.6	−0.50
J091409.6+511433	09:14:09.60	51:14:32.96	230.9	235.5	79.6	35.5	−1.33
J091352.1+511949	09:13:52.13	51:19:48.86	54.6	51.5	34.5	11.4	−0.49
J091340.9+520416	09:13:40.94	52:04:15.67	211.2	223.1	125.1	21.2	−0.71
J091315.2+520853	09:13:15.24	52:08:53.48	1536.7	1746.7	997.1	216.6	−0.69
J091312.8+510152	09:13:12.81	51:01:52.14	95.0	99.7	52.4	12.1	−0.79
J091303.1+520849	09:13:03.14	52:08:48.52	50.0	44.4	18.9	6.9	−1.05
J091305.8+511433	09:13:05.84	51:14:32.96	72.5	73.8	32.7	5.8	−1.00
J091235.6+515351	09:12:35.58	51:53:50.89	111.7	105.1	76.2	24.8	−0.39
J091209.8+513808	09:12:09.79	51:38:07.55	71.0	51.7	24.1	10.9	−0.94

Bibliography

[1] McNamara,B. R., Wise,M., Nulsen,P. E. J., David,L. P., Sarazin,C. L., Bautz,M., Markevitch,M., Vikhlinin,A., Forman,W. R., Jones,C., and Harris,D. E. Chandra X-Ray Observations of the Hydra A Cluster: An Interaction between the Radio Source and the X-Ray-emitting Gas. *ApJL*, 534:L135–L138, (2000).

[2] McNamara,B. R., Nulsen,P. E. J., Wise,M. W., Rafferty,D. A., Carilli,C., Sarazin,C. L., and Blanton,E. L. The heating of gas in a galaxy cluster by X-ray cavities and large-scale shock fronts. *Nat.*, 433:45–47, (2005).

[3] Nulsen,P. E. J., McNamara,B. R., Wise,M. W., and David,L. P. The Cluster-Scale AGN Outburst in Hydra A. *ApJ*, 628:629–636, (2005).

[4] Million,E. T. and Allen,S. W. Chandra measurements of non-thermal-like X-ray emission from massive, merging, radio halo clusters. *MNRAS*, 399(3):1307–1327, (2009).

[5] Ferrari,C., Govoni,F., Schindler,S., Bykov,A. M., and Rephaeli,Y. Observations of Extended Radio Emission in Clusters. *SSRv*, 134:93–118, (2008).

[6] Feretti,L., Giovannini,G., Govoni,F., and Murgia,M. Clusters of galaxies: Observational properties of the diffuse radio emission. *A&ARv*, 20(1), (2012).

[7] Venturi,T., INAF, and di Radioastronomia,I. Observational properties of diffuse radio sources in Galaxy Clusters. Current knowledge and open questions. *MSAIt*, 82:499–506, (2011).

[8] Willson,M. A. G. Radio observations of the cluster of galaxies in Coma Berenices - the 5C4 survey. *MNRAS*, 151:1–44, (1970).

[9] Hanisch,R. J. Diffuse radio emission in the Coma cluster and Abell 1367 - Observations at 430 and 1400 MHz. *AJ*, 85:1565–1576, (1980).

[10] Kim,K.-T., Kronberg,P. P., Dewdney,P. E., and Landecker,T. L. The halo and magnetic field of the Coma cluster of galaxies. *ApJ*, 355:29, (1990).

[11] Giovannini,G., Feretti,L., Venturi,T., Kim,K.-T., and Kronberg,P. P. The halo radio source Coma C and the origin of halo sources. *ApJ*, 406:399, (1993).

[12] Deiss,B. M., Reich,W., Lesch,H., and Wielebinski,R. The large-scale structure of the diffuse radio halo of the Coma cluster at 1.4GHz. *A&A*, 321:55–63, (1997).

[13] Thierbach,M., Klein,U., and Wielebinski,R. The diffuse radio emission from the Coma cluster at 2.675 GHz and 4.85 GHz. *A&A*, 397:53–61, (2003).

[14] Liang,H., Hunstead,R. W., Birkinshaw,M., and Andreani,P. A Powerful Radio Halo in the Hottest Known Cluster of Galaxies 1E 0657-56. *ApJ*, 544:686–701, (2000).

[15] Markevitch,M., Gonzalez,A. H., David,L., Vikhlinin,A., Murray,S., Forman,W., Jones,C., and Tucker,W. A Textbook Example of a Bow Shock in the Merging Galaxy Cluster 1E 0657-56. *ApJL*, 567:L27–L31, (2002).

[16] Govoni,F., Markevitch,M., Vikhlinin,A., VanSpeybroeck,L., Feretti,L., and Giovannini,G. *Chandra* Temperature Maps for Galaxy Clusters with Radio Halos. *ApJ*, 605(2):695–708, (2004).

[17] Giovannini,G., Bonafede,A., Feretti,L., Govoni,F., Murgia,M., Ferrari,F., and Monti,G. Radio halos in nearby (z<0.4) clusters of galaxies. *A&A*, 507(3):16, (2009).

[18] Giovannini,G., Tordi,M., and Feretti,L. Radio halo and relic candidates from the NRAO VLA Sky Survey. *NewA*, 4:141–155, (1999).

[19] Kempner,J. C. and Sarazin,C. L. Radio Halo and Relic Candidates from the Westerbork Northern Sky Survey. *ApJ*, 548:639–651, (2001).

[20] Venturi,T., Giacintucci,S., Brunetti,G., Cassano,R., Bardelli,S., Dallacasa,D., and Setti,G. GMRT radio halo survey in galaxy clusters at z = 0.2-0.4. I. The REFLEX sub-sample. *A&A*, 463:937–947, (2007).

[21] Venturi,T., Giacintucci,S., Dallacasa,D., Cassano,R., Brunetti,G., Bardelli,S., and Setti,G. GMRT radio halo survey in galaxy clusters at z = 0.2-0.4. II. The eBCS clusters and analysis of the complete sample. *A&A*, 484:327–340, (2008).

[22] Kale,R., Venturi,T., Giacintucci,S., Dallacasa,D., Cassano,R., Brunetti,G., Macario,G., and Athreya,R. The Extended GMRT Radio Halo Survey. I. New upper limits on radio halos and mini-halos. *A&A*, 557:A99, (2013).

[23] Kale,R., Venturi,T., Giacintucci,S., Dallacasa,D., Cassano,R., Brunetti,G., Cuciti,V., Macario,G., and Athreya,R. The Extended GMRT Radio Halo Survey II: Further results and analysis of the full sample. *A&A*, 92:1–22, (2015).

[24] Macario,G., Venturi,T., Intema,H. T., Dallacasa,D., Brunetti,G., Cassano,R., Giacintucci,S., Ferrari,C., Ishwara-Chandra,C. H., and Athreya,R. 153 MHz GMRT follow-up of steep-spectrum diffuse emission in galaxy clusters. *A&A*, 141, (2013).

[25] Sarazin,C. L. The Energy Spectrum of Primary CosmicâRay Electrons in Clusters of Galaxies and Inverse Compton Emission. *ApJ*, 520(2):529–547, (1999).

[26] Brunetti,G. and Jones,T. W. Cosmic Rays in Galaxy Clusters and Their Nonthermal Emission. *IJMPD*, 23:1430007-98, (2014).

[27] Buote,D. A. On The Origin of Radio Halos in Galaxy Clusters. *ApJ*, pages 15–18, (2001).

[28] Cassano,R., Ettori,S., Giacintucci,S., Brunetti,G., Markevitch,M., Venturi,T., and Gitti,M. On the connection between giant radio halos and cluster mergers. *ApJL*, 721(2 PART 2):2008–2011, (2010).

[29] Giovannini,G. and Feretti,L. Radio halos in merging clusters. *Highlights of Astronomy*, 12:513–515, (2002).

[30] Brunetti,G., Venturi,T., Dallacasa,D., Cassano,R., Dolag,K., Giacintucci,S., and Setti,G. Cosmic Rays and Radio Halos in Galaxy Clusters: New Constraints from Radio Observations. *ApJ*, 670(1):L5–L8, (2007).

[31] van Weeren,R. J., de Gasperin,F., Akamatsu,H., Brüggen,M., Feretti,L., Kang,H., Stroe,A., and Zandanel,F. Diffuse Radio Emission from Galaxy Clusters. *SSRv*, 215:16, (2019).

[32] Govoni,F., Feretti,L., Giovannini,G., Böhringer,H., Reiprich,T. H., and Murgia,M. Radio and X-ray diffuse emission in six clusters of galaxies. *A&A*, 376:803–819, (2001).

[33] Bacchi,M., Feretti,L., Giovannini,G., and Govoni,F. Deep images of cluster radio halos. *A&A*, 400:465–476, (2003).

[34] Feretti,L., Boehringer,H., Giovannini,G., and Neumann,D. The radio and X-ray properties of Abell 2255. *A&A*, 317:432–440, (1997).

[35] Giacintucci,S., Venturi,T., Brunetti,G., Bardelli,S., Dallacasa,D., Ettori,S., Finoguenov,A., Rao,A. P., and Zucca,E. Spectral properties and origin of the radio halo in A3562. *A&A*, 440:867–879, (2005).

[36] Brunetti,G., Giacintucci,S., Cassano,R., Lane,W., Dallacasa,D., Venturi,T., Kassim,N. E., Setti,G., Cotton,W. D., and Markevitch,M. A low-frequency radio halo associated with a cluster of galaxies. *Nat.*, 455:944–947, (2008).

[37] Feretti,L., Orrù,E., Brunetti,G., Giovannini,G., Kassim,N., and Setti,G. Spectral index maps of the radio halos in Abell 665 and Abell 2163. *A&A*, 423(1):111–119, (2004).

[38] Orru',E., Murgia,M., Feretti,L., Govoni,F., Brunetti,G., Giovannini,G., Girardi,M., Setti,G., ., Orrù,E., Murgia,M., Feretti,L., Govoni,F., Brunetti,G., Giovannini,G., Girardi,M., and Setti,G. Low-Frequency study of two clusters of galaxies: A2744 and A2219. *A&A*, 467(3):943–954, (2007).

[39] Pizzo,R. F. and de Bruyn,a. G. Radio spectral study of the cluster of galaxies Abell 2255. *A&A*, 507:639–659, (2009).

[40] Kale,R. and Dwarakanath,K. S. Spectral index studies of the diffuse radio emission in abell 2256: Implications for merger activity. *ApJ*, 718(2):939–946, (2010).

[41] Shimwell,T. W., Brown,S., Feain,I. J., Feretti,L., Gaensler,B. M., and Lage,C. Deep radio observations of the radio halo of the bullet cluster 1E 0657-55.8. *MNRAS*, 440:2901–2915, (2014).

[42] Vacca,V., Feretti,L., Giovannini,G., Govoni,F., Murgia,M., Perley,R. A., and Clarke,T. E. Spectral index image of the radio halo in the cluster Abell 520, which hosts the famous bow shock. *A&A*, 561:A52, (2014).

[43] van Weeren,R. J., Röttgering,H. J. A., Intema,H. T., Rudnick,L., Brüggen,M., Hoeft,M., and Oonk,J. B. R. The "toothbrush-relic": evidence for a coherent linear 2-Mpc scale shock wave in a massive merging galaxy cluster? *A&A*, 546: A124, (2012).

[44] Hoang,D. N., Shimwell,T. W., Stroe,A., Akamatsu,H., Brunetti,G., Donnert,J. M. F., Intema,H. T., Mulcahy,D. D., Röttgering,H. J. A., van Weeren,R. J., Bonafede,A., Brüggen,M., Cassano,R., Chyży,K. T., Enßlin,T., Ferrari,C., de Gasperin,F., Gu,L., Hoeft,M., Miley,G. K., Orrú,E., Pizzo,R., and White,G. J. Deep LOFAR observations of the merging galaxy cluster CIZA J2242.8+5301. *MNRAS*, 20(July):1–20, (2017).

[45] Brunetti,G., Setti,G., Feretti,L., and Giovannini,G. Particle reacceleration in the Coma cluster: Radio properties and hard X-ray emission. *MNRAS*, 320(3):365–378, (2001).

[46] Brunetti,G. Particle acceleration and non-thermal emission from galaxy clusters. *JKAS*, pages 493–500, (2004).

[47] Petrosian,V. On the Nonthermal Emission and Acceleration of Electrons in Coma and Other Clusters of Galaxies. *ApJ*, 557:560–572, (2001).

[48] Fujita,Y., Takizawa,M., and Sarazin,C. L. Nonthermal Emissions from Particles Accelerated by Turbulence in Clusters of Galaxies. *ApJ*, 584:190–202, (2003).

[49] Brunetti,G. and Blasi,P. Alfvénic reacceleration of relativistic particles in galaxy clusters in the presence of secondary electrons and positrons. *MNRAS*, 363:1173–1187, (2005).

[50] Petrosian,V. and Bykov,A. M. Particle acceleration mechanisms. *SSRv*, 134(1-4): 207–227, (2008).

[51] Jaffe,W. J. Origin and transport of electrons in the halo radio source in the Coma cluster. *ApJ*, 25(1975):1–7, (1977).

[52] Miniati,F., Ryu,D., Kang,H., Jones,T. W., Cen,R., and Ostriker,J. P. Properties of Cosmic Shock Waves in Large-Scale Structure Formation. *ApJ*, 542:608–621, (2000).

[53] Blandford,R. and Eichler,D. Particle acceleration at astrophysical shocks: A theory of cosmic ray origin. *PhR*, 154:1–75, (1987).

[54] Markevitch,M., Govoni,F., Brunetti,G., and Jerius,D. Bow Shock and Radio Halo in the Merging Cluster A520. *ApJ*, 627:733–738, (2005).

[55] Gabici,S. and Blasi,P. Nonthermal Radiation from Clusters of Galaxies: The Role of Merger Shocks in Particle Acceleration. *ApJ*, 583:695–705, (2003).

[56] Kang,H., Ryu,D., and Jones,T. W. Diffusive Shock Acceleration Simulations of Radio Relics. *ApJ*, 756:97, (2012).

[57] Brüggen,M., Heinz,S., Roediger,E., Ruszkowski,M., and Simionescu,A. Shock heating by Fanaroff-Riley type I radio sources in galaxy clusters. *MNRAS*, 380: L67–L70, (2007).

[58] Brunetti,G., Cassano,R., Dolag,K., and Setti,G. On the evolution of giant radio halos and their connection with cluster mergers. *A&A*, 507:661–669, (2009).

[59] Cassano,R., Brunetti,G., and Venturi,T. The Connection between Radio Halos and Cluster Mergers and the Statistical Properties of the Radio Halo Population. *JApA*, 32:519–527, (2011).

[60] Dolag,K., Vazza,F., Brunetti,G., and Tormen,G. Turbulent gas motions in galaxy cluster simulations: the role of smoothed particle hydrodynamics viscosity. *MNRAS*, 364:753–772, (2005).

[61] Cassano,R. and Brunetti,G. Cluster mergers and non-thermal phenomena: a statistical magneto-turbulent model. *MNRAS*, 357(4):1313–1329, (2005).

[62] Cassano,R., Brunetti,G., and Setti,G. Statistics of giant radio haloes from electron reacceleration models. *MNRAS*, 369(4):1577–1595, (2006).

[63] Vazza,F., Tormen,G., Cassano,R., Brunetti,G., and Dolag,K. Turbulent velocity fields in smoothed particle hydrodymanics simulated galaxy clusters: scaling laws for the turbulent energy. *MNRAS*, 369:L14–L18, (2006).

[64] Churazov,E., Forman,W., Jones,C., Sunyaev,R., and Böhringer,H. XMM-Newton observations of the Perseus cluster - II. Evidence for gas motions in the core. *MNRAS*, 347:29–35, (2004).

[65] Schuecker,P., Finoguenov,A., Miniati,F., Böhringer,H., and Briel,U. G. Probing turbulence in the Coma galaxy cluster. *A&A*, 426:387–397, (2004).

[66] Jaffe,W. J. and Perola,G. C. Dynamical Models of Tailed Radio Sources in Clusters of Galaxies. *A&A*, 26:423, (1973).

[67] Pacholczyk,A. G. *Radio astrophysics. Nonthermal processes in galactic and extragalactic sources*. (1970).

[68] Komissarov,S. S. and Gubanov,A. G. Relic radio galaxies: evolution of synchrotron spectrum. *A&A*, 285:27–43, (1994).

[69] Dennison,B. Formation of radio halos in clusters of galaxies from cosmic-ray protons. *ApJL*, 239:L93–L96, (1980).

[70] Blasi,P. and Colafrancesco,S. Cosmic rays, radio halos and nonthermal X-ray emission in clusters of galaxies. *APh*, 12:169–183, (1999).

[71] Dolag,K. and Enßlin,T. A. Radio halos of galaxy clusters from hadronic secondary electron injection in realistic magnetic field configurations. *A&A*, 362:151–157, (2000).

[72] Bagchi,J., Durret,F., Neto,G. B. L., and Paul,S. Giant Ringlike Radio Structures Around Galaxy Cluster Abell 3376. *Sci*, 314:791–794, (2006).

[73] Brown,S., Duesterhoeft,J., and Rudnick,L. Multiple Shock Structures in a Radio-selected Cluster of Galaxies. *ApJL*, 727:L25, (2011).

[74] Vazza,F., Brunetti,G., and Gheller,C. Shock waves in Eulerian cosmological simulations: main properties and acceleration of cosmic rays. *MNRAS*, 395:1333–1354, (2009).

[75] Brüggen,M., Bykov,A., Ryu,D., and Röttgering,H. Magnetic Fields, Relativistic Particles, and Shock Waves in Cluster Outskirts. *SSRv*, 166:187–213, (2012).

[76] Enßlin,T. and Gopal-Krishna. Reviving fossil radio plasma in clusters of galaxies by adiabatic compression in environmental shock waves. *A&A*, 366:26–34, (2001).

[77] Clarke,T. E. and Ensslin,T. A. Deep 1.4 GHz Very Large Array Observations of the Radio Halo and Relic in Abell 2256. *AJ*, 131:2900–2912, (2006).

[78] van Weeren,R. J., Röttgering,H. J. A., Brüggen,M., and Hoeft,M. Particle Acceleration on Megaparsec Scales in a Merging Galaxy Cluster. *Sci.*, 330:347, (2010).

[79] Dolag,K., Bartelmann,M., and Lesch,H. SPH simulations of magnetic fields in galaxy clusters. *A&A*, 348:351–363, (1999).

[80] Brüggen,M., Ruszkowski,M., Simionescu,A., Hoeft,M., and Dalla Vecchia,C. Simulations of Magnetic Fields in Filaments. *ApJL*, 631:L21–L24, (2005).

[81] Roettiger,K., Burns,J. O., and Stone,J. M. A Cluster Merger and the Origin of the Extended Radio Emission in Abell 3667. *ApJ*, 518:603–612, (1999).

[82] Carilli,C. L. and Taylor,G. B. Cluster Magnetic Fields. *ARA&A*, 40:319–348, (2002).

[83] Bonafede,A., Feretti,L., Murgia,M., Govoni,F., Giovannini,G., and Vacca,V. Galaxy cluster magnetic fields from radio polarized emission. *ArXiv e-prints*, (2010).

[84] Kale,R. and Dwarakanath,K. S. Diffuse radio emission in abell 754. *ApJ*, 699(2): 1883–1890, (2009).

[85] Shimwell,T. W., Luckin,J., Brüggen,M., Brunetti,G., Intema,H. T., Owers,M. S., Röttgering,H. J. A., Stroe,A., van Weeren,R. J., Williams,W. L., Cassano,R., de Gasperin,F., Heald,G. H., Hoang,D. N., Hardcastle,M. J., Sridhar,S. S., Sabater,J., Best,P. N., Bonafede,A., Chyży,K. T., Enßlin,T. A., Ferrari,C., Haverkorn,M., Hoeft,M., Horellou,C., McKean,J. P., Morabito,L. K., Orrù,E., Pizzo,R., Retana-Montenegro,E., and White,G. J. A plethora of diffuse steep spectrum radio sources in Abell 2034 revealed by LOFAR. *MNRAS*, 459:277–290, (2016).

[86] Bonafede,A., Brüggen,M., Rafferty,D., Zhuravleva,I., Riseley,C. J., van Weeren,R. J., Farnes,J. S., Vazza,F., Savini,F., Wilber,A., Botteon,A., Brunetti,G., Cassano,R., Ferrari,C., de Gasperin,F., Orrú,E., Pizzo,R. F., Röttgering,H. J. A., and Shimwell,T. W. LOFAR discoveryof radio emission in MACS J0717.5+3745. *MNRAS*, 478:2927–2938, (2018).

[87] Botteon,A., Shimwell,T. W., Bonafede,A., Dallacasa,D., Brunetti,G., Mandal,S., van Weeren,R. J., Brüggen,M., Cassano,R., de Gasperin,F., Hoang,D. N., Hoeft,M., Röttgering,H. J. A., Savini,F., White,G. J., Wilber,A., and Venturi,T. LOFAR discovery of a double radio halo system in Abell 1758 and radio/X-ray study of the cluster pair. *MNRAS*, 478:885–898, (2018).

[88] Wilber,A., Brüggen,M., Bonafede,A., Savini,F., Shimwell,T., van Weeren,R. J., Rafferty,D., Mechev,A. P., Intema,H., Andrade-Santos,F., Clarke,A. O., Mahony,E. K., Morganti,R., Prandoni,I., Brunetti,G., Röttgering,H., Mandal,S., de Gasperin,F., and Hoeft,M. LOFAR discovery of an ultra-steep radio halo and giant head-tail radio galaxy in Abell 1132. *MNRAS*, 473:3536–3546, (2018).

[89] Kim,K.-T., Kronberg,P. P., Giovannini,G., and Venturi,T. Discovery of intergalactic radio emission in the Coma-A1367 supercluster. *Nat.*, 341:720–723, (1989).

[90] Venturi,T., Giovannini,G., and Feretti,L. High-sensitivity radio observations of the Coma cluster of galaxies. *AJ*, 99:1381–1396, (1990).

[91] Brown,S. and Rudnick,L. Diffuse radio emission in/around the Coma cluster: beyond simple accretion. *MNRAS*, 412:2–12, (2011).

[92] Clarke,T. E., Enßlin,T., Finoguenov,A., Intema,H., Pfrommer,C., van Weeren,R., Röttgering,H., and Oonk,R. The curious case of Abell 2256 . *MmSAI*, 82:547, (2011).

[93] Trasatti,M., Akamatsu,H., Lovisari,L., Klein,U., Bonafede,A., Brüggen,M., Dallacasa,D., and Clarke,T. The radio relic in Abell 2256: overall spectrum and implications for electron acceleration. *A&A*, 575:A45, (2015).

[94] van Weeren,R. J., Brunetti,G., Brüggen,M., Andrade-Santos,F., Ogrean,G. A., Williams,W. L., Röttgering,H. J. A., Dawson,W. A., Forman,W. R., de Gasperin,F., Hardcastle,M. J., Jones,C., Miley,G. K., Rafferty,D. A., Rudnick,L., Sabater,J., Sarazin,C. L., Shimwell,T. W., Bonafede,A., Best,P. N., Bîrzan,L., Cassano,R., Chyży,K. T., Croston,J. H., Dijkema,T. J., Enßlin,T., Ferrari,C., Heald,G., Hoeft,M., Horellou,C., Jarvis,M. J., Kraft,R. P., Mevius,M., Intema,H. T., Murray,S. S., Orrú,E., Pizzo,R., Sridhar,S. S., Simionescu,A., Stroe,A., van der Tol,S., and White,G. J. LOFAR, VLA, and Chandra Observations of the Toothbrush Galaxy Cluster. *ApJ*, 818:204, (2016).

[95] Govoni,F., Murgia,M., Feretti,L., Giovannini,G., Dallacasa,D., and Taylor,G. B. A2255: The first detection of filamentary polarized emission in a radio halo. *A&A*, 430:L5–L8, (2005).

[96] Bonafede,A., Feretti,L., Giovannini,G., Govoni,F., Murgia,M., Taylor,G. B., Ebeling,H., Allen,S., Gentile,G., and Pihlström,Y. Revealing the magnetic field in a distant galaxy cluster: discovery of the complex radio emission from MACS J0717.5 +3745. *A&A*, 503:707–720, (2009).

[97] van Weeren,R. J., Röttgering,H. J. A., Brüggen,M., and Cohen,A. Diffuse radio emission in the merging cluster MACS J0717.5+3745: the discovery of the most powerful radio halo. *A&A*, 505:991–997, (2009).

[98] Pandey-Pommier,M., Richard,J., Combes,F., Dwarakanath,K. S., Guiderdoni,B., Ferrari,C., Sirothia,S., and Narasimha,D. Low-frequency radio emission in the massive galaxy cluster MACS J0717.5 + 3745. *A&A*, 557:A117, (2013).

[99] van Weeren,R. J., Ogrean,G. A., Jones,C., Forman,W. R., Andrade-Santos,F., Pearce,C. J. J., Bonafede,A., Brüggen,M., Bulbul,E., Clarke,T. E., Churazov,E., David,L., Dawson,W. A., Donahue,M., Goulding,A., Kraft,R. P., Mason,B., Merten,J., Mroczkowski,T., Nulsen,P. E. J., Rosati,P., Roediger,E., Randall,S. W., Sayers,J., Umetsu,K., Vikhlinin,A., and Zitrin,A. Chandra and JVLA Observations of HST Frontier Fields Cluster MACS J0717.5+3745. *ApJ*, 835:197, (2017).

[100] Edge,A. C., Ebeling,H., Bremer,M., Röttgering,H., van Haarlem,M. P., Rengelink,R., and Courtney,N. J. D. The discovery of two distant, massive clusters of galaxies in the ROSAT All-Sky Survey. *MNRAS*, 339:913–924, (2003).

[101] Swarup,G. Giant metrewave radio telescope (GMRT). In *IAU Colloq. 131: Radio Interferometry. Theory, Techniques, and Applications*, volume 19 of *ASPCS*, pages 376–380, (1991).

[102] Athreya,R. A new approach to mitigation of radio frequency interference in interferometric data. *ApJ*, 696(1):885–890, (2009).

[103] Perley,R. A. and Butler,B. J. An Accurate Flux Density Scale from 50 MHz to 50 GHz. In *American Astronomical Society Meeting Abstracts #225*, volume 225 of *American Astronomical Society Meeting Abstracts*, page 311.06, (2015).

[104] Cornwell,T. and Fomalont,E. B. Self-Calibration. In *Synthesis Imaging in Radio Astronomy*, volume 6 of *Astronomical Society of the Pacific Conference Series*, page 185, (1989).

[105] Schwab,F. R. Relaxing the isoplanatism assumption in self-calibration; applications to low-frequency radio interferometry. *AJ*, 89:1076–1081, (1984).

[106] Sekhar,S. and Athreya,R. Two Procedures to Flag Radio Frequency Interference in the UV Plane. *AJ*, 156:9, (2018).

[107] Lal,D. V. *GMRT Observer's Manual*. NCRA-TIFR, (2013).

[108] Högbom,J. A. Aperture Synthesis with a Non-Regular Distribution of Interferometer Baselines. *A&AS*, 15:417, (1974).

[109] Clark,B. G. An efficient implementation of the algorithm 'CLEAN'. *A&A*, 89:377, (1980).

[110] Mohan,N. and Rafferty,D. PyBDSF: Python Blob Detection and Source Finder. Astrophysics Source Code Library, (2015).

[111] Intema,H. T., Jagannathan,P., Mooley,K. P., and Frail,D. A. The GMRT 150 MHz all-sky radio survey. First alternative data release TGSS ADR1. *A&A*, 598: A78, (2017).

[112] Condon,J. J., Cotton,W. D., Greisen,E. W., Yin,Q. F., Perley,R. A., Taylor,G. B., and Broderick,J. J. The NRAO VLA Sky Survey. *AJ*, 115:1693–1716, (1998).

[113] Taylor,M. B. TOPCAT STIL: Starlink Table/VOTable Processing Software. In Shopbell,P., Britton,M., and Ebert,R., editors, *Astronomical Data Analysis Software and Systems XIV*, volume 347 of *Astronomical Society of the Pacific Conference Series*, page 29, (2005).

[114] Rengelink,R. B., Tang,Y., de Bruyn,A. G., Miley,G. K., Bremer,M. N., Roettgering,H. J. A., and Bremer,M. A. R. The Westerbork Northern Sky Survey (WENSS), I. A 570 square degree Mini-Survey around the North Ecliptic Pole. *A&AS*, 124:259–280, (1997).

[115] Mahony,E. K., Morganti,R., Prandoni,I., van Bemmel,I. M., Shimwell,T. W., Brienza,M., Best,P. N., Brüggen,M., Calistro Rivera,G., de Gasperin,F., Hardcastle,M. J., Harwood,J. J., Heald,G., Jarvis,M. J., Mandal,S., Miley,G. K., Retana-Montenegro,E., Röttgering,H. J. A., Sabater,J., Tasse,C., van Velzen,S., van Weeren,R. J., Williams,W. L., and White,G. J. The Lockman Hole project: LOFAR observations and spectral index properties of low-frequency radio sources. *MNRAS*, 463:2997–3020, (2016).

[116] Feretti,L., Fusco-Femiano,R., Giovannini,G., and Govoni,F. The giant radio halo in Abell 2163. *A&A*, 373(1):106–112, (2001).

[117] Herbig,T. and Birkinshaw,M. Discovery of a Radio Halo Source in Abell 2163. In *American Astronomical Society Meeting Abstracts*, volume 26 of *Bulletin of the American Astronomical Society*, page 1403, (1994).

[118] Dallacasa,D., Brunetti,G., Giacintucci,S., Cassano,R., Venturi,T., Macario,G., Kassim,N. E., Lane,W., and Setti,G. Deep 1.4 GHz Follow-up of the Steep Spectrum Radio Halo in A521. *ApJ*, 699:1288–1292, (2009).

[119] Macario,G., Venturi,T., Brunetti,G., Dallacasa,D., Giacintucci,S., Cassano,R., Bardelli,S., and Athreya,R. The very steep spectrum radio halo in Abell 697. *A&A*, 517:A43, (2010).

[120] Maurogordato,S., Cappi,A., Ferrari,C., Benoist,C., Mars,G., Soucail,G., Arnaud,M., Pratt,G. W., Bourdin,H., and Sauvageot,J.-L. A 2163: Merger events in the hottest Abell galaxy cluster. I. Dynamical analysis from optical data. *A&A*, 481:593–613, (2008).

[121] Bourdin,H., Arnaud,M., Mazzotta,P., Pratt,G. W., Sauvageot,J.-L., Martino,R., Maurogordato,S., Cappi,A., Ferrari,C., and Benoist,C. A2163: Merger events in the hottest Abell galaxy cluster. *A&A*, 527:A21, (2011).

[122] Govoni,F. and Feretti,L. Magnetic Field in Clusters of Galaxies. *IJMPD*, (2004).

[123] Kellermann,K. I. and Owen,F. N. *Galactic and Extragalactic Radio Astronomy: Radio galaxies and quasars*, pages 563–602. (1988).

[124] Sarazin,C. L. The Physics of Cluster Mergers. In *Merging Processes in Galaxy Clusters*, volume 272 of *Astrophysics and Space Science Library*, pages 1–38, (2002).

[125] Marscher,A. P. Relativistic Jets in Active Galactic Nuclei. In *Relativistic Jets: The Common Physics of AGN, Microquasars, and Gamma-Ray Bursts*, volume 856 of *AIPCS*, pages 1–22, (2006).

[126] Rajpurohit,K., Hoeft,M., van Weeren,R. J., Rudnick,L., Röttgering,H. J. A., Forman,W. R., Brüggen,M., Croston,J. H., Andrade-Santos,F., Dawson,W. A., Intema,H. T., Kraft,R. P., Jones,C., and Jee,M. J. Deep VLA Observations of the Cluster 1RXS J0603.3+4214 in the Frequency Range of 12 GHz. *ApJ*, 852:65, (2018).

[127] Landau,L. D. and Lifshitz,E. M. *Fluid mechanics*. (1959).

[128] Giovannini,G., Feretti,L., and Stanghellini,C. The Coma cluster radio source 1253 + 275, revisited. *A&A*, 252:528–537, (1991).

[129] van Weeren,R. J., Andrade-Santos,F., Dawson,W. A., Golovich,N., Lal,D. V., Kang,H., Ryu,D., Brìggen,M., Ogrean,G. A., Forman,W. R., Jones,C., Placco,V. M., Santucci,R. M., Wittman,D., Jee,M. J., Kraft,R. P., Sobral,D., Stroe,A., and Fogarty,K. The case for electron re-acceleration at galaxy cluster shocks. *NatAs.*, 1:0005, (2017).

[130] Tribble,P. C. Magnetic fields and radio halos in galaxy clusters. In Lynden-Bell,D., editor, *Cosmical Magnetism*, pages 140–143, (1994).

[131] Schoenmakers,A. P., de Bruyn,A. G., Röttgering,H. J. A., van der Laan,H., and Kaiser,C. R. Radio galaxies with a 'double-double morphology' - I. Analysis of the radio properties and evidence for interrupted activity in active galactic nuclei. *MNRAS*, 315:371–380, (2000).

[132] Kaiser,C. R., Schoenmakers,A. P., and Röttgering,H. J. Radio galaxies with a 'double-double' morphology - II. the evolution of double-double radio galaxies and implications for the alignment effect in FRII sources. *MNRAS*, 315(2):381–394, (2000).

[133] Miley,G. and De Breuck,C. Distant radio galaxies and their environments. *A&ARv*, 15:67–144, (2008).

[134] Moffet,A. T. *Strong Nonthermal Radio Emission from Galaxies*, page 211. The University of Chicago Press, (1975).

[135] Beck,R. and Krause,M. Revised equipartition and minimum energy formula for magnetic field strength estimates from radio synchrotron observations. *AN*, 326: 414–427, (2005).

[136] Giacintucci,S., Venturi,T., Macario,G., Dallacasa,D., Brunetti,G., Markevitch,M., Cassano,R., Bardelli,S., and Athreya,R. Shock acceleration as origin of the radio relic in A 521? *A&A*, 486:347–358, (2008).

[137] Brunetti,G., Setti,G., and Comastri,A. Inverse Compton X-rays from strong FRII radio-galaxies. *A&A*, 325:898–910, (1997).

[138] Moffet,A. T. and Birkinshaw,M. A VLA survey of the three clusters of galaxies 0016 + 16, Abell 665, and Abell 2218. *AJ*, 98:1148–1174, (1989).

[139] Jones,M. and Saunders,R. Optimising H_0 determination from the X-ray plus Sunyaev-Zel'dovich route. In Zimmermann,H. U., Trümper,J., and Yorke,H., editors, *Roentgenstrahlung from the Universe*, pages 553–556, (1996).

[140] Giovannini,G. and Feretti,L. Halo and relic sources in clusters of galaxies. *NewA*, 5:335–347, (2000).

[141] Markevitch,M. and Vikhlinin,A. Merger Shocks in Galaxy Clusters A665 and A2163 and Their Relation to Radio Halos. *ApJ*, 563:95–102, (2001).

[142] Dasadia,S., Sun,M., Sarazin,C., Morandi,A., Markevitch,M., Wik,D., Feretti,L., Giovannini,G., Govoni,F., and Vacca,V. A Strong Merger Shock in Abell 665. *ApJL*, 820:L20, (2016).

[143] Gómez,P. L., Hughes,J. P., and Birkinshaw,M. A Merger Scenario for the Dynamics of Abell 665. *ApJ*, 540:726–740, (2000).

[144] Geller,M. J. and Beers,T. C. Substructure within clusters of galaxies. *PASP*, 94: 421–439, (1982).

[145] Vacca,V., Murgia,M., Govoni,F., Feretti,L., Giovannini,G., Orrù,E., and Bonafede,A. The intracluster magnetic field power spectrum in Abell 665. *A&A*, 514:A71, (2010).

[146] Giacintucci,S. Diffuse radio sources in colliding galaxy clusters . Low frequency follow up of the GMRT Radio Halo Survey. *MmSAI*, 82:541, (2011).

[147] Pearce,C. J. J., van Weeren,R. J., Andrade-Santos,F., Jones,C., Forman,W. R., Brüggen,M., Bulbul,E., Clarke,T. E., Kraft,R. P., Medezinski,E., Mroczkowski,T., Nonino,M., Nulsen,P. E. J., Randall,S. W., and Umetsu,K. VLA Radio Observations of the HST Frontier Fields Cluster Abell 2744: The Discovery of New Radio Relics. *ApJ*, 845:81, (2017).

[148] Boschin,W., Girardi,M., Spolaor,M., and Barrena,R. Internal dynamics of the radio halo cluster Abell 2744. *A&A*, 449:461–474, (2006).

[149] Kempner,J. C. and David,L. P. A Chandra view of the multiple merger in Abell 2744. *MNRAS*, 349:385–392, (2004).

[150] Eckert,D., Jauzac,M., Vazza,F., Owers,M. S., Kneib,J.-P., Tchernin,C., Intema,H., and Knowles,K. A shock front at the radio relic of Abell 2744. *MNRAS*, 461:1302–1307, (2016).

[151] Ensslin,T. A., Biermann,P. L., Klein,U., and Kohle,S. Cluster radio relics as a tracer of shock waves of the large-scale structure formation. *A&A*, 332:395–409, (1998).

[152] Hoeft,M. and Brüggen,M. Radio signature of cosmological structure formation shocks. *MNRAS*, 375:77–91, (2007).

[153] Ryu,D., Kang,H., Hallman,E., and Jones,T. W. Cosmological Shock Waves and Their Role in the Large-Scale Structure of the Universe. *ApJ*, 593:599–610, (2003).

[154] Pinzke,A., Oh,S. P., and Pfrommer,C. Giant radio relics in galaxy clusters: reacceleration of fossil relativistic electrons? *MNRAS*, 435:1061–1082, (2013).

[155] Ogrean,G. A., Brüggen,M., van Weeren,R. J., Röttgering,H., Croston,J. H., and Hoeft,M. Challenges to our understanding of radio relics: X-ray observations of the Toothbrush cluster. *MNRAS*, 433:812–824, (2013).

[156] Skillman,S. W., Xu,H., Hallman,E. J., O'Shea,B. W., Burns,J. O., Li,H., Collins,D. C., and Norman,M. L. Cosmological Magnetohydrodynamic Simulations of Galaxy Cluster Radio Relics: Insights and Warnings for Observations. *ApJ*, 765:21, (2013).

[157] Bonafede,A., Intema,H. T., Brüggen,M., Girardi,M., Nonino,M., Kantharia,N., van Weeren,R. J., and Röttgering,H. J. A. Evidence for Particle Re-acceleration in the Radio Relic in the Galaxy Cluster PLCKG287.0+32.9. *ApJ*, 785:1, (2014).

[158] Medezinski,E., Umetsu,K., Okabe,N., Nonino,M., Molnar,S., Massey,R., Dupke,R., and Merten,J. Frontier Fields: Subaru Weak-Lensing Analysis of the Merging Galaxy Cluster A2744. *ApJ*, 817:24, (2016).

[159] Finoguenov,A., Sarazin,C. L., Nakazawa,K., Wik,D. R., and Clarke,T. E. XMM-Newton Observation of the Northwest Radio Relic Region in A3667. *ApJ*, 715: 1143–1151, (2010).

[160] Botteon,A., Gastaldello,F., Brunetti,G., and Dallacasa,D. A shock at the radio relic position in Abell 115. *MNRAS*, 460:L84–L88, (2016).

[161] Paul,S., Iapichino,L., Miniati,F., Bagchi,J., and Mannheim,K. Evolution of Shocks and Turbulence in Major Cluster Mergers. *ApJ*, 726:17, (2011).

[162] Carretti,E., Brown,S., Staveley-Smith,L., Malarecki,J. M., Bernardi,G., Gaensler,B. M., Haverkorn,M., Kesteven,M. J., and Poppi,S. Detection of a radio bridge in Abell 3667. *MNRAS*, 430:1414–1422, (2013).

[163] Giacintucci,S., Venturi,T., Brunetti,G., Dallacasa,D., Mazzotta,P., Cassano,R., Bardelli,S., and Zucca,E. Testing the radio halo-cluster merger scenario. The case of RXC J2003.5-2323. *A&A*, 505:45–53, (2009).

[164] Owers,M. S., Randall,S. W., Nulsen,P. E. J., Couch,W. J., David,L. P., and Kempner,J. C. The Dissection of Abell 2744: A Rich Cluster Growing Through Major and Minor Mergers. *ApJ*, 728:27, (2011).

[165] Feretti,L., Bonafede,A., Giovannini,G., Govoni,F., and Murgia,M. Cosmic rays in magnetized intracluster plasma. *Highlights of Astronomy*, 15:459–460, (2010).

[166] Rizza,E., Burns,J. O., Ledlow,M. J., Owen,F. N., Voges,W., and Bliton,M. X-ray observations of distant Abell clusters. *MNRAS*, 301:328–342, (1998).

[167] Wang,Q. H. S., Giacintucci,S., and Markevitch,M. Bow Shock in Merging Cluster A520: The Edge of the Radio Halo and the Electron-Proton Equilibration Timescale. *ApJ*, 856:162, (2018).

[168] Wang,Q. H. S., Markevitch,M., and Giacintucci,S. The Merging Galaxy Cluster A520A Broken-up Cool Core, A Dark Subcluster, and an X-Ray Channel. *ApJ*, 833:99, (2016).

[169] Girardi,M., Barrena,R., Boschin,W., and Ellingson,E. Cluster Abell 520: a perspective based on member galaxies. A cluster forming at the crossing of three filaments? *A&A*, 491:379–395, (2008).

[170] Mahdavi,A., Hoekstra,H., Babul,A., Balam,D. D., and Capak,P. L. A Dark Core in Abell 520. *ApJ*, 668:806–814, (2007).

[171] Okabe,N. and Umetsu,K. Subaru Weak Lensing Study of Seven Merging Clusters: Distributions of Mass and Baryons. *PASJ*, 60:345–375, (2008).

[172] Jee,M. J., Mahdavi,A., Hoekstra,H., Babul,A., Dalcanton,J. J., Carroll,P., and Capak,P. A Study of the Dark Core in A520 with the Hubble Space Telescope: The Mystery Deepens. *ApJ*, 747:96, (2012).

[173] Clowe,D., Markevitch,M., Bradač,M., Gonzalez,A. H., Chung,S. M., Massey,R., and Zaritsky,D. On Dark Peaks and Missing Mass: A Weak-lensing Mass Reconstruction of the Merging Cluster System A520. *ApJ*, 758:128, (2012).

[174] Barrena,R., Boschin,W., Girardi,M., and Spolaor,M. Internal dynamics of the radio halo cluster Abell 773: a multiwavelength analysis. *A&A*, 467:37–48, (2007).

[175] Pizzo,R. F., de Bruyn,A. G., Bernardi,G., and Brentjens,M. A. Deep multi-frequency rotation measure tomography of the galaxy cluster A2255. *A&A*, 525: A104, (2011).

[176] Lindner,R. R., Baker,A. J., Hughes,J. P., Battaglia,N., Gupta,N., Knowles,K., Marriage,T. A., Menanteau,F., Moodley,K., Reese,E. D., and Srianand,R. The Radio Relics and Halo of El Gordo, a Massive z = 0.870 Cluster Merger. *ApJ*, 786:49, (2014).

[177] Giovannini,G., Feretti,L., Girardi,M., Govoni,F., Murgia,M., Vacca,V., and Bagchi,J. A giant radio halo in the low luminosity X-ray cluster Abell 523. *A&A*, 530:L5, (2011).

[178] Cassano,R., Brunetti,G., Röttgering,H. J. A., and Brüggen,M. Unveiling radio halos in galaxy clusters in the LOFAR era. *A&A*, 509:A68, (2010).

[179] Norris,R. P., Hopkins,A. M., Afonso,J., Brown,S., Condon,J. J., Dunne,L., Feain,I., Hollow,R., Jarvis,M., Johnston-Hollitt,M., Lenc,E., Middelberg,E., Padovani,P., Prandoni,I., Rudnick,L., Seymour,N., Umana,G., Andernach,H., Alexander,D. M., Appleton,P. N., Bacon,D., Banfield,J., Becker,W., Brown,M. J. I., Ciliegi,P., Jackson,C., Eales,S., Edge,A. C., Gaensler,B. M., Giovannini,G., Hales,C. A., Hancock,P., Huynh,M. T., Ibar,E., Ivison,R. J., Kennicutt,R., Kimball,A. E., Koekemoer,A. M., Koribalski,B. S., López-Sánchez,Á. R., Mao,M. Y., Murphy,T., Messias,H., Pimbblet,K. A., Raccanelli,A., Randall,K. E., Reiprich,T. H., Roseboom,I. G., Röttgering,H., Saikia,D. J., Sharp,R. G., Slee,O. B., Smail,I., Thompson,M. A., Urquhart,J. S., Wall,J. V., and Zhao,G.-B. EMU: Evolutionary Map of the Universe. *PASA*, 28:215–248, (2011).